

International Workshop on Light-Matter Coupling in Nitrides

Proceedings *R D8914-PH-03*

St. Nectaire, France, October 8-12, 2000 *N 68171-com-6255*



20010508 067

Guest Editors: A. Kavokin, B. Gil

Reprinted from Volume 183 Number 1

physica status solidi (a)

 WILEY-VCH

DISTRIBUTION STATEMENT A
Approved for Public Release
Distribution Unlimited

Program Committee

B. GIL (Chairman)
J.J. BAUMBERG
M. COLOCCI
A. DI CARLO
J.Y. DUBOZ
A. KAVOKIN
P. LEFEBVRE
J. MASSIES
B. MONEMAR
A. SHIELDS
M. SKOLNICK

Organizing Committee

A. KAVOKIN (Chairman)
P. DISSEIX (Secretary)
A. TRASSOUDAIN
J. LEYMAIRE
A. PIMPINELLI
G. MALPUECH

Sponsors

Thomson-CSF (France)
United States Navy (USA)
Spectra Physics (France)
ADDON (France)
JEOL (France)
LASMEA (France)
AIXTRON (Germany)
LASMEA (France)
University Blaise Pascal (France)

AD NUMBER	DATE	DTIC ACCESSION NOTICE
1. REPORT IDENTIFYING INFORMATION		REQUES 1. Put your on rever 2. Comple 3. Attach fo mailed 4. Use unc inform 5. Do not c for 6 to DTIC: 1. Assign 2. Return 20010508 067
A. ORIGINATING AGENCY Univ. Blaise Pascal, France		
B. REPORT TITLE AND/OR NUMBER Interact. between Light-Matter Coupling in Ritrodes		
C. MONITOR REPORT NUMBER R-D 8914-PH-03		
D. PREPARED UNDER CONTRACT NUMBER N68171-00-M-6255		
2. DISTRIBUTION STATEMENT APPROVED FOR PUBLIC RELEASE DISTRIBUTION UNLIMITED PROCEEDINGS		

DTIC

OCT 95

EDITIONS ARE OBSOLETE

physica status solidi (a)
applied research

Proceedings
of the
International Workshop
on
Light–Matter Coupling in Nitrides

St. Nectaire, France, October 8–12, 2000

Guest Editors: A. Kavokin, B. Gil

Reprinted from

Volume 183 · Number 1 · Pages 1 to 206 · January 2001

 **WILEY-VCH**

Where to order:

Please place your order with

WILEY-VCH, P.O. Box 101161, D-69451 Weinheim, FRG; telephone: (06201)606152;
telefax: (06201)606184; telex: 467155 vchwh d, e-mail: subservice@wiley-vch.de.

For our American customers:

physica status solidi (b), ISSN 0370-1972, is published monthly by WILEY-VCH Verlag Berlin GmbH, Böhrlingstr. 10, D-13086 Berlin, Germany, and distributed by John Wiley & Sons, Inc., Distribution Centre, 1 Wiley Drive, Somerset, New Jersey 08875-1272; telephone: (908) 469-4400; fax: (908) 302-2300; telex: 833434.

Annual subscription price 2000: US\$ 3088.00 including postage and handling.

Personal rate US\$ 258.00.

Periodicals postage paid at Jamaica, NY 11431. Air freight and mailing in the USA by Publications Expediting Services Inc., 200 Meacham Ave., Elmont NY 11003. Send address changes to: physica status solidi, c/o Publications Expediting Services Inc., 200 Meacham Ave., Elmont NY 11003.

Editorial Note:

"physica status solidi (a)" undertakes that an original paper *accepted for publication* before the 23rd of any month will be published within 50 days of this date unless the author requests a postponement. In special cases there may be some delay between *receipt* and *acceptance* of a paper due to the review and, if necessary, revision of the paper.

physica status solidi (a) — applied research

Editor-in-Chief: Professor Dr. Martin Stutzmann, Böhrlingstr. 10, D-13086 Berlin or
Am Coulombwall, D-85748 Garching; telephone: (089) 2891 2760.

Managing Editor: Dr. Stefan Hildebrandt.

Editorial Office: Böhrlingstr. 10, D-13086 Berlin, telephone: (030) 470 31 331,
telefax: (030) 470 31 334.

Editorial Staff: Dr. Hans-Jürgen Hänsch, Dr. Horst Lange, Dipl.-Phys. Karin Müller,
Prof. Dr. Martin Stutzmann (consulting: Dr. Siegfried Oberländer).

Publishers: WILEY-VCH Verlag Berlin GmbH, Böhrlingstr. 10, D-13086 Berlin; telephone:
(030) 470 31 350 or 470 31 325; telefax: (030) 470 31 399; Bank account: Dresdner
Bank Weinheim, account no. 754 624 500; BLZ: 670 800 50.

Managing Director: Dr. Eva E. Wille.

Advertisement: telephone: (030) 470 31 325.

Production: Druckhaus „Thomas Müntzer“ GmbH, D-99947 Bad Langensalza.

"physica status solidi (a)" is published in twelve numbers (six volumes) per year, in 2001 with increased frequency of fifteen numbers (six volumes). The annual subscription price 2001 in Europe is € 2698.— (DM 5276.83); in the Rest of the World \$ 3548.00 incl. postage and handling; personal rate in Europe € 218.— (DM 426.37); in the Rest of the World \$ 298.00.

The publisher must be notified of a cancellation of a subscription not later than three months before the end of the calendar year. After that date the subscription is automatically prolonged for another year.

Authorization to photocopy items for internal or personal use, or the internal or personal use of specific clients, is granted by WILEY-VCH Verlag Berlin GmbH, provided that the base fee of US\$ 17.50 per copy, plus US\$ 0.50 per page is paid directly to Copyright Clearance Center, 27 Congress Street, SALEM, MA 01970, USA. For those organizations that have been granted a photocopy license by CCC, a separate system of payment has been arranged. The fee code for users of the Transactional Reporting Service is: 0031-8965/98 \$ 17.50 + 0.50.

All rights reserved (including those of translations into foreign languages). No part of this issue may be reproduced in any form, by photoprint, microfilm or any other means, nor transmitted or translated into a machine language, without written permission from the publishers.

© 2001 by WILEY-VCH Verlag Berlin GmbH. Printed in the Federal Republic of Germany.

Printed on chlorine- and acid-free paper.

Contents

Papers presented at the International Workshop on Light-Matter Coupling in Nitrides, St. Nectaire, France, October 8–12, 2000

Preface	3–4
Computed Growth Rates of (001)GaN Substrates in the Hydride Vapour Phase Method R. CADORET, A. TRASSOUDAINE, and E. AUJOL	5–9
Exciton–Light Interaction in Three-Dimensional Microcavities L.C. ANDREANI, G. PANZARINI, and J.-M. GÉRARD	11–16
Photonic Band Gap Microcavities in Nitrides M. LE VASSOR D'YERVILLE, D. CASSAGNE, and C. JOUANIN	17–22
<i>Editor's Choice</i>	
Drift and Diffusion of Exciton–Polaritons in a Graded Quantum Micocavity B. SERMAGE, G. MALPUECH, A.V. KAVOKIN, and V. THIERRY-MIEG	23–27
Evidence of Polariton Stimulation in Semiconductor Microcavities F. BŒUF, R. ANDRÉ, R. ROMESTAIN, LE SI DANG, E. PÉRONNE, J.F. LAMPIN, D. HU- LIN, and A. ALEXANDROU	29–33
Dielectric Microcavity in GaN/Si J.-Y. DUBOZ, L. DUA, G. GLASTRE, P. LEGAGNEUX, J. MASSIES, F. SEMOND, and N. GRANDJEAN	35–39
Radiative and Nonradiative Recombination Processes in GaN-Based Semiconductors Y. KAWAKAMI, K. OMAE, A. KANETA, K. OKAMOTO, T. IZUMI, S. SAIJOU, K. INOUE, Y. NARUKAWA, T. MUKAI, and SG. FUJITA	41–50
Absorption Spectroscopy and Band Structure in Polarized GaN/Al _x Ga _{1-x} N Quantum Wells C. WETZEL, M. KASUMI, H. AMANO, and I. AKASAKI	51–60
Reduction of Carrier In-Plane Mobility in Group-III Nitride Based Quantum Wells: The Role of Internal Electric Fields M. GALLART, P. LEFEBVRE, A. MOREL, T. TALIERCIO, B. GIL, J. ALLÈGRE, H. MATHIEU, B. DAMILANO, N. GRANDJEAN, and J. MASSIES	61–66
Optical Properties of Cubic Gallium Nitride on SiC/Si Pseudo-Substrates C. BRU-CHEVALLIER, S. FANGET, A. PHILIPPE, C. DUBOIS, E. MARTINEZ-GUERRERO, B. DAUDIN, P. ABOUGHÉ NZÉ, and Y. MONTEIL	67–73
Propagation of Exciton–Polaritons in Nitride-Based Multiple Quantum Wells G. MALPUECH and A. KAVOKIN	75–80

II

Tuning Optical Properties of GaN-Based Nanostructures by Charge Screening A. DI CARLO	81-85
Exciton/Free-Carrier Plasma in GaN-Based Quantum Wells: Scattering and Screening M.E. PORTNOI and I. GALBRAITH	87-90
Impact of Internal Electric Field and Localization Effect on Quantum Well Excitons in AlGaIn/GaN/InGaIn Light Emitting Diodes S.F. CHICHIBU, T. SOTA, K. WADA, O. BRANDT, K.H. PLOOG, S.P. DENBAARS, and S. NAKAMURA	91-98
Optical and Structural Properties of Quantum Dots in Wide-Bandgap Semiconductors M. STRASSBURG, A. HOFFMANN, I.L. KRESTNIKOV, and N.N. LEDENTSOV	99-104
Optical Properties and Lasing in (In,Al)GaN Structures S. BIDNYK, G.H. GAINER, S.K. SHEE, J.B. LAM, B.D. LITTLE, T. SUGAHARA, J. KRASIN- SKI, Y.H. KWON, G.H. PARK, S.J. HWANG, J.J. SONG, G.E. BULMAN, and H.S. KONG	105-109
Exciton Binding Energies and Oscillator Strengths in GaAsN-GaAs Quantum Wells B. GIL and P. BIGENWALD	111-115
A Mystery Wrapped in an Enigma: Optical Properties of InGaIn Alloys K.P. O'DONNELL	117-120
Optical and Electronic Properties of GaN Based Heterostructures: A Self-Consistent Time-Dependent Approach A. REALE, A. DI CARLO, P. LUGLI, and A. KAVOKIN	121-124
Temperature Induced Enhancement of the Exciton Binding Energy in Nitride Quan- tum Structures P. BIGENWALD, B. GIL, A. KAVOKIN, and P. CHRISTOL	125-128
Phonon Replica Dynamics in High Quality GaN Epilayers and AlGaIn/GaN Quan- tum Wells D. ALDERIGHI, A. VINATIERI, F. BOGANI, M. COLOCCI, S. GOTTARDO, N. GRAND- JEAN, and J. MASSIES	129-134
First Observations of 2D Photonic Crystal Band Structure in GaN-Sapphire Epitaxial Material D. COQUILLAT, A. RIBAYROL, R.M. DE LA RUE, M. LE VASSOR D'YERVILLE, D. CAS- SAGNE, and C. JOUANIN	135-138
Absorption and Emission of (In,Ga)N/GaN Quantum Wells Grown by Molecular Beam Epitaxy L. SIOZADE, P. DISSEIX, A. VASSON, J. LEYMARIE, B. DAMILANO, N. GRANDJEAN, and J. MASSIES	139-143
Buried Dielectric Mirrors for the Lateral Overgrowth of GaN-Based Microcavities R.W. MARTIN, P.R. EDWARDS, R. PECHARROMAN-GALLEGO, C. TRAGER-COWAN, T. KIM, H-S. KIM, K-S. KIM, I.M. WATSON, M.D. DAWSON, T.F. KRAUSS, J.H. MARSH, and R.M. DE LA RUE	145-149
Time-Resolved Photoluminescence in Strained GaN Layers G. POZINA, N.V. EDWARDS, J.P. BERGMAN, B. MONEMAR, M.D. BREMSER, and R.F. DAVIS	151-155

III

Inelastic Light Scattering by Phonons in Hexagonal GaN–AlN Nanostructures J. GLEIZE, F. DEMANGEOT, J. FRANDON, M.A. RENUCCI, M. KUBALL, B. DAUDIN, and N. GRANDJEAN	157–161
Growth by Molecular Beam Epitaxy and Optical Properties of a Ten-Period AlGaN/AlN Distributed Bragg Reflector on (111)Si F. SEMOND, N. ANTOINE-VINCENT, N. SCHNELL, G. MALPUECH, M. LEROUX, J. MAS- SIES, P. DISSEIX, J. LEYMARIE, and A. VASSON	163–167
Investigation of Low-Resistance Metal Contacts on p-Type GaN Using the Linear and Circular Transmission Line Method A. WEIMAR, A. LELL, A. BRÜDERL, S. BADER, and V. HÄRLE	169–175
Photon Recycling White Light Emitting Diode Based on InGaN Multiple Quantum Well Heterostructure V.V. NIKOLAEV, M.E. PORTNOI, and I. ELIASHEVICH	177–182
Optical Eigenmodes of a Spherical Microcavity R.A. ABRAM, S. BRAND, M.A. KALITEEVSKI, and V.V. NIKOLAEV	183–187
Study of MBE-Grown GaN/AlGaN Quantum Well Structures by Two Wavelength Excited Photoluminescence J.M. ZANARDI OCAMPO, H. KLAUSING, O. SEMCHINOVA, J. STEMMER, M. HIRASAWA, N. KAMATA, and K. YAMADA	189–195
Defect Reduction in HVPE Growth of GaN and Related Optical Spectra T. PASKOVA, P.P. PASKOV, V. DARAKCHIEVA, S. TUNGASMITA, J. BIRCH, and B. MONEMAR	197–203

Preface

This volume contains the paper versions of some of the contributions to the International Workshop on Light-Matter Coupling in Nitrides which was held in Saint-Nectaire, October 8–12, 2000. This workshop was an append manifestation of the contract “Clermont”, Physics of nitrides based microcavities, funded by the Commission of the European Communities and that assembles the Universities of Clermont-Ferrand, Florence, Linköping, Montpellier, Sheffield, Southampton, Rome, and the CNRS laboratory of Sophia-Antipolis.

GaN and its related materials appear to be extremely promising for opto-electronic and electronic applications. It is often said that GaN is likely to become one of the “materials of the 21st century”. The nitrides’ community includes brilliant researchers and engineers, which are used to meet and exchange their ideas at the occasions of crowded conferences that are both material science- and basic-physics oriented. The rapid developments of the fields of the passed years have recently brought into the play a lot of scientists devoted to what is said to be more fundamental physical effects, and who continue or gave up to work on traditionally studied GaAs-based quantum structures. Optics of excitons in low-dimensional semiconductor structures is a subject that attracted many of these physicists during the past three decades. A variety of intriguing phenomena caused by the exciton–light coupling in quantum wells, wires, dots and microcavities have made this area of solid state physics really delightful for the experts of quantum mechanics and optics. The nitrides represent a domain of natural interest for the adepts of exciton–light coupling, since as we published it, the strength of this coupling in GaN is an order of magnitude larger than in GaAs. So, we felt that there were strong objective factors for offering to this community, a forum towards the presentation of the potentialities of the nitrides for the investigations of fundamental physics phenomena such as the strength of exciton–light coupling interaction. To ensure the optimized conditions for scientific exchanges and a lively atmosphere, we have decided to start a series of small-format and high scientific level meetings strictly restricted to the light–matter coupling in nitrides.

We have then suggested this event to a number of well-known scientists working in two above-mentioned areas in Japan, USA, European Union and Russia. They felt immediately very excited by the idea, and they agreed to attend this workshop at St.Nectaire. Many interesting contributions have been received from the Great Britain, USA, France, Germany and other countries. Finally, the scientific program of the workshop appeared to be quite intensive and the scientific level of the contributed papers was extremely high.

Now, after the end of the workshop, we can confirm that the idea of its organization was fruitful. Actually, it had an outstanding success that has left behind our most optimistic expectations. And we should say honestly that this was not only because of its high-level scientific content. We must thank also the great French gastronomy, which made our stay in St.Nectaire also to be some kind of luxury vacation. During these four days in October 2000 we have been accommodated in the comfortable hotel “Mercure” in the beautiful medieval village of St.Nectaire, where we were offered delicious lunches and dinners accompanied by unlimited quantities of wine. An in-formal relaxing atmosphere stimulates the exchange of ideas, makes contacts to be easier, and even occasionally, via spontaneous brainstorming, furnishes the opportunity to resolve complicated physical problems.

The Workshop has coincided with an award of a Nobel Prize on Physics to Zh. Alferov, H. Kroemer and J.S. Kilby for their pioneering contributions to the development of fast electronics and optoelectronics. This was a good new not only for Russian participants whom used to work with Zh. Alferov, but also for all of us working on semiconductor heterostructures. A special night "session" was improvised to celebrate this event.

In this brief preface, we cannot list all the new important findings presented in St.Nectaire. The only topic we that would like to emphasize is the *strong coupling regime* in GaN-based microcavities. You will not find a paper on that in this volume. Though Prof. Arakawa and Dr. Duboz paved the way towards this observation, the strong coupling condition has not yet been achieved up to now. It is a challenge for many of us to obtain it experimentally. A tough international competition for this ambitious objective is under way. We may hope that at the occasion of the next International Workshop on the Light-Matter Coupling in Nitrides (to be organized in 2001, September 26–29, in Rome by Professor Aldo Di Carlo), the experimental evidence for the strong coupling regime in nitrides will be reported.

We would like to wish you a pleasant reading. Just one advice: why not to read it with a glass of red wine and a piece of cheese? In this way you will better feel the relaxing atmosphere of St.Nectaire!

Alexey Kavokin and Bernard Gil
Clermont-Ferrand
October 17, 2000

phys. stat. sol. (a) **183**, 5 (2001)

Subject classification. 68.03.Fg; 68.43.Mn; S7.14

Computed Growth Rates of (001) GaN Substrates in the Hydride Vapour Phase Method

R. CADORET¹⁾, A. TRASSOUDAIN, and E. AUJOL

*LASMEA, UMR 6602, CNRS, Université Blaise Pascal de Clermont Ferrand,
Les Cézeaux, F-63177 Aubière cedex, France*

(Received October 8, 2000)

A theoretical model developed to account for the (001) GaN growth by hydride vapour phase epitaxy in H₂ or neutral carrier gases is applied to investigate the variation of the growth rate with the temperature and input partial pressure of GaCl. The curves computed by taking into account the mass transfer and GaN parasitical depositions illustrate the possibilities of the model in analysing and predicting the experimental results, other than the deposition obtained in N₂/H₂ mixtures without parasitical nucleation at very negative supersaturation values, which seems to indicate a third chlorine desorption mechanism.

1. Introduction The modelling of the Hydride Vapour Phase Epitaxy (HVPE) of GaN in the (001) direction has been previously published in detail [1]. (001) GaAs was used as model [2] based on the numerous experiments carried out under various conditions of the chloride method. As explained in [1] the only experimental curves available for computing the model parameters in the GaN HVPE system were the curves reported by Seifert et al. [3]. With respect to the GaAs model we have only added a HCl adsorption step in agreement with the quantum chemical study of Seifert et al. [4] and we have not overlooked the GaN adsorption. The objective of this paper is only to present a few theoretical results making it possible to approach the mass transfer and parasitical nucleation effects on the growth rate. In the first part of the paper we recall briefly the physics of the model, then we discuss the theoretical curves obtained by Seifert et al. [3] and Paskova et al. [5]. These parts are followed by a short conclusion.

2. Growth Mechanisms The growth process of the model is a surface process involving the adsorption of NH₃ molecules, the adsorption of N atoms resulting from NH₃ decomposition, then the adsorption of GaCl molecules on the N atoms and finally the chlorine desorption.

Two desorption mechanisms of chlorine are considered, desorption in HCl_g molecules following a surface reaction with H_{2g} leading to an intermediate HCl adsorption state, and desorption in GaCl_{3g} molecules following an absorption of GaCl on two GaCl underlying molecules, according to the following reactions:



¹⁾ Present address: 3, rue Emile Zola, F-63400 Chamalières, France;
e-mail: Robert.Cadoret@wanadoo.fr



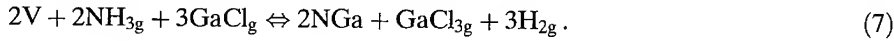
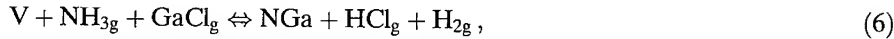
where the subscript g is used for gas phase species.

The two mechanisms are labelled H_2 and GaCl_3 mechanisms. They are approached by applying the Bragg-Williams approximation to a one-monolayer model of adsorption on a (001) Ga surface. The surface coverage θ_V of the Ga surface sites, labelled as V, free for the NH_3 adsorption is then expressed by

$$\theta_V = 1 - \sum_{i \neq V} \theta_i = 1 - \theta_{\text{NH}_3} - \theta_N - \theta_{\text{NGaCl}} - \theta_{\text{HCl}} - \theta_{\text{GaCl}_3} \theta_{\text{NGa}}, \quad (5)$$

where the admolecules NGa-HCl and 2NGa-GaCl_3 are denoted as HCl and GaCl_3 .

The two overall reactions corresponding to the two growth mechanisms can be written as



The GaCl_3 formation reaction in the gas phase is



The spiral growth and step flow mechanisms are applied to the surface diffusion of both NGa and NGaCl molecules. The solutions of the diffusion equations are approached in a simple way by considering separate balance equations. The θ_V surface coverage is computed by considering surface-vapour equilibrium at a distance of the steps much larger than the diffusion mean free paths of NGa and NGaCl molecules. These approximations gave a good agreement between the computed and experimental curves of the GaAs growth by the chloride method [2]. The growth rate so obtained was the product of the surface diffusion term by the maximal velocity, V_{GMax} , reached for a distance between steps higher than the double of the NGa and NGaCl mean free paths. The V_{GMax} expressions in the H_2 and GaCl_3 mechanisms are

$$V_{\text{GMaxH}_2} = k_{\text{H}_2} \theta_V \frac{P_{\text{NH}_3} P_{\text{GaCl}}}{P_{\text{H}_2} K_6(T)} \frac{\gamma}{(1 + \gamma)} \exp\left(-\frac{\varepsilon_{\text{H}_2}}{kT}\right), \quad (9)$$

$$V_{\text{GMaxGaCl}_3} = k_{\text{GaCl}_3} \theta_V \frac{P_{\text{NH}_3}^2 P_{\text{GaCl}}^3}{P_{\text{H}_2}^3 K_7(T)} \frac{\left((1 + \gamma)^2 - \frac{P_{\text{GaCl}_3}}{P_{\text{GaCl}_{3g}}^e}\right)}{(1 + \gamma)^2} \exp\left(-\frac{\varepsilon_{\text{GaCl}_3}}{kT}\right). \quad (10)$$

The pre-exponential terms include the θ_V surface coverage, the P_i partial pressures, the relative supersaturation, the degree of excess and the k_i terms explicitly expressed in [1]. ε_i are the activation energy terms. $P_{\text{GaCl}_{3g}}^e$ is the homogeneous GaCl_3 equilibrium partial pressure. The relative supersaturation is the degree of excess of the deposition reaction minus one, defined in the H_2 and GaCl_3 mechanism by the relations

$$\frac{P_{\text{NH}_3} P_{\text{GaCl}}}{P_{\text{H}_2} P_{\text{HCl}} K_6(T)} = 1 + \gamma, \quad (11)$$

$$\frac{P_{\text{NH}_3}^2 P_{\text{GaCl}}^3}{P_{\text{H}_2}^3 P_{\text{GaCl}_3} K_7(T)} = (1 + \gamma)^2 \frac{P_{\text{GaCl}_{3g}}^e}{P_{\text{GaCl}_3}} \quad (12)$$

with

$$P_{\text{GaCl}_3}^e = \frac{P_{\text{GaCl}} P_{\text{HCl}}^2}{P_{\text{H}_2} K_8(T)}, \quad (13)$$

$K_i(T)$ is the equilibrium constant of the i -th reaction.

3. Research of the Mass Transfer and Parasitical Nucleation Effects In most of the published experiments of GaN epitaxy by HVPE the degrees of excess of the deposition reactions are so high, that the ratios between the relative supersaturations and the corresponding degrees of excess are very close to unity. The kinetics are then proportional to the vacant surface site coverage, to the source species concentrations and to the reverse of the hydrogen concentration. The equilibrium constants, the activation terms and the value of θ_v mainly govern the kinetic variations with the substrate temperature. The H_2 concentration in N_2 , Ar or He gas transport systems mainly depends on the rate of NH_3 decomposition. The mass transfer reduces the partial pressures of the source species and increases the partial pressures of the produced species. The resulting increase of the H_2 partial pressure can induce a H_2 mechanism in a neutral input atmosphere. The mass of GaN deposited on the substrate has the same effect: if high it can reduce the degrees of excess to a value close to unity. The mass transfer effect is approached by considering a diffusion layer thickness equal to the velocity gradient thickness of an established Poiseuille regime, providing that the substrate is parallel to the flow and that the total flow is not too low. When the substrate makes an angle with respect to the horizontal plane, the mass transfer effect can be approached by varying the wall-substrate distance, equal to the double of the distance diffusion layer thickness in the model.

All these effects are illustrated in Figs. 1–3. The experimental points measured by Seifert et al. [3] in H_2 and He atmospheres and the related kinetic theoretical curves (dashed lines) are plotted in Fig. 1. The solid curves represent the results computed by assuming a substrate-wall distance of 1.5 cm. In H_2 atmosphere the growth rate increases slightly with $1/T$ up to about 1050 K. At lower temperatures the kinetic slope arising from the surface saturation by HCl and GaCl adsorptions appears progressively. Figure 1 shows that in He atmosphere the H_2 vapour concentration enhancement re-

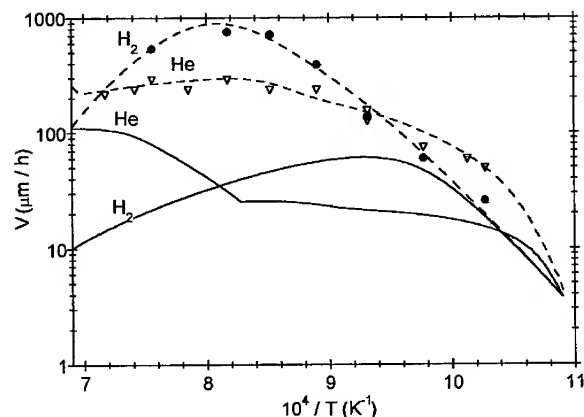


Fig. 1. Experimental growth rates measured by Seifert et al. [3] in H_2 and He as carrier gas on substrates 3° misoriented from the (001) orientation (full circles and empty triangles, respectively). The theoretical growth kinetics obtained by matching the experimental points and the growth rates deduced from these curves by taking into account the mass transfer are drawn by dashed and solid lines

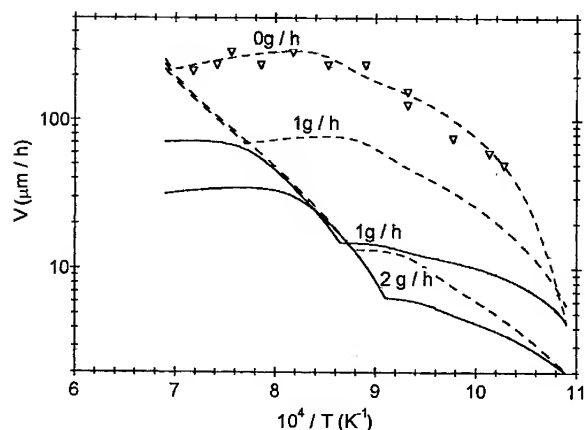


Fig. 2. Theoretical kinetics and growth rates taking into account the mass transfer are drawn by dashed and solid lines, respectively, considering parasitical deposition rates of 0, 1 and 2 g/h on the substrate. The experimental conditions of Seifert et al. [3] in He (empty triangles) have been used

sulting from the mass transfer effect shifts the transition point between the H_2 and $GaCl_3$ mechanisms from 1430 to 1220 K. The theoretical curve exhibits the H_2 mechanism kinetic slope in the range $1400\text{ K} < T < 1220\text{ K}$. According to the computed surface coverage results this kinetic comportment is mainly due to the θ_v decrease, resulting from the $GaCl$ surface coverage increase from 0.75 at 1430 K to a value close to unity at 1220 K. The solid lines drawn in Fig. 2 show that the transition point between the two mechanisms is moved from 1220 to 1175 and 1111 K considering GaN parasitical deposition rates of 1 and 2 g/h on the substrate. The kinetic curves corresponding to 0, 1 and 2 g/h are drawn by dashed lines. The emergence point of the H_2 mechanism slope moves from 1400 to 1280 and 1210 K. At 2 g/h of parasitical deposited mass the growth rate value is $35\text{ }\mu\text{m/h}$ at temperatures higher than 1210 K and $8\text{ }\mu\text{m/h}$ in the range 1111–960 K.

The theoretical curves obtained under experimental conditions of Paskova et al. [5] are reported in Fig. 3 as a function of the ratio of the Ga source HCl flow to the total flow considering the mass transfers computed with substrate–wall distances of 1 and 2 cm. No and two GaN parasitical deposition rates, 1 and 2 g/h have been considered. The three experimental points are given as triangles. The first point corresponds to a parasitical deposition rate of 1–2 g/h. The second point is located in a domain where

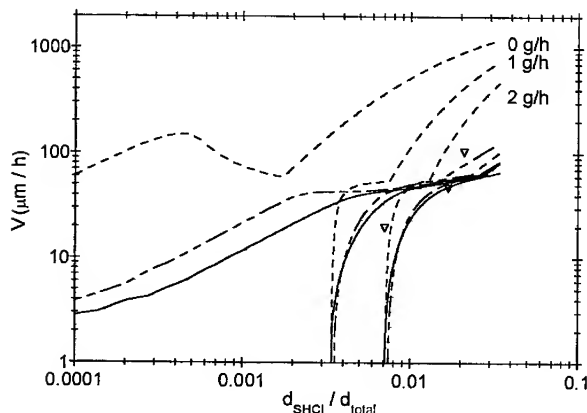


Fig. 3. Theoretical kinetics and growth rates taking into account the mass transfer and wall–substrate distances of 1 and 2 cm drawn by dashed, dash-dotted and solid lines, respectively, considering parasitical deposition rates of 0, 1 and 2 g/h on the substrate. The experimental conditions of Paskova et al. [4] (empty triangles) have been used

the growth rate is practically independent of the investigated wall-substrate distances and on GaN parasitical deposition rates, which is in agreement with the constant value obtained by the authors for different experimental times. The last point is the only one corresponding to the GaCl_3 mechanism. The drastic change of the experimental slope can be related to the H_2 - GaCl_3 mechanism transition as well as it seems that the first point is not far from the growth rate drop before the zero point. An incomplete GaCl_3 formation reaction in the gas phase and/or, a not perfect mixing of the vapour species could explain the too high value of the third point with respect to the computed curves.

4. Conclusion With respect to GaAs there are very few systematic experimental growth rate studies published in the literature. Furthermore, the experimental conditions are, in most of the published papers, not enough detailed to be introduced in the software developed with the model. Nevertheless, the few exploitable results show that the GaN HVPE system is quite different than the GaAs chloride method. The input supersaturations and then the corresponding kinetic values are usually very high, which results in very important effects of the mass transfer and GaN parasitical deposition on the substrate. The NH_3 decomposition and the GaCl_3 formation rates can differ from one to another reactor as well as the homogeneity of the gas mixture. The latter effect is evidenced by the observed variations of growth rate with the distance between the substrate and the gas mixing point [6, 7]. These effects will shift the curves but will not change drastically their general comportment. The results presented here show a few predicted comportments such as the kinetic decrease in the H_2 mechanism versus $1/T$, before the H_2 - GaCl_3 mechanism transition, which arises from the mass transfer effect. The kinetic curves show also that a constant value of the growth rate as a function of $1/T$ can come from a high supersaturation value and not from a mass transfer limited process. The research of the zero point of relative supersaturation performed by Aujol et al. [8, 9] has shown the possible effect of an incomplete GaCl_3 formation in N_2 atmosphere. The zero point reached at relative supersaturation values as low as -0.8 in N_2/H_2 mixture seems to be related to a third deposition reaction [9].

References

- [1] R. CADORET, *J. Cryst. Growth* **205**, 123 (1999).
- [2] R. CADORET and E. GIL-LAFON, *J. Physique I* **7**, 889 (1997).
- [3] W. SEIFERT, G. FITZL, and E. BUTTER, *J. Cryst. Growth* **52**, 257 (1981).
- [4] W. SEIFERT, S. SWCHATLICK, J. REINHOLD, and E. BUTTER, *J. Cryst. Growth* **66**, 333 (1984).
- [5] T. PASKOVA, E. B. SVEDBERG, L. D. MADSEN, R. YAKIMOVA, I. G. IVANOV, A. HENRY, and B. MONEMAR, *MRS Internet J. Nitride Semicond. Res.* **4S1**, G3.16 (1999).
- [6] T. PASKOVA, E. M. GOLDS, R. YAKIMOVA, E. B. SVEDBERG, A. HENRY, and B. MONEMAR, *J. Cryst. Growth* **208**, 18 (2000).
- [7] A. TRASSOUDAIN, E. AUJOL, P. DISSEIX, D. CASTELLUCI, and R. CADORET, *phys. stat. sol. (a)* **176**, 425 (1999).
- [8] E. AUJOL, A. TRASSOUDAIN, D. CASTELLUCI, and R. CADORET, submitted to *Mater. Sci. Engng.*
- [9] E. AUJOL, A. TRASSOUDAIN, L. SIOZADE, A. PIMPINELLI, and R. CADORET, submitted to *J. Cryst. Growth*.

phys. stat. sol. (a) **183**, 11 (2001)

Subject classification: 71.35.Cc; 78.67.De; 78.67.Hc; S7.12

Exciton–Light Interaction in Three-Dimensional Microcavities

L. C. ANDREANI¹) (a), G. PANZARINI (a), and J.-M. GÉRARD (b)

(a) *INFM-Dipartimento di Fisica “A. Volta”, Università di Pavia, Via Bassi 6,
I-27100 Pavia, Italy*

(b) *France Télécom/CNET, 196 avenue H. Ravera, F-92220 Bagneux, France*

(Received October 8, 2000)

A theoretical description of the interaction between confined excitons and photonic modes in pillar microcavities is given. For quantum-well excitons in the strong coupling regime, the Rabi splitting is reduced compared to the reference planar cavity and a radiative splitting of exciton states coupled to cavity modes with different symmetries is found. In the case of zero-dimensional excitations, the conditions for achieving the strong-coupling regime are determined. For InAs quantum dots the oscillator strength is too low to yield a vacuum-field Rabi splitting, while excitons bound to monolayer fluctuations in quantum wells behave as quantum dots with a large oscillator strength and can more easily be in the strong-coupling regime.

A planar semiconductor microcavity consists of a cavity region, usually containing an active medium like quantum wells or quantum dots, surrounded by multilayer dielectric mirrors (for recent reviews on microcavity physics, see e.g. papers in [1]). Each Fabry-Pérot resonance of the cavity can be viewed as a photonic mode which is partially confined in the growth direction. The Fabry-Pérot frequency has a dispersion as a function of in-plane wavevector. In addition to the Fabry-Pérot resonances, a planar cavity has a continuum of leaky modes which arise from the side-bands of the dielectric mirrors. The interaction between a dipole-active excitation and the cavity modes leads to a modification of the spontaneous emission *pattern*. However, the radiative *decay rate* is not substantially modified in planar cavities: when integrating over all emission directions, including those of the leaky modes, the regions of high and low photonic density of states compensate to a large extent [2]. In order to achieve a good control of spontaneous emission lifetime three-dimensional (3D) microcavities are needed.

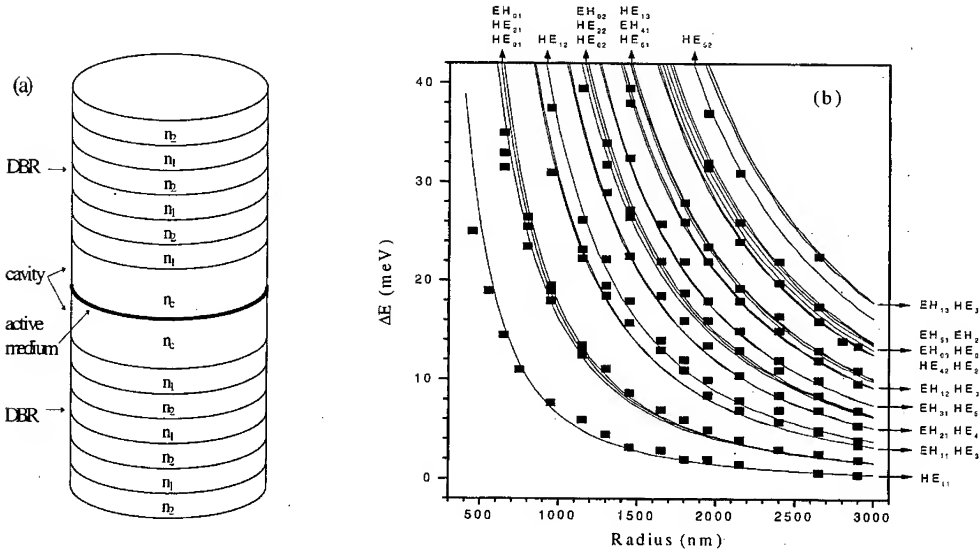
If the emission line is narrow and the quality factor of the cavity mode is high, as it happens for quantum-well (QW) excitons in III–V or II–VI microcavities, the radiation–matter interaction can be in the strong-coupling regime characterized by a vacuum-field Rabi splitting and the formation of cavity polaritons [3]. Due to the *bosonic* character of the exciton, the Rabi splitting is basically independent of field intensity for weak excitation. A single quantum dot (QD) in interaction with confined photonic modes has much different properties: indeed, a zero-dimensional transition can be modelled by a two-level system and is intrinsically *fermionic*. A QD transition in a 3D

¹) Corresponding author; Tel.: +39-0382-507.491; Fax: +39-0382-507.563;
e-mail: andreani@pv.infn.it

microcavity is the “ultimate” confined system and should display interesting quantum electrodynamic effects, in analogy to atoms in optical cavities. The strong-coupling regime for QDs in 3D microcavities has not been observed yet.

In this paper, we deal with 3D microcavities with cylindrical structure: these are called pillar microcavities, or micro-pillars (MPs). After describing the confined photonic modes, we discuss a quantum-mechanical model of QW excitons in interaction with cavity modes in the strong-coupling regime. Next we develop a model for a single QD transition radiatively coupled to a cavity mode, including also dampings in a master equation scheme. In the weak-coupling regime the model gives the change of spontaneous emission lifetime, known as Purcell effect [4]. The conditions for achieving the strong-coupling regime are examined for two kinds of QDs: self-assembled InAs quantum dots and QW excitons bound to monolayer fluctuations.

A micro-pillar is obtained by lateral etching of a planar microcavity, typically consisting of a GaAs cavity region and GaAs/AlAs Bragg reflectors. The resulting structure is a cylinder of dielectric layers surrounded by air, see Fig. 1a. Since the refractive indices of GaAs and AlAs are high and close to each other, the micro-pillar acts as a dielectric waveguide with an average refractive index. Thus, vertical (z) confinement of the electromagnetic field is provided by the dielectric mirrors of the epitaxial structure, while lateral (xy) confinement results from total internal reflection at the dielectric–air interfaces. The radius of the pillar is usually such that vertical confinement dominates for the lowest modes, i.e., the energy shifts of the optical modes due to lateral confinement are much smaller than the energy of the Fabry-Pérot mode of the planar cavity. Under this condition an “adiabatic” approximation can be adopted by assuming that vertical and lateral degrees of freedom are decoupled: the z dependence of the electric field is



identical to that of the planar cavity, while the xy dependence is that of a cylindrical dielectric waveguide [5]. The modes are labelled as EH_{lm} and HE_{lm} , where l is the z -projection of the total angular momentum, n is a radial quantum number and m is the order of the Fabry-Pérot mode of the planar cavity. The eigenfrequencies are discrete and increase on decreasing the pillar radius, see Fig. 1b. They can be measured from the energies of photoluminescence peaks when a broad-band emitter, like a sheet of InAs quantum dots with size distribution, is embedded in the cavity [6].

When the cavity contains one or several quantum wells, the interaction between the cavity modes and the QW excitons can be described by choosing suitable basis functions for the exciton states. While momentum eigenstates (i.e., plane waves with well defined in-plane center of mass wavevector) are the natural eigenstates in a planar cavity, for a pillar microcavity it is convenient to consider linear combinations of center-of-mass wavefunctions which have the same spatial and polarization dependence as the cavity mode. A detailed procedure is presented in Ref. [7]; here it suffices to say that the resulting exciton states are labelled by the same quantum numbers (l, n) of the electromagnetic waveguide problem. Exciton-photon interaction takes place only between states with the same l , due to cylindrical symmetry. However, interaction between exciton and photon states with different radial numbers n is allowed by the different quantization conditions on the wavefunction: exciton states are perfectly confined in the pillar, while photonic modes partially leak into the air region.

The exciton-photon Hamiltonian in second quantization can be derived from the standard electromagnetic interaction: it has the form of a generalized polariton Hamiltonian with quadratic couplings between exciton and photon states with different quantum numbers. Diagonalization of this Hamiltonian leads to a secular equation for mixed exciton-photon modes in the form of a determinantal equation which must be solved numerically. The main results can be summarized as follows [7]: when a cavity mode is in resonance with the exciton a Rabi splitting occurs. The splitting is close to that of the planar cavity for large pillar radius, but it decreases for a radius smaller than $\sim 1 \mu\text{m}$ due to leak-out of the cavity modes and reduction of overlap with the exciton states. This result is consistent with the observation of a constant Rabi splitting for micro-pillars with radius $> 1.25 \mu\text{m}$ [8]. Even when no resonance condition occurs, exciton levels with different quantum numbers are split by radiative coupling with the corresponding cavity modes. This radiative splitting is a peculiar effect of exciton-light coupling in a 3D microcavity: however, it is difficult to observe since it is smaller than 1 meV and will usually be washed out by line broadenings.

A quantum dot transition in a micro-pillar must be described by a different quantum-mechanical scheme. If the QD can be modeled as a two-level system in interaction with a single cavity mode, the Hamiltonian is

$$H = \hbar\omega_0\hat{\sigma}_3 + \hbar\omega_\mu(\hat{a}_\mu^\dagger\hat{a}_\mu + \frac{1}{2}) + i\hbar g(\hat{\sigma}_-\hat{a}_\mu^\dagger - \hat{\sigma}_+\hat{a}_\mu), \quad (1)$$

where $\hat{\sigma}_+$, $\hat{\sigma}_-$, $\hat{\sigma}_3$ are pseudo-spin operators for the two-level system with ground (excited) state $|g\rangle$ ($|e\rangle$) and \hat{a}_μ^\dagger , \hat{a}_μ are creation/destruction operators for the cavity mode μ . The coupling constant of the QD-cavity interaction is

$$g = \left(\frac{1}{4\pi\epsilon_r\epsilon_0} \frac{\pi e^2 f}{m\tilde{V}_\mu(\mathbf{r}_1)} \right)^{1/2}, \quad (2)$$

where f is the oscillator strength of the transition, $\tilde{V}_\mu(\mathbf{r}_1) = |\alpha(\mathbf{r}_1)|^{-2}$ is the mode volume evaluated at the QD position ($\alpha(\mathbf{r})$ is the normalized mode profile), ϵ_r (ϵ_0) is the relative (vacuum) permittivity and m is the free electron mass. The basis states of the Hamiltonian (1) consist of a ground state $|g, 0\rangle$ and of a ladder of doublets $|e, n_\mu\rangle, |g, n_\mu + 1\rangle$, $n_\mu = 0, 1, \dots$, where n_μ is the number of photons in the mode. In the resonance case $\omega_0 = \omega_\mu$ each doublet gives rise to dressed states split by $2\hbar g\sqrt{n_\mu + 1}$. For $n_\mu = 0$ one has a vacuum-field Rabi splitting, while for $n_\mu \gg 1$ the physical behavior becomes that of the dynamical Stark effect with the classical Rabi splitting.

In order to incorporate finite linewidths of the QD transition (γ_a) and of the cavity mode ($\gamma_{c,\mu}$) one has to work with a master equation for the density matrix of the QD-cavity system [9, 10]. The luminescence spectrum can be calculated by photodetection theory. This model can be solved analytically in the limit of weak excitation, i.e., by keeping only the ground state $|g, 0\rangle$ and the first excited doublet $|e, 0\rangle, |g, 1\rangle$. The spontaneous emission spectrum in the resonant case $\omega_0 = \omega_\mu$ contains energy denominators $\omega - \Omega_\pm$, where the complex frequencies Ω_\pm are given by

$$\Omega_\pm = \omega_0 - \frac{i}{4} (\gamma_a + \gamma_c) \pm \sqrt{g^2 - \left(\frac{\gamma_a - \gamma_{c,\mu}}{4}\right)^2}. \quad (3)$$

For $g > |\gamma_a - \gamma_{c,\mu}|/4$ the spectrum consists of a doublet of lines split by twice the square root in Eq. (3). This is the condition for the occurrence of a vacuum-field Rabi splitting, i.e., the strong-coupling regime in the lowest doublet. On the other hand, for $g \ll |\gamma_a - \gamma_{c,\mu}|/4$ the QB-cavity system is in a weak-coupling regime with a modified spontaneous emission rate. Evaluating the imaginary part of Eq. (3) in this limit gives the expression for the enhanced radiative decay rate, known as Purcell effect [4]. This effect was recently demonstrated for InAs QDs in micro-pillars [11].

When applying the above model to the specific case of pillar microcavities it turns out that the optimal condition for strong coupling is for a cavity radius around $0.5 \mu\text{m}$, for which the mode volume is small and the quality factor Q_μ is still large. Calculations [10] show that the oscillator strength must be larger than about 100 in order to achieve a vacuum-field Rabi splitting. InAs quantum dots have an oscillator strength $f \sim 10$ for the lowest excitonic transition, which is an order of magnitude smaller than the crossover value: *InAs quantum dots cannot show a vacuum-field Rabi splitting for state-of-the-art micro-pillars*. This conclusion is likely to hold even for micro-disk cavities with whispering-gallery modes, through their quality factor can reach values up to 12000 [12].

A Rabi splitting can be achieved if the number of photons in the mode is large enough. This number can be made larger than unity by pumping resonantly with a laser beam. The number of photons in the mode is given by the number of incoming photons per unit time, $P_{\text{in}}/(\hbar\omega_\mu)$ (P_{in} is the incident power), multiplied by the lifetime of photons in the cavity: thus $n_\mu \sim P_{\text{in}}/(\hbar\omega_\mu\gamma_{c,\mu})$, with numerical factors depending on the details of the structure and on the matching between incoming field and mode profile. A simple estimate suggests that even for powers as low as $1 \mu\text{W}$ there are several photons in the mode. For $n_\mu \gg 1$ the electromagnetic field can be treated classically; when $g\sqrt{n_\mu + 1} \gg \gamma_{c,\mu}, \gamma_a$ the QD-cavity interaction is described by the optical Bloch equations and the formation of mixed eigenstates corresponds to the dynamical Stark effect, the Rabi frequency being given by $-\mathbf{d} \cdot \mathbf{E}/\hbar$. A Mollow triplet is expected to occur in the luminescence spectrum [13].

In order to obtain a vacuum-field Rabi splitting one needs a zero-dimensional emitter with a larger oscillator strength. This can be provided by excitons localized by interface defects in quantum wells. QW excitons bound to monolayer fluctuations are observed as ultra-narrow lines in photoluminescence in samples produced with growth interruption at the interfaces [14]. Each of these lines corresponds to a single bound exciton, i.e., to a zero-dimensional transition, for which the model Hamiltonian (1) applies.

The simplest model of an interface defect in a QW of width L_1 consists in assuming that the QW thickness becomes $L_2 = L_1 + \text{one monolayer}$ in a disk of radius b . When the defect radius b is much larger than the exciton Bohr radius a_B the in-plane center-of-mass wavefunction of the exciton is quantized in a circular potential well: in this regime the oscillator strength is proportional to the area occupied by the center of mass and increases rapidly with the defect radius. In the opposite case $b \ll a_B$ the defect resembles a neutral impurity center: the exciton center-of-mass can become weakly localized to the defect, and in this case the oscillator strength is expected to increase on decreasing the defect radius. One therefore expects a large oscillator strength for both very small or very large defects and a minimum of the oscillator strength in between. These expectations are confirmed by detailed calculations of the exciton states bound to monolayer fluctuations in narrow GaAs/AlAs QWs, see Fig. 2. The oscillator strength has a minimum value $f \sim 50$ at $b \sim 100$ Å and increases for small or large defects. The oscillator strength can reach values larger than 200–300: thus we conclude that *excitons bound to monolayer fluctuations in narrow QWs can be in the strong coupling regime when embedded in state-of-the-art micro-pillars*.

In conclusion, three-dimensional microcavities are seen to yield several new phenomena compared to their planar counterparts. In the weak-coupling regime full control of spontaneous emission can be achieved. For the strong-coupling regime one has to distinguish between the cases of quantum-well excitons or of single zero-dimensional (quantum-dot) excitations. For QW excitons, the main effects of 3D photon confine-

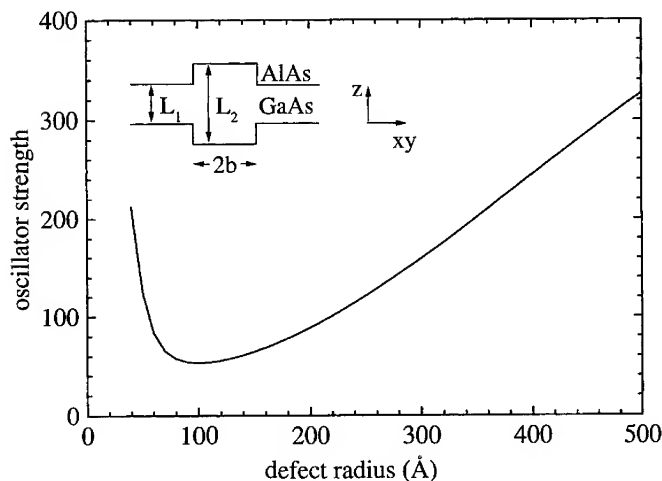


Fig. 2. Oscillator strength of the ground heavy-hole exciton bound to a monolayer fluctuation in a GaAs/AlAs quantum well of width $L_1 = 40$ Å. Inset: model for the attractive defect

ment are a reduction of the Rabi splitting and a (small) radiative splitting of exciton states coupled to different cavity modes. For QD transitions the physical behavior is much different due to the fermionic character of the excitations: physical properties depend strongly on excitation intensity. A vacuum-field Rabi splitting can hardly be achieved for InAs QDs, due to their low oscillator strength. A Rabi splitting in the classical limit can be obtained by increasing the excitation intensity. A zero-dimensional emitter with large oscillator strength is provided by excitons bound to monolayer fluctuations in narrow QWs: this system could show a vacuum-field Rabi splitting when placed in micro-pillars obtained with present-day technologies.

References

- [1] H. BENISTY et al. (Ed.), *Confined Photon Systems: Fundamentals and Applications*, Springer-Verlag, Berlin 1999.
- [2] G. BJÖRK and Y. YAMAMOTO, in: *Spontaneous Emission and Laser Oscillations in Microcavities*, Eds. H. YOKOYAMA and K. UJIHARA, CRC Press, New York 1995.
- [3] C. WEISBUCH, M. NISHIOKA, A. ISHIKAWA, and Y. ARAKAWA, *Phys. Rev. Lett.* **69**, 3314 (1992).
- [4] E. M. PURCELL, *Phys. Rev.* **69**, 681 (1946).
- [5] A. YARIV, *Optical Electronics*, Holt-Rinehart, New York 1985.
- [6] J.-M. GÉRARD et al., *Appl. Phys. Lett.* **69**, 449 (1996).
- [7] G. PANZARINI and L. C. ANDREANI, *Phys. Rev. B* **60**, 16799 (1999).
- [8] J. BLOCH et al., *Physica* **2E**, 915 (1998).
- [9] H. CARMICHAEL et al., *Phys. Rev. B* **40**, 5516 (1989).
- [10] L.C. ANDREANI, G. PANZARINI, and J.-M. GÉRARD, *Phys. Rev. B* **60**, 13276 (1999).
- [11] J. M. GÉRARD et al., *Phys. Rev. Lett.* **81**, 1110 (1998).
- [12] B. GAYRAL et al., *Appl. Phys. Lett.* **75**, 1908 (1999).
- [13] C. COHEN-TANNOUDJI, J. DUPONT-ROC, and G. GRYNBERG, *Atom–Photon Interactions: Basic Processes and Applications*, Wiley, New York 1992.
- [14] A. ZRENNER et al., *Phys. Rev. Lett.* **72**, 3382 (1994).
 K. BRUNNER et al., *Phys. Rev. Lett.* **73**, 1138 (1994).
 D. GAMMON et al., *Phys. Rev. Lett.* **76**, 3005 (1996); *Science* **273**, 87 (1996).
 R. GROUSSON et al., *Phys. Rev. B* **55**, 5253 (1997).

phys. stat. sol. (a) **183**, 17 (2001)

Subject classification: 71.20.Nr; 77.84.Bw; 78.20.Ci; S7.14

Photonic Band Gap Microcavities in Nitrides

M. LE VASSOR D'YERVILLE¹), D. CASSAGNE, and C. JOUANIN

*Groupe d'Etude des Semiconducteurs, UMR 5650, CNRS, Université Montpellier II,
Place Eugène Bataillon, F-34095 Montpellier cedex 05, France*

(Received October 8, 2000)

To optimize the appearance of photonic band gaps in nitrides, we study photonic crystals based on low dielectric constant materials. By calculating the photonic band structures we investigate the gap opening. In the case of microcavities, we have calculated the cavity modes by the plane wave method and a supercell approach. We have classified the modes using group theory. Our results demonstrate that gallery-like modes are more sensitive to a variation of the filling factor.

1. Introduction Photonic crystals are periodic dielectric structures that allow the control of the propagation of electromagnetic waves [1–3]. Various applications, such as zero-threshold lasers, polarization splitters, superprisms, and sharp bend waveguides, are expected by using complete or incomplete photonic band gaps [4]. The artificial introduction of defects in the periodicity is used to create microcavities, which can trap the light in tiny volumes and control the emission properties. The realization of blue emitter diodes and lasers makes the control of short wavelength light be an important task for the future. Photonic crystals could be used to control the visible light but the fabrication of convenient structures poses two problems. To avoid light absorption by the photonic crystal, wide gap semiconductors, as for example GaN, must be used. Unfortunately, these materials have weak dielectric constants, which reduces the photonic band gap width. Photonic crystals must have a period smaller than the wavelength of light to be controlled. But etching at submicronic scale remains a technological challenge. To optimize the appearance of photonic band gaps in the visible, we study photonic crystals based on low dielectric constant materials. By calculating the photonic band structures we investigate the gap opening. In the case of microcavities, we have calculated the cavity modes by the plane wave method and a supercell approach. We have classified the modes using group theory.

2. 2D Absolute Photonic Band Gaps The most promising two-dimensional (2D) photonic crystals (PCs) are the triangular disposition of air holes in dielectrics [5–7] and the graphite arrangement of dielectric rods in air [8, 9], which present photonic band gaps (PBGs) for a high air filling factor. Both of these structures present similar performances in obtaining PBGs in the infrared range. As the spatial period of a PC must be smaller than the wavelength of light to be controlled, these crystals have been fabricated in the near-infrared range, in GaAs ($\epsilon = 13.6$) [10, 11]. The situation is more difficult in the visible. In that range, wide gap semiconductors must be used so that the

¹) Corresponding author; Fax: +33(0)467143760;
e-mail: levassor@ges.univ-montp2.fr; http: //w3.ges-univ-montp2.fr

PCs do not absorb the waves. But these materials have small refractive indices (~ 2.6 for GaN), which decreases the width of the gaps. To control the visible light, PCs must have submicronic periods and submicronic etching in wide gap semiconductors remains a technological challenge [12]. In this paper we consider that the PBGs opened for all the directions of propagation of the waves, so-called complete PBGs, in 2D triangular and graphite structures made with low dielectric constant materials. For 2D PCs, two kinds of polarizations can be defined according to whether the electric field (E polarization) or the magnetic field (H polarization) is parallel to the non-periodic dimension of the structure. The overlap of complete gaps of E and H polarizations is called a complete absolute band gap. In our model, we suppose that the length of the columns is infinite. The filling factor β is defined as the fractional cylinder volume in the total volume. For the triangular structure of air cylinders, β is equal to the air filling factor β_{air} , whereas for the graphite structure of dielectric rods, $\beta = 1 - \beta_{\text{air}}$. In both cases, a is the distance between the first neighbor rod axes and the normalized frequency is defined as $\omega a/2\pi c = a/\lambda$. We denote by E_i (respectively H_i) the gap occurring between the i -th and the $(i+1)$ -th bands of E (respectively H) polarization.

To understand the appearance of absolute PBG when the refractive index of the dielectric material is decreased, we first consider the gap opening as a function of the filling factor at an intermediate value of the dielectric constant $\epsilon = 8$. In the case of triangular structure only one E polarized gap exists in the vicinity of the large lower H gap. When the refractive index decreases, the gap width decreases and a blue shift of the gap centers is produced. However, it is worth noting that this blue shift is not the same for the gaps of both polarizations. This effect will play a key role in the appearance of the absolute PBGs. In Fig. 1, we present the band structure of the triangular PC of air holes in dielectric material versus β , for $\epsilon = 8$. Only one absolute PBG exists in this range, originating from the overlap of H_1 and E_2 gaps. It exists from $\beta = 0.65$ to 0.83 . Its maximum width is 5% of the midgap frequency for $\beta = 0.74$. The midgap normalized frequency is around $\omega a/2\pi c = 0.5$. As, to our knowledge, the fabrication of thin dielectric walls between holes is a real challenge using Reactive Ion Etching (RIE) techniques [13], we consider in the following that maximum β that can be obtained is about 70%. Hereafter, this structure will be noted 70%-triangular, and its absolute gap, T_{70} . Figure 2 shows the variation of T_{70} as a function of the dielectric

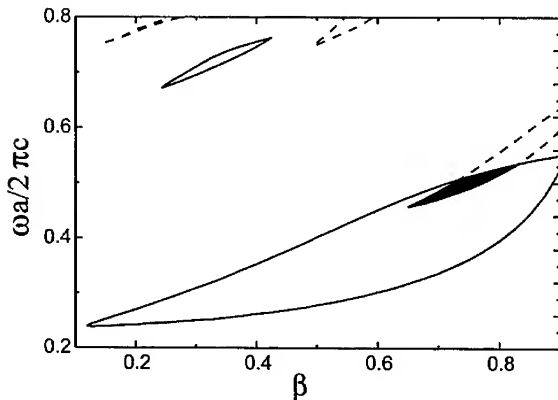


Fig. 1. Photonic band gaps of E (dashed lines) and H (solid lines) polarizations vs. filling factor β for the triangular structure of air holes in dielectric material with $\epsilon = 8$. In black are the absolute band gaps due to the overlapping of H and E polarization gaps

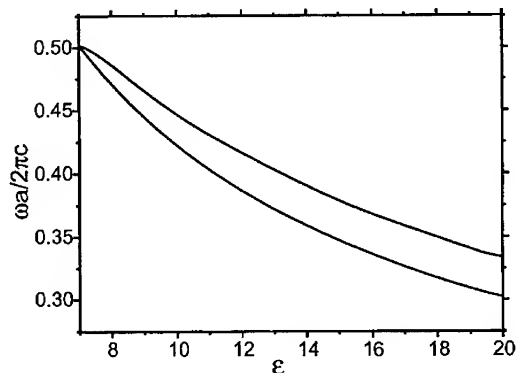


Fig. 2. Absolute photonic band gap of a triangular structure of air holes in dielectric material (T_{70}) vs. the dielectric constant of the background ϵ for the filling factor $\beta = 70\%$

constant ϵ . T_{70} opens up at $\epsilon = 7.2$ and its width always increases with ϵ . For $\epsilon = 20$, the gap to midgap ratio is 10%. The normalized midgap frequency strongly decreases with ϵ , from 0.5 ($\epsilon = 7.1$) to 0.32 ($\epsilon = 20$). As a result, a decreases for a fixed wavelength.

The second structure we have studied is formed by a graphite arrangement of dielectric rods in air. For $\epsilon = 8$, Fig. 3 shows that three absolute PBGs have been found in the frequency range where only one was appearing for the triangular case. G1 and G3 occur for β between 0.3 and 0.4 and G2 for β about 0.2. As for the triangular PC, complete absolute PBGs exist for high air filling factors. The most promising in obtaining absolute PBGs for small dielectric constant ($\epsilon < 10$) is due to the overlap between E_6 and H_5 for β about 35%. It will be noted G1. The evolution of the boundaries of G1 and the corresponding β value that optimizes the gap width with respect to ϵ are presented in Fig. 4. The gap opens up for $\epsilon = 6.5$ and $\beta = 38\%$ and closes when ϵ goes beyond 20 at $\beta = 30\%$. The evolution of G1 is more complicated than for T_{70} . This results from the joint action of two mechanisms. Firstly, E and H gaps enlarge with ϵ for both the triangular as well as the graphite structure. Secondly, the gap centers are not varying in the same way for both polarizations, which modifies the overlap of the E and H gaps. This effect is not noticeable for T_{70} because H_1 is much larger than E_2 and contains it over all the variation range of ϵ . As a result, T_{70} has the same width as E_2 and enlarges with ϵ . Concerning G1, the overlap diminishes when ϵ increases and, at large values of ϵ , G1 narrows and then closes when ϵ goes beyond 20. This demon-

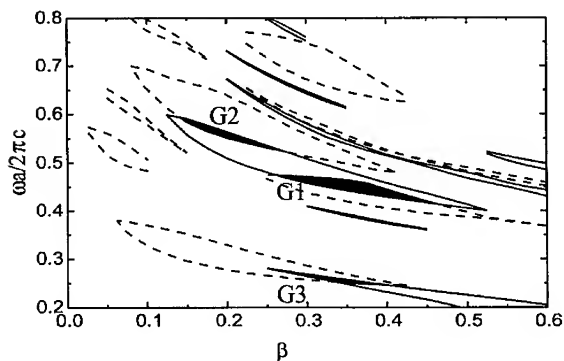


Fig. 3. Same as Fig. 1 for the graphite structure of dielectric rods in air

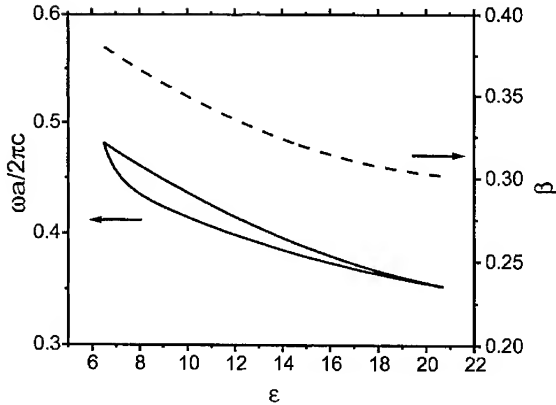
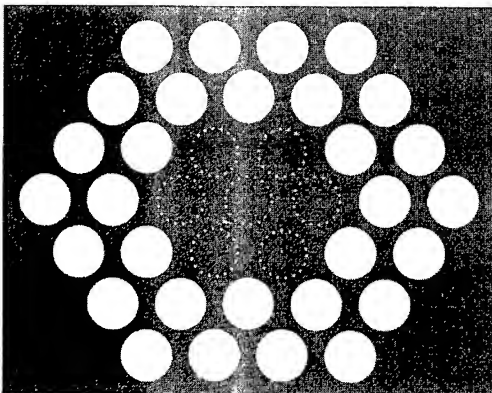


Fig. 4. Maximum absolute photonic band gap between E_6 and H_5 (G1) achievable for different dielectric constants (solid line) and the optimal filling factor β for which the gap is obtained (dashed line) for the graphite structure of dielectric rods in air

strates that, if an absolute PBG is needed in low dielectric constant materials, the graphite structure is more suitable. At very low dielectric constants, no absolute PBG is achievable in both triangular and graphite structures, but PBGs for a single polarization still exist.

3. Hexagonal Microcavities A microcavity can be obtained in a PC by inserting a defect in the periodic structure. Here we consider a triangular structure of air holes where we have removed seven holes in order to achieve the hexagonal defect (H2-cavity) shown in Fig. 5. This defect introduces authorized modes within the PBG, and since light cannot propagate inside the PC, it remains confined inside the cavity. For the calculations, we have chosen $n = 2.6$, which corresponds approximately to the refractive index of GaN. As this small index does not generate any absolute band gap for the triangular structure, we have only considered the H-polarized modes. The size of the H2-cavity is small enough to support a small number of modes and large enough to enable an experimental characterization of the modes. The cavity modes and the gap edges were calculated by the plane wave method and a supercell approach [14, 15]. Figure 6 shows the evolution of these modes as a function of the air filling factor. We have classified the cavity modes according to their symmetry using group theory [16], and we have confirmed that each cavity mode belongs to one of the irreducible representations of the group-symmetry D_{6h} of the hexagonal cavity. These irreducible representations are reported in Fig. 6, using the notation of Lomer [17]. The representations that are even (odd) under the inversion operation are labeled with the subscript g (u). In the case of H polarization, all the modes are even



representations of the group-symmetry D_{6h} of the hexagonal cavity. These irreducible representations are reported in Fig. 6, using the notation of Lomer [17]. The representations that are even (odd) under the inversion operation are labeled with the subscript g (u). In the case of H polarization, all the modes are even

Fig. 5. Sketch of the H2-cavity in the triangular structure of air holes. The dotted circles indicate the removed holes

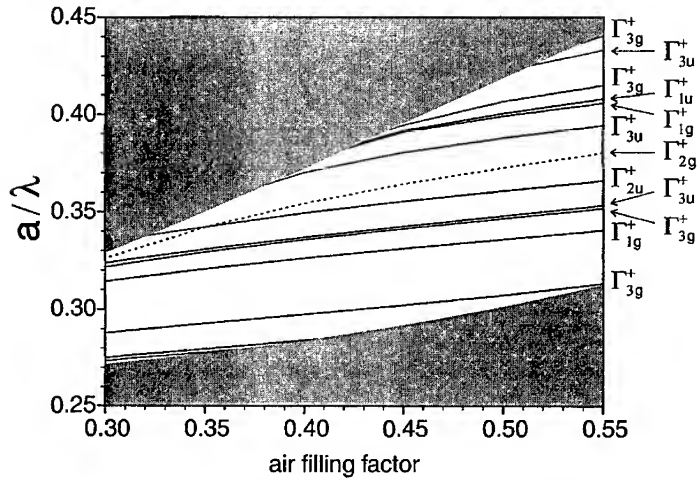


Fig. 6. H2-cavity mode evolution as a function of the filling factor ($n = 2.6$)

with respect to the reflection in the plane of periodicity, which is indicated by the superscript +. Doubly degenerated modes are represented by Γ_{3g}^+ or by Γ_{3u}^+ , while others are non-degenerated. Typical magnetic field maps of two modes are displayed in Fig. 7. The cavity modes, which are blue-shifted when the filling factor increases, have similar evolution, except the Γ_{2g}^+ mode indicated by a dashed line in Fig. 6. This mode is a whispering gallery-like mode as shown in Fig. 7b. Our results demonstrate that this whispering gallery-like mode is much more sensitive to a variation of the filling factor whereas the spectral distance between the other modes is generally kept constant. This can be easily understood if we consider the spatial shape of this mode: it shows that the energy is strongly localized near the edge of the cavity and in the medium between the holes of the first PC row, which explains the stronger influence of the diameter of the holes on the gallery mode. Moreover, the analysis of the field maps shows that the spatial extensions of the cavity modes are generally roughly independent of the filling factor, whereas the gallery mode becomes more and more confined as the holes widen. For small filling factors (small holes) the gallery mode spreads out of the cavity but its

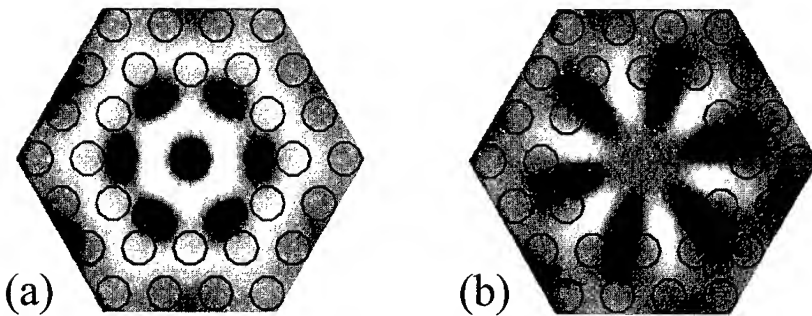


Fig. 7. Simulated magnetic field maps of two modes. a) Γ_{1g}^+ symmetry mode, and b) whispering gallery-like modes of Γ_{2g}^+ symmetry

spatial extension is visibly reduced when the filling factor increases. Therefore the faster increase of the gallery mode frequency is due to a larger variation of the spatial extension of this mode.

4. Conclusion To obtain 2D absolute photonic band gaps in the visible using nitrides, the graphite structure of dielectric rods is much more promising than the triangular structure of holes because it allows the existence of absolute band gaps at lower dielectric constant due to a larger number of gaps for E and H polarizations. If a gap is needed for a single polarization, the triangular structure can be used. In the case of an H₂-cavity in the triangular structure of holes in GaN a large variety of cavity modes exists. A whispering gallery-like mode is obtained and this mode is much more sensitive to the filling factor.

Acknowledgements The authors thank the "Centre Informatique National de l'Enseignement Supérieur" for an allowance of computer time.

References

- [1] E. YABLONOVITCH, Phys. Rev. Lett. **58**, 2059 (1987).
- [2] S. JOHN, Phys. Rev. Lett. **58**, 2486 (1987).
- [3] J. D. JOANNOPOULOS, R. D. MEADE, and J. N. WINN, Photonic Crystals, Molding the Flow of Light, Princeton University Press, 1995.
- [4] J. Lightwave Technol. **17**, 1999 (special issue).
- [5] M. PLIHAL and A. A. MARADUDIN, Phys. Rev. B **44**, 8565 (1991).
- [6] R. D. MEADE et al., Appl. Phys. Lett. **61**, 495 (1992).
- [7] P. R. VILLENEUVE and M. PICHE, Phys. Rev. B **46**, 4969 (1992).
- [8] D. CASSAGNE, C. JOUANIN, and D. BERTHO, Phys. Rev. B **52**, R2217 (1995).
- [9] F. GADOT et al., Appl. Phys. Lett. **71**, 1780 (1997).
- [10] T. F. KRAUSS, R. M. DE LA RUE, and S. BRAND, Opt. Photonics News **7**, 26 (1996).
- [11] Y. CHEN et al., Superlattices and Microstructures **22**, 109 (1997).
- [12] D. COQUILLAT et al., Proc. ICSCIII-N'97, Stockholm; Mater. Sci. Forum **264/268**, 1403 (1998).
- [13] T. KRAUSS et al., Electron. Lett. **30**, 1444 (1994).
- [14] D. CASSAGNE, A. BARRA, and C. JOUANIN, Superlattices and Microstructures **25**, 343 (1999).
- [15] P. POTTIER et al., J. Lightwave Technol. **17**, 2058 (1999).
- [16] D. CASSAGNE, C. JOUANIN, and D. BERTHO, Phys. Rev. B **53**, 7134 (1996).
- [17] W. M. LOMER, Proc. Roy. Soc. A **227**, 330 (1955).

Editor's Choice

phys. stat. sol. (a) **183**, 23 (2001)

Subject classification: 71.36.+c; 73.23.Ad

Drift and Diffusion of Exciton–Polaritons in a Graded Quantum Microcavity

B. SERMAGE (a), G. MALPUECH (b), A. V. KAVOKIN (b), and V. THIERRY-MIEG (c)

(a) *France TELECOM, Centre National d'Etudes des Télécommunications, BP 107,
F-92225 Bagneux, France*

(b) *Laboratoire des Sciences et Matériaux pour l'Electronique et d'Automatique,
UMR 6602 du CNRS, Université Blaise Pascal, Clermont-Ferrand II,
F-63177 Aubière Cedex, France*

(c) *Laboratoire de Microstructures et de Microélectronique, CNRS, BP 107,
F-92225 Bagneux, France*

(Received October 8, 2000)

We report an experimental evidence of the acceleration of exciton–polaritons propagating in-plane of a semiconductor microcavity in the regime of the ballistic transport. The acceleration is achieved due to the gradient of the thickness of the cavity and results from the reciprocal space filtering effect of the cavity. The wave packet propagating in the cavity plane is constantly filtered by the cavity eigenmode that shifts towards larger wave vectors as the cavity width increases. The theory based on the extended scattering state technique reproduces the polariton transport in a graded cavity with a good accuracy.

Ballistic propagation of mixed exciton–photon states, i.e. exciton–polaritons [1] in a plane of a semiconductor microcavity [2] is a striking manifestation of the photon-induced transport of electronic excitations in solids. Enhanced efficiency of the light–matter coupling and a macroscopic coherence length of the exciton–polaritons in high-quality microcavities allows one to expect pronounced ballistic transport phenomena which are of extreme interest for applications in ultra-fast optoelectronics. First indirect and controversial studies of the in-plane polariton transport in microcavities have been undertaken since the end of 1980s [3, 4], while a direct evidence for such a phenomenon has been obtained quite recently with use of spatially and time-resolved optical spectroscopy [5]. The free-path length of tens to hundreds microns and the typical group velocities of the polaritons of the order of 10^6 – 10^7 m/s have been measured.

Is there any way to alter the velocity of polariton drift in the cavities? This question has a double importance – for optoelectronic applications like optical transistors, and from the fundamental point of view. How far goes the analogy between electrons and photon-like neutral quasi-particles (exciton–polaritons)? Whether the latter ones can be accelerated and which factor plays role of the electric field for them? The present paper addresses these questions and gives an experimental evidence of the acceleration of the coherent polariton drift by the gradient of the thickness of the microcavity.

The basic physics behind the acceleration effect is simple and can be understood from the scheme shown in Fig. 1. It displays the calculated dispersion of the lower

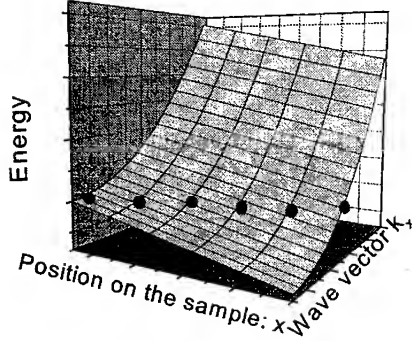


Fig. 1. Dispersion of the lower cavity-polariton branch calculated as a function of the coordinate x in the plane of the cavity

polariton branch of our microcavity structure (described below) as a function of the in-plane coordinate x . As the cavity gets wider, the entire polariton branch shifts towards lower energies. If the energy of the propagating cavity polariton is fixed (which is the case of ballistic transport), its in-plane wave vector k_x increases

with x , so that the polariton group velocity $v_x = \partial\omega(k_x)/\partial k_x$ increases too.

This over-simplified picture of acceleration is incomplete if one does not address the wave vector conservation problem. We remind that in the discussed regime of the coherent ballistic transport there is no scattering of exciton-polaritons in the cavity plane. Thus, k_x must be conserved, which is in visible disagreement with the above scheme.

The controversy is resolved if one takes into account that the polaritons propagating in the plane of the cavity represent the wave packets containing harmonics characterized by a continuous spectrum of k_x . The weight $g(k_x)$ of each harmonic in the wave packet initially is given by the form of the incident pulse $f(x)$,

$$g(k_x) = \frac{1}{2\pi} \int_{-\infty}^{\infty} dx f(x) \exp(-ik_x x). \quad (1)$$

As the wave packet starts to propagate in the plane its shape in the reciprocal space is modified due to the *filtering effect* of the cavity mode. Namely, harmonics characterized by k_x different from the k_x of the cavity mode at the given frequency and given coordinate are being suppressed (reflected), while those resonant with k_x of the cavity mode propagate freely. Thus, the cavity works as a spatially distributed filter in the reciprocal space. The shape of the propagating wave packet experiences continuous changes while moving along the sample, so that the role of harmonics characterized by large values of k_x increases, and the group velocity of the entire wave packet increases.

Below we present the experimental evidence of this phenomenon by means of time- and spatially-resolved spectroscopy.

We excite resonantly the lower branch of the exciton-photon coupled modes with 1.5 ps long pulses coming from a Ti-sapphire mode-locked laser. The sample maintained at low temperature (9 K) represents a λ GaAs microcavity with a 8 nm thick $\text{In}_{0.05}\text{Ga}_{0.95}\text{As}$ quantum well located at the antinode of the electromagnetic field. The Bragg reflectors are made of 26 and 22 pairs of $\text{AlAs}/\text{Al}_{0.1}\text{Ga}_{0.9}\text{As}$ quarter-wavelength layers, giving a calculated photon lifetime of 14 ps. The vacuum field Rabi splitting is $\Omega_R = 3.6$ meV. The sample has a thickness gradient along the x -axis, so that the bare cavity mode energy derivative over x obtained from the spatially resolved luminescence spectra is

$$\partial E_c / \partial x = 0.135 \text{ eV/cm}. \quad (2)$$

The exciton resonance energy in the quantum well is $E_{\text{ex}} = 1.4765$ eV.

The laser beam is focused on the sample at normal incidence with a 80 mm focal length lens so that the diameter of the spot on the sample is about 35 μm . The averaged excitation power is maintained below 100 nW which corresponds to about 2.5×10^7 excitons/ cm^2 . The light coming from the sample is collected by the same lens and focalized by a second lens on the entrance slit of a monochromator and time dispersed by a synchroscan streak camera. It is very essential to note that we excite *at normal incidence*, i.e. the average in-plane wave vector of the incident pulse is zero.

The experimental procedure is as follows. In the focus mode (i.e. using the streak camera without temporal scanning), we mask the reflected beam and we put the grating at first order. We adjust the laser wavelength so that the secondary emission (Rayleigh scattering plus photoluminescence) is maximum (resonance condition). Then we suppress the mask on the reflected beam, we turn the grating at zero order, we open the entrance slit of the monochromator to maximum and we use the streak camera in the synchroscan mode. We then observe the displacement of the emission source as a function of time.

The traces obtained for different detunings $\delta = E_c - E_{\text{ex}}$ are shown in Fig. 2a. Since we do not mask the reflected beam, the light which comes from the sample is mostly the reflection of the laser beam. We check with a 4 mm diameter aperture that the emission is in the specular direction. At very short times we see a very intensive spot which is due to the reflection by the free surface of the sample and then a tail which is caused by the reflection by the microcavity itself. The intensity of the reflected signal decreases with a decay time which corresponds to the photon lifetime in the cavity. This tail has a velocity which is nearly zero at the early times and then increases with time achieving a value about 2×10^6 m/s.

In the case of negative or zero detuning, the polaritons propagate as a unique beam (sometimes there are one or two other weak traces as shown in Fig. 2a). This shows that polaritons are very little scattered and that they keep their coherence in agreement with the fact the emission is in the specular direction. The coherence time is only limited by their lifetime in this case. For positive detuning, the intensity of the polariton beam is much smaller, that means that the most part of polaritons is scattered towards the reservoir. The role of detuning is quite clear in light of the model of the cavity-filtered polariton drift described above. In the case of the positive detuning the lower polariton branch is exciton-like. The polariton group velocity is very small in this case. Contrary, in case of negative detuning, the fast photon-like polaritons are excited, that results in a large in-plane group velocity of the wave packet.

We model these experiments using the scattering state technique described in Ref. [6]. We chose the incident pulse in the form

$$f(\omega, x) = j(\omega) \exp\left(-\left(\frac{x}{\Delta}\right)^2\right), \quad (3)$$

where $j(\omega)$ is the spectral function of the incident pulse taken as a Gaussian function in our case. We have taken $\Delta = 30 \mu\text{m}$. The time-resolved x -dependent reflection coefficient is given by

$$R(x, t) = \frac{1}{2\pi} \int_{-\infty}^{+\infty} j(\omega) \exp(-i\omega t) \left(\int_{-\infty}^{+\infty} g(k_x) r(x, \omega, k_x) \exp(ik_x x) dk_x \right) d\omega, \quad (4)$$

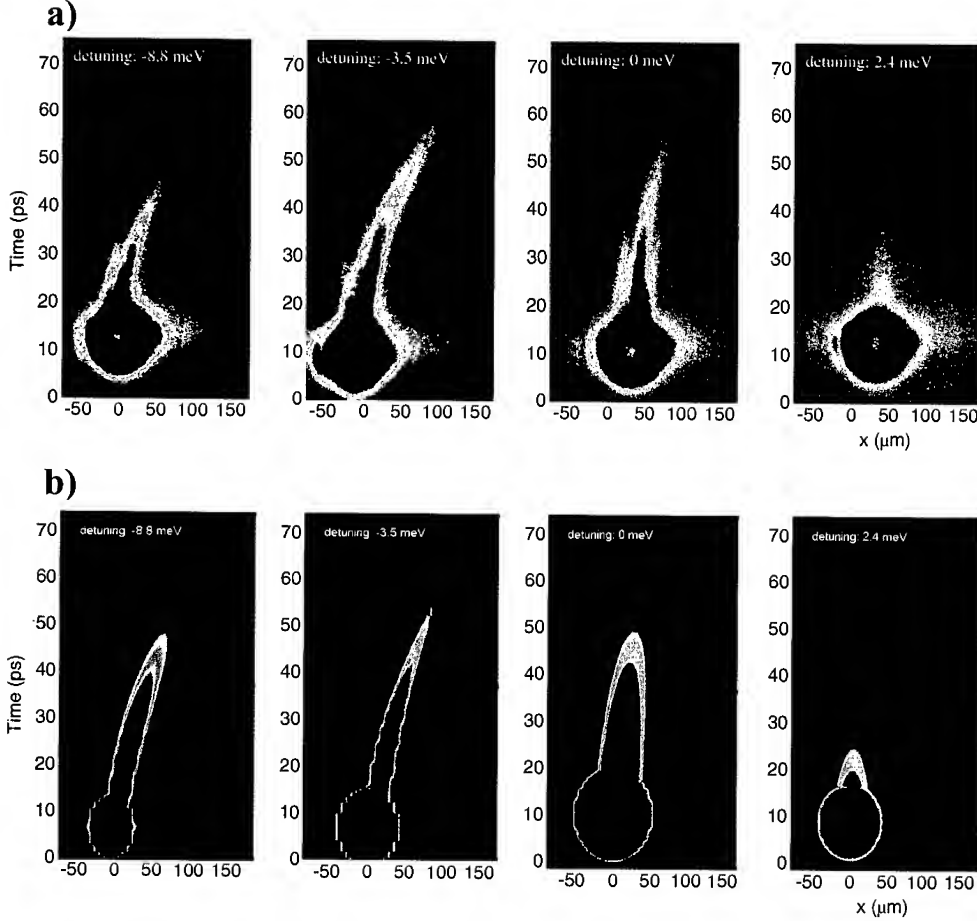


Fig. 2. Movement of the reflection source for four different values of the detuning δ between the cavity mode energy and the exciton energy: a) experiment, b) theory

with $r(x, \omega, k_x)$ being the reflection coefficient of the structure calculated at the given coordinate x for the light characterized by the frequency ω and the in-plane wave vector k_x . We have calculated it taking into account the exciton inhomogeneous broadening as described in Ref. [7]. The function g is given by Eqs. (1) and (3). This formalism neglects the scattering of light due to the in-plane gradient of the cavity and is valid for the in-plane coordinate range given by

$$|x| \ll \frac{E_c}{\partial E_c / \partial x}, \quad (5)$$

where $x = 0$ denotes the center of the incident light spot. As one can see from Eq. (2), the criterion (5) is largely satisfied in our case.

Figure 2b shows the calculated time- and spatially-resolved intensity of the reflected light for the experimental configuration of Fig. 2a. One can see a fairly good agreement between simulation and the experimental data. This is an additional evidence that the observed acceleration effect is purely due to the k -space filtering of the coherent ballis-

tic polariton drift, and does not involve any substantial diffusion of the polaritons. The only important deviation between theory and experiment is that the experimental light spot becomes narrower in space as time increases, while the linear theory predicts the opposite tendency. This might be a manifestation of a nonlinear effect like a self-induced transparency, that needs, of course, further experimental verification.

In conclusion, let us list a few essential consequences of the present experimental finding.

(i) Since the emission comes from the specular direction, the polaritons we observe stay in phase. The decay time of this emission is then an easy way to measure the dephasing time T_2 of the polaritons. At large negative detuning, it yields the cavity photon lifetime. However, due to their movement even if they are excited at normal incidence, one has to check carefully that the polaritons do not move out of the detected zone which would shorten the apparent decay time

(ii) The thickness gradient induces a movement of the polaritons in real space and also in k -space. For this reason after some ten picoseconds, the in-plane k -vector increases up to about 10^4 cm^{-1} . This explains the time behavior of the intensity observed in the experiments of Ref. [5]. In these experiments, the resonant excitation of the cavity polaritons has been done with average $k_x \neq 0$ and $k_y = 0$ and the reflected beam is stopped by a 4 mm wide mask in the collimated beam region. Since the cavity thickness gradient is in the y -direction, after 10–20 ps, the k_y component is no more zero and the reflected beam from the cavity does not hit the mask any more and one can see the reflected beam on the streak camera.

(iii) The observed strong acceleration of the in-plane motion of exciton-polaritons allows us to expect the optical Doppler effect which might be detected in the secondary emission spectra.

Finally, here we reported the first experimental evidence of the acceleration of a ballistic transport of exciton-polaritons in a plane of a graded semiconductor microcavity.

Acknowledgements We acknowledge the partial support from the EU “CLERMONT” program, contract No. HPRN-CT-1999-00132. We would like to acknowledge also E. Giacobino for communication of experimental results before publication and J. Bloch and T. Freixanet for many helpful discussions.

References

- [1] V. M. AGRANOVICH and V. L. GINZBURG, *Crystal Optics with Spatial Dispersion and Excitons*, Springer-Verlag, Berlin 1984.
- [2] C. WEISBUCH et al., *Phys. Rev. Lett.* **69**, 3314 (1992); for a review see M. S. SKOLNICK, T. A. FISHER, and D. M. WHITTAKER, *Semicond. Sci. Technol.* **13**, 645 (1998).
- [3] K. OGAWA, T. KATSUYAMA, and H. NAKAMURA, *Appl. Phys. Lett.* **53**, 1077 (1988); *Phys. Rev. Lett.* **64**, 796 (1990).
- [4] K. OIMATSU, T. IIDA, H. NISHIMURA, K. OGAWA, and T. KATSUYAMA, *J. Lum.* **48/49**, 713 (1991).
- [5] T. FREIXANET et al., *Phys. Rev. B* **61**, 7233 (2000).
- [6] A. KAVOKIN et al., *Phys. Rev. B* **60**, 15554 (1999).
- [7] L. C. ANDREANI et al., *Phys. Rev. B* **57**, 4670 (1998).

phys. stat. sol. (a) **183**, 29 (2000)

Subject classification: 71.35.Lk; 71.36.+c; 78.45.+h

Evidence of Polariton Stimulation in Semiconductor Microcavities

F. BÉUF (a), R. ANDRÉ (a), R. ROMESTAIN (a), LE SI DANG (a), E. PÉRONNE (b),
J. F. LAMPIN (b), D. HULIN (b), and A. ALEXANDROU (b)

(a) *Laboratoire de Spectrométrie Physique (CNRS UMR 5588), Université J. Fourier,
Grenoble, F-38402 Saint Martin d'Hères Cedex, France*

(b) *Laboratoire d'Optique Appliquée (CNRS UMR 7639), ENSTA, Ecole Polytechnique,
F-91761 Palaiseau Cedex, France*

(Received October 8, 2000)

Stimulated photoluminescence of the lower polariton in CdTe microcavities is studied at low temperature, using nonresonant excitation. The stimulation threshold is found to be independent of the number of quantum wells in the microcavities, which rules out the stimulation model based on population inversion of either localized excitons or electron-hole plasma. On the other hand, the bosonic final state stimulation process, or boson effect, is clearly evidenced by tuning the lower polariton to one LO phonon below the exciton reservoir. For detunings closer to zero, the stimulation is dominated by another physical mechanism, that could be the exciton-exciton scattering into the upper and lower polariton states.

Cavity polaritons are two-dimensional eigenstates of semiconductor microcavities which result from the strong coupling between cavity photon modes and excitons in embedded quantum wells (QWs) [1]. Due to their mixed photon-exciton nature, they acquire some of the photon features which markedly differ from those of excitons. For example, the strong in-plane dispersion of cavity modes gives rise to an in-plane polariton effective mass of about $10^{-4} m_e$, and correspondingly, a density of states reduced by four orders of magnitude as compared to excitons. This would favor collective effects for densities well below the exciton saturation density, and the purpose of this paper is to discuss evidence of such phenomenon in CdTe-based microcavities.

Samples used are grown by molecular beam epitaxy on $\text{Cd}_{0.88}\text{Zn}_{0.12}\text{Te}$ substrates. They consist of 2λ $\text{Cd}_{0.40}\text{Mg}_{0.60}\text{Te}$ cavities containing various numbers of CdTe QWs, $N = 1, 2, 4, 6, 8, 12, 16, 24$. Depending on the samples, QWs are about 50 to 70 Å thick, yielding fundamental (heavy-hole) exciton energy $E_X \approx 1.67$ eV and binding energy $E_{BX} \approx 20$ –25 meV. The top and bottom cavity mirrors are distributed Bragg reflectors made of seventeen and twenty pairs of $\text{Cd}_{0.75}\text{Mn}_{0.25}\text{Te}/\text{Cd}_{0.40}\text{Mg}_{0.60}\text{Te}$ $\lambda/4$ layers, respectively. Rabi splittings vary from 7.8 meV for the $N = 1$ microcavity to 29 meV for the $N = 24$ microcavity.

We have previously shown that the lower polariton photoluminescence (PL) can be stimulated by nonresonant excitation with a threshold density about two orders of magnitude smaller than the exciton saturation density [2]. In this work, we investigate the influence of two parameters controlling this stimulated PL, namely the number N of QWs and the detuning $\delta = E_C - E_X$ between the cavity mode energy E_C and the QW exciton energy E_X .

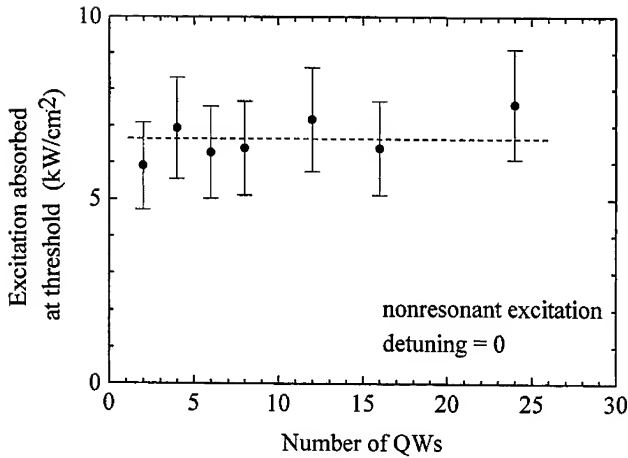


Fig. 1. Variation of the excitation density absorbed at threshold as a function of the number of QWs, measured for detuning $\delta = 0$ meV and nonresonant excitation at 1.8 eV

Figure 1 shows the excitation density absorbed by microcavities at threshold as a function of their number of QWs (there is no data for the $N = 1$ microcavity since it only exhibits stimulation in the weak coupling regime). The PL is excited at 1.8 eV, in the QW exciton continuum and below the barrier energy bandgap. Because the QW absorption is very weak at this photon energy ($\alpha \approx 1\%$), this nonresonant excitation insures a uniform pumping of QWs in microcavities. Thus, the absorbed excitation is obtained by multiplying the excitation incident upon the sample by αN . All measurements are done for the detuning $\delta = 0$ which corresponds to the most favorable condition for the PL stimulation (see below). As shown in Fig. 1, the total absorbed excitation at threshold does not depend at all on the number of QWs and the Rabi splitting. This remarkable behavior is not consistent with the localized exciton model proposed by Fan et al. [3] to explain the PL stimulation they observed in the strong coupling regime of GaAs microcavities. In this model, the stimulation results from the population inversion of localized exciton states that are in resonance with the lower polariton state. Since the total number of localized states varies with the number of QWs and the Rabi splitting, the stimulation threshold should vary, as commonly observed for the population inversion of the electron-hole plasma in multi-QW lasers [4]. Thus, from the fact that the number of QWs has no influence on the stimulation condition we rule out the localized exciton model as well as the electron-hole plasma model, and conclude that polaritonic effects should be involved.

Stimulated PL in the strong coupling regime can also be explained in terms of the boson model [5]. Consider a microcavity excited by a nonresonant external pump. The created electron-hole pairs form a reservoir of hot excitons with large in-plane wave vectors k_{\parallel} that will relax down into the lower polariton state with $k_{\parallel} = 0$ by multiple emissions of phonons. Due to the bosonic nature of excitons and polaritons, the relaxation rate is enhanced by the occupancy of the final state, resulting in stimulated scatterings into the lower polariton state at $k_{\parallel} = 0$ when its occupancy is of the order of one. This is the so-called boson effect [5] whose threshold should strongly dependent on the polariton-exciton energy splitting, or similarly on the cavity-exciton detuning. We have carefully measured the variation of the threshold with detuning, and the results for the 16-QW microcavity are plotted in Fig. 2. It is shown that stimulated PL is observed for

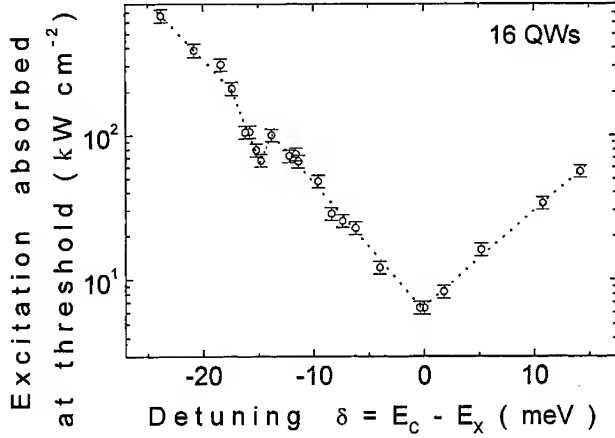


Fig. 2. Variation of the excitation density absorbed by the 16-QW microcavity at threshold as a function of the cavity detuning, measured for nonresonant excitation at 1.8 eV. The dotted curve is a guide for the eye

a wide range of detunings, and not only limited to some negative detunings as in GaAs microcavities [3, 6]. In fact, all our microcavities display a similar detuning dependence, the lowest threshold being obtained for $\delta \approx 0$, regardless of the number of QWs and the Rabi splitting. Among the various stimulated scatterings recently discussed by Tassone and Yamamoto [7], the exciton-exciton scattering into the upper and lower polariton state could qualitatively explain most of our results. First, the minimum threshold for $\delta \approx 0$ can be accounted for by the fact that the exciton reservoir is then halfway between the upper and lower polariton states, so that most excitons can satisfy the conservation of energy and momentum in the scattering process,

$$X1(E_X, \mathbf{k}_{\parallel}) + X2(E_X, -\mathbf{k}_{\parallel}) \rightarrow UP(E_X + \Omega/2, \mathbf{0}) + LP(E_X - \Omega/2, \mathbf{0}), \quad (1)$$

where $X1$ and $X2$ are two exciton states of the reservoir, UP and LP the upper and lower polariton states at $k_{\parallel} = 0$, respectively. Second, only "hot" excitons at $\sim E_X + \delta$ will contribute to the scattering for positive detunings, which could explain why there is no stimulation beyond some positive detuning as shown in Fig. 2. Third, the above discussion remains valid whatever the Rabi splitting value. However, we should emphasize that, in contradiction to Eq. (1), no stimulated PL of the upper polariton has been observed simultaneously with that of the lower polariton. A plausible explanation is that the upper polariton can be strongly scattered back to exciton states because of the huge difference between their densities of states. Further PL studies at high temperature could clarify this issue.

Another remarkable result in Fig. 2 is the sharp minimum observed for $\delta \approx -15$ meV. It can be most easily understood by a closer look at the microcavity in-plane dispersion. Figure 3 displays the polariton-exciton dispersion of the 16-QW microcavity calculated within the two-oscillator model [1], $\delta = 15$ meV, and using the following parameter values: detuning $\delta = -15$ meV, Rabi splitting $\Omega = 26$ meV, $m_e = 0.096$, $m_h = 0.72$ for the electron and hole in-plane masses, respectively, $n = 2.875$ for the cavity refractive index. The dotted lines represent the uncoupled cavity photon mode and the dark exciton states, and the solid lines are the upper and lower polariton states (the lower polariton state is 1/4 exciton and 3/4 photon for this detuning value). Due to the bottleneck effect [7], a large exciton population is distributed over the range of

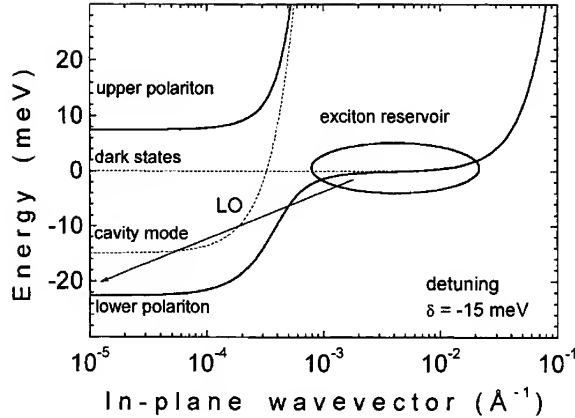


Fig. 3. In-plane dispersions of the 16-QW microcavity calculated for detuning $\delta = -15$ meV, showing the exciton reservoir at one LO phonon (21.4 meV) above the lower polariton state

$k_{\parallel} \approx 10^{-2} \text{ \AA}^{-1}$. Our calculations show that, for the detuning $\delta = -15$ meV, this exciton reservoir is just one LO phonon (about 21.4 meV in bulk CdTe) above the lower polariton state at $k_{\parallel} = 0$. Therefore, excitons in the reservoir can directly relax to the final polariton state by emission of a single LO phonon, with a rate much higher than with acoustic phonons, as recently demonstrated in a GaAs microcavity by Pau et al. [8]. To our knowledge, the relaxation rate of LO phonons is not known in CdTe, but in ZnSe QW it is found to be on the subpicosecond timescale [9]. This is on the order of the polariton radiative lifetime in our microcavities, so that a high occupancy of the lower polariton state could be induced. Therefore, we assign the sharp threshold minimum around $\delta = -15$ meV to a boson effect mediated by the relaxation of LO phonons. It is qualitatively different from the stimulated polariton-polariton scattering recently demonstrated in GaAs microcavities [10], since in the latter case a population of $k_{\parallel} = 0$ lower polaritons has to be externally injected in order to initiate the final state stimulation process.

In conclusion, we have studied the stimulated PL of the lower polariton in CdTe microcavities at low temperature, using nonresonant excitation. The stimulation threshold, in terms of total absorbed excitation, is found to be independent of the number of quantum wells, which rules out the localized exciton model and the electron-hole plasma model. Several stimulation mechanisms are revealed by the detuning study. The LO phonon relaxation mechanism is unambiguously evidenced for a narrow range of negative detunings. For detunings close to zero, the stimulation is dominated by another mechanism, possibly the exciton-exciton scattering into the upper and lower polaritons [7]. In any case it cannot be the acoustic phonon relaxation mechanism [5, 6] since the expected threshold should be higher than for the LO phonon relaxation mechanism. Our study suggests that the combined use of multi-QW microcavities and wide bandgap semiconductors with stronger excitonic effects, such as ZnSe, ZnO, or GaN, could open the way for boson quantum statistic effects at room temperature.

Acknowledgements We would like to thank M. Müller and J. Bleuse for fruitful discussions. This work is done within the CEA-CNRS joint research program "Nanophysique et Semiconducteurs", and supported by the DSP (DGA Ministère de la Défense).

References

- [1] V. SAVONA et al., Solid State Commun. **93**, 733 (1995).
M. S. SKOLNICK et al., Semicond. Sci. Technol. **13**, 645 (1998).
- [2] LE SI DANG et al., Phys. Rev. Lett. **81**, 3920 (1998).
- [3] X. FAN et al., Phys. Rev. B **56**, 15256 (1997).
- [4] K. LAU, in: Quantum Well Lasers, Ed. P. ZORY, Academic Press, Inc., New York 1993.
- [5] A. IMAMOGLU and R. J. RAM, Phys. Lett. A **214**, 193 (1996).
A. IMAMOGLU et al., Phys. Rev. A **53**, 4250 (1996).
S. PAU et al., Phys. Rev. A **54**, R1789 (1996).
- [6] P. SENELLART and J. BLOCH, Phys. Rev. Lett. **82**, 1233 (1999).
- [7] F. TASSONE and Y. YAMAMOTO, Phys. Rev. B **59**, 10830 (1999).
- [8] S. PAU et al., Phys. Rev. B **55**, R1942 (1997).
- [9] H. KALT et al., J. Cryst. Growth **184/185**, 795 (1998).
- [10] P. G. SAVVIDIS et al., Phys. Rev. Lett. **84**, 1547 (2000).
R. HUANG et al., Phys. Rev. B **61**, R7854 (2000).

phys. stat. sol. (a) **183**, 35 (2001)

Subject classification: 77.55.+f; 78.66.Fd; S7.14

Dielectric Microcavity in GaN/Si

J.-Y. DUBOZ¹) (a), L. DUA (a), G. GLASTRE (a), P. LEGAGNEUX (a), J. MASSIES (b), F. SEMOND (b), and N. GRANDJEAN (b)

(a) *Laboratoire Central de Recherches, Thomson-CSF, F-91404 Orsay, France*

(b) *CRHEA-CNRS, rue B. Gregory, F-06560 Sophia Antipolis, France*

(Received October 8, 2000)

We have demonstrated an original approach for fabricating microcavities in GaN grown on Si. Holes are etched in the Si substrate and highly reflective dielectric mirrors are deposited on both front and back sides. The cavity has been optically characterized and the results validate our approach.

Thanks to sophisticated deposition or growth methods, vertical cavities (i.e. along the growth direction) can be made much shorter than horizontal cavities. As a first result, the density of optical modes (especially longitudinal modes) can be made much smaller in vertical cavities than in classical cavities. Second, the field-matter coupling can be made stronger in vertical cavities. From the physical point of view, both effects lead to the possibility of achieving structures where interesting physical phenomena can occur (strong coupling regime [1], excitonic polariton [2], vertical motional narrowing [3, 4], boson effect [5, 6]). From the device point of view, the optical mode reduction is the main interesting effect that leads to an increased external light coupling efficiency, an increased emittance and a better monochromaticity in cavity LEDs. In VCSELs, it gives rise to longitudinal single mode operation (in addition the small cavity volume and the vertical geometry lead to a low threshold current and on wafer testing, respectively). These devices are currently gaining wider acceptance for communication in the near infrared spectral range (for instance 850 and 1300 nm). In the visible range, applications go from monochromatic LEDs for displays to VCSEL arrays for parallel optical storage or printing. GaN has undoubtedly proven that it is the best current candidate for blue LEDs and lasers [7]. Developing vertical cavity GaN devices is the next step [8, 9]. In addition to device applications, the physics of light-matter coupling in nitrides also appears very exciting due to the strong exciton binding energy and the strong oscillator strengths [10] allowing for the observation of a strong coupling regime at high temperature.

The fabrication of microcavities requires the deposition of high reflectivity mirrors on both sides of the active region. The mirrors can be grown by epitaxy or by dielectric deposition. In general, dielectric mirrors have a larger reflectivity with a smaller number of periods than epitaxial mirrors due to the larger index contrast available, and their fabrication is faster and easier than that of epitaxially (MBE or MOCVD) grown mirrors [11, 12]. This is particularly true in the case of GaN where the index contrast

¹) e-mail: duboz@lcr.thomson-csf.com

available in the GaN/AlN system is about 0.4 and 35 GaN/AlGaIn pairs are needed to achieve a modest 0.96 reflectivity [13]. While top mirrors are easily deposited on the GaN surface, the fabrication of bottom dielectric mirrors is more complicated. A first solution consists in bounding the epitaxial layer to a host substrate and removing the initial substrate by various techniques such as plasma or chemical etching, laser lift off [14, 15]. Then, the mirror can be deposited on the bottom of the active layer. This, however, requires sophisticated techniques. Our approach is simpler: we keep the initial substrate as a mechanical support and remove the substrate only locally by classical reactive ion etching techniques. As a result, via holes are etched in the substrate leading to the formation of self-supported membranes of GaN, as shown in Fig. 1.

Such an approach would be very difficult on sapphire due to its high chemical stability. We used a 1.8 μm thick GaN layer grown on Si by MBE. GaN grown on Si (111) has been shown to be of comparable quality to that of GaN grown on sapphire. Via holes (diameter of 250 μm) were defined in the silicon by lithography and reactive ion etching (RIE) with SF_6 . The filling factor of the photolithography mask was about 15% (15% of the Si was removed). Due to the good mechanical properties of Si, much higher filling factors are possible, although we did not investigate this point yet. Thus, the via hole diameter and density are compatible with the fabrication of LEDs or VCSELs. About 10% only of the self-supported membranes were broken during the process (non-optimized first process), probably due to cracks present in the GaN layer grown in tension on Si. Improving the layer quality, reducing the via hole diameter and optimizing the process will lead to higher yields.

We measured the optical transmission through the GaN membrane at 300 K. We observed interference at below gap energies which we use to deduce the membrane thickness; we found 1.8 μm , which is exactly the initial GaN thickness. This shows that the selectivity of the RIE process is excellent and allows to completely remove the silicon without etching the GaN film, making the process reliable. In addition, we measured the GaN residual absorption below the gap. We then measured the photoluminescence (PL) from the front and back sides at low temperature (Fig. 2). On the front side, there is no difference between the PL from the membrane and from outside the membrane, showing the front side is not affected by the process. The PL from the membrane back side is degraded compared to that of the front side, which in our opinion, is largely due to the initial layer quality. Indeed, the same difference is observed in GaN grown on sapphire, where both front and back side PL can be measured easily. Assuming that the PL in Fig. 2 is dominated by the D^0X line, the back side PL peak

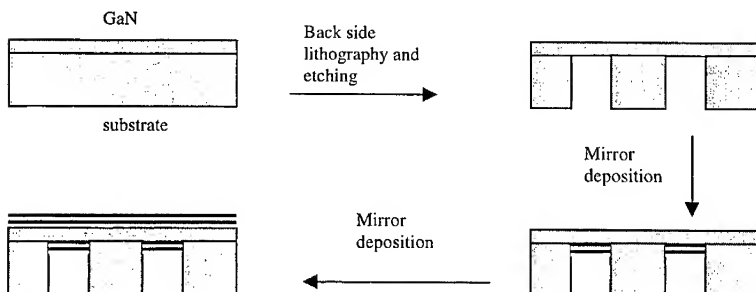


Fig. 1. Schematics of the dielectric mirror microcavity fabrication

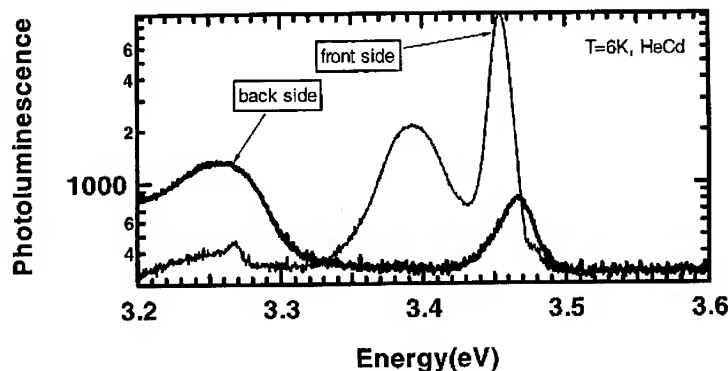


Fig. 2. PL spectra (in arb. units) at 10 K of GaN grown on Si (111), with excitation and collection on the top or bottom side

energy (3.467 eV) indicates a very weak strain while the front side PL peak energy is 3.455 eV, indicating a strong tensile strain [16] (as expected for GaN on Si). It is, however, not clear whether this difference is due to the via hole etching process or not. More precisely, we do not know whether the back side GaN is already relaxed before removing the Si substrate. Finally, we observe a strong donor-acceptor pair line at 3.27 eV (380 nm) in the back face PL which we will use as the emitting line of the microcavity. In this region, GaN remains quite transparent, hopefully leading to a high finesse cavity. Of course, in the future, we will use blue emission from InGaN/GaN quantum wells and work in an even higher transparency region. Then, we deposited $\text{TiO}_2/\text{SiO}_2$ dielectric mirrors (four pairs) on both sides. Mirrors were designed with a maximum reflectivity at 380 nm, and the cavity length was adjusted by deposition of a thin TiO_2 layer so as to present a transmission peak at 380 nm.

We measured the cavity optical transmission. As can be seen in Fig. 3, the transmission spectrum shows oscillations the amplitude of which is damped as the wavelength decreases. We do not really observe the cavity peaks in the mirror stop band. At 380 nm, the transmission is very small. Many factors can explain this result: first, the

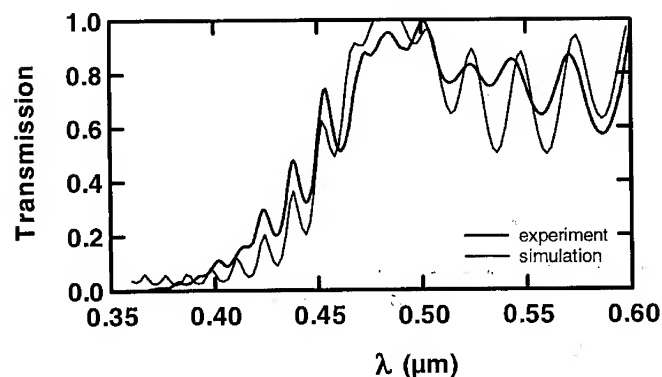


Fig. 3. Experimental and calculated cavity transmission. The simulation includes the GaN dispersion and the residual absorption, and a 15 nm RMS roughness. $T = 300$ K

residual absorption and index dispersion in GaN; second, thickness non-uniformities; third, residual absorption and index dispersion in TiO_2 (that strongly depends on the deposition process). Let us note that the first two factors are very important here as the GaN film is very thick ($1.8 \mu\text{m}$ corresponds to $26 \lambda/2$, which makes this cavity a macrocavity rather than a microcavity). We performed an optical simulation including the GaN index dispersion [17], the residual absorption deduced from our optical transmission measurements through the bare GaN membrane and the thickness non-uniformity (a Gaussian distribution with a typical roughness of 15 nm was assumed). The result is shown in Fig. 3, the agreement with the experimental result is satisfactory. Finally, we measured the cavity PL at 4 K, with excitation and the collection from the back side. The PL signal was very weak due to the strong absorption of the pump (HeCd at 325 nm) in the TiO_2 layers. The result is shown in Fig. 4 and compared with the initial GaN PL spectrum. The PL is clearly modified by the presence of the cavity. The changes cannot be explained by the simple filter effect of the bottom mirror (the mirror transmission is shown in the figure). On the contrary, Fig. 4 shows that the cavity spectrum closely follows the cavity transmission spectrum, indicating that the emission is modified by the microcavity. In particular, the emission around 430 nm already visible in the PL spectrum of the back side membrane (it is a mixture of the LO phonon replica at higher energy and of a very broad defect related band centered at 600 nm) is increased by the cavity. The microcavity effect remains however limited due to the poor cavity factor Q . Note that the transmission was measured at 300 K while the PL was recorded at 10 K, explaining that the agreement between both measurements is only qualitative.

The origins of the observed limitations have been understood and the following changes should lead to much better results: first, the emission line will be at longer wavelength (we will add InGaN quantum wells), thus avoiding the absorption and dispersion of GaN, and also TiO_2 . Second, the GaN thickness will be considerably reduced. As a result, we should get a much larger transmission coefficient (>0.5) at the

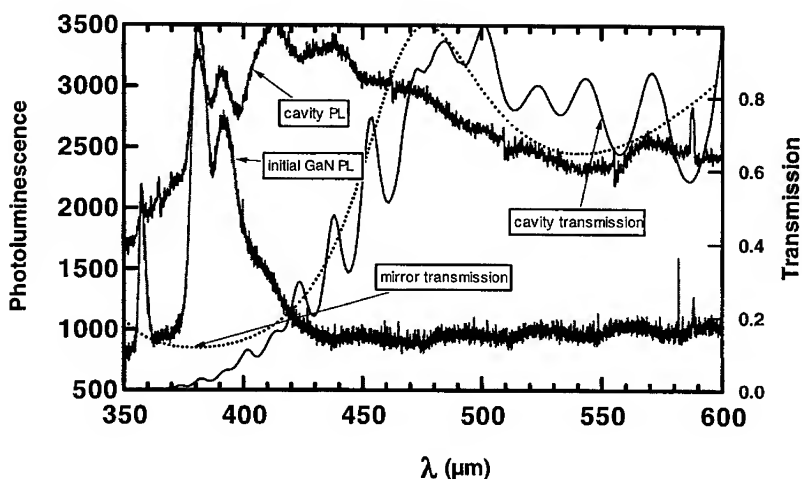


Fig. 4. Photoluminescence at 10 K of the cavity, compared with the initial GaN PL spectrum. The bottom mirror and cavity transmission curves show that the difference between the PL spectra is due to a cavity effect

emitting wavelength and a PL spectrum dominated by the InGaN emission line with a linewidth imposed by the cavity, i.e. much smaller than the initial InGaN linewidth. The fabrication of new structures that include these changes is under way.

References

- [1] C. WEISBUCH, M. NISHIOKA, A. ISHIKAWA, and Y. ARAKAWA, *Phys. Rev. Lett.* **69**, 3314 (1992).
- [2] F. TASSONE, C. PIERMAROCCHI, V. SAVONA, A. QUATTROPANI, and P. SCHWENDIMANN, *Phys. Rev. B* **53**, R7642 (1996).
- [3] J. J. BAUMBERG, A. P. HERBERLE, A. V. KAVOKIN, M. R. VLADIMIROVA, and K. KÖHLER, *Phys. Rev. Lett.* **80**, 3567 (1998).
- [4] G. MALPUECH and A. V. KAVOKIN, *Appl. Phys. Lett.* **76**, 3049 (2000).
- [5] S. PAU, H. CAO, J. JACOBSON, G. BJÖRK, and Y. YAMAMOTO, *Phys. Rev. A* **54**, R1789 (1996).
- [6] M. KIRA, F. JAHNKE, S. KOCH, J. D. BERGER, D. V. WICK, G. KHITROVA, and H. M. GIBBS, *Phys. Rev. Lett.* **79**, 5170 (1997).
- [7] S. NAKAMURA and G. FASOL, *The Blue Laser Diode*, Springer-Verlag, Berlin/Heidelberg 1997.
- [8] T. SOMEYA, K. TACHIBANA, J. LEE, T. KAMIYA, and Y. ARAKAWA, *Jpn. J. Appl. Phys.* **37**, L1424 (1998).
- [9] I. L. KRESTNIKOV, W. V. LUNDIN, A. V. SAKHAROV, V. A. SEMENOV, A. S. USIKOV, A. F. TSATSULNIKOV, Z. I. ALFEROV, N. N. LEDENTSOV, A. HOFFMANN, and D. BMBERG, *Appl. Phys. Lett.* **75**, 1192 (1999).
- [10] A. KAVOKIN and B. GIL, *Appl. Phys. Lett.* **72**, 2880 (1998).
- [11] H. M. NG, D. DOPPALAPUDI, E. ILIOPOULOS, and T. D. MOUSTAKAS, *Appl. Phys. Lett.* **74**, 1036 (1999).
- [12] R. LANGER, A. BARSKI, J. SIMON, N. T. PELEKANOS, O. KONOVALOV, R. ANDRÉ, and D. L. S. DANG, *Appl. Phys. Lett.* **74**, 3610 (1999).
- [13] T. SOMEYA and Y. ARAKAWA, *Appl. Phys. Lett.* **73**, 3653 (1998).
- [14] Y. K. SONG, H. ZHOU, M. DIAGNE, I. OZDEN, A. VERTIKOV, A. V. NURMIKKO, C. CARTER-COMAN, R. S. KERN, F. A. KISH, and M. R. KRAMES, *Appl. Phys. Lett.* **74**, 3441 (1999).
- [15] Y. K. SONG, M. DIAGNE, H. ZHOU, A. V. NURMIKKO, C. CARTER-COMAN, R. S. KERN, F. A. KISH, and M. R. KRAMES, *Appl. Phys. Lett.* **74**, 3720 (1999).
- [16] B. GIL, O. BRIOT, and R. L. AULOMBART, *Phys. Rev.* **52**, 17028 (1995).
- [17] H. Y. ZHANG, X. H. HE, Y. H. SHIH, M. SCHURMAN, Z. C. FENG, and R. A. STALL, *Optics Lett.* **21**, 1519 (1996).

phys. stat. sol. (a) **183**, 41 (2001)

Subject classification: 72.20.Jv; 78.47.+p; S7.14

Radiative and Nonradiative Recombination Processes in GaN-Based Semiconductors

Y. KAWAKAMI (a), K. OMAE (a), A. KANETA (a), K. OKAMOTO (a), T. IZUMI (a),
S. SAJOU (a), K. INOUE (a), Y. NARUKAWA (b), T. MUKAI (b), and SG. FUJITA (a)

(a) *Department of Electronic Science and Engineering, Kyoto University,
Kyoto 606-8501, Japan*

(b) *Nitride Semiconductor Research Laboratory, Nichia Corporation, 491 Oka,
Kaminaka, Anan, Tokushima 774-8601, Japan*

(Received October 8, 2000)

Time-resolved optical characterization is an indispensable tool to study the recombination mechanisms of excitons and/or carriers based on radiative, non-radiative, localization and many-body processes. In this paper, we review the instrumentation of various spectroscopic techniques for the assessment of $\text{In}_x\text{Ga}_{1-x}\text{N}$ -based semiconductors such as time-resolved photoluminescence (TRPL), time-resolved electroluminescence (TREL), transient grating (TG) method to probe photothermal processes, microscopic TRPL using optical microscope, submicroscopic TRPL using scanning near field optical microscopy (SNOM) and pump-and-probe spectroscopy for the measurement of transient absorption/gain spectra. The obtained results are cited in the references.

1. Introduction Time-resolved spectroscopy is a useful technique to evaluate the optical properties of semiconductors. As for GaN-based semiconductors, targets as photonic devices can be classified in three subjects.

The first subject is to achieve efficient light emitting diodes (LEDs). Typical blue or green LEDs commercially available show an external quantum efficiency (η_{ext}) of about 10% [1, 2]. However, further improvement of the efficiency is desired to extend the application area of LEDs, such as a replacement of light bulb or fluorescent lamp (vacuum tubes) by LEDs (solid state devices). Luminescence spectroscopy reveals that performances of LEDs at room temperature (RT) are still limited by non-radiative recombination processes, and that it should be possible to achieve $\eta_{\text{ext}} > 40\%$ if the pathway to the non-radiative recombination centers is eliminated sufficiently. Therefore, it is very important to assess the mechanism of both radiative and non-radiative processes in order to clarify a key to get higher efficiency.

The second subject is related to the laser diodes (LDs). Since the first operation of LD has been demonstrated at 400 nm under a continuous wave (CW) mode at RT [3], the device lifetime has been made good progress, and at current stage the maximum operation time is estimated to be 10000 h [4]. However, the tuning wavelength for the stable continuous wave (CW) operation of LDs is currently in the range between 376 nm [5] and 450 nm [6], which is much narrower than that of LEDs due to the dramatic increase of I_{th} with increasing emission wavelength from 420 to 450 nm. This

¹) Corresponding author; Tel.: +81-75-753-7573; Fax: +81-75-753-7579;
e-mail: kawakami@kuee.kyoto-u.ac.jp

may be because internal electric field [7] is so large in In-rich active layers that the oscillator strength between electron and hole is suppressed, and/or because the optical gain cannot be generated sufficiently due to the limited number of density-of-states caused by the effect of localization [8–16]. Further breakthrough is therefore required to realize pure blue and green LDs using $\text{In}_x\text{Ga}_{1-x}\text{N}$ -based semiconductors. Such targets can be facilitated by well-understanding the emission mechanism, as well as by the well-designing of the LD structures.

The third subject is related to the development of new photonic devices besides LEDs or LDs utilising ultrafast phenomena or optical nonlinearity.

For such purposes, it is essential to understand the recombination mechanism by assessing the dynamical behavior of excitons and/or carriers based on radiative, non-radiative, localization and many-body processes, and then to make a positive feedback to the fabrication of photonic devices.

In this paper, instrumentation of time-resolved spectroscopy developed by our group is reviewed for the assessment of recombination dynamics in $\text{In}_x\text{Ga}_{1-x}\text{N}$ -based semiconductors.

2. Instrumentation of Time-Resolved Spectroscopy

2.1 Time-resolved photoluminescence (TRPL) Figure 1 shows the experimental apparatus for the time-resolved photoluminescence (TRPL). Pulsed photo-excitation for the TRPL is provided by the frequency doubled (2ω) or frequency tripled (3ω) beams of a mode-locked $\text{Al}_2\text{O}_3:\text{Ti}$ laser (ω) which was pumped by Ar^+ laser. It is possible to make a selective excitation to $\text{In}_x\text{Ga}_{1-x}\text{N}$ active layers by using a frequency doubled beam whose tuning range is from 350 to 530 nm. Two types of pulse width, 1.5 and 100 fs can be selected by adjusting the optics in $\text{Al}_2\text{O}_3:\text{Ti}$ laser. The pulse width of 1.5 ps is suitable

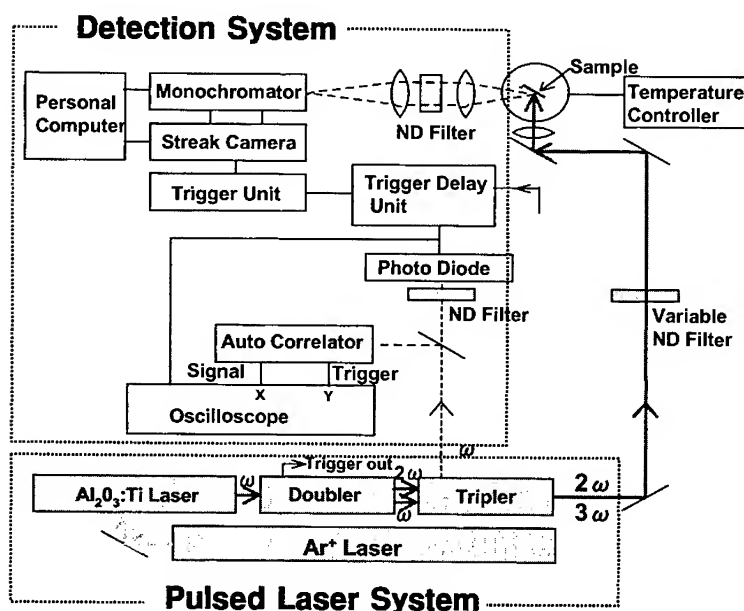


Fig. 1. Experimental apparatus for time-resolved photoluminescence

ble for the TRPL measurement if monochromaticity is needed for photoexcitation. The repetition rate of the laser is 80 MHz whose time interval is 12.5 ns. It can be reduced to 4 MHz by an acousto-optic (AO) modulator in order to avoid multi-excitation depending on the decay times. The detection is performed by means of a fast scan streak camera in conjunction with monochromator using gratings whose grooves are 100, 300 and 1200 lines/grooves. Time-resolution for the detection is about 2 ps.

The transient luminescence intensity obtained by the data of TRPL shown in Fig. 2 is generally expressed by the following equation as a function of time after excitation:

$$I(t) = I_0 \exp\left(-\frac{t}{\tau_{PL}(T)}\right), \quad (1)$$

where $\tau_{PL}(T)$ is the decay time of luminescence at a given temperature (T in K). The inverse of $\tau_{PL}(T)$ is the sum of three different types of transition probability,

$$\frac{1}{\tau_{PL}(T)} = \frac{1}{\tau_{rad}(T)} + \frac{1}{\tau_{non-rad}(T)} + \frac{1}{\tau_{trans}(T)}, \quad (2)$$

where $\tau_{rad}(T)$ and $\tau_{non-rad}(T)$ denote the radiative and non-radiative lifetimes, and $\tau_{trans}(T)$ is the transfer time toward lower-lying energy levels. If radiative recombination occurs at the bottom of energy levels, the term of the transfer time can be neglected so that the equation is simplified as shown below.

The internal quantum efficiency ($\eta_{int}(T)$) of the emission can also be written in terms of $\tau_{rad}(T)$ and $\tau_{non-rad}(T)$, where

$$\frac{1}{\tau_{PL}(T)} = \frac{1}{\tau_{rad}(T)} + \frac{1}{\tau_{non-rad}(T)}, \quad \eta_{int}(T) = \frac{\tau_{non-rad}(T)}{\tau_{rad}(T) + \tau_{non-rad}(T)}. \quad (3), (4)$$

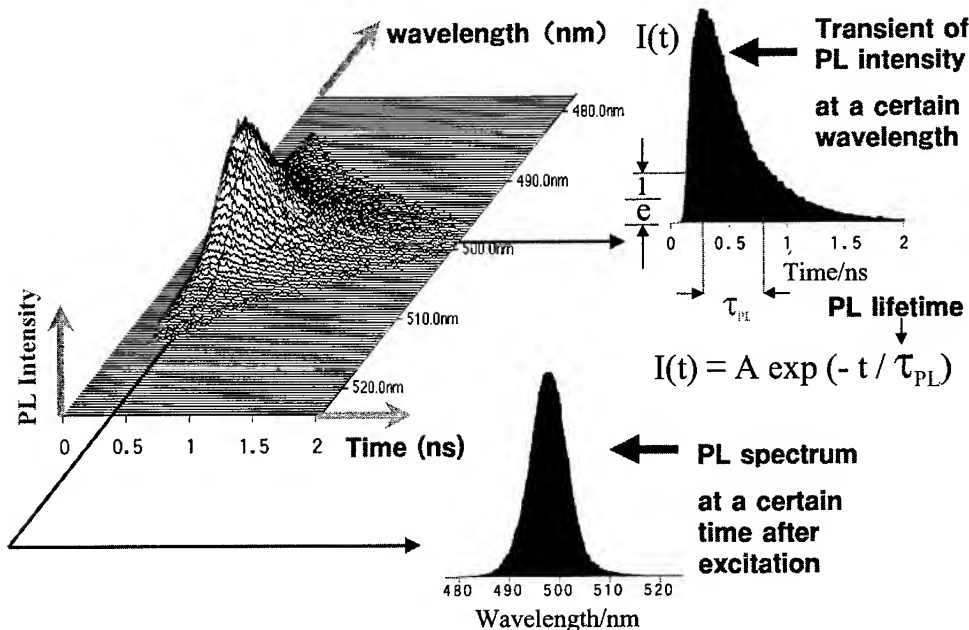


Fig. 2. Typical data obtained by time-resolved photoluminescence spectroscopy

Therefore, it is possible to estimate the temperature dependence of radiative and non-radiative lifetimes, by monitoring both $\tau_{\text{PL}}(T)$ and $\eta_{\text{int}}(T)$. However, it is generally difficult to measure the $\eta_{\text{int}}(T)$ value directly by experiment.

$\tau_{\text{non-rad}}(T)$ can be expressed by the following equation:

$$\frac{1}{\tau_{\text{non-rad}}(T)} = v_{\text{th}} \sigma N_{\text{t}}, \quad (5)$$

where v_{th} , σ and N_{t} denote the thermal velocity, cross section captured to non-radiative recombination center (NRC) and the density of NRC, respectively. There is a case where the non-radiative recombination process can be ignored, if the crystal quality is relatively good (low N_{t}) and the measurement is done at sufficiently low temperature. In fact, we sometimes see the temperature dependence of luminescence intensity $I(T)$, where $I(T)$ is constant ($I(T) = I_{\text{C}}$) in a low temperature region ($T < T_{\text{C}}$), and then decreases gradually with increasing temperature ($T > T_{\text{C}}$). In such a case, it can be assumed that internal quantum efficiency is nearly equal to unity at temperature below T_{C} , so that the luminescence decay time in this temperature range corresponds to the radiative lifetime. If necessary, validity of such an assumption can be tested by means of the detection of photothermal processes as described in Section 2.3. Then, the internal quantum efficiency can be expressed by $\eta_{\text{int}}(T) = I(T)/I_{\text{C}}$, and both radiative and non-radiative lifetimes at temperature above T_{C} can be given by the following equations [17]:

$$\tau_{\text{rad}}(T) = \tau_{\text{PL}}(T) \frac{I_{\text{C}}}{I(T)}, \quad (6)$$

$$\tau_{\text{non-rad}}(T) = \tau_{\text{PL}}(T) \frac{I_{\text{C}}}{I_{\text{C}} - I(T)}. \quad (7)$$

The temperature dependence of radiative lifetimes reveals the dimensionality of excitons [18, 19]. The dynamical behaviour of excitons based on localization, radiative and non-radiative recombination processes has been studied in $\text{In}_x\text{Ga}_{1-x}\text{N}$ -based light emitting devices. It was found that excitons were weakly localized mainly due to the small fluctuation of alloy content if the In alloy content was less than about 10%. The depth of exciton localization grew with increasing In content, and the self-formation of deep localization centers was observed in the sample with $x > 20\%$ [9, 13]. In such highly localized samples almost no temperature dependence of radiative lifetimes was observed suggesting the zero-dimensional feature of excitons [14, 15].

2.2 Time-resolved electroluminescence (TREL) Even if there is no short-pulse laser system, the luminescence dynamics can be assessed by applying pulsed voltage across p-i-n junction. Figure 3 shows the time-resolved electroluminescence (TREL) system [20, 21]. The pulse width and repetition rate of voltage applied to LEDs are 8 ns and 4 MHz, respectively. The condition of impedance matching can be attained with a variable resistor by minimizing the reflected current pulse monitored by a fast digital oscilloscope. Although the pulse width of applied voltage is rather broad, a time resolution of about 500 ps can be achieved by deconvoluting the current-pulse signal with the transient EL signal monitored by the streak camera. Recent progress of experimental technique has led to the TREL measurement using a pulse generator with pulse width of 150 ps.

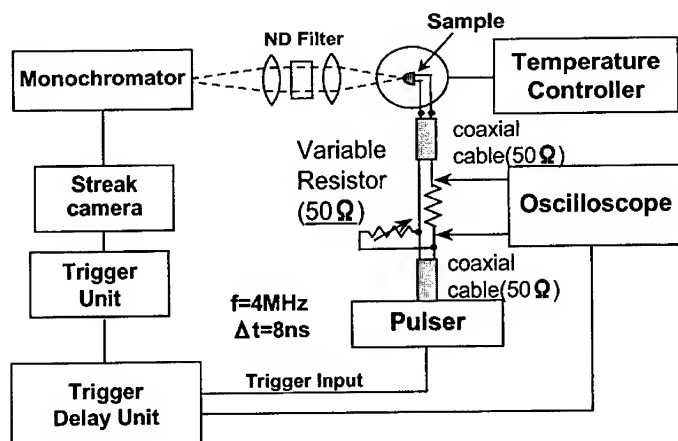


Fig. 3. Experimental apparatus for time-resolved electroluminescence

2.3 Transient grating (TG) method to probe photothermal processes The heat dynamics generated by non-radiative recombination processes can be assessed by measuring the photo-induced refractive index change (Δn) by using the transient grating (TG) method based on third-order nonlinear spectroscopy [22–24]. The experimental set-up of the excitation and probe beams of the TG method are shown in Fig. 4. A frequency tripled beam of Nd:YAG laser (355 nm) was used for excitation. The interference pattern is created by crossing two excitation beams with an angle θ in the sample materials. The fringe spacing Λ is given by

$$\Lambda = \frac{\lambda_e}{2 \sin \left(\frac{\theta}{2} \right)}. \quad (8)$$

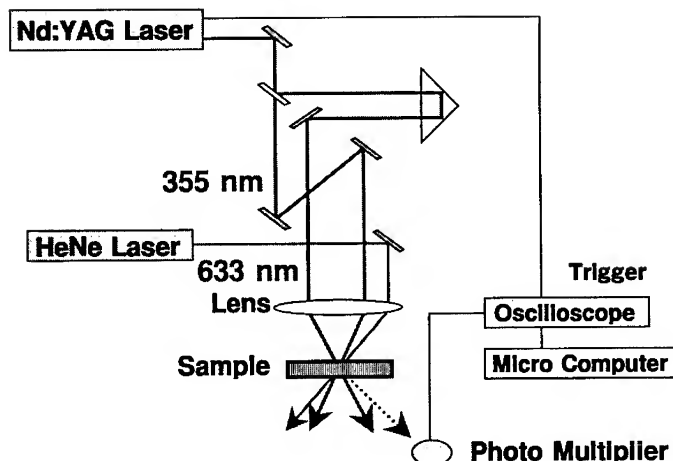


Fig. 4. Experimental apparatus for transient grating spectroscopy

Then, the light intensity in the crossing region is modulated as follows:

$$I(x) = \frac{I(1 + \cos qx)}{2}, \quad (9)$$

where q is the grating vector given by

$$q = \frac{2\pi}{\Lambda}. \quad (10)$$

The densities of carriers and/or excitons are modulated along this optical grating (population grating). The excited area releases the heat by the non-radiative recombination of carriers and/or excitons and the temperature of the sample is modulated (thermal grating). The refractive index (n) and the absorbance (k) of the materials are also modulated by these gratings. Such modulation of optical properties (Δn , Δk) are similar to the refractive grating. A probe beam from a He-Ne laser (633 nm) was partly diffracted (TG signal) by these gratings. The intensity of the TG signal can be written by

$$I_{TG} = \alpha \Delta n^2 + \beta \Delta k^2, \quad (11)$$

where α and β are constants. The TG signal was detected by a photomultiplier tube after isolation from the probe light with a pinhole and a glass filter, recorded with a digital oscilloscope, and analyzed with a microcomputer.

2.4 Microscopic TRPL using optical microscope In order to assess the correlation between PL lifetimes and macroscopic dislocations, TRPL spectroscopy with micron spatial resolution [25, 26] was performed on the epitaxially laterally overgrown GaN (ELO-GaN) and $\text{In}_x\text{Ga}_{1-x}\text{N}$ quantum wells (QWs) grown on ELO-GaN [25] by using the apparatus as shown in Fig. 5. The beam is focused down to the size of about $1\text{ }\mu\text{m}$ using air-gapped object lens made of quartz. The fluorescence image can be observed by an optical microscope in conjunction with a CCD camera, and be detected through

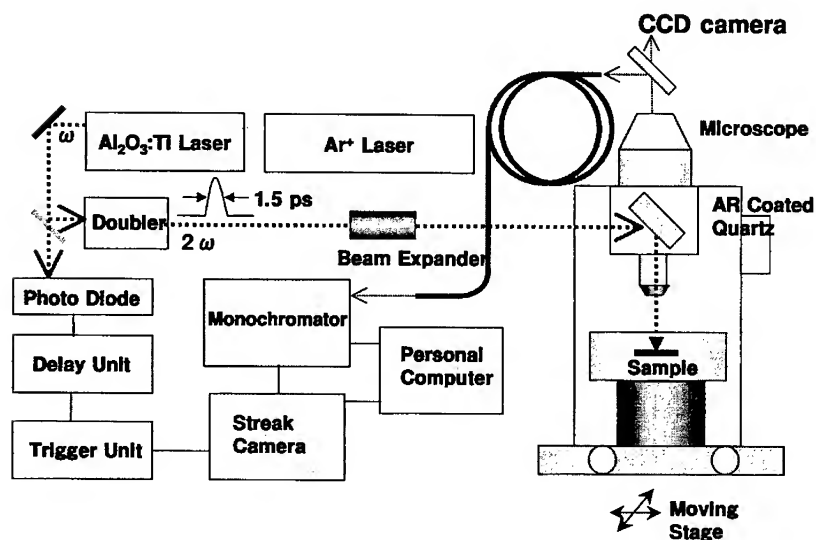


Fig. 5. Time-resolved photoluminescence with spatial resolution of about $1\text{ }\mu\text{m}$

an UV-optical fiber in order to measure TRPL using the system shown in Fig. 1. It was found that threading dislocations act as non-radiative recombination centers, but they are not the factor to limit the internal quantum efficiency at RT [25]. The dependence of dislocation density on τ_{PL} for $\text{In}_x\text{Ga}_{1-x}\text{N}$ QWs became less dominant with increasing In mole fraction (x value) [27]. This result suggests that the capture cross sections of non-radiative recombination centers are greatly reduced once excitons are trapped at deep localization centers in In-rich $\text{In}_x\text{Ga}_{1-x}\text{N}$ active layers [9].

2.5 Submicroscopic TRPL using scanning near field optical microscopy (SNOM) If the TRPL with nanoscopic spatial resolution could be achieved, five-dimensional (5D) data composed of space, wavelength and time would give us a more clear view on the correlation between nanoscopic structures and macroscopic optical properties. We have recently performed the first PL imaging of an $\text{In}_x\text{Ga}_{1-x}\text{N}$ -SQW-based LED structure using scanning near field optical microscopy (SNOM) under illumination-collection mode, where photo-excitation and the PL probing are performed using the same fiber tip as shown in Fig. 6 [28].

This was achieved by tailoring the tapered structure of fiber tip composed of a pure SiO_2 core to transmit UV light with low transmission loss, and to eliminate the emission background from the fiber. The measured PL mapping image revealed the variation of both peak and intensity in PL spectra according to the probing location with a resolution of about $0.1 \mu\text{m}$.

The variation in PL intensity observed in a yellowish green LED was from 0.8 to 1.8 (in arb. units) indicating that internal quantum efficiency fluctuates from 10% to 50% within the active layer. TRPL spectroscopy using this system is now under progress.

2.6 Pump and probe spectroscopy for the transient absorption/gain measurement The pump and probe spectroscopy depicted in Fig. 7 was performed for the measurements of the temporal behavior of differential absorption using a dual photo-diode array in conjunction with a 25 cm monochromator [29]. The white light used for the probe beam was generated by focusing the part of output beam from the regenerative amplifier on a D_2O cell. Detailed optical paths of both pump and probe beams are drawn in Fig. 3. The delay time of the probe beam with respect to the pump beam was tuned by changing the position of retroreflector which could be controlled by the pulse stage. Since the minimum difference in optical path was $2 \mu\text{m}$, a time resolution down to 6.7 fs was

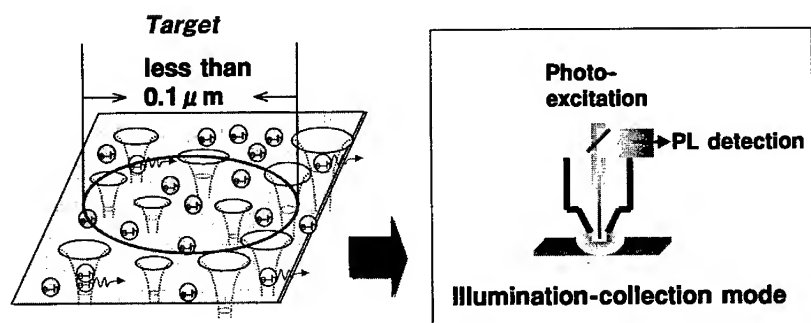


Fig. 6. An approach to improve the resolution less than $0.1 \mu\text{m}$ by using scanning near field microscopic technique

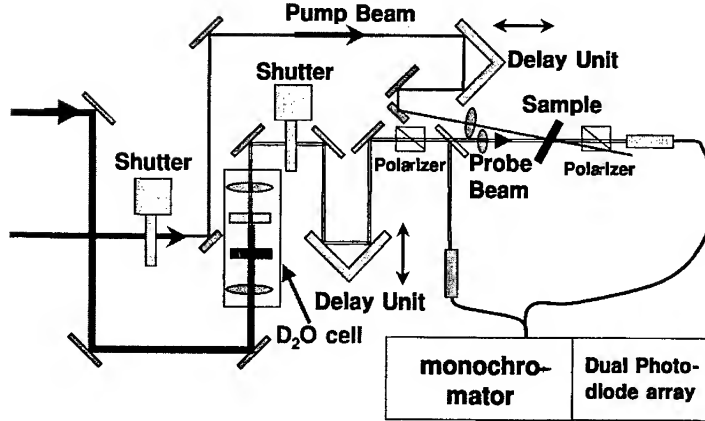


Fig. 7. Experimental set-up for the pump and probe spectroscopy

achieved. In order to detect the probe beam with spatially uniform carrier distribution in the sample, the focus size of the pump beam ($600\ \mu\text{m}$ in diameter) was set so as to be much larger than that of the probe beam ($200\ \mu\text{m}$ in diameter). Furthermore, the probe beam was perpendicularly polarized with respect to the pump beam, and the transmitted probe beam polarized in this direction was detected to avoid scattering of the pump beam.

In the pump and probe spectroscopy, the transmission spectrum of the probe beam detected in the presence of the pump beam ($T + \Delta T$) is compared to the spectrum without pump beam (T), giving the frequency (ω)-dependent $\Delta T(\omega, I_{\text{ex}}, t_d)$ of the sample for different intensities of the pump (I_{ex}), and for different time delays after the pulse pumping (t_d). The photo-induced change of optical density ($\Delta OD(\omega, I_{\text{ex}}, t_d)$) is expressed by the following equation:

$$\Delta OD = \log \left(\frac{T}{T + \Delta T} \right) = 0.434 \Delta \alpha d, \quad (12)$$

where $\Delta \alpha(\omega, I_{\text{ex}}, t_d)$ is the photo-induced change of absorption coefficient, d is the thickness of absorbing layer. A schematic of α and $\alpha + \Delta \alpha$ is illustrated in Fig. 8. In

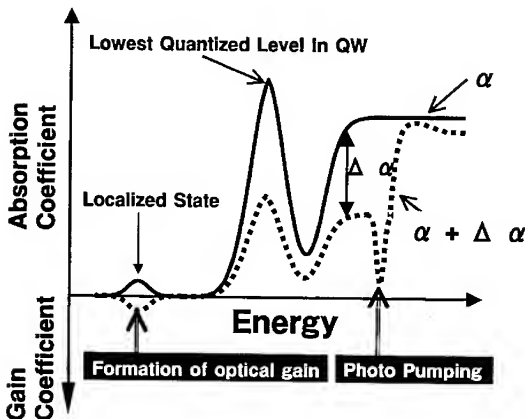


Fig. 8. Schematic of carrier dynamics in a localized system. α and $\alpha + \Delta \alpha$ denote absorption coefficient under low photoexcitation and under photo pumping, respectively

normal case, photo-bleaching ($\alpha + \Delta\alpha < \alpha$) is observed because of the state-filling of photo-induced carrier, and $\alpha + \Delta\alpha$ becomes negative, giving rise to optical gain if population inversion is achieved. As can be observed in the modulation spectroscopy such as photoreflectance (PR) or electroreflectance (ER), it is likely that the ΔOD signal would not be affected by the interference of transmittance because of the cancellation between the denominator and numerator in Eq. (1). However, interference oscillation was observed probably because of the change of refractive index induced by photo-excitation. Therefore, it was necessary to reduce the internal reflection of the probe beam by means of the Brewster angle of incidence (about 70°) with p-polarization.

Dynamical behavior of optical gain formation has been assessed at RT in the $\text{In}_x\text{Ga}_{1-x}\text{N}$ multi-quantum-well (MQW)-based LD structures by employing pump and probe spectroscopy with a pulse width of 150 fs. The LDs are composed of a) $\text{In}_{0.1}\text{Ga}_{0.9}\text{N}$ – $\text{In}_{0.02}\text{Ga}_{0.98}\text{N}$ MQW and b) $\text{In}_{0.3}\text{Ga}_{0.7}\text{N}$ – $\text{In}_{0.05}\text{Ga}_{0.95}\text{N}$ MQW, whose stimulated emissions correspond to near ultraviolet (390 nm) and blue (440 nm), respectively. The optical gain was contributed from the nearly delocalized states (the lowest-quantized MQW levels (LQL)) in the sample a, while it was from highly localized levels with respect to LQL by 500 meV for the sample b. It was found that the photo-generated carriers rapidly (less than 1 ps) transferred to LQL, and then relaxed to the localized tail within the time scale of about 5 ps, giving rise to the optical gain. Such gain spectra were saturated and other bands appeared in the vicinity of LQL under higher photo-excitation [30].

Acknowledgements The authors are grateful for the financial support of the Grant-in-Aid for Scientific Research from the Ministry of Education, Science, Sports and Culture. A part of this work was performed using the facility at the Venture Business Laboratory in Kyoto University (KU-VBL).

References

- [1] S. NAKAMURA, M. SENOH, N. IWASA, S. NAGAHAMA, T. YAMADA, and T. MUKAI, *Jpn. J. Appl. Phys.* **34**, L1332 (1995).
- [2] S. NAKAMURA, M. SENOH, N. IWASA, S. NAGAHAMA, T. YAMADA, and T. MUKAI, *Jpn. J. Appl. Phys.* **37**, L479 (1998).
- [3] S. NAKAMURA, M. SENOH, S. NAGAHAMA, N. IWASA, T. YAMADA, T. MATSUSHITA, H. KİYOKU, and Y. SUGIMOTO, *Jpn. J. Appl. Phys.* **35**, L74 (1996).
- [4] S. NAKAMURA, M. SENOH, S. NAGAHAMA, T. MATSUSHITA, H. KİYOKU, Y. SUGIMOTO, T. KOZAKI, H. UMEMOTO, M. SANO, and T. MUKAI, *Jpn. J. Appl. Phys.* **38**, L226 (1999).
- [5] I. AKASAKI, H. AMANO, S. SOTA, H. SAKAI, T. TANAKA, and M. KOIKE, *Electron. Lett.* **32**, 1105 (1996).
- [6] S. NAKAMURA, M. SENOH, S. NAGAHAMA, N. IWASA, T. MATSUSHITA, and T. MUKAI, *Appl. Phys. Lett.* **76**, 22 (2000).
- [7] T. TAKEUCHI, C. WETZEL, S. YAMAGUCHI, H. SAKAI, H. AMANO, I. AKASAKI, Y. KANEKO, S. NAKAGAWA, Y. YAMAOKA, and N. YAMADA, *Appl. Phys. Lett.* **73**, 1691 (1998).
- [8] S. CHICHIBU, T. AZUHATA, T. SOTA, and S. NAKAMURA, *Appl. Phys. Lett.* **69**, 4188 (1996).
- [9] Y. NARUKAWA, Y. KAWAKAMI, M. FUNATO, S. FUJITA, S. FUJITA, and S. NAKAMURA, *Appl. Phys. Lett.* **70**, 868 (1997).
- [10] Y. NARUKAWA, Y. KAWAKAMI, S. FUJITA, and S. NAKAMURA, *phys. stat. sol. (a)* **176**, 39 (1999).
- [11] T. DEGUCHI, T. AZUHATA, T. SOTA, S. CHICHIBU, and S. NAKAMURA, *Mater. Sci. Engng. B* **50**, 251 (1997).
- [12] A. SATAKE, Y. MASUMOTO, T. MIYAJIMA, T. ASATSUMA, and M. IKEDA, *Phys. Rev. B* **60**, 16660 (1999).

- [13] Y. NARUKAWA, Y. KAWAKAMI, SZ. FUJITA, SG. FUJITA, and S. NAKAMURA, *Phys. Rev. B* **55**, R1938 (1997).
- [14] Y. NARUKAWA, Y. KAWAKAMI, SG. FUJITA, and S. NAKAMURA, *Phys. Rev. B* **59**, 10283 (1999).
- [15] Y. KAWAKAMI, Y. NARUKAWA, K. OMAE, SG. FUJITA, and S. NAKAMURA, *phys. stat. sol. (a)* **178**, 331 (2000).
- [16] Y. CHO, T. J. SCHMIDT, S. BIDNYK, G. H. GAINER, J. J. SONG, S. KELLER, U. K. MISHRA, and S. P. DENBAARS, *Phys. Rev. B* **61**, 7571 (2000).
- [17] R. C. MILLER, D. A. KLEINMAN, W. A. NORDRAND, JR., and A. C. GOSSARD, *Phys. Rev. B* **22**, 863 (1980).
- [18] P. LEFEBVRE, J. ALLÈGRE, B. GIL, A. KAVOKIN, H. MATHIEU, W. KIM, A. SALVADOR, A. BOTCHKAREV, and H. MORKOÇ, *Phys. Rev. B* **57**, R9447 (1998).
- [19] Y. NARUKAWA, S. SAIJOU, Y. KAWAKAMI, SG. FUJITA, T. MUKAI, and S. NAKAMURA, *Appl. Phys. Lett.* **74**, 558 (1999).
- [20] Y. NARUKAWA, S. SAIJOU, Y. KAWAKAMI, SZ. FUJITA, SG. FUJITA, and S. NAKAMURA, *J. Cryst. Growth* **189/190**, 593 (1998).
- [21] Y. KAWAKAMI, Y. NARUKAWA, K. SAWADA, S. SAIJOU, SZ. FUJITA, SG. FUJITA, and S. NAKAMURA, *Mater. Sci. Engng. B* **50**, 256 (1997).
- [22] H. HAAG, B. HÖNERLAGE, O. BRIOT, and R. L. AULOMBARD, *Phys. Rev. B* **60**, 11624 (1999).
- [23] K. OKAMOTO, Y. KAWAKAMI, SG. FUJITA, and M. TERAZIMA, *Anal. Sci.*, in press.
- [24] K. OKAMOTO, Y. KAWAKAMI, SG. FUJITA, M. TERAZIMA, and S. NAKAMURA, *Jpn. J. Appl. Phys.*, in press.
- [25] T. IZUMI, Y. NARUKAWA, K. OKAMOTO, Y. KAWAKAMI, SG. FUJITA, and S. NAKAMURA, *J. Lum.* **87/89**, 1196 (2000).
- [26] K. OKAMOTO, H. C. KO, Y. KAWAKAMI, and SG. FUJITA, *J. Cryst. Growth* **214/215**, 639 (2000).
- [27] T. IZUMI, K. INOUE, Y. NARUKAWA, K. OKAMOTO, Y. KAWAKAMI, SG. FUJITA, A. TSUJIMURA, I. KIDOGUCHI, and Y. BAN, *Jpn. J. Appl. Phys.*, in press.
- [28] A. KANETA, T. IZUMI, K. OKAMOTO, Y. KAWAKAMI, SG. FUJITA, Y. NARITA, T. INOUE, and T. MUKAI, *Jpn. J. Appl. Phys.*, in press.
- [29] Y. NARUKAWA, Ph.D. Thesis, Kyoto University, 2000.
- [30] Y. KAWAKAMI, Y. NARUKAWA, K. OMAE, S. NAKAMURA, and SG. FUJITA, *Appl. Phys. Lett.* **77**, 2151 (2000).

phys. stat. sol. (a) **183**, 51 (2001)

Subject classification: 73.21.Fg; 77.65.Ly; 77.84.Bw; 78.67.De; S7.14

Absorption Spectroscopy and Band Structure in Polarized GaN/Al_xGa_{1-x}N Quantum Wells

C. WETZEL¹) (a), M. KASUMI (b), H. AMANO (c), and I. AKASAKI (c)

(a) *High Tech Research Center, Meijo University, 1-501 Shiogamaguchi, Tempaku-ku, Nagoya 468-8502, Japan*

(b) *Department of Electrical and Electronic Engineering, Meijo University, 1-501 Shiogamaguchi, Tempaku-ku, Nagoya 468-8502, Japan*

(c) *High Tech Research Center and Department of Materials Science and Engineering, Meijo University, 1-501 Shiogamaguchi, Tempaku-ku, Nagoya 468-8502, Japan*

(Received October 8, 2000)

The absorption properties in hetero-polarization GaN/Al_xGa_{1-x}N ($x = 0.06$) quantum well structures are studied in reflection, photoreflexion, and photoluminescence excitation spectroscopy and compared with the results of band structure calculations. Above the energy of the main luminescence transitions we observe three distinct absorption thresholds. From Franz-Keldysh oscillations in the absorption spectra we directly derive the value of the acting electric field within the barriers. Upon this field strength we base a calculation of the electronic band structure and interband transition energies. The results suggest that the observed absorption edges are the AlGa_xN band edge and two quantized levels involving the crystal-field split-off hole.

1. Introduction Identification of the electronic band structure in wide band gap group-III nitrides is of a high current concern for the scientific and commercial exploitation of this new class of electronic materials in high brightness light emitting devices and high power, high frequency, and high temperature electronic devices [1–3]. Besides covering a wide range of the electronic band gap, due to the uniaxial nature of its wurtzite lattice the system exhibits strong electric polarization effects. Moreover, large lattice strain inducing piezoelectric charges is readily supported up to unusually large critical layer thicknesses [4]. Despite significant progress in initial device applications it will not be until a full parameterization and consistent description of the electronic band structure in thin films and quantum well (QW) structures becomes available that devices can be tuned to their optimum performance.

Guided by its major purpose as a light emitter GaN/AlGa_xN QW structures have most commonly been characterized by their luminescence properties in either steady-state experiments or time-resolved spectroscopy [5–7]. In comparison with absorption-type experiments such as photovoltage, Chichibu et al. [8, 9] have demonstrated for the closely related case of GaInN/GaN QWs that significant discrepancies can appear which in that case has led to models of strong spatial fluctuations of the lattice potential in the ternary alloy due to compositional fluctuations. In contrast, in the present case of GaN/AlGa_xN, a system with binary well and ternary barriers, such an effect is

¹) Present address: Uniroyal Optoelectronics, 3401 Cragmont Dr., Tampa, Florida 33619, USA; e-mail: Wetzel@ieee.org

thought of playing only a minor role due to the invariant composition of the binary well. GaN/AlGaN QWs therefore also provide a good test for the findings in GaInN/GaN QWs.

In an independent development Takeuchi et al. [10] reported a strong variation of the light emission peak wavelength on optical pumping power and externally applied bias voltage [11]. They interpreted this in terms of the quantum confined Stark effect and concluded the presence of very large electric fields induced by the piezoelectric properties of the system. In fact, Bernardini et al. [12] in first principles calculations predict huge piezoelectric and pyroelectric coefficients for the nitride compounds AlN, GaN, and InN that lead to maximum field strengths of some 15 MV/cm across AlN/GaN or InN/GaN heterointerfaces. The very power of absorption-type experiments such as photoreflection (PR) spectroscopy to derive accurate density of state (DOS) band gap values [13] and electric field values in the piezoelectric GaInN/GaN system then has been demonstrated by the present authors [14–16]. The case of GaN/AlGaN heterostructures has furthermore been studied by Liu Wei et al. [17] and Ochalski et al. [18] in PR. Here we apply this range of powerful tools to a set of highly optimized GaN/AlGaN QW layers. In order to derive a quantitative model of the observations we compare our results with band structure calculations in the envelope wave function approximation.

2. Experimental Samples have been prepared by metal organic vapor phase epitaxy (MOVPE) using trimethyl aluminum, trimethyl gallium, and ammonia. Based on (0001) sapphire, a low temperature deposited GaN buffer layer and a 2 μm GaN epilayer sets of 10.5 GaN/Al_xGa_{1-x}N QWs were grown [19]. An AlN fraction $x = 0.06$ as well as well width $L_w = 60$ Å (GaN) and barrier width $L_b = 120$ Å (AlGaN) were determined using high resolution X-ray diffraction and a dynamical model analysis. A second set of samples with nominally identical parameters was grown at slightly different temperatures of 1200 °C (C) and 1175 °C (D), respectively. Samples A and B are Si doped to $2 \times 10^{18} \text{ cm}^{-3}$ while samples C and D are nominally undoped.

Dc reflection and photomodulated reflection were performed of the *c*-plane of the samples in near-to-perpendicular geometry using a Xe white light source, 0.25 m spectrometer and CCD detection. Photomodulation was performed using a diffused beam of a 40 mW 325 nm HeCd laser. Photoluminescence was measured in the same configuration after blocking of the white light source. For photoluminescence excitation (PLE) the following sequence of Xe lamp, 0.25 m monochromator, sample, 1 m spectrometer, and CCD detection was chosen. Variable temperature in the range from 12 to 300 K was applied using a closed cycle cryostat.

3. Photoreflection and the Electric Field Strength Photoreflection as a highly sensitive method to derive the properties of the DOS has widely been employed in the literature for the study of compound semiconductors and their low-dimensional structures [20, 21]. The dominant mechanism is the modulation of internal electric fields by means of photogenerated charge carriers. In dependence of their sensitivity to applied electric fields the critical points in the joint DOS will produce a derivative-like signal feature that can be described in sums of third derivatives of Lorentzians. A second important form of signal that is typically observed in the limit of higher electric fields is the modulation of the reflection signal by Franz-Keldysh oscillations (FKOs) that in well-re-

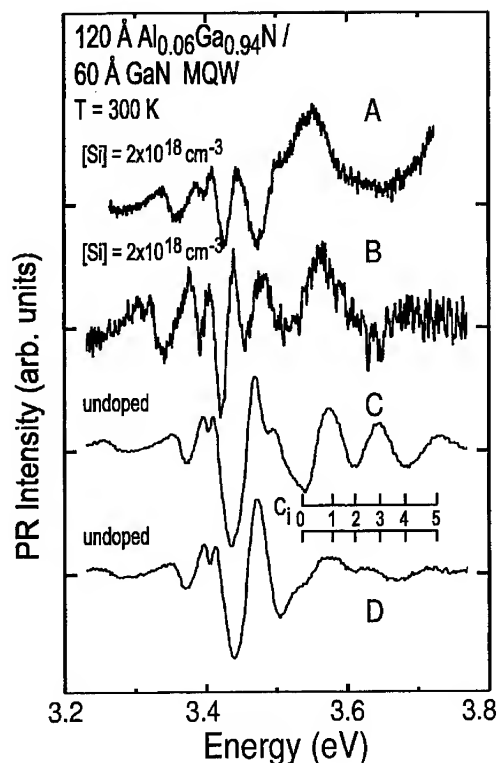


Fig. 1. Photoreflectance spectra of four GaN/Al_{0.06}Ga_{0.94}N QW samples with nominal identical structural parameters at room temperature. In sample C and D grown at slightly different temperatures the oscillation amplitude in the entire range of 3.5 to 3.7 eV ($C_0 \dots C_5$) is modulated supporting an assignment to Franz-Keldysh oscillations. These start at the band gap energy of the AlGa_{1-x}N barrier and reveal the strength of the electric field in the barriers. The derivative-like features between 3.4 and 3.5 eV are assigned to transitions between the excited states of the well

solved cases show several full oscillation periods near and above a single critical point. The distinction of both cases is not necessarily an easy task and it is an important advantage to study and compare a preferably large number of samples.

Figure 1 shows the PR spectra of four GaN/Al_xGa_{1-x}N QW samples with nominal identical structural parameters at room temperature. From the AlN frac-

tion of the AlGa_{1-x}N barriers we expect a band gap energy of 3.574 eV in bulk layers. We accordingly distinguish two spectral regions above and below this energy. In the lower half an abundance of narrow oscillations must be associated with the quantized states of the well. No such levels should be expected in the higher spectral range.

In general the fact that the well of the QW structure is the binary of GaN with a band gap of 3.42 eV (RT) in the volume material does not exclude the existence of quantized levels below this energy due to the presence of the large polarization in the heterostructure. This similarly implies that the bulk band gap value of the barrier is not the highest value achievable for a quantized state. Both effects result from the fact that transitions between states predominantly controlled by the potential at different locations along the electric field can significantly offset such limits. At the same time, though, the dipole matrix element is typically strongly reduced for transitions between such states leading only to a weak contribution in the absorption spectrum.

The case of recombination through luminescence is an essentially different situation. Here in principle localization of non-equilibrium carriers into transient potential minima can lead to reduced emission energies and in absence of alternate recombination routes will lead to a strong emphasis on the lowest localization stage even if the matrix element is only small. It is for this complication that we essentially limit our study to the absorption properties and the absorption branch of PLE to establish the basic parameters of the DOS.

Quantized states near the edge of the barrier appear in series of little separated energy levels. A sequence like the one observed in samples C and D above 3.5 eV

cannot be produced by transitions between such states. The slightly different growth temperature modulates the amplitude of several oscillations strongly supporting a nature in a single process rather than in a set of transitions. We therefore assign the oscillations in $C_0 \dots C_5$ to FKOs in the presence of a large electric field. Similar to our interpretation in GaInN thin films [15] and QW structures [16] we apply a model of Airy functions for their description and derive electric field values of $F = 130$ kV/cm. Also in this case we assume the value of the reduced effective mass at the value of the effective electron mass in GaN $m^* = 0.2m_0$ [22].

The value of the joint DOS mass is the only material dependent parameter in the interpretation of the electric field strength and it enters sublinearly with $m^{1/2}$. The accuracy of the electric field reading therefore is given by the sum of error margins of $\pm 10\%$ due to the limited accuracy of the mass values and $\pm 15\%$ due to the limited number of observed oscillation periods totaling to an error of $\pm 25\%$.

Electric fields of this high magnitude are the consequence of the discontinuity of the polarization properties across the interfaces of GaN and AlGaIn. While with help of the theoretical results the dominant contribution in this discontinuity is piezoelectricity for the case of GaInN on GaN the discontinuity of the equilibrium or spontaneous polarization should dominate for AlGaIn on GaN [12]. Across an interface with a variation in the AlN fraction of 6% net polarization charges of the order of $6 \times 10^{12} \text{ cm}^{-2}$ should be induced according to theory. This should result in electric field values of $F = 1$ MV/cm if screening by mobile charges is ignored. The significant discrepancy of both values reveals the necessity to assess the actual field conditions of the structure by such direct means to properly describe the electronic band structure. The fact of doping is furthermore expected to reduce the field in the present case. The fields in the doped samples A and B may therefore be even smaller than the one derived in samples C and D.

The appearance of the FKOs above the band gap energy of the AlGaIn barrier leads us to the assignment that this is the strength of the field acting in the barriers. The measured field strength is the result of free charge rearrangement in the entire structure to equilibrate a Fermi level. The principle of actio and reactio results in a field in the well of opposite polarity. Its strength can be approximated by

$$F_b L_b = -F_w L_w . \quad (1)$$

For the present structure and a barrier field of $F_b = 130$ kV/cm we find a field in the well of $F_w = -260$ kV/cm. These field values are an essential input parameter in the theoretical description of the electronic band structure in such QW layers.

4. Photoreflexion Signal of the Quantized States The PR signal in the lower part of the spectrum is best analyzed as a function of temperature (Fig. 2). The positive signal of the AlGaIn barrier layer can be well traced to the lowest temperature of 13 K. The shift to higher energies closely corresponds to the established temperature dependence of the GaN band gap. In parallel, a pronounced edge near 3.5 eV (RT) evolves into a second maximum at low temperature. A sharp double oscillation at 3.45 eV (RT) revealing the energy derivative of a narrow peak transforms into a singular narrow maximum at low temperature. A fourth signal in form of a sharp minimum can be traced at the lower side at 3.39 eV (RT). Additional oscillations appear at lower energy that cannot be traced at low temperature due to the strong increase of the PL intensity.

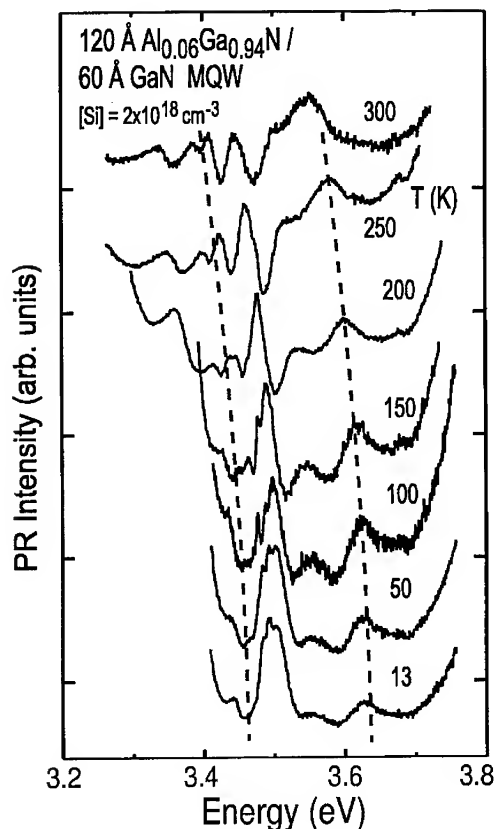


Fig. 2. Photoreflection in sample A as a function of temperature. Towards lower temperature edges and oscillations as seen at RT evolve into individual interband transitions. Lines should guide the eye. A shift towards higher energies follows the shift of the GaN band gap. For lower temperature a strong luminescence background below 3.4 eV complicates the interpretation of the PR spectra

The luminescence on an arbitrary but fixed intensity scale is shown in Fig. 3. The spectra are dominated by strong luminescence at 3.275 eV the intensity of which grows by 2.4 decades when cooling from RT to 100 K. It is worthwhile, however, to analyze the higher energy region on a fine and individually adjusted scale (Fig. 4). A narrow PL maximum at 3.45 eV follows the temperature dependence of the GaN band gap and a weaker signal appears at the lower energy side. The stronger PR features closely correspond to both PL maxima of which they appear to represent a derivative at RT. At low temperature, however, the PR in 3.5 eV cannot be distinguished from the associated PL and a possible cross-talk of both signals cannot be excluded. A possible origin in the GaN epilayer is very unlikely due to the large optical thickness of the multiple QW region. Raman lines and spectrometer ghosts appear at

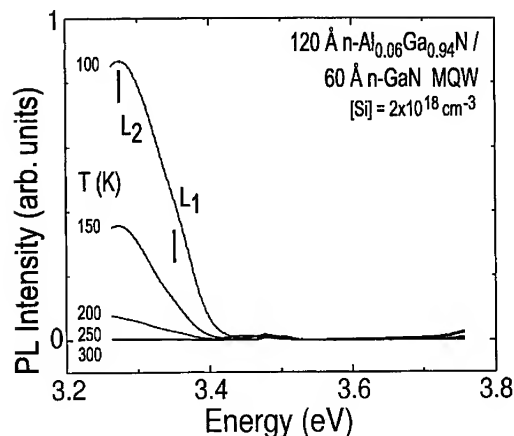


Fig. 3. Photoluminescence on the high energy side of the main luminescence maximum at variable temperature on a common scale. At room temperature a maximum at 3.5 eV dominates that can be traced to lowest temperatures. The strong emission near 3.275 eV only appears at low temperature

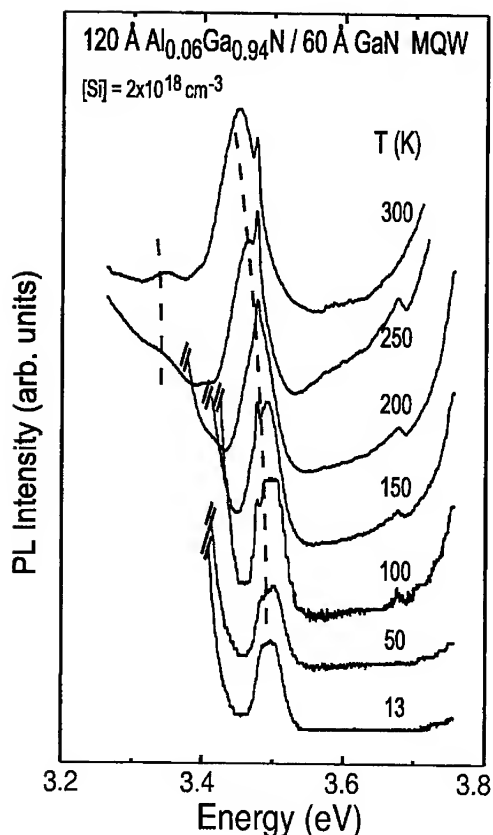


Fig. 4. Temperature dependence of the photoluminescence on an individually adjusted scale to emphasize the high energy part. A pronounced maximum assigned to the QW can be traced to lowest temperatures. It follows the temperature shift of the GaN band gap. A further maximum can be identified at lower energies. Both are highlighted by lines to guide the eye. Two narrow irrelevant peaks show no temperature shift

3.476 and 3.677 eV. The identified lines have furthermore clear parallels in the dc reflection signal where two local maxima appear at 3.47 and 3.55 eV (RT). For lower temperature an increasingly clearer signal correlates with the narrow minimum in PR.

For completeness PL at low temperature is shown in Fig. 5. A series of three strong emission lines (L_2 , L_3 , L_4) and a high energy shoulder (L_1) can be identified. In the present state of experimental investigations no distinctive absorption signal could be identified at the respective energy levels. More details, however,

are revealed on the excitation path of the luminescence for the different emission maxima (Fig. 6). Overall three clear steps can be identified in this absorption measurement weighed by the different recombination paths. The threshold energies at the steps clo-

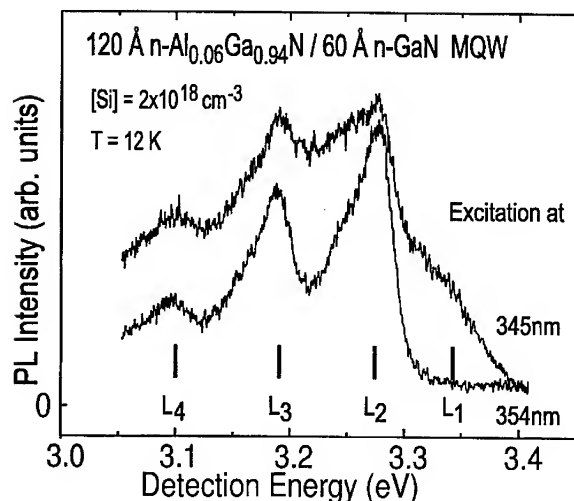


Fig. 5. Low temperature luminescence including the low energy side of the maximum. Three individual contributions are identified that strongly resemble replica of the higher one. Luminescence excitation spectra were obtained on those lines associated to the quantum well

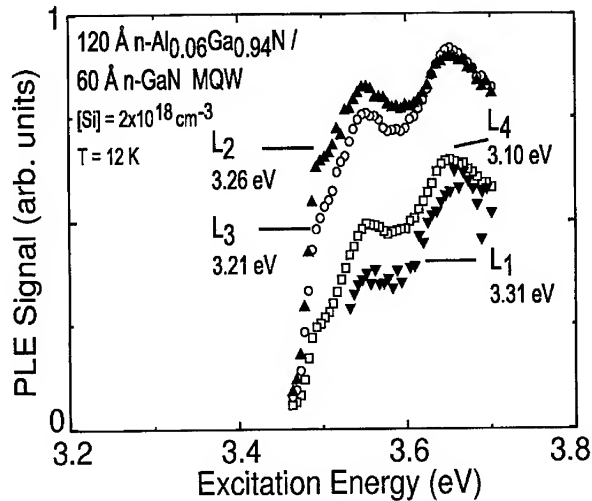


Fig. 6. Photoluminescence excitation spectra for the three major emission channels and the high energy shoulder. Three distinct absorption edges are identified for all lines. The relative intensities of these absorption spectra show slight variations supporting that there is a common carrier relaxation process in all emission channels

sely match with the levels identified in PR and reflection. In this case there is only a slight variation of the relative intensities at the three steps revealing a common feeding channel into the four luminescence lines. This observation suggests that the lower lying luminescence maxima are replica of the higher ones by means of higher order interactions such as phonon replica.

5. Model of the Electronic Band Structure On the basis of the structural parameters as derived from the X-ray analysis and the strength of the electric field as derived from the FKO's we model the electronic band structure of the QW system. We solve the Schrödinger equation for electrons (e), heavy (hh), light (lh) and crystal-field (ch) split-off holes within a single QW structure subjected to the measured electric field

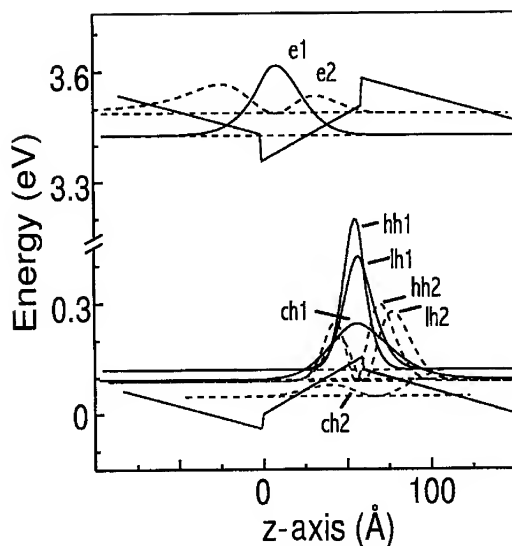


Fig. 7. Quantized states of the hetero-polarization GaN/AlGaIn QW structure and respective quantized levels of electrons, heavy-holes, light-holes, and crystal-field split-off hole states. This calculation is based on the electric field value derived from the Franz-Keldysh oscillations above the barrier band gap. The relative charge distributions are superimposed on the levels, respectively. Heavy-hole and light-hole states are subjected to large shifts along the electric field due to their high effective mass along *z*. This is not the case for electron and crystal-field split-off hole

strengths. For the well we assume a field $F_w = F_b L_b / L_w = 2F_b$ according to Eq. (1). For the band gap energy in AlGa_xN we use a bowing parameter of $b = 1$ eV for pseudomorphically strained layers on GaN. The band dispersion is assumed fixed at the theory values of GaN [23]. Biaxial strain is considered on the basis of linear interpolation of the elastic constants of the binaries [24]. Linear interpolations are also used for theoretical deformation potentials [25]. The relative bandoffset dE_c/dE_g is assumed at 80.3% [25]. Figure 7 summarizes the results superimposed on the lattice potential of the multiple QW structure. We also include higher excited states of the quantized levels.

Even though the experimentally derived electric field strength is significantly below the theoretical maximum it is apparent that the lattice potential and consequently the spectrum of the electronic levels is to a very large extent controlled by the polarization effect. A variation of the well width in contrast is of minor influence. Moreover, it is apparent how a variation of the barrier width controls the energy of the quantized levels. The transition energies derived in dc reflection, PR, PL, and PLE are collected in Fig. 8 as a function of the sample temperature. Most features closely follow the well-known temperature dependence of the band gap energy in GaN. For the lowest temperature and RT the results of the calculation are included for comparison.

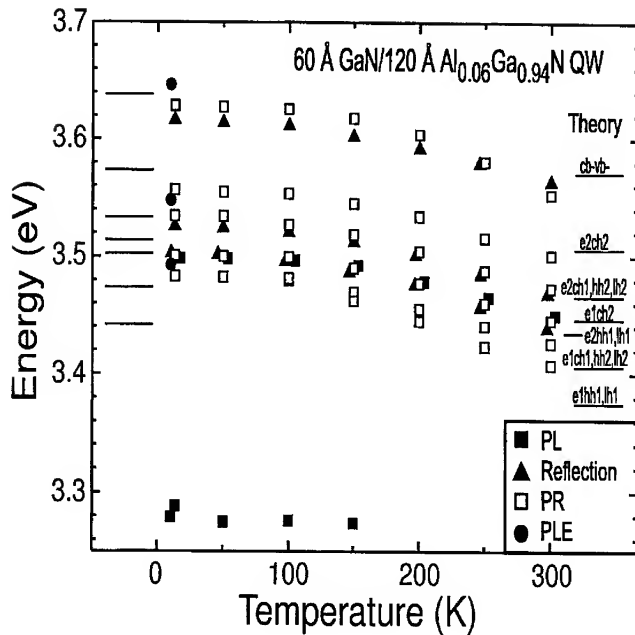


Fig. 8. Collected interband transition energies of extrema in the absorption and luminescence spectra as a function of temperature. The results of the band structure calculation are added on the high and low temperature sides. The highest transitions are so identified as the band gap in the Al_xGa_{1-x}N barrier. The observed set of interband transitions falls well into the range of the e1ch1 and e1ch2. Both transitions are expected to show the least reduction of transition probability by means of the quantum confined Stark effect

6. Discussion We so assign the highest experimental feature to the interband transition within the AlGaN barrier in good agreement with the analysis of the FKO's in samples C and D. The narrow set of PR oscillations around 3.5 eV falls in the range where transitions involving the crystal-field split-off hole state is expected. Due to their rather high effective mass values along *z* heavy-hole and light-hole experience a strong quantum confined Stark effect and an associated reduction in the wave function overlap and transition matrix element. This can be seen from the square of the wave functions in Fig. 7. In turn this mechanism should lead to strong emphasis of the crystal-field split-off hole transitions due to a mass along *z* that is as light as that of the electron. From this picture the lowest transition doublet of e1hh1, lh1 should be expected near 3.38 eV at RT and 3.44 eV (12 K). In this range we do observe pronounced maxima in PR that cannot clearly be distinguished from interference fringes superimposed on a strong luminescence background. Moreover, the very maxima of luminescence appear at energies as low as 3.1–3.3 eV.

This case study shows that a significant discrepancy exists between the levels of light emission and a band structure model based on the parameters derived in absorption-type photoreflection data. A very similar case had been established in GaInN/GaN QWs by direct comparison of luminescence with absorption-type experiments [9] and by comparison of PR data with band structure calculations similar to the present study [26].

The strength of the present approach lies in the fact that a number of interband transitions are observed and modeled. By means of the correlation of PR, reflection, PL and PLE data we obtain a broader bandwidth of information effectively eliminating several fitting parameters such as the barrier band gap energy and the value of the acting electric field. These are the essential advantages over experiments that are essentially limited to the study of the luminescent state itself. The combination of both approaches then provides accurate numbers for the discrepancy that has to be accounted for in future work.

7. Conclusion In summary, we determined the optical absorption properties in GaN/AlGaN QWs by a comparison of photoreflection, dc reflection, and photoluminescence excitation in relation to photoluminescence. We directly derive the energy of the AlGaN alloy barrier and the strength of the acting large electric field. This value is significantly below the theoretical maximum indicating an effective screening of polarization charges. We observe a set of excited states which appear above the main luminescence lines. By means of a band structure calculation based on the established parameters of GaN and linear interpolations of elastic properties and deformation potentials we assign those to transitions involving the crystal-field split-off holes states. Our findings provide a quantitative basis for the further analysis of such structures.

Acknowledgements This work was supported in part by the Japan Society for the Promotion of Science "Research for the Future Program in the Area of Atomic Scale Surface and Interface Dynamics" under the project of "Dynamic Process and Control of the Buffer Layer at the Interface in a Highly-Mismatched System (JSPS96P00204)" and the Ministry of Education, Science, Sports and Culture of Japan (contract numbers 11450131, 12450017 and 12875006). C. W. thanks the A. C. Bindereif foundation for a time grant.

References

- [1] I. AKASAKI, in: Nitride Semiconductors, Mater. Res. Soc. Symp. Proc. **482**, 3 (1998).
- [2] I. AKASAKI and H. AMANO, in: High Brightness Light Emitting Diodes, Eds. G. B. STRINGFELLOW and M. G. CRAFT, Semiconductors and Semimetals, Vol. 48, Academic Press, London 1997 (p. 357).
- [3] I. AKASAKI and C. WETZEL, Proc. IEEE **85**, 1750 (1997).
- [4] H. AMANO, T. TAKEUCHI, S. SOTA, H. SAKAI, and I. AKASAKI, in: III-V Nitrides, Eds. F. PONCE, T. D. MOUSTAKAS, I. AKASAKI, and B. MONEMAR, Mater. Res. Soc. Symp. Proc. **449**, 1143 (1997).
- [5] JIN SEO IM, H. KOLLMEYER, J. OFF, A. SOHMER, F. SCHOLZ, and A. HANGLEITER, Phys. Rev. B **57**, R9435 (1998).
- [6] M. SMITH, J. Y. LIN, H. X. JIANG, A. SALVADOR, A. BOTCHKAREV, W. KIM, and H. MORKOÇ, Appl. Phys. Lett. **69**, 2453 (1996).
- [7] H. S. KIM, J. Y. LIN, H. X. JIANG, W. W. CHOW, A. BOTCHKAREV, and H. MORKOÇ, Appl. Phys. Lett. **73**, 3426 (1998).
- [8] S. CHICHIBU, T. AZUHATA, T. SOTA, and S. NAKAMURA, Appl. Phys. Lett. **70**, 2822 (1997).
- [9] S. CHICHIBU, T. AZUHATA, T. SOTA, and S. NAKAMURA, Appl. Phys. Lett. **69**, 4188 (1996).
- [10] T. TAKEUCHI, S. SOTA, M. KATSURAGAWA, M. KOMORI, H. TAKEUCHI, H. AMANO, and I. AKASAKI, Jpn. J. Appl. Phys. **36**, L382 (1997).
- [11] T. TAKEUCHI, C. WETZEL, S. YAMAGUCHI, H. SAKAI, H. AMANO, I. AKASAKI, Y. KANEKO, S. NAKAGAWA, Y. YAMAOKA, and N. YAMADA, Appl. Phys. Lett. **73**, 1691 (1998).
- [12] F. BERNARDINI, V. FIORENTINI, and D. VANDERBILT, Phys. Rev. B **56**, R10024 (1997).
- [13] C. WETZEL, T. TAKEUCHI, S. YAMAGUCHI, H. KATOH, H. AMANO, and I. AKASAKI, Appl. Phys. Lett. **73**, 1994 (1998).
- [14] C. WETZEL, H. AMANO, I. AKASAKI, T. SUSKI, J. W. AGER, E. R. WEBER, E. E. HALLER, and B. K. MEYER, in: Nitride Semiconductors, Mater. Res. Soc. Symp. Proc. **482**, 489 (1998).
- [15] C. WETZEL, T. TAKEUCHI, H. AMANO, and I. AKASAKI, J. Appl. Phys. **85**, 3786 (1999).
- [16] C. WETZEL, T. TAKEUCHI, H. AMANO, and I. AKASAKI, Phys. Rev. B **61**, 2159 (2000).
- [17] LIU WEI, K. L. TEO, M. F. LI, S. J. CHUA, K. UCHIDA, H. TOKUNAGA, N. AKUTSU, and K. MATSUMOTO, J. Cryst. Growth **189/190**, 648 (1998).
- [18] T. J. OCHALSKI, B. GIL, P. LEFEBVRE, N. GRANDJEAN, J. MASSIES, and M. LEROUX, Solid State Commun. **109**, 567 (1999).
- [19] H. AMANO, M. IWAYA, N. HAYASHI, T. KASHIMA, S. NITTA, C. WETZEL, and I. AKASAKI, phys. stat. sol. (b) **216**, 683 (1999).
- [20] M. CARDONA, K. L. SHAKLEE, and F. H. POLLAK, Phys. Rev. **154**, 696 (1967).
- [21] F. H. POLLAK and H. SHEN, Mater. Sci. Engng. R **10**, 275 (1993), and references therein.
- [22] M. DRECHSLER, D. M. HOFMANN, B. K. MEYER, T. DETCHPROHM, H. AMANO, and I. AKASAKI, Jpn. J. Appl. Phys. **34**, 1178 (1995).
- [23] K. KIM, W. R. L. LAMBRECHT, B. SEGALL, and M. VAN SCHILFGAARDE, Phys. Rev. B **56**, 7363 (1997).
- [24] A. F. WRIGHT, J. Appl. Phys. **82**, 2833 (1997).
- [25] C. G. VAN DE WALLE and J. NEUGEBAUER, Appl. Phys. Lett. **70**, 2577 (1997).
- [26] C. WETZEL, T. TAKEUCHI, H. AMANO, and I. AKASAKI, Phys. Rev. B (2000), in print.

phys. stat. sol. (a) **183**, 61 (2001)

Subject classification: 73.21.Fg; 77.65.Ly; 77.84.Bw; 78.47.+p; 78.67.De; S7.14

Reduction of Carrier In-Plane Mobility in Group-III Nitride Based Quantum Wells: The Role of Internal Electric Fields

M. GALLART (a), P. LEFEBVRE¹⁾ (a), A. MOREL (a), T. TALIERCIO (a), B. GIL (a),
J. ALLÈGRE (a), H. MATHIEU (a), B. DAMILANO (b), N. GRANDJEAN (b),
and J. MASSIES (b)

(a) *Groupe d'Etude des Semiconducteurs, CNRS, Université Montpellier II,
Case courrier 074, F-34095 Montpellier Cedex 5, France*

(b) *Centre de Recherche sur l'Hétéro-Epitaxie et ses Applications, CNRS,
rue Bernard Grégory, Sophia Antipolis, F-06560 Valbonne, France*

(Received October 8, 2000)

Localized and free excitons in GaN/Al_{0.17}Ga_{0.83}N quantum wells are studied by time-resolved photoluminescence (PL) versus temperature. We focus more particularly on 16-monolayer wide quantum wells for which, at $T = 8$ K, we observe double excitonic features. We assign the latter to two different localization states of excitons, from the temperature dependence of PL energies and of recombination dynamics. We discuss the reasons why double PL lines are observed in terms of the limitation of carrier in-plane mobility by interface roughness. We emphasize, in particular, the strong effect of the longitudinal electric field on the in-plane motion of carriers.

The internal efficiency of light emission in semiconductor-based devices is simply a matter of competition between radiative and nonradiative recombination lifetimes. To this extent, group-III nitrides are, a priori, very bad candidates. Indeed, they are most commonly grown on lattice-mismatched substrates which induce large densities of nonradiative defects. Therefore the overall recombination lifetimes of excitons in GaN micro-metric epilayers seldom exceed a few tens of picoseconds, see [1], being essentially dominated by nonradiative processes. Nevertheless, low-dimensional structures made of InGaN and Ga(Al)N are well known to provide efficient light-emitting diodes and laser diodes, operating at room temperature, if properly grown and processed [2, 3]. It has been understood recently [4–10] that such an efficiency was merely due to carrier localization on deep (over 0.1 eV) potential fluctuations in InGaN, which is a disordered ternary alloy. This localization allows the carriers to avoid getting trapped into nonradiative centers. In other words, potential fluctuations increase drastically the nonradiative recombination time τ_{NR} so that the latter is not too small compared to the radiative lifetime τ_R , even at room temperature. Now, τ_R also depends drastically on the huge electric fields along the growth axis of these quantum wells (QWs) made of wurtzite materials [11–18]. These fields of several hundred kV/cm result in a strong quantum-confined Stark effect, which allows e.g. an InGaN QW to emit light over the entire

¹⁾ Corresponding author; Tel.: +33 (0)4 67 14 37 56; Fax: +33 (0)4 67 14 37 60;
e-mail: lefebvre@ges.univ-montp2.fr

visible spectrum, simply by varying the well width between 2 nm (UV) and 6 nm (red) [19]. The drawback of the Stark shift, however, is that it is accompanied by a strong on-axis separation of electrons and holes, yielding a nearly exponential increase of τ_R versus the well width [15, 17]. Thus, at first sight, these electric fields seem to be a severe obstacle to large radiative efficiencies, especially for QWs wide enough to produce light in low-energy regions of the visible spectrum.

In this paper, we wish to point out one beneficial effect of electric fields in group-III nitride QWs, i.e. the possibility to increase τ_{NR} by enhancement of interface-roughness effects. For this purpose, we present results of time-resolved photoluminescence (TRPL) obtained from 16-monolayer wide GaN/Al_{0.17}Ga_{0.83}N QWs, grown by molecular beam epitaxy (MBE) on sapphire substrates. We comment the observation of two distinct states of localization for excitons and we discuss the exchange of carriers between these states and the free exciton states, when the temperature is changed. In the discussion, we come to a comparison between GaAs- and GaN-based QWs where we emphasize the limitation of *in-plane* mobility by *on-axis* electric field.

TRPL experiments were performed on a conventional set-up, using a streak camera and the frequency-tripled 2 ps laser pulses from a titanium-sapphire cavity ($\lambda = 260$ nm) as excitation source. The sample temperature was controlled within a closed-cycle helium refrigerator. The overall time resolution of the set-up is of ~ 5 ps. We have studied four GaN/Al_{0.17}Ga_{0.83}N QWs grown by MBE on *c*-plane sapphire substrates. These QWs have all the same thickness of 16 atomic monolayers (MLs) – 1 ML = 0.26 nm – but they belong to different samples having different structures in terms of barrier thicknesses and of other QWs present in the sample. For instance, the samples contain either a single QW (SQW) or a multiple QW (MQW). The names and characteristics of the samples are summarized in Table 1. Experiments with variable temperature were difficult to perform because of the strong loss of PL signal above a few tens of Kelvin. This is characteristic of an efficient thermal excitation of carriers towards nonradiative defects. This is why we only show low-temperature results for two samples: sample 3 has very thin barriers (5 nm) which we have proven in a previous work [20] to enhance the nonradiative escape of carriers towards the GaN buffer layer. The 16 ML-wide QW in sample 4 is buried underneath three other QWs and four thick barriers, thus ~ 200 nm of material, which means that its excitation by the laser is very small, since nitrides have absorption coefficients of the order of 10^5 cm⁻¹.

The weakening of the signal-to-noise ratio, with increasing T , also forced us to use a poorer spectral resolution for experiments above 8 K. Nevertheless, at $T = 8$ K, we obtained the time-integrated PL spectra shown in Fig. 1 with a high resolution which reveals, *in all cases*, that the PL has two components. From previous works on this type of samples [16, 17, 20] it is easy to conclude that these two PL energies, E_1 and E_2 , correspond to recombinations of excitons in zones of the QW which exceed the average thickness (16 ML) by one (E_1) or two (E_2) monolayers. This is also illustrated by the comparison between experimental and calculated transition energies, gathered in Table 1. In fact, the absolute values E_1 and E_2 and the energy differences $E_1 - E_2$ are all very well fitted if we slightly change the value of the electric field F_W inside the QW. The variations of F_W that we found (see Table 1) are remarkably consistent with theoretical predictions [12, 16, 17] on the influence of the relative well and barrier thicknesses (L_W and L_B , respectively) on the electric field: F_W is roughly proportional to $L_B/(L_B + L_W)$ for MQWs. This explains quite well the change of transition energies between the dif-

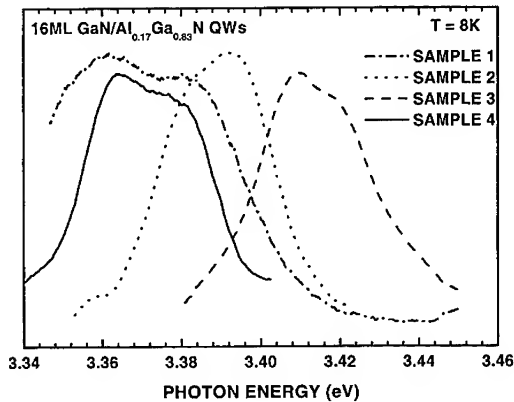


Fig. 1. Time-integrated PL spectra of the four GaN/Al_{0.17}Ga_{0.83}N QWs, taken at $T = 8$ K with a high-resolution spectrometer (grating with 1200 grooves/mm)

ferent samples. As for the PL decay times, we observe the expected trend, i.e. the larger the field, the slower the decay.

As a matter of fact, these decays are always bi-exponential, with one small decay time τ_1 of the order of 0.6 ns for all samples and the slower decay on time scales of 2.5 to 4.7 ns. A careful examination of TRPL data allows us to understand that the shorter decay time corresponds to the high-energy contribution (E_1). We thus interpret this short time as resulting from decay of excitons localized on areas where the QW is wider by 1 ML than the average width (hereafter called “+1 ML” zones) *via two processes*. First, the radiative recombination should take place on time scales of ~ 1 or a few nanoseconds, typically, i.e. only slightly faster than the radiative recombination, τ_2 , of excitons localized on “+2 ML” zones, due to the above-mentioned well width effect on τ_R . Indeed, our calculation does not give more than a factor of two between excitonic oscillator strengths of QWs with thicknesses of 17 and 18 MLs. In fact, we believe that τ_1 is made shorter by the transfer of excitons (or individual carriers) towards the “+2 ML” zones. This interpretation is confirmed by the results shown in Fig. 2, i.e. the experimental redshift of the PL peak energy from E_1 to E_2 when the delay after excitation increases. We have checked that this was not an effect of screening of F_W by photocarriers, since this result was insensitive to excitation power. Figure 2 also shows that, when T is increased, the redshift becomes faster: this proves the thermally enhanced transfer from the “+1 ML” localization sites to the “+2 ML” ones. Another evidence of this transfer is given by the “S-shaped” change of the peak PL energy E_{PL} versus T , measured by low-resolution experiments and shown in Fig. 3. Between 8 and 40 K, E_{PL} first decreases against T because of the enhanced transfer from E_1 to E_2 . But

Table 1
Characteristics of the different samples

sample	well widths (ML)	barrier width (nm)	E_1 (eV)		E_2 (eV)		τ_1 (ns)	τ_2 (ns)	electric field (kV/cm)
			exp.	calc.	exp.	calc.			
1	16	30	3.382	3.384	3.364	3.364	0.60	3.3	868
2	4 × 16	30	3.395	3.398	3.379	3.379	0.62	3.3	814
3	4 × 16	5	3.422	3.426	3.407	3.408	0.58	2.5	705
4	4, 8, 12 and 16	50	3.381	3.384	3.363	3.363	0.68	4.7	870

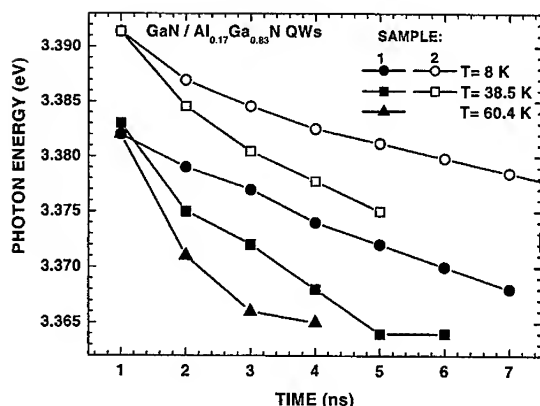
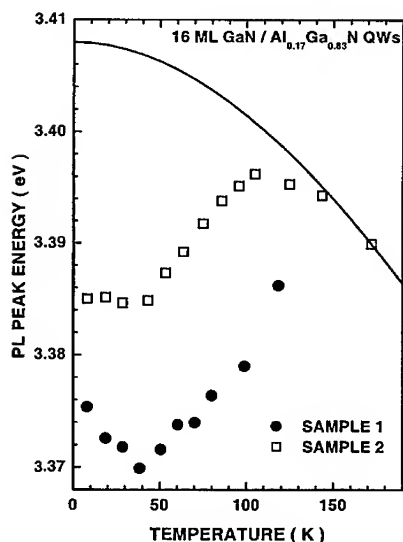


Fig. 2. Variation of the PL peak energy of samples 1 and 2 versus time, measured with a low-resolution set-up (150 grooves/mm), at three different temperatures

this mechanism competes with two other phenomena, which become dominant above 50 K. First, increasing T above 50 K makes the PL change progressively from a regime dominated by localized excitons to a regime dominated by free excitons, which is completely reached above 130–140 K for our samples. Indeed, above this temperature, E_{PL} follows a variation parallel to that of the GaN band gap, shown by the curve in Fig. 3, which was obtained by using Varshni's empirical formula: $E = E_0 - \alpha T^2/(T + \beta)$, where $E_0 = 3.408$ eV, $\alpha = 6.4 \times 10^{-4}$ eV/K and $\beta = 877.2$ K. The second mechanism becoming significant above 50 K is the nonradiative carrier loss, which drastically reduces the PL signal. Basically, this mechanism is a consequence of the previous one: it is really the de-localization of excitons which allows them to migrate towards nonradiative centers.

In fact, the present samples with only two levels of localization are a simplified version of what takes place in InGaN QWs [7], i.e. a quasi-continuous variety of energy levels for all configurations of potential fluctuations, separated by potential barriers which can be overcome by sufficient thermal excitation, yielding a similar "S-shaped" behavior. Now, we may wonder why we observe the two localization states on the same PL spectra.



PL spectra. In other words, why is the transfer time between "+1 ML" and "+2 ML" zones so slow? For GaAs/GaAlAs QWs, for instance, we would observe only the lowest-energy state in a PL experiment, whereas a reflectance spectrum could show several excitonic resonances, see e.g. [21]. In fact, one important difference between GaAs and GaN QWs, and thus the answer to the above questions is the presence of the strong electric field F_w .

Fig. 3. Variation of the time-integrated PL peak energy of samples 1 and 2 versus temperature, measured with a low-resolution set-up (150 grooves/mm)

For GaN/AlGa_N QWs, the envelope functions of the electron and hole are pushed apart towards the interfaces where they are strongly blocked due to high potential barriers with reverse electric fields and due to large effective masses (Fig. 4a). On the other hand, these envelope functions for GaAs/AlGaAs QWs are basically symmetrical and the presence probabilities at the interfaces are always weak (Fig. 4b): for wide wells, the wave functions are vanishingly small there and for narrow wells, they penetrate far into the barriers (small effective masses and no field). We have calculated the total probabilities P_e and P_h for finding the electron and the hole, in their ground states, within the two "critical" monolayers near both interfaces (i.e. a total of four monolayers). For GaN/Al_{0.3}Ga_{0.7}N QW and GaAs/Al_{0.3}Ga_{0.7}As QWs, having one excitonic Bohr radius in width, we obtain $P_e(\text{GaN}) = 0.16$, $P_h(\text{GaN}) = 0.41$ and $P_e(\text{GaAs}) = 0.019$, $P_h(\text{GaAs}) = 0.009$, respectively. These results, illustrated by Fig. 4, show that the particles (especially the holes) are much more influenced by local variations of well width in the nitride system than in the arsenide one. As a consequence, it is clear that the in-plane motion of excitons in GaAs QWs is almost de-coupled from the electron and hole on-axis motion. Then, the "quasi-zero-dimensional" localization of these excitons in GaAs QWs can be seen as a small perturbation. *This is not the case for GaN QWs*: the in-plane motion of excitons is strongly hindered because the electric field pushes the carriers against the interfaces, acting like a "brake". This induces a kind of "kinetic barrier" between the different localization states which cannot be accounted for by a model of thermal occupation, with a Boltzmann distribution, for instance. We wish also to remark that the in-plane sizes characteristic of the electron-hole relative motion (within the exciton) are so small in nitride QWs that the motion of the center-of-mass is sensitive to the random distribution of aluminum atoms in the barriers, *even for ideally smooth interfaces (with no steps)* [22].

In summary, we have shown that the overall effects of the on-axis electric field in GaN QWs are not only 1. to increase the radiative lifetime, but also 2. to increase the transfer time between "+1 ML" and "+2 ML" localization areas and 3. to increase the transfer time towards nonradiative centers, i.e. the nonradiative lifetime. Unfortunately, the localization is not strong enough in these GaN QWs to allow for a satisfactory preservation of radiative efficiency at room temperature, at least with the current densities of threading dislocations in layers grown on sapphire. Thus, for GaN QWs, there are two ways of having a good radiative efficiency at room temperature: either one can

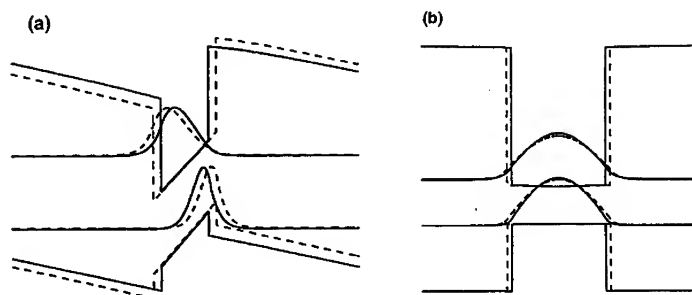


Fig. 4. Solid lines show the plot of the band profiles of quantized electron and hole levels and of the corresponding envelope functions calculated for a) a 3 nm wide GaN/Al_{0.3}Ga_{0.7}N QW and b) an 11 nm wide GaAs/Al_{0.3}Ga_{0.7}As QW. The dashed lines show the same for QWs wider by a total of four atomic monolayers

drastically reduce the density of dislocations and/or one can decrease even more the in-plane carrier mobility by enhancing roughness effects. An excellent way to do this is to grow quantum boxes instead of quantum wells.

Acknowledgements This work is supported by the EEC under contract No. HPRN-CT-1999-000132. We also acknowledge support of the French Ministry of Education, Research and Technology within the "BOQUANI" and "NANILUB" Research Programs.

References

- [1] P. LEFEBVRE, J. ALLÈGRE, and H. MATHIEU, *Mater. Sci. Engng. B* **59**, 307 (1999), and references cited therein.
- [2] B. GIL (Ed.), *Group III Nitride Semiconductor Compounds*, Clarendon Press, Oxford 1998.
- [3] S. NAKAMURA and G. FASOL, *The Blue Laser Diode*, Springer-Verlag, Berlin 1997.
- [4] S. CHICHIBU, T. AZUHATA, T. SOTA, and S. NAKAMURA, *Appl. Phys. Lett.* **69**, 4188 (1996).
- [5] Y. NARUKAWA, Y. KAWAKAMI, M. FUNATO, S. FUJITA, S. FUJITA, and S. NAKAMURA, *Appl. Phys. Lett.* **70**, 981 (1997).
- [6] J. ALLÈGRE, P. LEFEBVRE, S. JUILLAGUET, W. KNAP, J. CAMASSEL, Q. CHEN, and A. KHAN, *MRS Internet J. Nitride Semicond. Res.* **2**, 34 (1997).
- [7] Y.-H. CHO, G. H. GAINER, A. J. FISHER, J. J. SONG, S. KELLER, U. K. MISHRA, and S. P. DENBAARS, *Appl. Phys. Lett.* **73**, 1370 (1998).
- [8] Y. NARUKAWA, Y. KAWAKAMI, S. FUJITA, and S. NAKAMURA, *Phys. Rev. B* **59**, 10283 (1999).
- [9] K. P. O'DONNELL, R. W. MARTIN, and P. G. MIDDLETON, *Phys. Rev. Lett.* **82**, 237 (1999).
- [10] A. MOREL, M. GALLART, T. TALIERCIO, P. LEFEBVRE, B. GIL, J. ALLÈGRE, H. MATHIEU, B. DAMILANO, N. GRANDJEAN, and J. MASSIES, *phys. stat. sol. (a)* **180**, 375 (2000).
- [11] A. D. BYKHOVSKI, V. V. KAMINSKI, M. S. SHUR, Q. C. CHEN, and M. A. KHAN, *Appl. Phys. Lett.* **68**, 818 (1996).
- [12] F. BERNARDINI, V. FIORENTINI, and D. VANDERBILT, *Phys. Rev. B* **56**, R10026 (1997).
- [13] T. TAKEUCHI, S. SOTA, M. KATSURAGAWA, M. KOMORI, H. TAKEUCHI, H. AMANO, and I. AKASAKI, *Jpn. J. Appl. Phys.* **36**, L382 (1997).
- [14] C. WETZEL, T. TAKEUCHI, H. AMANO, and I. AKASAKI, *Phys. Rev. B* **61**, 2159 (2000).
- [15] J.-S. IM, H. KOLLMER, J. OFF, A. SOHMER, F. SCHOLZ, and A. HANGLEITER, *Phys. Rev. B* **57**, R9435 (1998).
- [16] M. LEROUX, N. GRANDJEAN, M. LAÛGT, J. MASSIES, B. GIL, P. LEFEBVRE, and P. BIGENWALD, *Phys. Rev. B* **58**, R13371 (1998).
- [17] P. LEFEBVRE, J. ALLÈGRE, B. GIL, H. MATHIEU, P. BIGENWALD, N. GRANDJEAN, M. LEROUX, and J. MASSIES, *Phys. Rev. B* **59**, 15363 (1999).
- [18] J. P. IBBETSON, P. T. FINI, K. D. NESS, S. P. DENBAARS, J. S. SPECK, and U. K. MISHRA, *Appl. Phys. Lett.* **77**, 250 (2000).
- [19] B. DAMILANO, N. GRANDJEAN, J. MASSIES, L. SIOZADE, and J. LEYMARIE, *Appl. Phys. Lett.* **77**, 1268 (2000).
- [20] P. LEFEBVRE, M. GALLART, T. TALIERCIO, B. GIL, J. ALLÈGRE, H. MATHIEU, N. GRANDJEAN, M. LEROUX, J. MASSIES, and P. BIGENWALD, *phys. stat. sol. (b)* **216**, 361 (1999).
- [21] H. MATHIEU, P. LEFEBVRE, J. ALLÈGRE, B. GIL, and A. REGRENY, *Phys. Rev. B* **36**, 6581 (1987), and references quoted therein.
- [22] M. GALLART, A. MOREL, T. TALIERCIO, P. LEFEBVRE, B. GIL, J. ALLÈGRE, H. MATHIEU, N. GRANDJEAN, M. LEROUX, and J. MASSIES, *phys. stat. sol. (a)* **180**, 127 (2000).

phys. stat. sol. (a) **183**, 67 (2001)

Subject classification: 68.55.Ac; 78.55.Cr; 78.66.Fd; S7.14

Optical Properties of Cubic Gallium Nitride on SiC/Si Pseudo-Substrates

C. BRU-CHEVALLIER¹⁾ (a), S. FANGET (a), A. PHILIPPE (a), C. DUBOIS (a),
E. MARTINEZ-GUERRERO (b), B. DAUDIN (b), P. ABOUGHÉ NZÉ (c), and Y. MONTEIL (c)

(a) *Laboratoire de Physique de la Matière (UMR, CNRS 5511), INSA,
20, Av. Albert Einstein, F-69621 Villeurbanne Cedex, France*

(b) *CEA Grenoble, Département de Recherche sur la Matière Condensée, SP2M/PSC,
17, rue des Martyrs, F-38054 Grenoble, France*

(c) *Laboratoire de Multimatériaux et Interfaces (UMR, CNRS 5615), UCBL,
43, Boulevard du 11 Novembre 1918, F-69100 Villeurbanne, France*

(Received October 8, 2000)

The cubic phase of III-nitrides has received much less attention than the hexagonal structure, because of difficulties inherent to the growth of this meta-stable phase. However, the possibility to avoid the effects of piezoelectric fields in cubic phase GaN grown on non-polar substrates gives new interest for this material. In this work, we present optical properties (photoluminescence and photoreflectance) of cubic GaN layers grown by MBE on c-SiC/Si pseudo-substrates at room and low temperature. Photoluminescence properties of doped (n- and p-type) c-GaN layers and of AlGaN layers are also presented.

1. Introduction The interest in cubic phase GaN (c-GaN) and related alloys is motivated by some expected technological advantages over the hexagonal phase of GaN, such as easy cleaving of laser facets, easier doping and contacting. Moreover, if c-GaN epitaxial layers are grown on non-polar substrates, they can be free of any piezoelectric fields which have a detrimental effect on optical properties of hexagonal GaN based emitting structures: the oscillator strength in such structures is much reduced due to the spatial separation of electrons and holes induced by the piezoelectric field [1]. However, the meta-stable cubic phase of GaN is rather difficult to grow and has therefore received much less attention than the hexagonal one. The challenge lies mainly in the heteroepitaxial growth due to the lack of lattice-matched substrate for this material. In this work, we use SiC/Si pseudo-substrates on which we grow c-GaN layers by molecular beam epitaxy (MBE). Our goal is to realize light emitting diodes in nitride based material on silicon compatible substrates. In this paper, the optical characterization of undoped and doped c-GaN epitaxial layers performed by photoluminescence and photoreflectance spectroscopy are presented.

2. Sample Preparation and Structural Properties The growth of c-GaN is usually achieved either on GaAs or on SiC substrates (see Okumura [4] and As and Lischka [5]). GaAs substrates do not allow high growth temperatures (less than 700 °C) and

¹⁾ e-mail: bru@insa-lyon.fr

cubic SiC substrates are not commercially available. So, we have chosen to prepare pseudo-substrates on a (100) Si substrate. First a thin c-SiC layer (2 to 3 nm) is grown by reactive chemical vapor deposition (CVD) at rather low temperature (1150 °C) using propane and H₂, silicon being supplied by the substrate. Then a thicker c-SiC layer (3 to 5 μm) is grown by CVD at 1350 °C using silane and propane. The typical structural properties for a 3 μm c-SiC/Si pseudo-substrate are: 7 to 9 nm roughness and a full width at half maximum (FWHM) for (200) X-ray diffraction peak of about 110 to 130 arcsec.

Cubic GaN epitaxial layers are grown by MBE using an rf-plasma cell as nitrogen source. The growth temperature is in the range 680 to 720 °C. The nucleation and layer growth processes are controlled in-situ by RHEED oscillation observation. A two-dimensional growth mode is obtained under stoichiometric conditions and results in the best structural quality for c-GaN, with a very low parasitic hexagonal phase [2]. The FWHM of the X-ray rocking curves in θ - ω geometry is 14 arcmin which corresponds to state of the art material. A large density of stacking faults is always observed along (111) planes by transmission electron microscopy.

The doping of cubic GaN is extremely important as far as realization of optoelectronic devices is planned. Following the work made for hexagonal GaN phase and also the few published works concerning the cubic phase, we have used Si for n-type doping and Mg for p-type doping. For p-type doping, the Mg cell is in the temperature range 200–300 °C, and for n-type doping, the Si cell is in the range 980–1200 °C. The doping profile was controlled by secondary ion mass spectroscopy (SIMS), and calibrated using Mg and Si implanted standards.

Low and room temperature PL and PR spectra were carried out using the 244 nm line of an intra-cavity frequency-doubled argon ion laser, as pump source. For PR measurements, a xenon lamp light dispersed through a monochromator was used as test beam.

3. Optical Properties of c-GaN Layers and Related Al Alloys Typical photoluminescence spectra recorded at 8 and 300 K in an undoped cubic GaN layer are plotted in

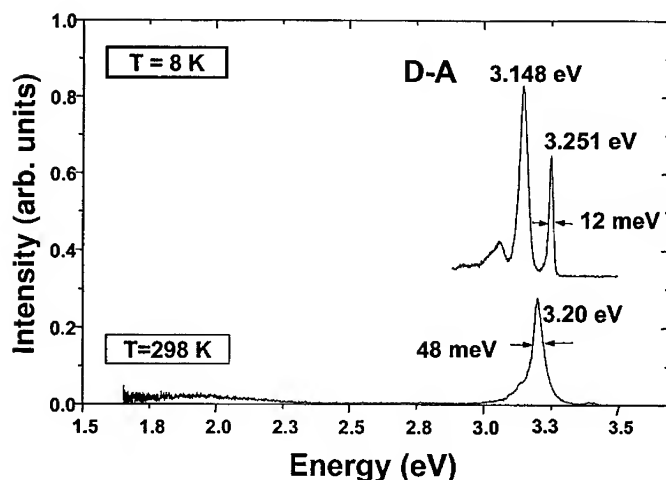


Fig. 1. PL spectra of an undoped cubic GaN layer on c-SiC/Si, at 8 K and 298 K

Fig. 1. The layer is 1.2 μm thick. At low temperature, the spectrum exhibits mainly two peaks, one at 3.251 eV which corresponds to the PR signal and has therefore been attributed to a combination of both free and bound excitons [3]. The FWHM (12 meV) is the lowest value reported for this semiconductor. The second main peak of the PL spectrum at 3.148 eV was attributed to a donor-acceptor recombination from temperature dependent measurements [3]. A third peak arises slightly above 3 eV and was also observed by Okumura et al. [4] and As and Lischka [5]: the radiative recombination process involves a localized state, either e-A or D-A recombination.

The PL spectrum recorded at room temperature in the same sample is dominated by the band to band recombination peak which arises at 3.2 eV with a FWHM of 48 meV. A very weak contribution of a deep band around 2 eV is apparent on the spectrum. This deep "red" band has to be compared with the yellow luminescence usually observed in the hexagonal phase of GaN, but its influence is rather low as compared with deep bands introduced in p-type doped samples as will be shown in the following section. For this undoped cubic GaN layer, the ratio of integrated PL intensity between 8 and 300 K is about 3000. A very low contribution of parasitic hexagonal phase is detected around 3.5 eV, showing a good control of nucleation and growth processes.

The analysis of the PR transitions recorded in different samples at low temperature (Fig. 2) was made and previously reported [6]. We have shown that the heavy- and light-hole exciton energies are separated and shifted in several of the c-GaN layers we have grown. This observation is attributed to the lift of degeneracy induced in the layers by some residual strain in the layers. Comparison between experimental exciton energies and theoretical calculations performed in the zinc-blende structure using elastic constants and deformation potentials from literature has been made and led us to conclude to a residual tensile strain in the layers. This is in good agreement with the

X-ray determination of the normal lattice parameter which is always slightly lower than that of the unstrained c-GaN, and also in agreement with measurements of the curvature of the pseudo-substrate before and after the c-GaN growth. This residual tensile strain is explained by the difference between the thermal coefficients of c-GaN and c-SiC.

In Fig. 3 typical PL spectra recorded at low temperature in Si-

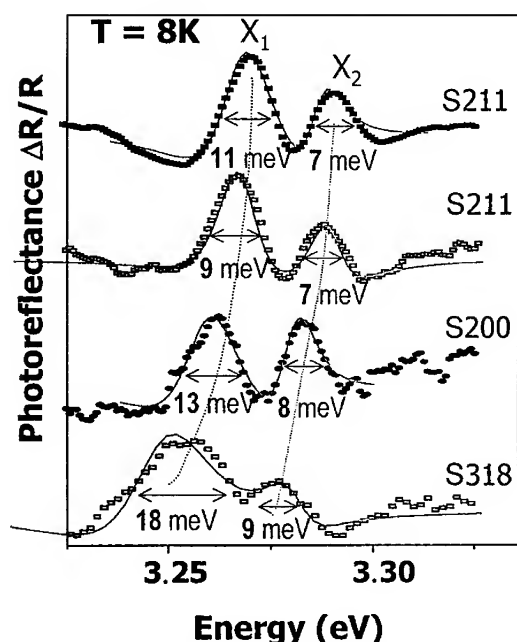


Fig. 2. Low temperature PR spectra recorded for different samples showing shifts in the energy of the excitons depending on the sample. Symbols experiments, — FDFIT fit

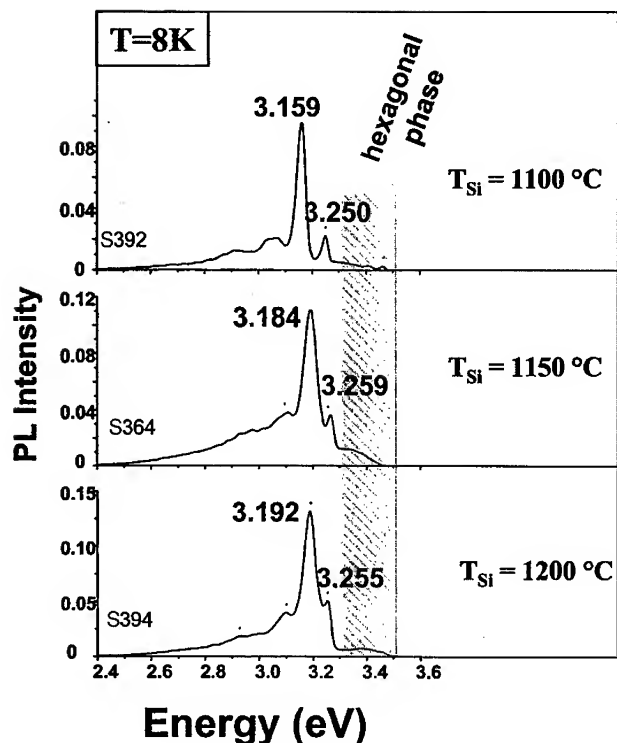


Fig. 3. Low temperature PL spectra of Si-doped cubic GaN layers

doped samples are plotted for three values of Si effusion cell temperature. At low Si incorporation, the PL spectrum is very similar to that of Fig. 1 for the undoped material. The D-A peak is blue-shifted and broadens as the Si cell temperature is increased. For higher Si content ($T_{\text{Si}} = 1200^\circ\text{C}$), both lines merge into one broad band as usually observed for doped semiconductors. This is described by electron-impurity interaction (band tailing) and also conduction band filling effects. The influence of parasitic hexagonal phase is more pronounced than in the undoped sample of Fig. 1, but does not seem to be related to the incorporated Si concentration. SIMS measurements realized on the Si doped c-GaN layers have shown that the Si incorporation is well correlated with evolution of the Si effusion cell temperature. The residual Si concentration in the non-intentionally doped cubic layers is about $2 \cdot 10^{17} \text{ cm}^{-3}$ [7].

Figure 4 shows the typical low temperature spectra of Mg doped c-GaN layers, for different Mg contents ranging between 10^{17} and 10^{19} cm^{-3} as determined from SIMS measurements. At low Mg content, the spectrum is still dominated by the bound exciton transition around 3.25 eV and the D-A pair around 3.15 eV. A deep blue band is also arising below 3 eV and increases as the Mg content increases. It is therefore attributed to Mg complexes. This deep blue band is much more intense than the "red" deep band recorded in the undoped sample (Fig. 1) and is therefore much more detrimental for the radiative efficiency of future light emitting diodes. An increasing influence of the parasitic hexagonal phase is also clearly evidenced in Fig. 4, especially for both spectra at the top of the figure.

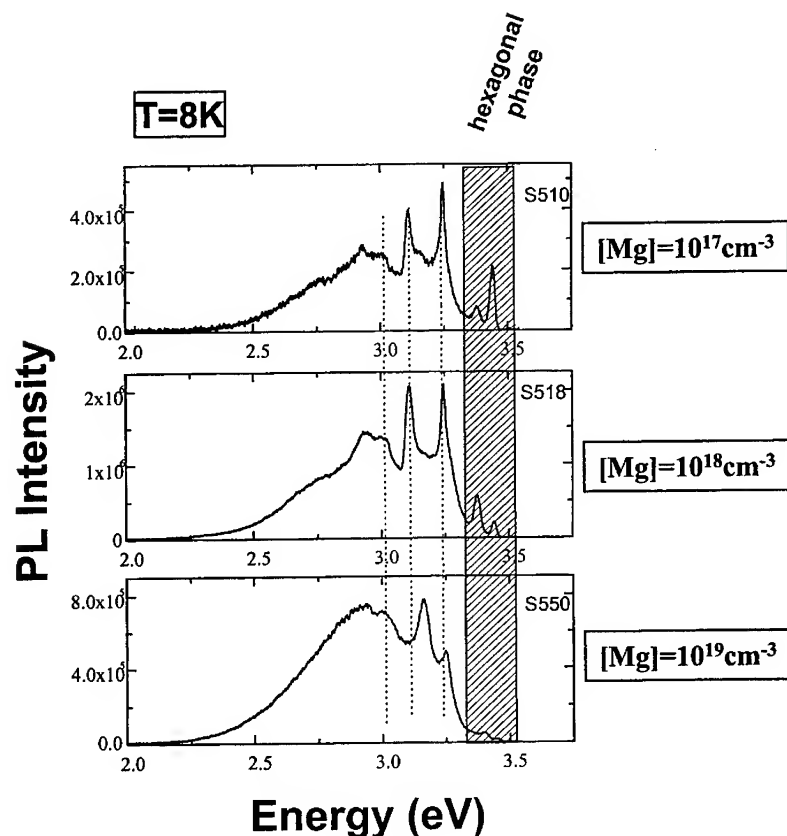


Fig. 4. Low temperature PL spectra of Mg doped cubic GaN layers

Incorporating Mg in cubic GaN layers is a challenging problem as Mg tends to segregate at the surface especially at high growth temperatures. As the activation energy of such an acceptor is rather high in GaN, only 10% of the Mg content will be ionized at room temperature. Therefore, we have to incorporate high quantities of Mg in order to make an operating p-n junction. A compromise has to be found in order to efficiently incorporate Mg in c-GaN: a lower temperature is used (680 °C) for the growth of the sample at the bottom of Fig. 3, which allows the incorporation of up to 10^{19} cm^{-3} Mg atoms. However, it should be mentioned that the electrical of these p-type doped c-GaN layers are not yet satisfying, as free carrier density and mobility are still not perfectly controlled. Problems of structural defects and/or compensating impurities are suspected.

First attempts to grow cubic AlGaIn alloys have been made in order to get a better optical confinement in the LED. Several layers have been grown and controlled by in-situ observation of RHEED oscillations. The Al content is also controlled by RBS measurements. Room temperature and low temperature PL spectra recorded on three AlGaIn alloys are reported in Fig. 5. The Al content is deduced from PL peak energy using the formula taken from [8] and is in rather good agreement with RBS determination. This proves an efficient incorporation of Al in cubic GaN layers up to 45%.

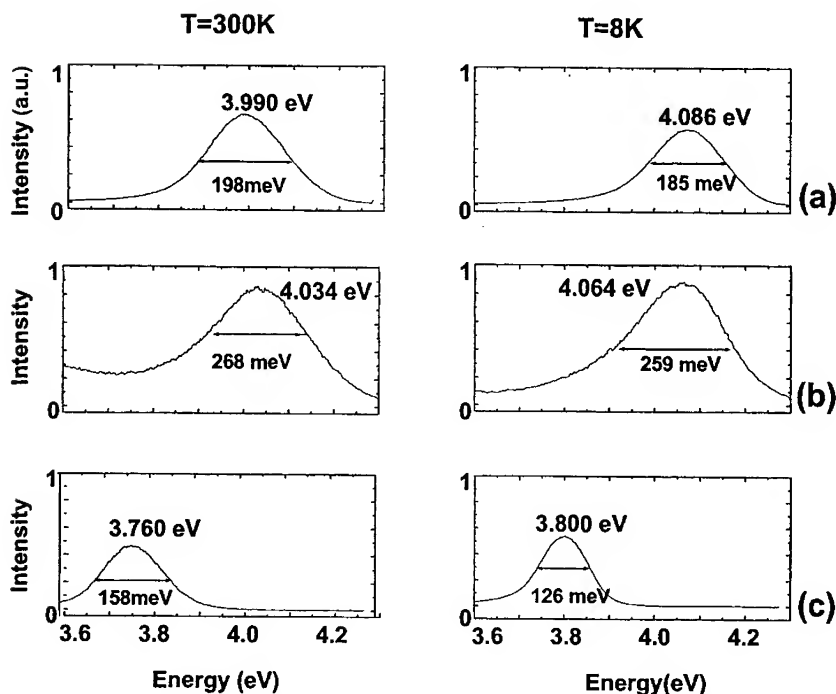


Fig. 5. PL spectra in three c-AlGaIn layers recorded at room temperature and at 8 K. Al content: a) 50% from RBS, 45% from PL; b) 40% from RBS, 45% from PL; c) 40% from RBS, 30% from PL

4. Conclusion Cubic GaN layers were successfully grown on SiC/Si pseudo-substrates and structural as well as optical properties were shown at the state of the art for this material. Both types of dopants (Mg and Si) were incorporated in the layers and exhibit PL spectra similar to those reported for the hexagonal phase of GaN. Al was also successfully alloyed with cubic GaN. In spite of the lower structural and optical quality of the cubic phase as compared to the hexagonal one, mainly due to inherent difficulties in the growth of the metastable phase, we have been able to show the feasibility of light emitting diodes using this material [9]. However, the future of cubic GaN as a candidate for device application is still dependent on necessary improvements of its quality especially for p-type doped material.

Acknowledgements This work was supported by Région Rhône-Alpes.

References

- [1] J. SIMON, E. MARTINEZ-GUERRERO, C. ADELMANN, G. MULA, B. DAUDIN, G. FEUILLET, H. MARIETTE, and N. T. PELEKANOS, Proc. Internat. Conf. Semiconductor Quantum Dots, Munich, July 31–August 3, 2000; phys. stat. sol. (b) **224** (2001).
- [2] B. DAUDIN, G. FEUILLET, J. HÜBNER, Y. SAMSON, F. WIDMANN, A. PHILIPPE, C. BRU-CHEVALLIER, G. GUILLOT, E. BUSTARRET, G. BENTOUMI, and A. DENEUVILLE, J. Appl. Phys. **84**, 2295 (1998).
- [3] A. PHILIPPE, C. BRU-CHEVALLIER, M. VERNAY, G. GUILLOT, J. HÜBNER, B. DAUDIN, and G. FEUILLET Mater. Sci. Engng. B **59**, 168 (1999).

- [4] H. OKUMURA, H. HAMAGUCHI, G. FEUILLET, Y. ISHIDA, and S. YOSHIDA, *Appl. Phys. Lett.* **68**, 244 (1996).
- [5] D. J. As and K. LISCHKA, *phys. stat. sol. (a)* **176**, 475 (1999).
- [6] A. PHILIPPE, C. BRU-CHEVALLIER, H. GAMEZ-CUATZIN, G. GUILLOT, E. MARTINEZ-GUERRERO, G. FEUILLET, P. ABOUGHÉ-Nzé, Y. MONTEIL, and B. DAUDIN, *phys. stat. sol. (b)* **216**, 247 (1999).
- [7] E. MARTINEZ-GUERRERO, B. DAUDIN, G. FEUILLET, H. MARIETTE, S. FANGET, A. PHILIPPE, C. DUBOIS, C. BRU-CHEVALLIER, G. GUILLOT, P. ABOUGHÉ-Nzé, T. CHASSAGNE, Y. MONTEIL, H. GAMEZ-CUATZIN, and J. TARDY, *Mater. Sci. Engng. B*, in press.
- [8] A. NAKADAIRA and H. TANAKA, *Appl. Phys. Lett.* **70**, 2720 (1997).
- [9] H. GAMEZ-CUATZIN, J. TARDY, P. ROJO-ROMEO, A. PHILIPPE, C. BRU-CHEVALLIER, A. SOUFI, G. GUILLOT, E. MARTINEZ-GUERRERO, G. FEUILLET, B. DAUDIN, P. ABOUGHÉ-Nzé, and Y. MONTEIL, *phys. stat. sol. (a)* **176**, 131 (1999).

phys. stat. sol. (a) **183**, 75 (2001)

Subject classification: 71.36.+c; 73.21.Fg; 78.35.+c; 78.47.+p; S7.14

Propagation of Exciton–Polaritons in Nitride-Based Multiple Quantum Wells

G. MALPUECH and A. KAVOKIN

*LASMEA, UMR 6602 du CNRS, Université Blaise Pascal, Clermont-Ferrand II,
F-63177 Aubière Cedex, France*

(Received October 8, 2000)

We present a semi-classical theory of exciton–polariton effects in disordered multiple quantum well (MQW) structures in application to GaN/AlGa_N MQWs. An original micro-model is proposed that allows to calculate all types of coherent optical spectra of MQWs. We show that GaN/AlGa_N MQWs should exhibit pronounced propagation effects in the resonant Rayleigh scattering and the vertical motional narrowing effect in the time-resolved transmission. We predict polariton-induced oscillations in the time-resolved coherent optical spectra of GaN/AlGa_N MQWs having a period of the order of hundreds of femtoseconds.

1. Introduction The interplay between light-induced exciton coupling and disorder-induced exciton scattering in multiple quantum well (MQW) structures is responsible for striking effects like resonant Rayleigh scattering of light (RRS) [1] and vertical motional narrowing (VMN) of exciton–polaritons [2]. Both effects have been recently observed in time-resolved optical spectra of GaAs/AlGaAs MQWs and interpreted theoretically in the framework of a semi-classical approach. Here, we extend the theoretical model of Ref. [1] by consideration of light scattering by individual localized exciton states within a non-local model and taking into account the exciton–polariton effects. This allows us to prove by a micro-model analysis the validity of the widely used phenomenological theory of exciton inhomogeneous broadening in quantum wells (QWs) [3]. We use this original technique to describe the coherent optical spectra of a new and promising semiconductor heterosystem, GaN/AlGa_N. Note the essential difference between the present model and earlier works on the RRS [4, 5] which neglect the polariton effect.

The specifics of GaN-based heterostructures is that the exciton oscillator strength is enhanced by an order of magnitude as compared to the GaAs-based quantum structures [6]. On the other hand, the disorder in presently available GaN/AlGa_N MQWs is much stronger than in GaAs/AlGaAs MQWs. This makes the nitride-based heterostructures particularly promising for observation of the VMN effect, and study of disorder effects on the exciton–polariton propagation. A strong potential disorder induces a strong elastic scattering of light (Rayleigh scattering) in nitrides. At present, there is no available experimental data on time-resolved reflection or RRS in nitride-based MQWs, as far as we know, and this work is aimed to stimulate such studies.

2. The Formalism Our formalism is based on the Green function approach to the problem of light–exciton coupling in low-dimensional structures [7] and the generalized scattering state technique for calculation of light-pulse propagation in multilayer sys-

tems [1]. We consider each QW as an irregular array of quantum dots (QDs). Each QD is characterized by a given exciton resonance frequency ω_n , and radius vector \mathbf{R}_n . We assume ω_n to be distributed by a Gaussian function

$$f(\omega_n) = \frac{1}{\sqrt{\pi} \Delta} \exp \left[-\left(\frac{\omega_n - \omega_0}{\Delta} \right)^2 \right], \quad (1)$$

where Δ is the parameter of exciton inhomogeneous broadening.

Neglecting the deviations in a shape of exciton wave function localized in different dots, we solve the following Maxwell equation:

$$\nabla \times \nabla \times \mathbf{E} = k_0^2 \mathbf{D}, \quad (2)$$

where

$$\mathbf{D} = \varepsilon_b \mathbf{E} + 4\pi \mathbf{P}_{\text{exc}} \quad (3)$$

and

$$4\pi \mathbf{P}_{\text{exc}} = \sum_{n=1}^N T_n \Phi(\mathbf{r} - \mathbf{R}_n) \int \mathbf{E}(\mathbf{r}') \Phi(\mathbf{r}' - \mathbf{R}_n) d\mathbf{r}', \quad (4)$$

with

$$T_n = \frac{\varepsilon_b \omega_{\text{LT}} \pi a_B^3}{\omega_n - \omega - i\gamma},$$

where k_0 is the wave vector of the incident light in the media, ω_{LT} the longitudinal-transverse splitting, ε_b the background dielectric constant, a_B the Bohr radius of the exciton in the bulk, γ the homogeneous broadening, and $\Phi(\mathbf{r})$ is the localized exciton wave function taken with equal electron and hole coordinates. Further we neglect the polarization of light, which is a strong approximation, of course. Also we assume the same shape of $\Phi(\mathbf{r})$ for all QDs. We solve Eq. (2) in a similar way to the procedure described in Ref. [7]. Namely, we represent an electric field as

$$\begin{aligned} \mathbf{E}(\omega, \mathbf{r}) \\ = \mathbf{E}_0 \exp(i\mathbf{k}\mathbf{r}) + k_0^2 \sum_{n=1}^N T_n e^{i\mathbf{k}\mathbf{R}_n} \int d\mathbf{r}' \Phi(\mathbf{r}' - \mathbf{R}_n) G_0(\mathbf{r} - \mathbf{r}') \int \mathbf{E}(\mathbf{r}'') \Phi(\mathbf{r}'' - \mathbf{R}_n) d\mathbf{r}'', \end{aligned} \quad (5)$$

where $G_0(\mathbf{r} - \mathbf{r}') = e^{ik|\mathbf{r} - \mathbf{r}'|} / (4\pi |\mathbf{r} - \mathbf{r}'|)$ is the Green function for a zero-dimensional system, $\mathbf{k} = \mathbf{k}_0 \sqrt{\varepsilon_b}$ is the wave vector of the incident light in the media. It is convenient to multiply the left and right parts of Eq. (5) by $\Phi(\mathbf{r} - \mathbf{R}_m)$ and integrate over \mathbf{r} . This procedure yields the following expression:

$$\begin{aligned} A_m \equiv \int \mathbf{E}(\mathbf{r}) \Phi(\mathbf{r} - \mathbf{R}_m) d\mathbf{r} \\ = \frac{\int \mathbf{E}_0 e^{i\mathbf{k}\mathbf{r}} \Phi(\mathbf{r} - \mathbf{R}_m) d\mathbf{r} + k_0^2 \sum_{n=1, n \neq m}^N T_n e^{i\mathbf{k}\mathbf{R}_n} \Theta_{mn} A_n}{1 - k_0^2 T_m e^{i\mathbf{k}\mathbf{R}_m} \Xi}, \end{aligned} \quad (6)$$

where

$$\begin{aligned} \Theta_{mn} &= \int d\mathbf{r} \int d\mathbf{r}' G_0(\mathbf{r} - \mathbf{r}' + \mathbf{R}_m - \mathbf{R}_n) \Phi(\mathbf{r}) \Phi(\mathbf{r}'), \\ \Xi &= \int d\mathbf{r} \int d\mathbf{r}' G_0(\mathbf{r} - \mathbf{r}') \Phi(\mathbf{r}) \Phi(\mathbf{r}'). \end{aligned}$$

The procedure we apply to solve Eqs. (5) and (6) consists of two steps. First, we neglect the *scattering* of light and calculate the *reflection* and *transmission* accurately accounting for polariton effects. Then we consider a correction to the electric field of light due to the scattering. Normally, less than 1% of light is resonantly diffused by a QW [3], that justifies this procedure.

Let us first neglect the scattering and assume therefore $A_m = A_n \equiv A$ for all values of m and n ,

$$A = \frac{\int \mathbf{E}_0 e^{i\mathbf{k}\mathbf{r}} \Phi(\mathbf{r} - \mathbf{R}_m) d\mathbf{r}}{1 - k_0^2 \sum_{n=1}^N T_n e^{i\mathbf{k}\mathbf{R}_n} \Omega_{mn}}. \quad (7)$$

For the normal incidence case and assuming that the second term in the denominator in Eq. (7) is much smaller than unity (which means that the transmission strongly dominates resonant reflection for a QW) we substitute

$$\sum_{n=1}^N T_n e^{i\mathbf{k}\mathbf{R}_n} G_0(\mathbf{r} - \mathbf{r}' - \mathbf{R}_n + \mathbf{R}_m) \rightarrow \int d\nu \frac{\varepsilon_b \omega_{LT} \pi a_B^3}{\nu - \omega - i\gamma} f(\nu) \frac{1}{Ld^2} \sum_{\mathbf{q}_\perp} e^{i\mathbf{q}_\perp(\mathbf{q} - \mathbf{q}')} \sum_{q_z} \frac{e^{iq_z(z-z')}}{q_\perp^2 + q_z^2 - k_s^2}. \quad (8)$$

Here \mathbf{q} and \mathbf{q}_\perp are the in-plane components of the radius vector \mathbf{r} and wave vector \mathbf{q} , z and q_z are their normal-to-the-plane components, respectively, d is the average distance between dots (which is supposed to be less than the wavelength of light in the media). Substituting the Eq. (6) modified in this way into Eq. (5) one can obtain the reflection and transmission coefficients of light incident on a QW, r_{QW} and t_{QW} as

$$r_{QW} = \frac{\beta}{1 - \beta}, \quad t_{QW} = \frac{1}{1 - \beta}, \quad (9)$$

where

$$\beta = i\Gamma_r \int d\nu \frac{f(\nu)}{\nu - \omega - i\gamma}, \quad \Gamma_r = \frac{k}{2d^2} \omega_{LT} \pi a_B^3 \left[\int \Phi(\mathbf{r}) \cos(\mathbf{k}\mathbf{r}) d\mathbf{r} \right]^2. \quad (10)$$

Equations (9) and (10) are formally equivalent to the well-known expressions for the reflection and transmission coefficients of a QW [3] if one takes d and the in-plane size of a QD equal to the in-plane Bohr radius of a free exciton in a QW. Here, for the first time, we have proved the validity of the phenomenological approach to the problem of light coupling with an inhomogeneously broadened exciton resonance using a micro-model of an array of QDs. Note that in this approach the possibility of absorption of photon by more than one exciton state from the inhomogeneous distribution is accounted for. The multiple absorption-re-emission of light by different excitons has been shown to induce characteristic oscillations in time-resolved reflection and transmission spectra of a single QW [8]. To calculate the reflection or transmission spectra of MQWs, we use the standard transfer matrix procedure [3] with single-well reflection and transmission coefficients (9).

Now we can calculate the scattering of the light wave on a QW. The amplitude of the light field which is a subject to scattering is

$$\mathbf{E} = \frac{\mathbf{E}_0}{1 - \beta}. \quad (11)$$

This follows from Eq. (9) and accounts for the reflection and transmission. We shall neglect the *second term* in the numerator of the right part of Eq. (6). Physically, this means that we neglect the correction of the electric field at the m -th QD due to light scattered by other QDs. In other words, we neglect the possibility of re-absorption by one QD of a photon scattered by another QD. On the other hand, we fully take into account the retardation effect within each individual QD and re-absorption of light before the act of scattering. This approximation is quite reasonable having in mind that the diffused signal is much weaker than E_0 .

In this way, after substitution of Eq. (6) into Eq. (5) we obtain the amplitude of light scattered with the wave vector \mathbf{k}_s by the array of QDs as

$$\mathbf{E}_d(\omega, \mathbf{k}_s) = \frac{\mathbf{E}_0}{1 - \beta} \sum_{n=1}^N \frac{i\Gamma_0^{\text{QD}}}{\omega_n - \omega - i(\gamma + \Gamma_0^{\text{QD}})} \exp(i(\mathbf{k} - \mathbf{k}_s) \cdot \mathbf{R}_n), \quad (12)$$

with

$$\Gamma_0^{\text{QD}} = \frac{1}{6} \omega_{\text{LT}} k_0^3 a_B^3 \left(\int d\mathbf{r} \cos(\mathbf{k}_s \cdot \mathbf{r}) \Phi(\mathbf{r}) \right)^2. \quad (13)$$

Here $\mathbf{k}_s \neq \pm \mathbf{k}$.

In order to calculate the RRS spectra of a MQW structure we apply a procedure similar to that described in [1]:

- Using the transfer matrix method we calculate the coordinate and time-dependent electric field in the system illuminated by an initial pulse of light ignoring the RRS, initially.

- We consider the scattering of light waves incident on each individual QW from both sides. We obtain the amplitude $\mathbf{E}_d(\omega, \mathbf{k}_s)$ of light scattered in the direction \mathbf{k}_s from Eq. (12).

- Using the generalized scattering state technique [1] we calculate the propagation of light waves scattered by each individual QW properly accounting for all reflection and transmission acts but neglecting secondary scattering.

- We find the amplitude of light scattered by the entire structure summing up the amplitudes of waves scattered by different QWs.

- We repeat these operations for different diffusion angles close to the direction \mathbf{k}_s (within 3°). We then perform angle averaging of the diffused intensity (speckle averaging [9]) that yields the final result.

3. Numerical Results In the numerical calculations of the time-resolved transmission spectra, for all the MQWs under consideration we have taken a spacing between wells of 70 nm, and exciton resonance frequency $\hbar\omega_0 = 3.6$ eV. We consider either “disordered” QW structures with $\hbar\Delta = 5$ meV, or “homogeneous” QWs with $\Delta = 0$ (for the reference).

Figure 1 shows the time-resolved transmission spectra of a disordered SQW (curve a), a disordered MQW containing 10 wells (curve b), 50 wells (curve c), 100 wells (curve d), and of a homogeneous SQW (curve e). Comparing the curves a and e in Fig. 1, one can see that the exciton inhomogeneous broadening induces a dramatic decrease of the decay time of the time-resolved transmission. This reflects the appearance of additional channels of energy relaxation for excitons as the disorder increases in the structure [10]. Note the strong decrease of the exciton decay time with increase of the number of QWs in the structure. This is a manifestation of the VMN effect, which is

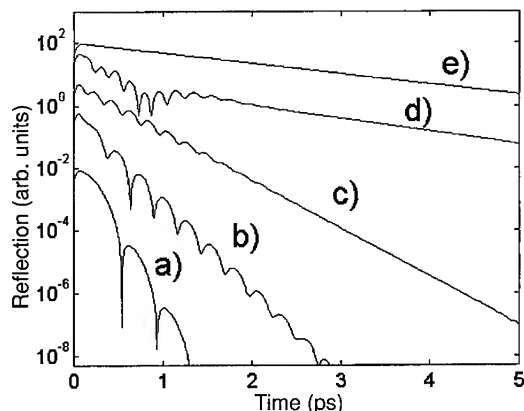


Fig. 1. Time-resolved transmission through GaN/AlGaIn quantum well structures: (a) SQW with $\hbar\Delta = 5$ meV; (b) MQW, $N = 10$, $\hbar\Delta = 5$ meV; (c) MQW, $N = 50$, $\hbar\Delta = 5$ meV; (d) MQW, $N = 100$, $\hbar\Delta = 5$ meV; (e) SQW with $\hbar\Delta = 0$ meV

visibly stronger than that observed experimentally in the GaAs/AlGaAs MQWs [2]. Note also the pronounced oscillations in the spectra of MQWs and the disordered SQW (Fig. 1a–d). They arise both from the interference of different exciton-polariton modes and the interference within each single exciton-polariton mode due to the inhomogeneous broadening.

Figure 2 shows the calculated RRS spectra for SQW, Bragg-arranged MQWs and short-period MQWs. The parameters of the model structures are summarized in Table 1. We always consider an array of 512×512 QDs spaced by 100 nm in average. One can see that both single QW and Bragg-arranged MQWs show a monotonously decaying signal, while the RRS spectrum of the short-period MQWs demonstrates pronounced oscillations. These oscillations are associated with the beats between different “super-radiant” polariton modes. In a single QW there is only one polariton state, while in the Bragg-arranged system only one optical polariton mode is optically active. That is why, in these two systems one does not see any beats in the RRS spectra.

Note, that the “level-repulsion model” [4, 5] predicts the oscillations in the RRS spectra of a single QW. This has never been observed experimentally and contradicts to the

present theory. Note also that the period of oscillations in the time-resolved RRS of nitride-based QWs is typically a factor of five to seven shorter than in GaAs/AlGaAs QWs. This is an indirect consequence of the larger exciton oscillator strength in nitrides which induces a stronger repulsion of the super-radiant exciton-polariton modes.

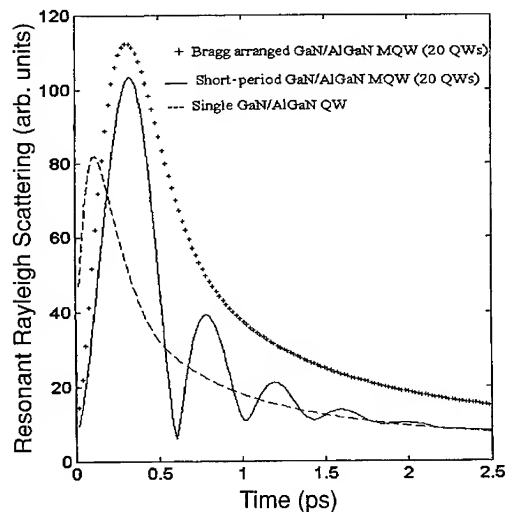


Fig. 2. Calculated RRS spectra of GaN/AlGaIn QW structures with different number of QWs and different spacing between the wells

Table 1
Parameters of three model structures used for the RRS calculations

	number of wells	period of the structure (nm)	exciton radiative damping $\hbar\Gamma_0$ (meV)	QD exciton radiative damping $\hbar\Gamma_0^{\text{QD}}$ (meV)	exciton inhom. broadening Δ (meV)
single QW	1		0.4	0.04	5
Bragg-MQW	20	67.6	0.4	0.04	5
short-period MQW	20	5	0.4	0.04	5

4. Conclusion In conclusion, we have presented a semi-classical theory of propagation and scattering of exciton-polaritons in heterostructures. We have applied this formalism to the case of GaN/AlGaIn MQWs. It is shown that nitrides are quite promising for observation of fine exciton-polariton effects despite of the poor quality of the structures available at present. Indeed, propagation effects are found to govern the RRS signal of GaN/AlGaIn MQWs while the VMN of the exciton-polaritons affects the time-resolved transmission.

Acknowledgements We thank Prof. E. L. Ivchenko for fruitful discussions. The work has been supported by the European Commission in the framework of a contract HPRN-CT-1999-00132.

References

- [1] G. MALPUECH, A. KAVOKIN, W. LANGBEIN, and J. M. HVAM, Phys. Rev. Lett. **85**, 650 (2000).
- [2] J. J. BAUMBERG et al., Phys. Rev. Lett. **80**, 3567 (1998).
A. V. KAVOKIN and J. J. BAUMBERG, Phys. Rev. B **57**, R12697 (1998).
- [3] L. C. ANDREANI, G. PANZARINI, A. V. KAVOKIN, and M. R. VLADIMIROVA, Phys. Rev. B **57**, 4670 (1998).
- [4] V. SAVONA, S. HAACKE, and B. DEVEAUD, Phys. Rev. Lett. **84**, 183 (2000).
- [5] V. SAVONA and R. ZIMMERMANN, Phys. Rev. B **60**, 4928 (1999).
- [6] B. GIL et al., Phys. Rev. B **59**, 10246 (1999).
- [7] E. L. IVCHENKO and A. V. KAVOKIN, Soviet Phys. — Solid State **34**, 1815 (1992).
- [8] G. MALPUECH, A. KAVOKIN, J. LEYMARIE, P. DISSEIX, and A. VASSON, Phys. Rev. B **60**, 13298 (1999).
- [9] W. LANGBEIN, J. M. HVAM, and R. ZIMMERMANN, Phys. Rev. Lett. **82**, 1040 (1999).
- [10] G. MALPUECH and A. KAVOKIN, Appl. Phys. Lett. **76**, 3049 (2000).

phys. stat. sol. (a) **183**, 81 (2001)

Subject classification: 71.15.Ap; 73.22.-b; 78.67.Bf; S7.14

Tuning Optical Properties of GaN-Based Nanostructures by Charge Screening

A. DI CARLO

*INFN and Dipartimento di Ingegneria Elettronica Università di Roma, Tor Vergata,
via di Tor Vergata 100, I-00133 Roma, Italy*

(Received October 8, 2000)

In this paper we will show the influence of doping and free charge screening of polarization fields on the optical and electronic properties of GaN-based nanostructures. Modulation-doped nanostructures can be used to enhance the oscillator strength of the fundamental transition energy. The free charge and doping are shown to be an additional degree of freedom for GaN-based device design.

1. Introduction Nitride-based nanostructures are nowadays used in both electronic and optoelectronic devices. In the first case, the large energy gap of GaN-related semiconductors allows for the building of high power devices with high breakdown voltages and high thermal conductivity. In the optoelectronic context, nitride materials are employed in blue emitters (LED and lasers) and in photodetection. The design of such structures is, however, complicated by the presence of internal polarization field, which induces a high junction field when a heterojunction between different nitride semiconductors is formed. The polarization field is the sum of piezoelectric polarization and spontaneous polarization [1]. There are several macroscopic manifestations of the polarization field; among them, the large Stark shift of the fundamental optical transition and the reduction of the oscillator strength of the fundamental optical transition for large wells are very crucial in any optical application of nitride materials.

In the case of nitride-based heterojunction devices, fix (doping) and free charges should be considered in the determination of the real electric field in the heterostructure. In fact, for the case of doping, the polarization field can ionize the donor (or acceptor) thus producing opposite charge that screens (partially) the bare polarization field [2]. The same screening of the polarization field arises when free charges (electrons and holes) are injected into the heterostructure. These charges form a dipole counterbalancing the polarization field [3].

We should point out that fix and free charges can be tailored by a proper choice of growth condition, for the doping, and by selecting a proper operation point (such as bias, current, optical pumping etc.) for the free charge. Thus, optical and electronic properties of nitride-based nanostructures can be tuned by using two new degrees of freedom: doping and free charges.

Experimentally, it has been established for both GaN/InGaN [4–11] and AlGaIn/GaN [12–14] heterostructures that doping of the active region produces a strong modification of the optical properties, namely: (i) a blue-shift of the photoluminescence (PL) peak, (ii) an enhancement of the emission intensity, (iii) a reduction of the laser

threshold current, (iv) a reduction of the carrier radiative recombination lifetime, and (v) a reduction of the Stokes shift between PL peak and the photoluminescence excitation (PLE) spectra. On the other hand, free carrier screening of the polarization field has been investigated experimentally in Ref. [15].

In this paper, we will discuss the charge screening of the polarization field by applying the self-consistent tight-binding (TB) model described in the following section. The use of microscopic models such as tight-binding will become necessary if band structure details are not known. This is the case, for example, of strained alloy layers where effective masses, band separation, band discontinuity etc. are not known. Moreover, tight-binding allows for a complete description of the band structure in the whole Brillouin zone. The TB is here used to describe charge screening in two reference multi-quantum-well (MQW) systems: AlGa_N/Ga_N MQW and Ga_N/InGa_N MQW.

2. Method We solve the Schrödinger equation on the nearest-neighbor $sp^3d^5s^*$ [16] tight-binding basis, self-consistently coupled with a 1D Poisson equation accounting for polarization, doping, and free carriers [3, 17, 18].

The macroscopic polarizations in the alloys are obtained by Vegard interpolation of ab-initio values [1] for the binary compounds. This procedure describes the interplay of polarization and dielectric, free carrier, and doping screening in a fully self-consistent and non-perturbative way, with band structure accuracy typical of ab-initio methods [16]. Optical properties are obtained via the theory of Graf and Vogl [19] without introducing additional fitting parameters.

We should mention that the Vegard interpolation may not be enough accurate and nonlinear terms are needed to be considered in the interpolation of ab-initio quantities. However, the alloys we consider are close to binary compounds and the linear interpolation error is quite small. We do feel, however, that an ab-initio inspection of the alloy problem should be considered.

3. Results We performed the calculations at room temperature for Al_{0.15}Ga_{0.85}N/GaN and In_{0.2}Ga_{0.8}N/GaN MQWs, with 10 nm barriers and several well widths, pseudomorphically grown on a GaN substrate. We considered purposely modulation-doped (doped barrier) structures, assuming a 10^{17} cm^{-3} residual doping in the wells. Here we consider a donor level of 20 meV.

Self-consistent results for a AlGa_N [10 nm]/Ga_N[4 nm] MQW are shown in Fig. 1, where we plot the electron density, ionized donor density, conduction band edge and Fermi level as a function of the MQW depth. If the conduction band energy is higher than the Fermi energy the donors become ionized. This occurs mainly in the left barrier and only with a minor extend in the right barrier. In the well region the donors are not ionized and an accumulation of electrons takes place. Since the donors ionize asymmetrically (in contrast to what happens in conventional modulation-doped MQW) the electrons in the well and the ionized donors in the left barrier form a dipole that screens the polarization field.

The effect of such doping screening is reflected on the optical properties of the nanostructure. In Fig. 2 we show the variation (ΔE) of the fundamental energy transition, that is the transition from the first valence level (V1) to the first conduction level (C1) by changing the doping density of the barrier layer from $N_D = 10^{17} \text{ cm}^{-3}$ (residual doping) to $N_D = 10^{18} \text{ cm}^{-3}$ and $2 \times 10^{18} \text{ cm}^{-3}$ as a function of well width. By increasing

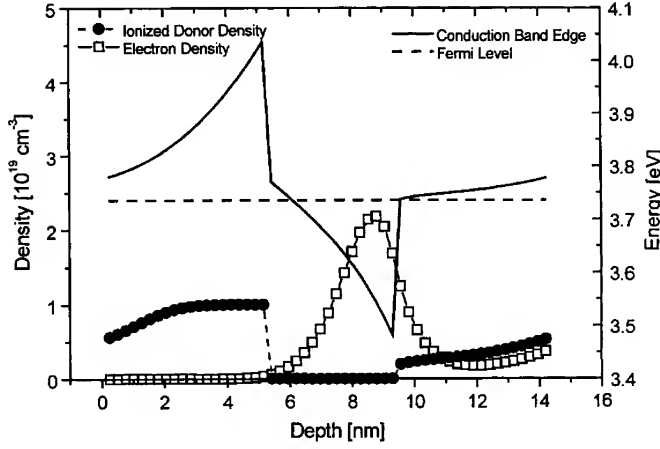


Fig. 1. Conduction band edge, ionized doping density and electron density as a function of MQW depth for the $\text{Al}_{0.15}\text{Ga}_{0.85}\text{N}$ [10 nm]/GaN [4 nm] MQW. The doping density of the barrier is $N_D = 10^{19} \text{ cm}^{-3}$

well width the shift in the fundamental transition energy becomes larger. The larger the doping density the higher the energy shift is. We notice that for a well width of 8 nm we can tailor the emission energy by $\approx 60 \text{ meV}$ simply changing the barrier doping from zero to $N_D = 2 \times 10^{18} \text{ cm}^{-3}$. Such tuning, apart from renormalization effects which are not considered in this discussion, is not present in conventional semiconductor nanostructures (AlGaAs/GaAs for example) [2].

The relation of the transition energy and oscillator strength with free charge screening is similar to the case of doping screening. A detailed discussion can be found in Refs. [3] and [17], while in the following we will analyze the combined effect of free charge and doping.

In Fig. 3 we show, for the AlGaN/GaN modulation-doped MQW and for the GaN/InGaN modulation-doped MQW, the oscillator strength and the fundamental

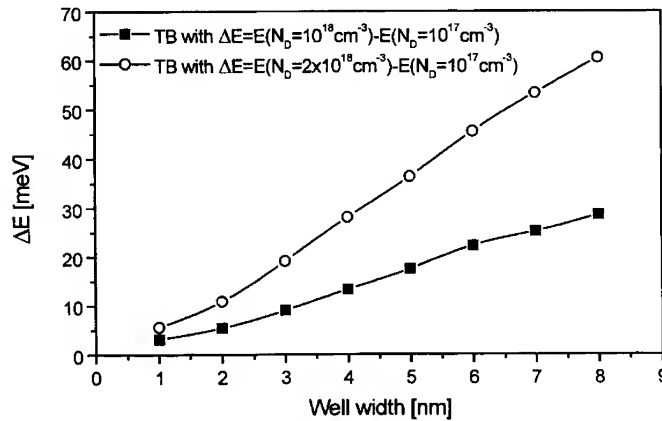


Fig. 2. Variation (ΔE) of the fundamental energy transition as a function of the well width for two doping densities in an $\text{Al}_{0.15}\text{Ga}_{0.85}\text{N}$ /GaN MQW

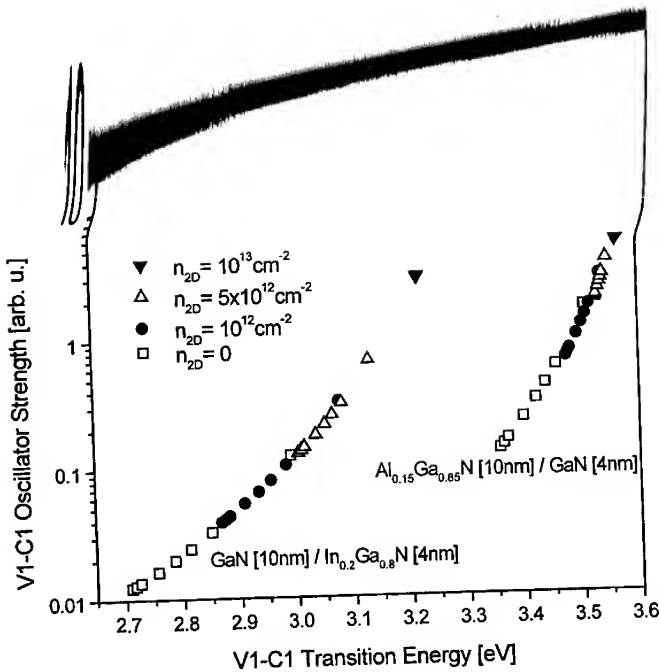


Fig. 3. Oscillator strength and fundamental transition energy for several doping and free charge densities in AlGaN/GaN and GaN/InGaN MQW. Each symbol corresponds to a well defined free charge density (labeled in the figure), while points having the same symbol correspond to different n-type doping densities. The doping levels are 10^{17} , 5×10^{17} , 10^{18} , 3×10^{18} , 5×10^{18} , 7×10^{18} , 10^{19} , $3 \times 10^{19} \text{ cm}^{-3}$ with the lower doping level corresponding to the lower transition energy

transition for various doping densities and free charge levels. Each symbol corresponds to a well defined free charge density, while points having the same symbol correspond to different n-type doping densities. The doping levels are 10^{17} , 5×10^{17} , 10^{18} , 3×10^{18} , 5×10^{18} , 7×10^{18} , 10^{19} , $3 \times 10^{19} \text{ cm}^{-3}$ with the lower doping level corresponding to the lower transition energy (low screening).

The figure clearly shows how free charge and doping screening are related. Moreover, oscillator strengths and transition energies are one-by-one related in both AlGaN/GaN and GaN/InGaN structures.

Thus, by proper choice of doping level and free charge (operation point of the device) of the nanostructure we can change both oscillator strength and fundamental transition energy. However, for a given well structure (well and barrier widths, alloy concentration) the oscillator strength and transition energy are uniquely related by a universal curve like that of Fig. 3. These curves show that the increasing of the oscillator strength by proper "charge-screening" design always induces a well defined increasing of the transition energy. Thus, the use of such curves will allow a proper design of GaN-based nanostructured devices.

We have shown how doping levels and free charges (i.e. currents) can

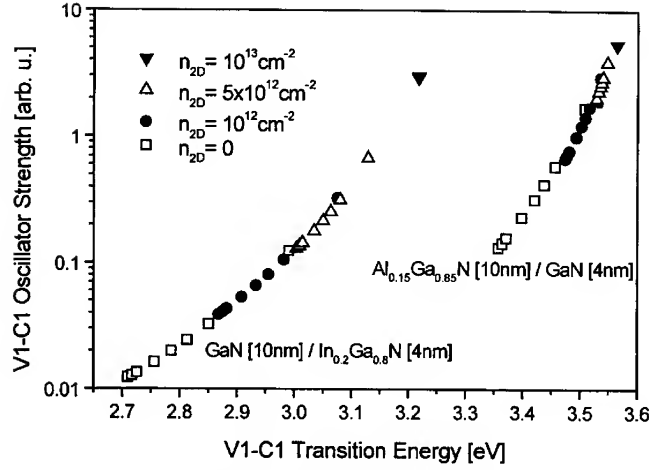


Fig. 3. Oscillator strength and fundamental transition energy for several doping and free charge densities in AlGaIn/GaN and GaN/InGaIn MQW. Each symbol corresponds to a well defined free charge density (labeled in the figure), while points having the same symbol correspond to different n-type doping densities. The doping levels are 10^{17} , 5×10^{17} , 10^{18} , 3×10^{18} , 5×10^{18} , 7×10^{18} , 10^{19} , $3 \times 10^{19} \text{ cm}^{-3}$ with the lower doping level corresponding to the lower transition energy

transition for various doping densities and free charge levels. Each symbol corresponds to a well defined free charge density, while points having the same symbol correspond to different n-type doping densities. The doping levels are 10^{17} , 5×10^{17} , 10^{18} , 3×10^{18} , 5×10^{18} , 7×10^{18} , 10^{19} , $3 \times 10^{19} \text{ cm}^{-3}$ with the lower doping level corresponding to the lower transition energy (low screening).

The figure clearly shows how free charge and doping screening are related. Moreover, oscillator strengths and transition energies are one-by-one related in both AlGaIn/GaN and GaN/InGaIn structures.

Thus, by proper choice of doping level and free charge (operation point of the device) of the nanostructure we can change both oscillator strength and fundamental transition energy. However, for a given well structure (well and barrier widths, alloy concentration) the oscillator strength and transition energy are uniquely related by a universal curve like that of Fig. 3. These curves show that the increasing of the oscillator strength by proper "charge-screening" design always induces a well defined increasing of the transition energy. Thus, the use of such curves will allow a proper design of GaN-based nanostructured devices.

4. Conclusion We have shown how doping levels and free charges (i.e. currents) can be used to tune the fundamental transition energy and oscillator strengths in GaN-based nanostructures. The variation of these optical parameters depends quite strongly on charge screening. However, for a well-defined structure, oscillator strength and transition energy are related and charge screening cannot vary one of them without changing the other.

Acknowledgement Work supported in part by MURST and "CLERMONT" UE Network (Contract No. HPRN-CT-1999-00132).

References

- [1] F. BERNARDINI, V. FIORENTINI, and D. VANDERBILT, *Phys. Rev. B* **56**, R10024 (1997).
F. BERNARDINI and V. FIORENTINI, *Phys. Rev. B* **57**, R9427 (1998).
- [2] A. DI CARLO, F. DELLA SALA, P. LUGLI, V. FIORENTINI, and F. BERNARDINI, *Appl. Phys. Lett.* **76**, 3950 (2000).
- [3] F. DELLA SALA, A. DI CARLO, P. LUGLI, F. BERNARDINI, V. FIORENTINI, R. SCHOLTZ, and J. M. JANCU, *Appl. Phys. Lett.* **74**, 2002 (1999).
- [4] P. A. GRUDOWSKI, C. J. EITING, J. PARK, B. S. SHELTON, D. J. H. LAMBERT, and R. D. DUPUIS, *Appl. Phys. Lett.* **71**, 1537 (1997).
S. BIDNYK, T. J. SCHMIDT, Y. H. CHO, G. H. GAINER, J. J. SONG, S. KELLER, U. K. MISHRA, and S. P. DENBAARS, *Appl. Phys. Lett.* **72**, 1623 (1998).
- [5] M. S. MINSKY, S. CHICHIBU, S. B. FLEISHER, A. C. ABARE, J. E. BOWERS, E. L. HU, S. KELLER, U. K. MISHRA, and S. P. DENBAARS, *Jpn. J. Appl. Phys.* **37**, L1362 (1998).
- [6] Y.-H. CHO, J. J. SONG, S. KELLER, M. S. MINSKY, E. HU, U. K. MISHRA, and S. P. DENBAARS, *Appl. Phys. Lett.* **73**, 1128 (1998).
- [7] T. DEGUCHI, A. SHIKANAI, K. TORII, T. SOTA, S. CHICHIBU, and S. NAKAMURA, *Appl. Phys. Lett.* **72**, 3329 (1998).
S. CHICHIBU, D. A. COHEN, M. P. MACK, A. C. ABARE, P. KOZODOY, M. MINSKY, S. FLEISHER, S. KELLER, J. E. BOWERS, U. K. MISHRA, L. A. COLDREN, D. R. CLARKE, and S. P. DENBAARS, *Appl. Phys. Lett.* **73**, 496 (1998).
- [8] J. DALFORS, J. P. BERGMAN, P. O. HOLTZ, B. E. SERNELIUS, B. MONEMAR, H. AMANO, and I. AKSAKI, *Appl. Phys. Lett.* **74**, 3299 (1999).
- [9] K. UCHIDA, T. TANG, S. GOTO, T. MISHIMA, A. NIW, and J. GOTOH, *Appl. Phys. Lett.* **74**, 1153 (1999).
- [10] Y.-H. CHO, F. FEDLER, R. J. HAUENSTEIN, G. H. PARK, J. J. SONG, S. KELLER, U. K. MISHRA, and S. P. DENBAARS, *J. Appl. Phys.* **85**, 3006 (1999).
- [11] H. JIANG, M. MINSKY, S. KELLER, E. HU, J. SINGH, and S. P. DENBAARS, *IEEE J. Quantum Electronics* **35**, 1483 (1999).
- [12] A. SALVADOR, G. LIU, W. KI, O. AKTAS, A. BOTCHKAREV, and H. MORKOÇ, *Appl. Phys. Lett.* **67**, 3322 (1995).
- [13] K. C. ZENG, J. Y. LIN, H. X. JIANG, A. SALVADOR, G. POPOVICI, H. TANG, W. KIM, and H. MORKOÇ, *Appl. Phys. Lett.* **71**, 1368 (1997).
- [14] H. HIRAJAMA and Y. AOYAGI, *MRS Internet J. Nitride Semicond. Res.* **4S1**, G3.74 (1999).
- [15] T. TAKEUCHI, S. SOTA, M. KASTURAGAWA, M. KOMORI, H. TAKEUCHI, H. AMANO, and I. AKASAKI, *Jpn. J. Appl. Phys.* **36**, L382 (1997).
- [16] J.-M. JANCU, R. SCHOLZ, F. BELTRAM, and F. BASSANI, *Phys. Rev. B* **57**, 6493 (1998).
- [17] V. FIORENTINI, F. BERNARDINI, F. DELLA SALA, A. DI CARLO, and P. LUGLI, *Phys. Rev. B* **60**, 8849 (1999).
- [18] A. DI CARLO, *phys. stat. sol. (b)* **217**, 703 (2000).
- [19] M. GRAF and P. VOGL, *Phys. Rev. B* **51**, 4940 (1995).

phys. stat. sol. (a) **183**, 87 (2001)

Subject classification: 71.35.Ee; 73.21.Fg; S7.14

Exciton/Free-Carrier Plasma in GaN-Based Quantum Wells: Scattering and Screening

M. E. PORTNOI (a) and I. GALBRAITH (b)

(a) *School of Physics, University of Exeter, Stocker Road, Exeter EX4 4QL, UK*

(b) *Physics Department, Heriot-Watt University, Edinburgh EH14 4AS, UK*

(Received October 8, 2000)

The degree of ionisation of a two-dimensional electron-hole plasma is calculated in the low-density (Boltzmann) limit. The electron-hole interaction is considered for all states: optically active and inactive, bound and unbound. The theory is applied to exciton/free-carrier plasma in GaN-based quantum wells at room temperature.

Room-temperature operation of blue quantum-well lasers, based on GaN [1] or ZnSe [2], is no longer a novelty. However, the nature of lasing in wide-gap semiconductors and quantum wells has not yet been completely understood. The large exciton binding energy in wide-gap semiconductors and quantum wells favours excitonic gain processes for which no satisfactory theoretical treatment exists [3]. A knowledge of the balance between excitons and free carriers is crucial in determining the dominant gain process. It is known that a naive application of the Mott criterion for the metal-insulator transition as well as the use of a single-bound-state law of mass action are insufficient, as screening of excitons by the electron-hole plasma and strong scattering of particles within the plasma both play a crucial role [4].

For a consistent description of the electron-hole plasma at a temperature which is higher than the exciton binding energy, bound states and unbound scattering states should be treated on the same footing. In what follows we present such a consistent treatment for the purely two-dimensional (2D) case in the low-density (Boltzmann) limit.

Following an approach applied in 3D to nuclear matter [5], an ionic plasma [6], and the electron-hole system in excited semiconductors [4], we divide the total electron (hole) density between two terms,

$$n_a = n_a^0 + n_a^{\text{corr}}. \quad (1)$$

The first term n_a^0 is the density of uncorrelated quasiparticles with renormalized energies. Only this term should be taken for the screening radius calculation [4]. All correlation effects both in the bound and continuum states are incorporated into the second term n_a^{corr} which is called the correlated density. The lower index in Eq. (1) is a species index, $a = e$ for electrons and $a = h$ for holes.

In the low-density limit there is no need to go beyond two-particle correlations. This allows us to separate clearly the role of the inter-particle Coulomb interaction from the phase-space filling effects. It is tempting to relate n_a^{corr} and n_a^0 by a simple law of mass

action with the single exciton bound state energy reduced by screening [3, 7]. The main shortcoming of this approach is a disregard of the strong scattering of unbound carriers. A complete account of scattering states as well as all (optically active and inactive) bound states requires the calculation of a two-body partition function which involves summation over all two-particle states. In the low-density (non-degenerate) limit, for which there is no Pauli blocking, a 2D analogue of the modified mass action law reads

$$n_a^{\text{corr}} = \sum_b n_a^0 n_b^0 \frac{2\pi\hbar^2}{\mu_{ab} k_B T} Z_{ab}, \quad (2)$$

where $\mu_{ab} = m_a m_b / (m_a + m_b)$ is the reduced effective mass, and Z_{ab} is the two-body interaction part of the partition function. Note that due to charge-neutrality the total electron-hole density $n_e = n_h = n$ is independent of species, whereas $n_e^0 \neq n_h^0$ and $n_e^{\text{corr}} \neq n_h^{\text{corr}}$ if the electron and hole have different masses.

The electron-hole part of the partition function which exhibits bound states (excitons) is given by

$$Z_{eh} = \sum_{m,v} \exp(-\beta E_{m,v}) + \frac{1}{\pi} \int_0^\infty \left(\sum_{m=-\infty}^\infty \frac{d\delta_m(k)}{dk} \right) \exp\left(-\beta \frac{\hbar^2 k^2}{2\mu_{eh}}\right) dk, \quad (3)$$

where $\beta = 1/(k_B T)$, $m\hbar$ is the projection of the angular momentum onto the axis normal to the plane of 2D motion ($m = 0, \pm 1, \pm 2, \dots$), $\hbar^2 k^2 / 2\mu_{eh}$ is the energy of the relative motion of the unbound (scattered) electron and hole, k is the absolute value of the relative motion momentum, $\delta_m(k)$ are the 2D scattering phase shifts introduced in the standard way [8], $E_{m,v}$ are the bound-state energies (index v enumerates bound states with given m), and the double sum in the first term ranges only over bound states. Equation (3) is the 2D analogue of the Beth-Uhlenbeck formula [9], and it is derived [10] in the same fashion as in the 3D case [11]. The scattering term in the right-hand side of Eq. (3) gives the contribution to Z_{eh} of the electron-hole attraction in the continuum part of the energy spectrum. The electron-electron and hole-hole parts of the partition function Z_{ee} and Z_{hh} contain the scattering term only.

Equations (1) to (3) provide a consistent description of the ionisation degree, defined as $\alpha = n_e^0 / (n_e^0 + n_e^{\text{corr}})$. Technically the most difficult problem is to calculate the binding energies and scattering phase shifts in a screened Coulomb potential. We use for this purpose the variable-phase method [12] known from scattering theory. In this method the scattering phase shift and the function defining bound-state energies can be obtained as a large distance limit of the phase function, which satisfies the first-order, nonlinear Riccati equation originating from the radial Schrödinger equation.

In this paper we model the screened Coulomb interaction in a 2D plasma by the well-known Thomas-Fermi expression for a statically screened Coulomb potential [8],

$$V_s(\rho) = \mp \frac{e^2}{\epsilon} \int_0^\infty \frac{q J_0(q\rho)}{q + q_s} dq = \mp \frac{e^2}{\epsilon} \left\{ \frac{1}{\rho} - \frac{\pi}{2} q_s [\mathbf{H}_0(q_s \rho) - \mathbf{Y}_0(q_s \rho)] \right\}, \quad (4)$$

where q_s is the 2D screening wavenumber (which depends on temperature and carrier density), ϵ is the static dielectric constant of the semiconductor, $J_0(x)$, $\mathbf{Y}_0(x)$, and $\mathbf{H}_0(x)$ are the Bessel functions of the first and of the second kind and the Struve function. The upper sign in Eq. (4) is for electron-hole attraction, the lower sign is for electron-

electron or hole-hole repulsion. Being the long-wavelength static limit of the random phase approximation for a purely 2D case, Eq. (4) is the simplest model for the screened Coulomb potential in 2D. Nevertheless, this expression reflects the fact that the statically screened potential in 2D decreases at large distances slower than in the 3D case. Despite numerous realistic corrections, Eq. (4) remains the most widely used approximation for the 2D screening, especially for the screened exciton problem. The variable-phase method application to scattering and bound states in the screened Coulomb potential (4) is described in detail in our recent paper [13]. The method is especially effective for calculation of shallow-state binding energies and low-energy scattering phase shifts. Applying the variable phase method together with a 2D analogue of the Levinson's theorem [14], we have found that with decreasing q_s several bound states with different angular momenta appear simultaneously at certain integer values of $1/(q_s a^*)$, where a^* is the effective (excitonic) Bohr radius. This degeneracy is different from the well-known degeneracy of the unscreened 2D exciton states. In the low-density limit ($q_s a^* \rightarrow 0$) the number of bound states oscillates around $1/(q_s a^*)$ with the period and amplitude of oscillations proportional to $1/\sqrt{q_s a^*}$. Then, using the expression for the Thomas-Fermi 2D screening wavenumber q_s for a two-component non-degenerate electron-hole plasma [15], $q_s a^* = 4\pi(Ry^*/k_B T)(n_e^0 a^{*2} + n_h^0 a^{*2})$, Ry^* being the excitonic Rydberg, one can find the ratio of the free-carrier density to the total density. For a model semiconductor with $m_e = m_h$, this ratio is equal to 2/3 in the low-density limit. This result is different from the single-bound-state law of the mass action, which gives a complete ionisation of bound states ($\alpha \rightarrow 1$) in the same limit.

Figure 1 shows the results from the calculation of the electron-hole part of the partition function, Z_{eh} , which contains both the bound state sum and the scattering phase shift integral. In this figure Z_{eh} is plotted as a function of the inverse screening wave number $1/q_s$ measured in units of the effective Bohr radius a^* . The temperature is given in units of the bulk excitonic Rydberg Ry^* . To emphasize the role of scattering we show on the same plot the bound-state sum, $Z_{bound} = \sum_{m,v} \exp(-\beta E_{m,v})$, which exhibits jumps whenever new bound states appear. These jumps become higher with increasing screening length $1/q_s$ since several bound states appear simultaneously [13]. A proper account of scattering eliminates these unphysical jumps.

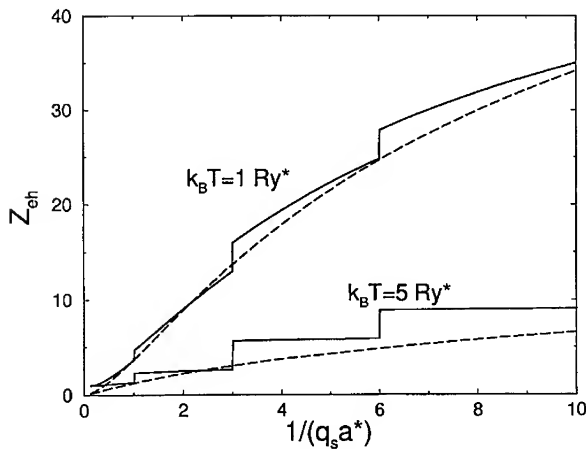


Fig. 1. The electron-hole part of the partition function, Z_{eh} versus the screening length $1/q_s$ for two values of $k_B T/Ry^*$. Solid lines show the bound state contributions Z_{bound} only. Dashed lines correspond to the total partition function with scattering states included

We calculated the density dependence of the degree of ionisation α in the 2D low-density (Boltzmann) limit for $k_B T = 1 \text{ Ry}^*$, which roughly corresponds to GaN at room temperature. Over a wide range of pair densities, $0.01 < na^{*2} < 0.1$, α is almost independent of density, and it increases outside this range. The minimal value of the degree of ionisation, $\alpha_{\min} \approx 0.34$, corresponds to $na^{*2} \approx 0.04$ ($n \approx 5 \times 10^{12} \text{ cm}^{-2}$ for GaN). Even at the relatively high densities of 10^{12} cm^{-2} we find that there is a single bound state having a binding energy of the order of $k_B T$ which is available to participate in excitonic lasing.

We also calculated the second virial coefficient of the dilute 2D electron-hole plasma in GaAs and GaN-based quantum wells at room temperature. These calculations show a striking difference between a nearly ideal electron-hole gas in GaAs and a strongly correlated exciton/free-carrier plasma in GaN. The calculation of optical gain in such a strongly-correlated plasma will be reported somewhere else.

References

- [1] S. NAKAMURA et al., Appl. Phys. Lett. **70**, 1417 (1997).
- [2] S. TANIGUCHI et al., Electron. Lett. **32**, 552 (1996).
- [3] I. GALBRAITH, in: Microscopic Theory of Semiconductors: Quantum Kinetics, Confinement and Lasers, Ed. S. W. KOCH, World Scientific Publ. Co., Singapore 1996 (p. 211), and references therein.
- [4] R. ZIMMERMANN and H. STOLZ, phys. stat. sol. (b) **131**, 151 (1985).
- [5] G. RÖPKE et al., Phys. Rev. Lett. **80**, 3177 (1998).
- [6] W.-D. KRAEFT, D. KREMP, W. EBELING, and G. RÖPKE, Quantum Statistics of Charged Particle Systems, Akademie-Verlag, Berlin 1986.
- [7] R. CINGOLANI et al., Phys. Rev. B **54**, 17812 (1996).
- [8] F. STERN and W. E. HOWARD, Phys. Rev. **163**, 816 (1967).
- [9] E. BETH and G. E. UHLENBECK, Physica (Amsterdam) **4**, 915 (1937).
- [10] M. E. PORTNOI and I. GALBRAITH, Phys. Rev. B **60**, 5570 (1999).
- [11] L. D. LANDAU and E. M. LIFSHITZ, Statistical Physics, Pt. 1, Pergamon Press, New York 1980 (p. 236).
- [12] F. CALOGERO, Variable Phase Approach to Potential Scattering, Academic Press, New York 1967.
- [13] M. E. PORTNOI and I. GALBRAITH, Solid State Commun. **103**, 325 (1997).
- [14] N. LEVINSON, Kong. Danske Vid. Selsk., Mat.-Fys. Medd. **25**, 3 (1949).
- [15] J. LEE, H. N. SPECTOR, and P. MELMAN, J. Appl. Phys. **58**, 1893 (1985).

phys. stat. sol. (a) **183**, 91 (2001)

Subject classification: 71.35.Fg; 78.55.Cr; 78.67.De; S7.14

Impact of Internal Electric Field and Localization Effect on Quantum Well Excitons in AlGa_N/Ga_N/InGa_N Light Emitting Diodes

S.F. CHICHIBU¹) (a), T. SOTA (b), K. WADA (c), O. BRANDT (d), K.H. PLOOG (d), S.P. DENBAARS (e), and S. NAKAMURA²) (f)

(a) *Institute of Applied Physics, University of Tsukuba, 1-1-1 Tennodai, Tsukuba, Ibaraki 305-8573, Japan*

(b) *Department of Electrical, Electronics, and Computer Engineering, Waseda University, 3-4-1 Ohkubo, Shinjuku, Tokyo 169-8555, Japan*

(c) *Department of Materials Science and Engineering, Massachusetts Institute of Technology, 77 Massachusetts Avenue, Cambridge, MA 02139, USA*

(d) *Paul-Drude-Institut für Festkörperelektronik, Hausvogteiplatz 5-7, D-10117 Berlin, Germany*

(e) *Department of Materials Engineering, University of California, Santa Barbara, CA 93106, USA*

(f) *Department of Research and Development, Nichia Chemical Industries Ltd., 491 Oka, Kaminaka, Anan, Tokushima 774-8601, Japan*

(Received October 8, 2000)

Strained In_xGa_{1-x}N quantum wells (QWs) on thick GaN base layers were investigated to verify the importance of localized QW excitons in their spontaneous emission mechanisms. A strength of the internal piezoelectric field (F_{PZ}) across the QW increases with increasing x up to 1.4 MV/cm for $x = 0.25$, since the in-plane strain increases. For the QWs with the well thickness L greater than 3 nm, F_{PZ} dominates the emission peak energy due to the quantum-confined Stark effect. Absorption spectra of both hexagonal and cubic InGa_N QWs exhibited a broad band-tail regardless of the presence of F_{PZ} normal to the QW plane. The luminescence peak energy of the 3 nm thick QWs was higher than the bandgap energy of the unstrained bulk crystal for $x < 0.15$, showing that doping of Si in barriers or injection of carriers effectively screens the field. The emission lifetime increased with increasing monitoring wavelength. Also, a temperature-induced change in the luminescence peak energy decreased with increasing x . The real-space variation of the luminescence peak energy was confirmed by the spatially-resolved monochromatic cathodoluminescence mapping method. The localization depth increases with increasing x . The carrier localization is confirmed to originate from the effective bandgap inhomogeneity due to a fluctuation of the local InN mole fraction, which is enhanced by the large and composition-dependent bowing parameter of InGa_N material.

1. Introduction InGa_N alloys are attracting special interest because they serve as active regions of UV and visible quantum-well (QW) structure light-emitting diodes

¹) Corresponding author; Tel.: +81(298) 53-5289; Fax: +81(298) 53-5205; e-mail: chichibu@bk.tsukuba.ac.jp

²) Present address: Department of Materials Engineering, University of California, Santa Barbara, CA 93106, USA.

(LEDs) [1–3] and purplish-blue QW laser diodes (LDs) [1, 2]. Blue, bluish-green, green, and white InGaN single-quantum-well (SQW) LEDs have already been commercialized and amber and red LEDs were made recently [3]. However, hexagonal (h-) $\text{In}_x\text{Ga}_{1-x}\text{N}$ visible LEDs in general have two disadvantages. One is the blueshift of the emission peak by the increase of the forward current. The other is that external quantum efficiency η_{ext} first increases with increasing emission wavelength (InN mole fraction x) from 360 nm (GaN) to 380 nm then levels off at 19% around 450–500 nm. However, η_{ext} decreases steeply with further increase of the emission wavelength longer than 530 nm, i.e. x greater than 20%. These two factors are considered to be due to a presence of large internal piezoelectric field (F_{PZ}) normal to the QW plane [4], i.e. quantum-confined Stark effects (QCSE). Nevertheless, $\text{In}_x\text{Ga}_{1-x}\text{N}$ QW LEDs exhibit bright emission in spite of the presence of huge amount of threading dislocations (TDs) up to 10^{10} cm^{-2} . Therefore, it is important to clarify what dominates the emission mechanisms in InGaN QW LEDs and LDs in order to find the way to obtain improved device performances. Static, modulated, and time-resolved spectroscopies were carried out for both h- and cubic (c-) phase $\text{In}_x\text{Ga}_{1-x}\text{N}$ QWs having various well thicknesses L and InN mole fraction x to explore the reason why InGaN devices emit bright luminescences. The importance of quantum confinement and quantum-disk (Q-disk) size [5] band-tail states where localized QW excitons [6, 7] recombine radiatively is described.

2. Experimental Three sets of samples were investigated. One was a series of multiple-quantum-wells (MQWs) with 14 periods of h- $\text{In}_{0.10}\text{Ga}_{0.90}\text{N}$ wells and GaN barriers grown on thick GaN base on sapphire (0001) substrates by metalorganic vapor phase epitaxy (MOVPE). The well thickness L was varied from 1.2 to 6 nm. The second set contained MQW structures and LED device wafers having a 3 nm thick $\text{In}_x\text{Ga}_{1-x}\text{N}$ SQW or a MQW grown on sapphire by MOVPE [1, 3, 8]. The InN mole fraction was varied from nearly zero (ultraviolet LED: 0.02) to 0.25 (amber LED) [8]. In these two sets, hexagonal InGaN QWs were confirmed to be strained using an X-ray reciprocal mapping of thick InGaN layers and transmission electron diffraction observation at the well/barrier interfaces. The InN mole fraction was calculated using the values of elastic stiffness constants and lattice constants that were estimated by linear interpolation of those in GaN and InN. For some samples x was measured directly by nanometer-probe compositional analysis using a KEVEX DELTA energy dispersive X-ray microanalysis (EDX) equipped on HB501 field emission scanning TEM. The probe diameter was 1 nm and the compositional resolution was better than a few percent. The third set was c- $\text{In}_{0.5}\text{Ga}_{0.5}\text{N}$ MQW structure with 4 periods of 6 nm thick c- $\text{In}_{0.5}\text{Ga}_{0.5}\text{N}$ wells and 4 nm thick c-GaN barriers, which was grown by RF plasma gas source molecular beam epitaxy on a c-GaN template [9]. This sample was prepared to eliminate the effect of F_{PZ} , which is parallel to the QW normal, and localization effect due to well thickness fluctuation in QWs on the optical properties of InGaN material.

3. Results and Discussion At first, static photoluminescence (PL), photoluminescence excitation (PLE), and time-resolved photoluminescence (TRPL) signal from the $\text{In}_{0.10}\text{Ga}_{0.90}\text{N}$ MQW structures were measured as a function of L [10]. It was demonstrated that QCSE controlled the PL peak energy under low excitation conditions especially for L larger than 3 nm. Indeed, the PL peak shifted to higher energy under high excitation conditions. However, the amount of the shift is remarkably small for thinner

wells, and high excitation PL peak energies nearly agreed with the low excitation ones for $L < 3$ nm. The high excitation PL peak energies were smaller than the average bandgap of the wells, which was defined as the energy where the broad PLE signal became half the maximum. In this case, the Stokes-like shift was nearly constant at 50 meV for $L < 3.5$ nm at 300 K. Note that this thickness corresponds to the free exciton effective Bohr radius a_B . The emission decay lifetime also decreased with decreasing L from 6.2 to 3 nm, showing that the effect of the electron-hole (e-h) wavefunction separation was relaxed for the wells with L smaller than 3 nm in case of $\text{In}_{0.10}\text{Ga}_{0.90}\text{N}$ QWs. The strength of F_{PZ} was estimated by calculating confined energy levels and wavefunctions in the $\text{In}_{0.10}\text{Ga}_{0.90}\text{N}$ wells as functions of F , L , and doping density n in the barriers by variational method neglecting exciton binding energy within the Hartree approximation solving the Schrödinger equation and Poisson equation simultaneously and self-consistently. The value of F_{PZ} was estimated to be about 350–400 kV/cm, which nearly agreed with previous reports [11].

To evaluate the balance between the field effect and localization effect, both of which change with the InN mole fraction x , static and dynamic optical processes in a series of device-grade 3 nm thick $\text{In}_x\text{Ga}_{1-x}\text{N}$ QWs were investigated. PL spectra at 300 K are shown in Fig. 1 as a function of x . As shown, the PL peak shows the redshift and the full width at half maximum (FWHM) increases simultaneously with increasing x . The PL peak energy and average bandgap of the well, the latter was obtained by absorption-type measurements like either PLE or photovoltaic (PV), are plotted as a function of x in Fig. 2. The bandgap energy of unstrained bulk $\text{In}_x\text{Ga}_{1-x}\text{N}$ alloys, which was calculated using the equation

$$E_g(x) = 3.42x + 1.89(1 - x) - b(x)x(1 - x), \quad (1)$$

where $E_g(x)$ is the energy gap and $b(x)$ is the composition-dependent bowing parameter of $\text{In}_x\text{Ga}_{1-x}\text{N}$ [12], is also plotted in Fig. 2. It should be noted that the energy gap of $\text{In}_x\text{Ga}_{1-x}\text{N}$ alloys cannot be fitted by quadratic dependence on x . [12]. The absorption edge of the $\text{In}_x\text{Ga}_{1-x}\text{N}$ QWs for $x < 0.15$ is remarkably higher than the bulk band-

gap. This is reasonable since both the compressive biaxial strain in InGaN and the quantum size effect increase the bandgap, and the effect of F_{PZ} is not so serious for the QWs with $x = 0.10$ and $L < 3$ nm [10]. The emission peak energy is higher than the bulk bandgap for $x < 0.12$. However, it is clear that the emission peak energy from the QWs is smaller than the bulk bandgap for $x > 0.15$, indicating that F_{PZ} plays a certain role in the wells with $x > 0.15$ even for $L = 3$ nm. Note that $x = 0.15$ corresponds to the practical blue SQW LEDs.

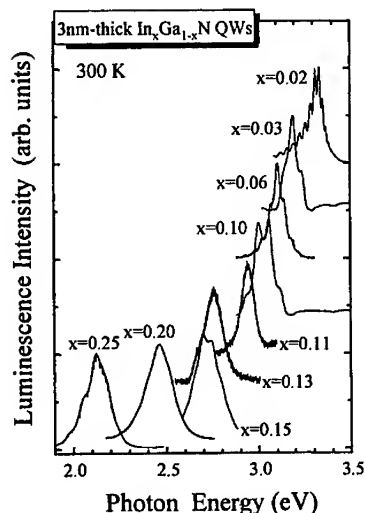


Fig. 1. PL spectra of 3 nm thick $\text{In}_x\text{Ga}_{1-x}\text{N}$ QWs at 300 K as a function of InN mole fraction x

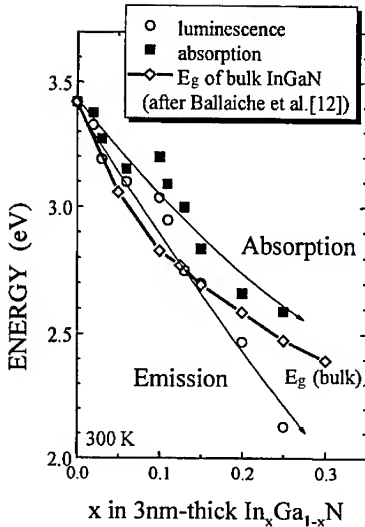


Fig. 2. Emission and absorption edge energies of 3 nm thick $\text{In}_x\text{Ga}_{1-x}\text{N}$ QWs. The bandgap of unstrained bulk InGaN estimated after Ref. [12] is also plotted

The FWHM of the PL, Stokes-like shift, and emission decaytime of the 3 nm thick $\text{In}_x\text{Ga}_{1-x}\text{N}$ QWs are summarized as a function of x in Fig. 3. Indeed the Stokes-like shift and the emission decaytime increase more rapidly for $x > 0.15$. This may be due to the reduction of e-h wavefunction overlap due to strong F_{PZ} in the QWs.

In order to estimate the *effective* field in the QWs, PL spectra of the 3 nm thick $\text{In}_x\text{Ga}_{1-x}\text{N}$ SQWs with $x = 0.20$ and 0.25 were measured as a function of external bias [6, 13]. The PL from the QWs was excited by the 457.9 and 488.0 nm line of a cw Ar^+ laser for $x = 0.20$ [6] and $x = 0.25$ [13], respectively, to selectively excite the well. Takeuchi et al. [14] have also used this method later to determine the direction and strength of F_{PZ} in $\text{In}_{0.16}\text{Ga}_{0.84}\text{N}$ QWs, and have found a blueshift of the PL peak with increasing reverse bias. Their conclusion that F_{PZ} pointed from the surface to the substrate seemed to be valid considering a Ga-face growth during MOVPE. The PL peak shift for $x = 0.20$ was so small that we could not determine the energy shift. The result meant that most of F_{PZ} was effectively screened by doped impurities in GaN and AlGaIn barriers [6] for $x = 0.20$ in our case. The PL peak of $x = 0.25$ shifted to the higher energy by up to 110 meV by changing the external bias from +2 to -10 V [13]. By solving again the Schrödinger equation and Poisson equation simultaneously and self-consistently to fit the peak energy shift, the value of $F_{PZ} = 1.4$ MV/cm was obtained for $x = 0.25$. The value is close to the one estimated from the strain and piezoelectric constants reported by Wetzel et. al. [11]. The strength of F_{PZ} in $\text{In}_x\text{Ga}_{1-x}\text{N}$ QWs is plotted as a function of x in Fig. 4. As shown, F_{PZ} naturally increases monotonically with increasing x . The value of F_{PZ}

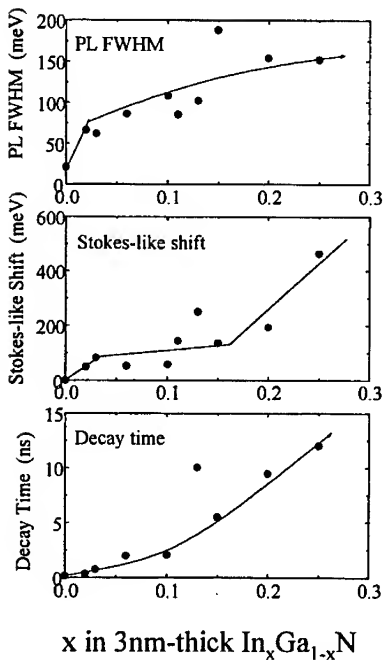


Fig. 3. FWHM of the PL, Stokes-like shift, and emission decaytime of 3 nm thick $\text{In}_x\text{Ga}_{1-x}\text{N}$ QWs as a function of x . All values are at 300 K

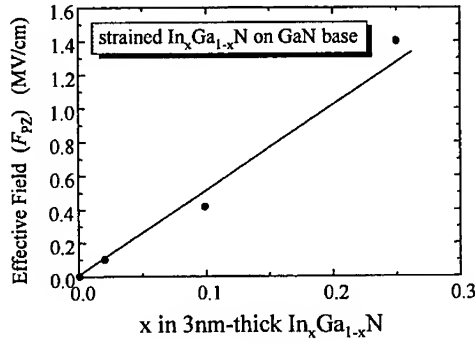


Fig. 4. Estimated effective field (F_{PZ}) in $\text{In}_x\text{Ga}_{1-x}\text{N}$ QWs

for the 3 nm thick $\text{In}_{0.15}\text{Ga}_{0.85}\text{N}$ QWs (critical $x = 0.15$ described above) is nearly 800 kV/cm. For $F_{PZ} = 800$ kV/cm, the potential drop across the 3 nm thick QW is 240 meV, and it increases with increasing x . The energy gap of bulk $\text{In}_{0.15}\text{Ga}_{0.85}\text{N}$ is calculated to be [12] 2.69 eV. Then the valence band discontinuity ΔE_V and conduction band discontinuity ΔE_C between the $\text{In}_{0.15}\text{Ga}_{0.85}\text{N}$ well and GaN barriers (3.42 eV) are estimated to be 548 and 183 meV, respectively, under the assumption that the ratio of ΔE_C and ΔE_V is 3:1. Then the potential drop is larger than ΔE_V and nearly half of ΔE_C , which corresponds to the pronounced CASE II in Ref. [10]. Therefore the effect of e-h wavefunction separation become serious for $x > 0.15$ for the 3 nm thick $\text{In}_x\text{Ga}_{1-x}\text{N}$ QWs.

The presence of both F_{PZ} and large density of TDs are only disadvantageous to obtain efficient emission from the QWs [6, 10, 11, 13–15]. However, η_{ext} of the practical blue ($x = 0.15$) and green ($x = 0.20$) SQW LEDs are as high as 19%. Therefore, $\text{In}_x\text{Ga}_{1-x}\text{N}$ QWs should have another dominant mechanism to obtain such η_{ext} . One is the quantum confinement [6], since the well thickness of 3 nm is smaller than a_B in bulk InGaIn. The other has been proposed to be a localization of QW excitons [1, 6, 7, 10, 13]. As a matter of fact, the PL lifetime of 2.5 nm thick $\text{In}_{0.06}\text{Ga}_{0.94}\text{N}$ MQW exhibits an increasing decay time with decreasing detection photon energy, as shown in Fig. 5. In this case, L and x are as small as 2.5 nm and 0.06, respectively, thus $F_{PZ} < 300$ kV/cm and the change in the lifetime in Fig. 5 can be attributed to nearly pure localization of QW excitons [16]. From the fitting curve based on the weak exciton localization model [17], the depth of the localized states (E_0 value) is estimated to be 35 meV.

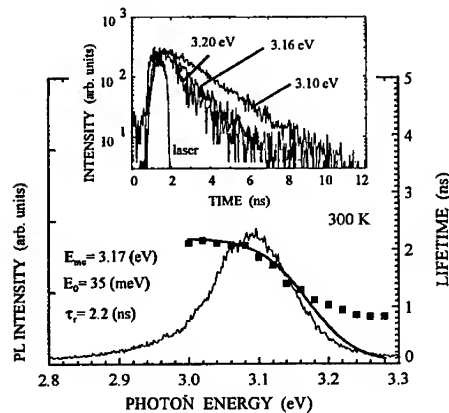


Fig. 5. Time-integrated PL spectrum and the emission lifetime as a function of detection photon energy at 300 K of $\text{In}_{0.06}\text{Ga}_{0.94}\text{N}$ MQW structure. The inset shows the PL intensity as a function of time after excitation

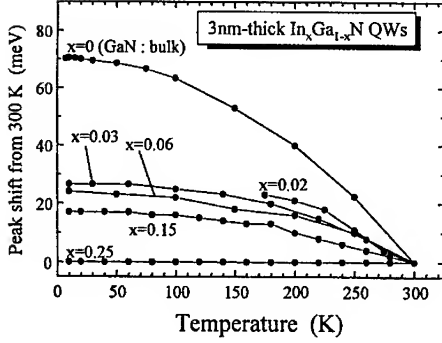


Fig. 6. Luminescence peak energy shift against that of 300 K for 3 nm thick $\text{In}_x\text{Ga}_{1-x}\text{N}$ QWs as a function of temperature

Similarly, E_0 is estimated to be 60 meV for $x = 0.13$ [18] and 120 meV for $x = 0.25$ [13]. The presence of these band-tail type localized states gives rise to a weakening of the temperature-induced change in emission peak energy, as shown in Fig. 6. In Fig. 6, energy shifts of the emission peak against that of 300 K for the 3 nm thick $\text{In}_x\text{Ga}_{1-x}\text{N}$ QWs are plotted as a function of temperature. Obviously, the luminescence energy shift decreases with increasing x , which implies the increase of the localization depth.

The depth of localization of the 3 nm thick QWs is plotted as a function of x in Fig. 7. The external quantum efficiency η_{ext} of corresponding SQW LEDs and the PL intensity ratio of the QWs at 300 K against that of 10 K (a measure of the internal quantum efficiency η_{int}) are also shown in Fig. 7. As shown, E_0 increases abruptly for very small x of 0.02 then increases gradually with x . Simultaneously, both η_{ext} and η_{int} increase rapidly for small x . This means that doping of In in GaN matrix drastically changes the electronic states [12] and carriers are localized at certain potential minima [6, 10] in the QWs due to the large and composition dependent $b(x)$ of $\text{In}_x\text{Ga}_{1-x}\text{N}$ alloys. Note that η decreases for $x > 0.2$, which may be due to F_{PZ} in the 3 nm thick QWs or simply to a degradation of the crystal quality.

The lateral size of the potential minima was estimated using spatially-resolved monochromatic cathodoluminescence (CL) mapping method to be smaller than 50 nm for $x = 0.10$ and 0.02 SQWs [6, 19], in which spatial inhomogeneity of the CL peak was observed and the quasi diffusion length was estimated. Note that structures with the lateral size between a_B and exciton resonance wavelength (emission wavelength divided by the refractive index) embedded in QWs are defined as Q-disks [5].

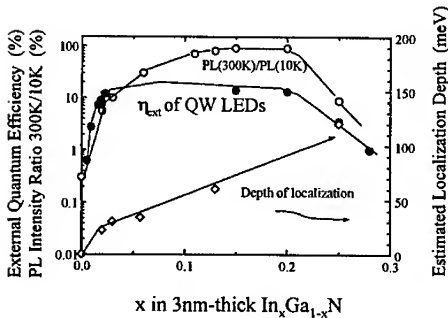


Fig. 7. Depth of localization, η_{ext} , and PL intensity ratio of the 3 nm thick $\text{In}_x\text{Ga}_{1-x}\text{N}$ QWs at 300 K against 10 K as a function of x

To prove that the tail states are originated from In compositional inhomogeneity, optical absorbance and PL spectra of c-In_{0.5}Ga_{0.5}N/c-GaN MQW [9] at 300 K were measured [19]. It has been revealed that c-In_{0.5}Ga_{0.5}N MQW exhibited a broad band-tail energetically lower than the c-GaN bandgap, and a broad PL band located in the band-tail. The results were similar to those obtained from thick c-InGaIn epilayers [9, 20]. Note that in c-InGaIn/GaN system, spontaneous polarization does not exist due to the crystal symmetry and the direction of F_{PZ} is not normal to the QW plane thus e-h separation at opposite sides of the well/barrier interfaces does not occur. Though the growth methods are not identical and the QW thickness fluctuation is not the same as in the hexagonal samples, the results confirmed the presence of localized energy tail states in In_xGa_{1-x}N QWs regardless of F_{PZ} .

4. Conclusions The spontaneous emission from strained In_xGa_{1-x}N QWs was verified to originate from the recombination of QW excitons localized at Q-disk size potential minima, which was formed due to the InN mole fraction fluctuation enhanced by the large and composition dependent bowing parameter of InGaIn alloys. F_{PZ} dominated the emission peak energy through QCSE especially for the thicker QWs with $L > 3.5$ nm and the 3 nm thick QWs with $x > 0.15$. The localized states were formed both in h- and c-InGaIn alloys regardless of the presence of F_{PZ} normal to the QW plane.

Acknowledgements The authors are grateful to Professor Fumio Hasegawa for continuous encouragements. This work was supported in part by Ministry of Education, Science, Sports, and Culture of Japan (Grant-in-Aid for Scientific Research #11750268), Ogasawara Foundation for the Promotion of Science & Engineering, Bundesministerium für Forschung und Bildung (BMBF) of the Federal Republic of Germany, Office of Naval Research (Dr. Colin Wood), and Air Force Office of Scientific Research (Dr. Jerry Witt).

References

- [1] S. NAKAMURA and G. FASOL, *The Blue Laser Diode*, Springer-Verlag, Berlin 1997.
- [2] I. AKASAKI and H. AMANO, *Jpn. J. Appl. Phys.* **36**, 5393 (1997).
- [3] T. MUKAI, M. YAMADA, and S. NAKAMURA, *Jpn. J. Appl. Phys.* **38**, 3976 (1999).
- [4] T. TAKEUCHI, H. TAKEUCHI, S. SOTA, H. SAKAI, H. AMANO, and I. AKASAKI, *Jpn. J. Appl. Phys.* **36**, L177 (1997).
- [5] M. SUGAWARA, *Phys. Rev. B* **51**, 10743 (1995).
- [6] S. CHICHIBU, T. AZUHATA, T. SOTA, and S. NAKAMURA, *Appl. Phys. Lett.* **69**, 4188 (1996).
S. CHICHIBU, K. WADA, and S. NAKAMURA, *Appl. Phys. Lett.* **71**, 2346 (1997).
S. CHICHIBU, T. SOTA, K. WADA, and S. NAKAMURA, *J. Vac. Sci. Technol. B* **16**, 2204 (1998).
S. F. CHICHIBU, T. SOTA, K. WADA, S. P. DENBAARS, and S. NAKAMURA, *MRS Internet J. Nitride Semicond. Res.* **4S1**, G2.7 (1999).
- [7] E. JEON, V. KOZLOV, Y. SONG, A. VERTIKOV, M. KUBALL, A. NURMIKKO, H. LIU, C. CHEN, R. KERN, C. KUO, and M. CRAWFORD, *Appl. Phys. Lett.* **69**, 4194 (1996).
Y. NARUKAWA, Y. KAWAKAMI, M. FUNATO, S. FUJITA, S. FUJITA, and S. NAKAMURA, *Appl. Phys. Lett.* **70**, 981 (1997).
C. KISIELOWSKI, Z. LILIENTAL-WEBER, and S. NAKAMURA, *Jpn. J. Appl. Phys.* **36**, 6932 (1997).
W. SHAN, W. WALUKIEWICZ, E. E. HALLER, B. D. LITTLE, J. J. SONG, M. D. MCCLUSKEY, N. M. JOHNSON, Z. C. FENG, M. SCHUMAN, and R. A. STALL, *J. Appl. Phys.* **84**, 4452 (1998).
P. ELISEEV, P. PERLIN, J. LEE, and M. OSINSKI, *Appl. Phys. Lett.* **71**, 569 (1997).
- [8] T. MUKAI, H. NARIMATSU, and S. NAKAMURA, *Jpn. J. Appl. Phys.* **37**, L479 (1998).

- [9] O. BRANDT, J. MÜLLHÄUSER, A. TRAMPERT, and K. H. PLOOG, *Mater. Sci. Engng. B* **59**, 73 (1999).
- [10] S. CHICHIBU, A. ABARE, M. MINSKY, S. KELLER, S. FLEISCHER, J. BOWERS, E. HU, U.K. MISHRA, L.A. COLDREN, S.P. DENBAARS, and T. SOTA, *Appl. Phys. Lett.* **73**, 2006 (1998).
S. CHICHIBU, A. ABARE, M. MACK, M. MINSKY, T. DEGUCHI, D. COHEN, P. KOZODOY, S. FLEISCHER, S. KELLER, J. SPECK, J.E. BOWERS, E. HU, U.K. MISHRA, L.A. COLDREN, S.P. DENBAARS, K. WADA, T. SOTA, and S. NAKAMURA, *Mater. Sci. Engng. B* **59**, 298 (1999).
- [11] C. WETZEL, T. TAKEUCHI, H. AMANO, and I. AKASAKI, *J. Appl. Phys.* **85**, 3786 (1999).
- [12] L. BELLAICHE, T. MATTILA, L.-W. WANG, S.-H. WEI, and A. ZUNGER, *Appl. Phys. Lett.* **74**, 1842 (1999).
- [13] S.F. CHICHIBU, T. AZUHATA, T. SOTA, T. MUKAI, and S. NAKAMURA, *J. Appl. Phys.* **88** (2000). (11/15 issue, in press).
- [14] T. TAKEUCHI, C. WETZEL, S. YAMAGUCHI, H. SAKAI, H. AMANO, I. AKASAKI, Y. KANEKO, S. NAKAGAWA, Y. YAMAOKA, and N. YAMADA, *Appl. Phys. Lett.* **73**, 1691 (1998).
- [15] J. IM, H. KOLLMER, J. OFF, A. SOHMER, F. SCHOLZ, and A. HANGLEITER, *Phys. Rev. B* **57**, R9435 (1998).
B. GIL, P. LEFEBVRE, J. ALLÈGRE, H. MATHIEU, N. GRANDJEAN, M. LEROUX, J. MASSIES, P. BIGENWALD, and P. CHRISTOL, *Phys. Rev. B* **59**, 10246 (1999).
- [16] D.A. MILLER, D.S. CHEMLA, T.C. DAMEN, A.C. GOSSARD, W. WIEGMANN, T.H. WOOD, and C.A. BURRUS, *Phys. Rev. Lett.* **53**, 2173 (1984); *Phys. Rev. B* **32**, 1043 (1985).
- [17] F. YANG, M. WILKINSON, E. AUSTIN, and K. O'DONNELL, *Phys. Rev. Lett.* **70**, 323 (1993).
- [18] S.F. CHICHIBU, H. MARCHAND, M.S. MINSKI, S. KELLER, P.T. FINI, J. IBBETSON, S.B. FLEISCHER, J.S. SPECK, J.E. BOWERS, E. HU, U.K. MISHRA, S.P. DENBAARS, T. DEGUCHI, T. SOTA, and S. NAKAMURA, *Appl. Phys. Lett.* **74**, 1460 (1999).
- [19] S.F. CHICHIBU, K. WADA, J. MÜLLHÄUSER, O. BRANDT, K.H. PLOOG, T. MIZUTANI, A. SETOGUCHI, R. NAKAI, M. SUGIYAMA, H. NAKANISHI, K. TORII, T. DEGUCHI, T. SOTA, and S. NAKAMURA, *Appl. Phys. Lett.* **76**, 1671 (2000).
- [20] J. HOLST, A. HOFFMANN, I. BROSER, D. RUDLOFF, F. BERTRAM, T. RIEMANN, J. CHRISTEN, T. FREY, D.J. AS, D. SCHIKORA, and K. LISCHKA, *phys. stat. sol. (b)* **216**, 471 (1999).
J. HOLST, A. HOFFMANN, D. RUDLOFF, F. BERTRAM, T. RIEMANN, J. CHRISTEN, T. FREY, D.J. AS, D. SCHIKORA, and K. LISCHKA, *Appl. Phys. Lett.* **76**, 2832 (2000).

phys. stat. sol. (a) **183**, 99 (2001)

Subject classification: 68.65.Hb; 78.67.Hc; S7.14

Optical and Structural Properties of Quantum Dots in Wide-Bandgap Semiconductors

M. STRASSBURG, A. HOFFMANN, I. L. KRESTNIKOV¹), and N. N. LEDENTSOV¹)

Institut für Festkörperphysik, Technische Universität Berlin, Germany

Tel.: +49-30-31422054, Fax: +49-30-31422064, e-mail: marburg@physik.tu-berlin.de

(Received October 8, 2000)

The optical and structural properties of ultrathin insertions in wide-bandgap semiconductors are studied. Structural investigations confirm that in nitride-based structures indium fluctuations lead to the formation of nano-islands. The zero-dimensional character in nitride- and II–VI-based quantum dot structures is demonstrated by its typical behaviour (splitting of the polarisation, optical gain mechanisms resulting from localised states, surface lasing without high-quality Bragg reflectors, etc.). Practical device applications of the structures based on ultrathin insertions for non-traditional devices are discussed.

Introduction For the fabrication wide-bandgap quantum dots (QDs) several selforganized growth approaches may be applied: islands can be formed by heteroepitaxial submonolayer deposition, by spinodal decomposition of a multi-component alloy, via Stranski-Krastanow (SK) or Volmer-Weber (VW) island growth mode, by growth on faceted or step-bunched surfaces, etc. [1–5]. Especially in ternary compounds based on InGa_N and CdZnSe interdiffusion and segregation influence strongly the formation of nano-islands. Consequently, similar approaches are applied for the growth of QD structures. Appropriate growth conditions, e.g. ultrathin (submonolayer and a few monolayer) insertions, lead to dense arrays of flat two-dimensional nano-islands with a lateral size comparable or much smaller than the exciton Bohr radii. In spite of the relatively small size of the islands, the QD characteristics are proven by direct observation of luminescence lines from single QDs up to elevated observation temperatures, by excitonic gain and by lateral squeezing of excitons revealed in magneto-optical studies [6]. The aim of the present paper is to show that group III nitrides became attractive candidates for the application of ultrathin insertions. Such insertions have already applied to the group III nitrides [7] and enabled gain in the green spectral range in InGa_N/Ga_N structures [8].

Experimental For the investigation of II–VI quantum dot structures samples were grown by molecular beam epitaxy (MBE). Further details of the growth are given in Ref. [9]. The nitride-based structures were grown in a horizontal flow MOVPE growth machine. To form nucleation layer, low-temperature AlGa_N deposition was applied. Ga_N and AlGa_N layers were grown at 1050 °C with H₂ carrier gas and at the total pressure of 200 mbar. For the growth of the InGa_N-based active region the temperature was reduced. The total pressure was 600 mbar and argon was used as carrier gas [10].

¹) Also at A. F. Ioffe Institute, St. Petersburg, Russia

The samples were studied by transmission electron microscopy (TEM) in plan-view and cross-section geometry using a Philips CM 200 FEG/ST electron microscope with an electron energy of 200 keV and a Scherzer resolution of 0.24 nm. For the optical investigations the samples were mounted in a He-flow cryostat providing temperatures between 4 and 300 K. The photoluminescence (PL) was excited by the 325 nm line of a cw He–Cd laser. Optical reflection (OR) spectra were recorded at normal incidence using a tungsten lamp dispersed by a double monochromator. For the high excitation density measurements pulsed excimer and nitrogen lasers were used. Luminescence was detected by a photomultiplier attached to a 0.85 m double monochromator.

Results and Discussion For the CdSe/ZnSe system the formation of nano-islands by the deposition of ultrathin insertions is confirmed by MOVPE and MBE grown samples. Their zero-dimensional character is proven by structural and optical investigations [6]. E.g., the polarisation of the PL in edge geometry enables a clear distinction between the quantum wells (QW) and QD cases. According to Kane's selection rule, the heavy-hole exciton luminescence in zinc-blende QWs grown on a high-symmetry (100) surface must be completely TE polarised as it was experimentally confirmed in numerous studies. In contrast, for spherical QDs no polarisation of the QD emission in edge geometry can be expected. As the CdSe nano-islands keep essentially a two-dimensional shape, the quantization in growth direction prevails, and the heavy-hole-like QD exciton luminescence in edge geometry is still TE-polarized. However, in contrast to the QW case, a significant contribution of the TM-polarised emission has been observed (Fig. 1). This underlines the role of the lateral exciton confinement. The most remarkable observation has been done however for the edge emission of vertically coupled QDs. This emission was found to be predominantly TM polarized. This indicates that the heavy-hole-like exciton wavefunction was more extended in the growth direction and, most probably, had a cylindrical shape. A similar polarisation of edge emission has been observed in the case of vertically coupled InGaAs–GaAs Stranski-Krastanow QDs [11].

While a lot of publications are available about II–VI wide-bandgap semiconductor quantum dots, in the case of the InGaN/GaN system the formation of quantum dots by ultrathin insertions is not so widely discussed. Fig. 2 shows the high-resolution (HR) TEM image of a InGaN/GaN multilayer structure, and the digital analyses of lattice images (DALI [13]). With respect to the investigations of similar II–VI QD structures, evaluation procedures have to be applied to reveal the nano-islands formed by ultrathin insertions in

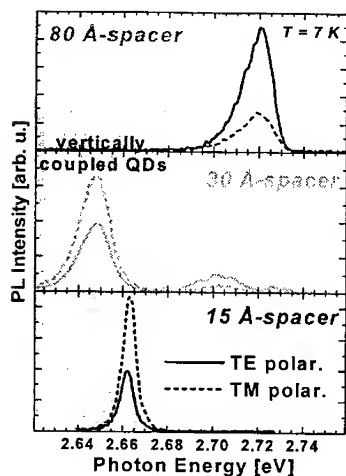


Fig. 1. Polarisation-dependent PL spectra of CdSe/ZnSe multilayer structures as a function of the thickness of the ZnSe spacer between adjacent CdSe layers. The polarisation splitting indicates the zero-dimensional character of the emission centres

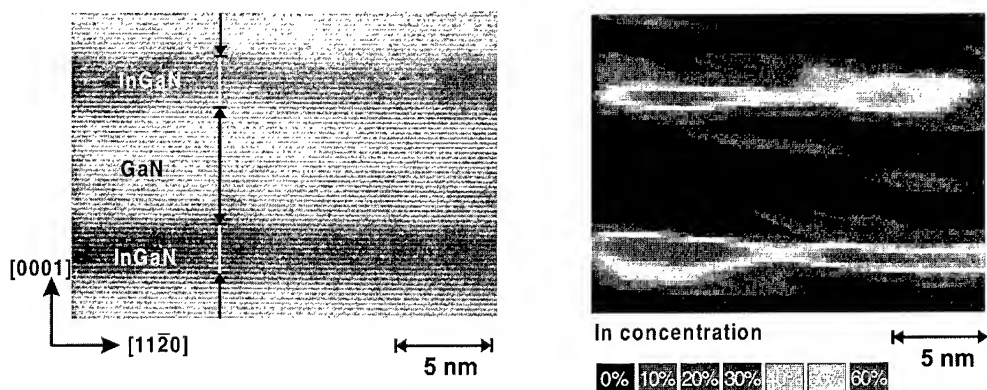


Fig. 2. High-resolution transmission electron microscopy image (left) and DALI evaluation (right) to reveal the indium distribution in an InGaN/GaN multi-quantum-well structure. The indium concentration is scaled from 0% to 60% (stepwidth: 10%) [12]

the InGaN/GaN system, too. These investigations support that the indium distribution is not homogeneous in the deposited layer and undergoes remarkable lateral variation. Areas with an indium content of up to 60% and a lateral size of 3–10 nm are revealed. A dense array (10^{18} cm^{-3}) of such nano-islands implicates a large potential for vertical cavity surface emitting laser (VCSEL) due to their enormous optical gain up to several 10^5 cm^{-1} .

Optical transmission, PL and stimulated emission recorded perpendicular to the surface at 16 K are shown in Fig. 3. The absorption in the active region (InGaN/GaN superlattice) leads to a decrease of the transmitted light at $\sim 3.0 \text{ eV}$, which is suppressed for light energies above the GaN bandgap. In comparison to the transmission spectrum the maximum of the PL band is shifted to lower energies. The shape of the emission band with extended tails on the low and the high energy side and the pronounced red-shift suggest the presence of indium-rich areas with a significant size and composition dispersion. Both were revealed in HRTEM investigations and DALI evaluation (compare Fig. 2). At higher excitation densities, the maximum of the PL band shifts to higher energies and a narrowing was observed. As it is shown in the inset of Fig. 3, the

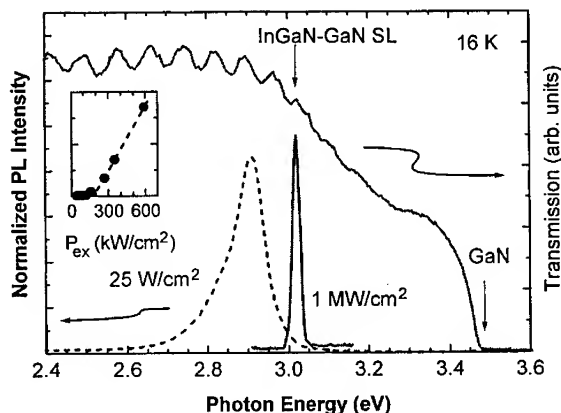


Fig. 3. Transmission and photoluminescence (PL) spectra of an InGaN/GaN multilayer structure. The absorption edges of GaN and the InGaN/GaN superlattice are marked by arrows. In the inset the integrated PL intensity as a function of the excitation density is depicted [10]

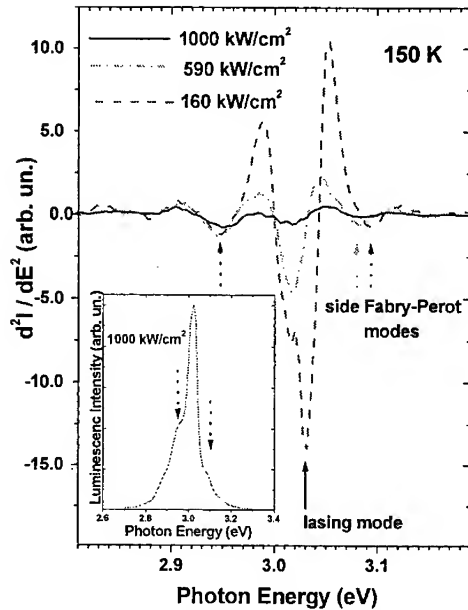


Fig. 4. Reflection spectra of an InGaN/GaN multilayer structure recorded at various excitation densities. The inset shows the photoluminescence spectrum at highest excitation density. Further cavity modes are marked by arrows

intensity of the emission band grows superlinearly. This behaviour hints to the observation of simulated emission in surface geometry, even when no Bragg reflectors are applied. We note, that the maximum of the PL band at high excitation densities remains in the vicinity of the onset of the absorption induced by the InGaN nano-islands.

The pronounced modulation of the light even in InGaN/GaN structures without Bragg reflectors is supported by optical reflection investigation at excitation densi-

ties when the gain overcomes the losses (Fig. 4). Deduced from the reflectivity coefficients of the GaN/AlGaIn (2.4%) and the GaN/air (17%) interfaces and the thickness of the active region, the threshold gain, which is necessary to overcome the external losses was estimated to be $2 \times 10^5 \text{ cm}^{-1}$. The behaviour of the second derivative normalised to the excitation density confirms that only one cavity mode exhibits superlinear growth. Side Fabry-Perot modes were detected even at highest excitation densities. The influence of the cavity modes on the PL emission are shown in the inset of Fig. 4. Although a superlinear growth of the main mode at 3.05 eV was observed, additionally emission bands appear fitting to other cavity modes according to the side Fabry-Perot modes. The observed chirp fits to the giant absorption-gain changes at threshold ($\sim 10^5 \text{ cm}^{-1}$). Despite the remarkably low finesse of the cavity, superlinear growth and narrowing of the emission band indicate the appearance of surface lasing supported by a cavity formed by the GaN/AlGaIn and GaN/air interfaces. For the fabrication of VCSEL with low threshold densities, the external optical losses have to be reduced. A promising way to achieve this is the enhancement of the reflectivity at the interfaces. Therefore, distributed Bragg reflectors (DBR) consisting of strain-compensated GaN/AlGaIn multilayer sheets are applied.

The introduction of a bottom AlGaIn/GaN Bragg reflector, with maximum reflectivity exceeding 90%, leads to a significant reduction of the external optical losses. Consequently, room temperature surface lasing [14] was achieved in structures with stacked InGaIn QD insertions. For the investigated structure, which is schematically drawn in the left inset of Fig. 5, no top DBR was applied. Nevertheless, as already mentioned, the high material gain in stacked InGaIn insertions enabled surface lasing even in case of very low finesse cavities (17% reflectivity on top due to the GaN/air interface, only). In Fig. 5 the room temperature PL spectra of the VCSEL structure recorded at different excitation densities are depicted. The observed surface lasing is confirmed by

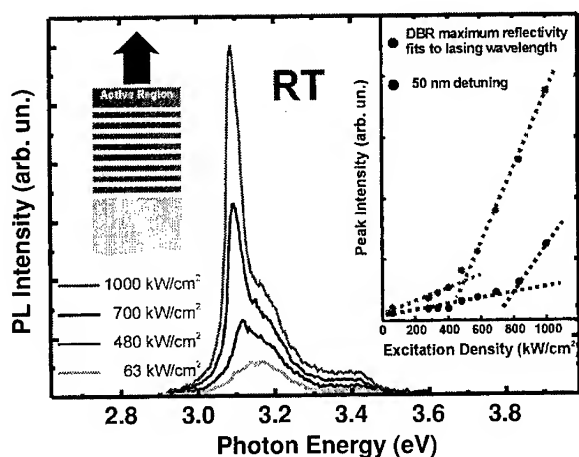


Fig. 5. Photoluminescence (PL) of an InGaN/GaN VCSEL structure recorded at various excitation densities at room temperature. The inset shows the peak intensity of the emission band as a function of the excitation density

the strong increase in the slope efficiency (see right inset of Fig. 5) and a narrowing of the PL emission band. From the farfield pattern of the emission of this structure a significant narrowing in comparison to the spontaneous emission of the same cavity was detected giving a further evidence of the lasing emission. The room-temperature threshold excitation density was 400 kW/cm². According to HRTEM investigations and the appearance of the lasing emission on the low energy tail of the PL band the lasing is attributed to recombination processes via localised states caused by In-rich nano-domains formed in the InGaN insertions (compare Fig. 2). The right inset of Fig. 5 shows peak intensity of the emission band as a function of the excitation density. The great impact of the DBR on the cavity quality is underlined by the observed behaviour. A detuning of the DBR out of the lasing wavelength leads to a decrease in the slope efficiency by a factor of two and to an enhancement of the threshold excitation density.

Conclusions The deposition of ultrathin insertions of ZnCdSe and InGaN leads to the formation of nano-islands. Structural investigations demonstrated that their diameter is in the range of the exciton Bohr-radii resulting in a three-dimensional confinement of excitons. It was shown, that the formation of cavity modes and surface lasing are enabled by the ultrahigh gain in QD structures. The reduction of the threshold excitation density and an increase of the slope efficiency was achieved by the introduction of bottom DBRs using GaN/AlGaIn multilayer sheets and by a tuning of the emission wavelength to the cavity mode of the laser. The high potential of InGaN nano-islands for the realisation of VCSELs emitting in the blue and green were demonstrated.

References

- [1] I. DARUKA and A.-L. BARABASI, *Phys. Rev. Lett.* **79**, 3708 (1997).
- [2] See, e.g., U. WOGGON, *Optical Properties of Semiconductor Quantum Dots*, Springer-Verlag, Berlin 1996.
- [3] D. HOMMEL, K. LEONARDI, H. HEINKE, H. SELKE, K. OHKAWA, F. GINDELE, and U. WOGGON, *phys. stat. sol. (b)* **202**, 835 (1997).
- [4] M. RABE, M. LOWISCH, F. KRELLER, and F. HENNEBERGER, *phys. stat. sol. (b)* **202**, 817 (1997).

- [5] M. GRÜN, F. FÜNFROCK, P. SCHUNK, TH. SCHIMMEL, M. HETTERICH, and C. KLINGSHIRN, *Appl. Phys. Lett.* **73**, 1343 (1998).
- [6] See, e.g. M. STRASSBURG, R. HEITZ, V. TÜRCK, S. RODT, U. W. POHL, A. HOFFMANN, D. BIMBERG, I. L. KRESTNIKOV, V. A. SHCHUKIN, N. N. LEDENTSOV, ZH. I. ALFEROV, D. LITVINOV, A. ROSENAUER, and D. GERTHSEN, *J. Electron. Mater.* **28**, 506 (1999).
- [7] S. NAKAMURA, M. SENOH, S. NAGAHAMA, N. IWASA, T. YAMADA, T. MATSUSHITA, Y. SUGIMOTO, and H. KIYOKU, *Appl. Phys. Lett.* **70**, 2753 (1997).
- [8] A. V. SAKHAROV, W. V. LUNDIN, I. L. KRESTNIKOV, V. A. SEMENOV, A. S. USIKOV, A. F. TSATSULNIKOV, YU. G. MUSIKHIN, M. V. BAIDAKOVA, ZH. I. ALFEROV, N. N. LEDENTSOV, J. HOLST, A. HOFFMANN, D. BIMBERG, I. P. SOSHIKOV, and D. GERTHSEN, *phys. stat. sol. (b)* **216**, 435 (1999).
- [9] S. V. IVANOV, S. V. SOROKIN, P. S. KOPEV, J. R. KIM, H. D. JUNG, and H. S. PARK, *J. Cryst. Growth* **159**, 1 (1996).
S. V. IVANOV, A. A. TOROPOV, T. V. SHUBINA, S. V. SOROKIN, A. V. LEBEDEV, I. V. SEDOVA, P. S. KOPEV, G. R. POZINA, J. P. BERGMAN, and B. MONEMAR, *J. Appl. Phys.* **83**, 3168 (1998).
- [10] A. V. SAKHAROV, W. V. LUNDIN, I. L. KRESTNIKOV, V. A. SEMENOV, A. S. USIKOV, A. F. TSATSULNIKOV, YU. G. MUSIKHIN, M. V. BAIDAKOVA, ZH. I. ALFEROV, N. N. LEDENTSOV, A. HOFFMANN, and D. BIMBERG, *Appl. Phys. Lett.* **74**, 3921 (1999).
- [11] P. YU, W. LANGBEIN, K. LEOSSEN, J. M. HVAM, N. N. LEDENTSOV, D. BIMBERG, V. M. USTINOV, A. YU. EGOROV, A. E. ZHUKOV, A. F. ISATSULNIKOV, YU. G. MUSIKHIN, *Phys. Rev. B* **60**, 16680 (1999).
- [12] HRTEM and DALI studies courtesy by A. SOSHIKOV, and D. GERTHSEN, University of Karlsruhe, (Germany), 2000.
- [13] A. ROSENAUER, S. KAISER, T. REISINGER, J. ZWECK, W. GEBHARDT, and D. GERTHSEN, *Optik* **102**, 63 (1996).
- [14] I. L. KRESTNIKOV, W. V. LUNDIN, A. V. SAKHAROV, V. A. SEMENOV, A. S. USIKOV, A. F. TSATSULNIKOV, ZH. I. ALFEROV, N. N. LEDENTSOV, A. HOFFMANN, and D. BIMBERG, *Appl. Phys. Lett.* **75**, 1192 (1999).

phys. stat. sol. (a) **183**, 105 (2001)

Subject classification: 78.45.+h; 78.55.Cr; 78.67.De; S7.14

Optical Properties and Lasing in (In, Al)GaN Structures

S. BIDNYK¹⁾ (a), G.H. GAINER (b), S.K. SHEE (b), J.B. LAM (b), B.D. LITTLE (b), T. SUGAHARA (b), J. KRASINSKI (b), Y.H. KWON (b), G.H. PARK (b), S.J. HWANG (b), J.J. SONG (b), G.E. BULMAN (c), and H.S. KONG (c)

(a) Zenastra Photonics, Inc., Ottawa, ON K1G 4J8, Canada

(b) Center for Laser and Photonics Research and Department of Physics, Oklahoma State University, Stillwater, OK 74078, USA

(c) Cree Research, Inc., Durham, NC 27713, USA

(Received October 8, 2000)

We achieved low-threshold ultra-violet lasing in optically pumped GaN/AlGaIn separate confinement heterostructures over a wide temperature range. Lasing modes of a single microcavity were examined from 20 to 300 K and gain mechanisms were compared to those of a thick GaN epilayer. We have also systematically studied InGaIn/(In)GaIn multiple quantum wells as a function of well and barrier thickness. We demonstrate that the stimulated emission threshold and photoluminescence (PL) decay time are strongly dependent on the well and barrier thickness. The experimental results indicate that the enhanced optical quality of samples with larger barrier thicknesses can be readily applied to the fabrication of InGaIn/(In)GaIn laser diodes.

1. Introduction GaN-based semiconductors and related materials have received growing interest due to their large direct band gap, making them promising materials for (ultraviolet) UV-blue-green light emitting devices, solar blind UV detectors, and high-power and high-temperature devices. However, due to the lack of ideal substrates for the growth of thin film nitrides, a large number of dislocations and cracks are naturally formed in the epitaxial layer to alleviate the lattice mismatch and the strain of postgrowth cooling. This does not always negatively affect lasing characteristics but sometimes introduces interesting lasing properties due to self-formed high-finesse microcavities [1] that could be utilized for the development of near- and deep-UV laser diodes (LDs). It is also necessary to optimize existing InGaIn/(In)GaIn-based structures to achieve improvements in laser power, lasing threshold, durability, and cost. In this work we describe the results of optical pumping experiments on GaN/AlGaIn separate confinement heterostructures (SCHs) with a large number of naturally formed microcavities. We achieved ultra-violet lasing in these structures over a wide temperature range. We also systematically studied a series of InGaIn/(In)GaIn MQWs to optimize the well and barrier thicknesses for LD performance. We found that the stimulated emission (SE) threshold density is strongly dependent on the well thickness.

2. Experiment The GaN/AlGaIn SCH samples used in this work were grown by metalorganic chemical vapor deposition on 6H-SiC (0001) substrates with $\sim 3 \mu\text{m}$ thick GaN epilayers deposited prior to the growth of the SCH region. The SCH sample under

¹⁾ Corresponding author; e-mail: bidnyk@mail.com

discussion has a 150 Å thick GaN active layer, surrounded by 1000 Å thick $\text{Al}_{0.05}\text{Ga}_{0.95}\text{N}$ cladding layers and 2500 Å thick $\text{Al}_{0.10}\text{Ga}_{0.90}\text{N}$ waveguide layers symmetrically located on each side. For the purpose of comparison, we also studied a 4.2 μm thick GaN epilayer grown on (0001) 6H-SiC. To investigate the well and barrier thickness effect, two series of five-period $\text{In}_{0.15}\text{Ga}_{0.85}\text{N}/\text{In}_{0.02}\text{Ga}_{0.98}\text{N}$ multiquantum well (MQW) structures were grown. For the first series, the well thickness was varied from 1.5 to 9.0 nm while keeping the barrier thickness constant at 4.0 nm. For the second series, the barrier thickness was varied from 4.0 to 15 nm while keeping the well thickness constant at 3.0 nm. Prior to growth of the MQWs, a 25 nm thick GaN nucleation layer and a 1.2 μm thick GaN buffer layer were grown on *c*-plane sapphire substrates.

The samples were mounted on a copper heat sink attached to a wide temperature range cryostat. Conventional photoluminescence (PL) spectra were measured in the back-scattering geometry using a frequency-doubled Ar^+ laser (244 nm) as the excitation source. In order to study the lasing phenomena, a tunable dye laser pumped by a frequency-doubled, injection-seeded Nd:YAG laser was used as the primary optical pumping source. Time-resolved PL (TRPL) measurements were made using a streak camera for detection and with sample excitation by a picosecond pulsed-laser system consisting of the second harmonic of a cavity-dumped dye laser synchronously pumped by a frequency-doubled modelocked Nd:YAG laser.

3. Results and Discussion

3.1 Microstructure-based lasing of GaN/AlGaN SCHs In order to evaluate the effects of cracks on the optical properties, we cleaved a GaN/AlGaN heterostructure sample into submillimeter-wide bars (note that when GaN is grown on SiC, it can be easily cleaved along the (11 $\bar{2}$ 0) direction [2]). Before cleaving, the samples did not exhibit any noticeable defects on the surface. After the cleaving process, however, cracks were observed along all three cleave planes associated with a hexagonal crystal structure, with the majority running parallel to the length of the bar. When a sample was excited above the lasing threshold, high-finesse cavity modes were observed. Typical emission spectra at pump densities above and below the lasing threshold are depicted in Fig. 1. A series of equally spaced and strongly polarized (TE:TM \geq 300:1) lasing modes with full width at half maximum of ~ 3 Å appears on the low energy side of the GaN-active-region peak. Lasing in our samples occurs in the wavelength range of 360 to 364 nm at

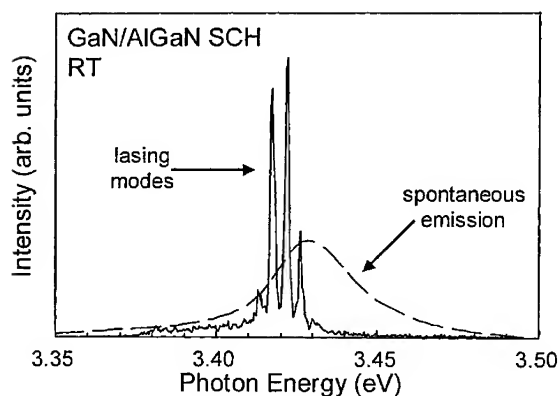


Fig. 1. Lasing and spontaneous emission in a GaN/AlGaN separate confinement heterostructure at room temperature. The lasing is believed to be of microcavity origin

room temperature (RT), which is much deeper in the UV than for InGaN/GaN-based structures. Assuming the unity round-trip condition is satisfied and there is no loss due to absorption in the GaN layer, the threshold gain can be estimated to be 500 cm^{-1} (see Ref. [3]).

It was found that by pumping different areas along the length of the bar, the emission exhibited varying degrees of cavity finesse. This is presumably due to the presence of cavities of varying quality formed by parallel cracks running through the active layer. Areas exhibiting high finesse consistently had a narrower far-field pattern than those exhibiting low finesse.

A dramatic decrease in the lasing threshold of our SCH structure in comparison to a bulk-like GaN epilayer was observed over the entire temperature range studied. For the SCH, the lasing threshold was measured to be as low as 65 kW/cm^2 at RT. We made a direct comparison of threshold carrier densities in GaN/AlGaN SCHs and bulk-like GaN epilayers and concluded that lasing in SCHs occurs at carrier densities $< 5 \times 10^{17} \text{ cm}^{-3}$, which is considerably lower than that required for the formation of an electron-hole plasma. By further examining the relative energy position between the spontaneous emission and lasing modes, we concluded that the exciton-exciton scattering gain mechanism remains dominant in the SCH lasing structures even at RT. The details of the carrier density calculations and photon energy analysis are given elsewhere [4].

The temperature dependence of the energy position of the lasing modes from a single microcavity was also studied. We used an optical multi-channel analyzer to consistently acquire spectra at 1.3 times the optical pumping stimulated emission threshold for each temperature. Figure 2 shows a plot of mode energy position versus temperature. The gray scale corresponds to different emission intensities. We note that the energy position of the gain maximum in the GaN/AlGaN SCH red shifts about 50 meV as the temperature is varied from 10 to 300 K, which is half that of a bulk-like GaN epilayer (solid line in Fig. 2) [5]. Such a reduced temperature sensitivity of the laser emission suggests that the GaN/AlGaN SCH could be well suited for UV applications that require increased temperature stability of the emission wavelength.

3.2 Well/barrier thickness dependence of $\text{In}_{0.15}\text{Ga}_{0.85}\text{N}/\text{In}_{0.02}\text{Ga}_{0.98}\text{N MQWs}$ To further investigate the recombination dynamics and device applicability of InGaN/(In)GaN

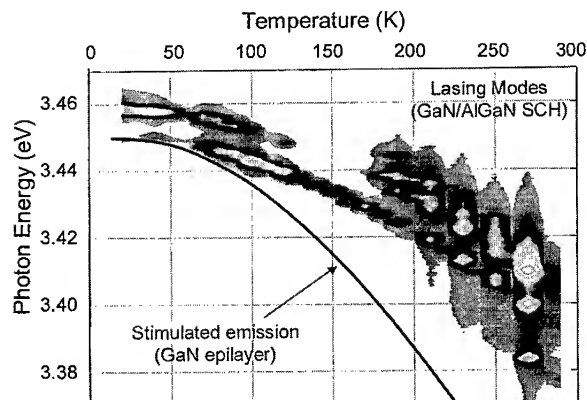


Fig. 2. Lasing modes as a function of temperature for a single microcavity. This image was obtained by consistently taking lasing spectra with an optical multi-channel analyzer at 1.3 times the stimulated emission threshold while the temperature was gradually varied from 20 to 300 K. For comparison, the position of the stimulated emission peak in a thick GaN epilayer is also plotted (solid line)

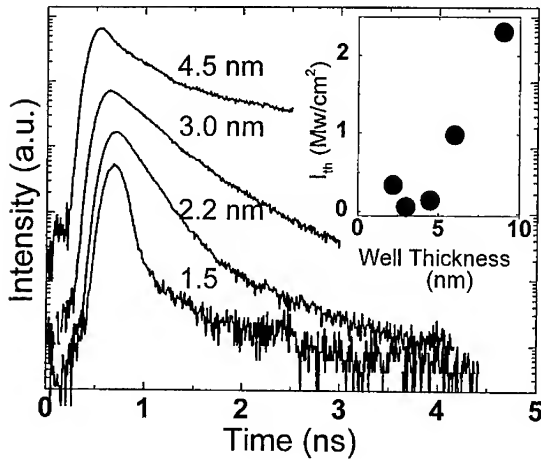


Fig. 3. Room-temperature photoluminescence decay curves as a function of well thicknesses (4.0 nm thick barriers) for $\text{In}_{0.15}\text{Ga}_{0.85}\text{N}/\text{In}_{0.02}\text{Ga}_{0.98}\text{N}$ MQWs. The inset shows the stimulated emission threshold versus well thickness at room temperature

MQWs, TRPL and SE measurements at RT were performed. Figure 3 shows RT TRPL decay curves as a function of well thickness. The carrier lifetime is seen to increase with increasing well thickness, because of greater electron-hole separation caused by piezoelectric fields [6]. The inset of Fig. 3 shows the SE threshold (I_{th}) versus well thickness at RT. The SE threshold is 340, 64, 150, 980, and 2300 kW/cm^2 for the well thicknesses of 2.2, 3.0, 4.5, 6.0, and 9.0 nm, respectively. SE was not observed for the 1.5 nm well sample, and the lowest SE threshold density of 64 kW/cm^2 was obtained for the 3.0 nm well sample. The extremely large values of SE threshold for the 6.0 and 9.0 nm well thickness samples can be attributed to strain-relaxation [7, 8] and the greater electron-hole separation. For narrower wells, such as 1.5 and 2.2 nm, much smaller RT lifetimes were observed, indicating a larger nonradiative recombination rate due to the greater influence of interface-related nonradiative recombination centers [6]. This may be the reason that SE was not observed for the 1.5 nm well sample and why the 2.2 nm well sample had an increased SE threshold.

Figure 4 compares the TRPL decays at RT for different barrier thicknesses and a constant well thickness of 3 nm. The decay time increases with increasing barrier thickness. The RT lifetime is 340, 595, 656, and 919 ps for a barrier thickness of 4.0, 7.0, 10.0, and 15.0 nm, respectively, indicating smaller RT nonradiative recombination rates

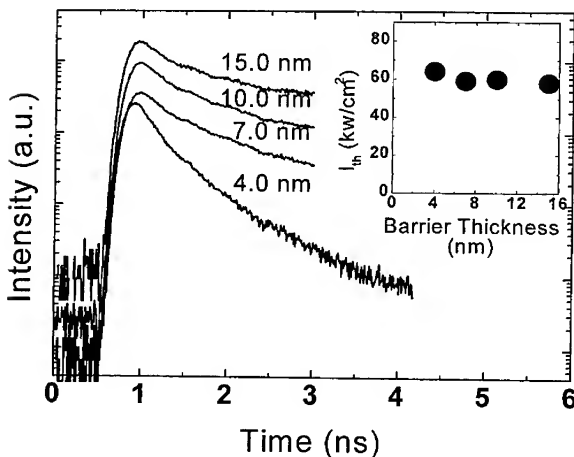


Fig. 4. Room-temperature time resolved photoluminescence of $\text{In}_{0.15}\text{Ga}_{0.85}\text{N}/\text{In}_{0.02}\text{Ga}_{0.98}\text{N}$ MQWs with for different barrier thicknesses, but a constant 3.0 nm well thickness. The inset shows the SE threshold versus barrier thickness at room temperature

for thicker barrier samples. For the origin of RT nonradiative recombination centers in the InGaN/(In)GaN MQW system, interface states related to In composition fluctuation and well-width fluctuations have been suggested [9]. The larger RT decay times for thicker barrier samples in our study represent improved interface quality and are consistent with X-ray reciprocal lattice mapping results (see Ref. [10]). We note however, that the increase in RT decay time with barrier thickness can also be explained by the piezoelectric field in the wells increasing with barrier thickness [6] and causing greater electron-hole separation in the wells.

The inset of Fig. 4 shows the SE threshold versus barrier thickness at RT. The SE thresholds were measured to be 64, 59, 60, and 58 kW/cm² for the 4.0, 7.0, 10.0, and 15.0 nm barrier thicknesses, respectively. Unlike the strong SE threshold dependence on well thickness, the SE threshold is almost independent of barrier thickness. However, the PL efficiency and RT lifetime increase greatly with barrier thickness. The enhanced optical and structural quality of samples with larger barrier thicknesses suggests that LDs utilizing barriers as thick as ~15 nm would be superior to traditional LDs, which have 4.0–7.0 nm thick barriers.

4. Conclusions We achieved ultraviolet lasing in optically pumped GaN/AlGaN separate confinement heterostructures over a wide temperature range. The lasing was shown to be of microcavity origin. The temperature sensitivity of the lasing wavelength was found to be half that of bulk-like GaN films, indicating that separate confinement heterostructures could be used in applications requiring increased temperature stability of the emission wavelength. We also systematically examined the optical properties of InGaN/(In)GaN multiquantum wells as a function of well and barrier thicknesses. For very narrow wells, smaller RT lifetimes were observed, indicating a larger nonradiative recombination rate due to the greater influence of interface-related nonradiative recombination centers. As the barrier thickness increases, the PL efficiency and RT lifetime significantly increase. We believe this optimization of well and barrier thicknesses can be readily applied to the fabrication of laser diodes with increased lifetimes and enhanced durability.

Acknowledgement The authors thank BMDO, AFOSR, ONR and NSF for financial support of this research.

References

- [1] S. BIDNYK, Ph.D. Dissertation, Oklahoma State University, 1999.
- [2] B.D. CULLITY, *Elements of X-Ray Diffraction*, 2nd ed., Addison-Wesley Publ. Co., Reading (Massachusetts) 1978 (p. 502).
- [3] M. BAGNALL and K.P. O'DONNELL, *Appl. Phys. Lett.* **68**, 3197 (1996).
- [4] S. BIDNYK, J.B. LAM, B.D. LITTLE, Y.H. KWON, J.J. SONG, G.E. BULMAN, H.S. KONG, and T.J. SCHMIDT, *Appl. Phys. Lett.* **75**, 3905 (1999).
- [5] S. BIDNYK, T.J. SCHMIDT, B.D. LITTLE, and J.J. SONG, *Appl. Phys. Lett.* **74**, 1 (1999).
- [6] P. LEFEBVRE, M. GALLART, T. TALIERCIO, B. GIL, J. ALLEGRE, H. MATHIEU, N. GRANDJEAN, M. LE-ROUX, J. MASSIES, and P. BIGENWALD, *phys. stat. sol. (b)* **216**, 361 (1999).
- [7] A.T. MENEV and E.P. O'REILY, *Appl. Phys. Lett.* **67**, 3013 (1995).
- [8] K. FUNATO, S. HASHIMOTO, K. YANASHIMA, F. NAKAMURA, and M. IKEDA, *App. Phys. Lett.* **75**, 1137 (1999).
- [9] C.K. SUN, T.L. CHIU, S. KELLER, G. WANG, M.S. MINSKY, S.P. DENBAARS, and J.E. BOWERS, *Appl. Phys. Lett.* **71**, 425 (1997).
- [10] S.K. SHEE, Y.H. KWON, J.B. LAM, G.H. GAINER, G.H. PARK, S.J. HWANG, B.D. LITTLE, and J.J. SONG, unpublished.

phys. stat. sol. (a) **183**, 111 (2001)

Subject classification: 73.21.Fg; S7.12; S7.14

Exciton Binding Energies and Oscillator Strengths in GaAsN–GaAs Quantum Wells

B. GIL (a) and P. BIGENWALD (b)

(a) CNRS, GES, Université de Montpellier II, Place Eugene Bataillon, CC 074, F-34095 Montpellier Cedex 5, France

(b) Département de Physique, UFR Sciences, Université d'Avignon et des Pays de Vaucluse, 33 rue Louis Pasteur, F-84000 Avignon, France

(Received October 8, 2000)

We propose the first tentative calculation of exciton binding energies and oscillator strengths in GaAs_{1-x}N_x–GaAs quantum wells with nitrogen contents below $x = 0.05$. Our model is based on the envelope function approximation and permits us to determine the excitonic properties of GaAs–GaAsN single quantum wells with a variational and self-consistent process for marginal type I or type II potentials due to the very small valence band offset for this combination. We conclude that this is a type I system.

1. Introduction Mixed-anion III–V–N alloys are very promising candidates for optoelectronic devices operating in the 1.3 and 1.55 μm range, since small nitrogen contents are very efficient to reduce the gap of the III–V compound. As an impurity in ordinary GaP and GaAs semiconductors, nitrogen is known to induce one or several special conduction states. For the different doping levels there is a series of bound exciton lines in GaP. In GaAs, nitrogen introduces a state which is resonant in the conduction band at ambient pressure conditions but can be boosted into the band gap by application of hydrostatic pressure. At higher composition, hybridization of the nitrogen wavefunctions with the rest of the conduction band increases which produces an additional band. The theoretical problem of the interaction of the nitrogen atom with the rest of the Bloch states of the band structure of GaAs has been analyzed by many authors; a review can be found in [1]. These methods are purely theoretical approaches and are hopeless for experimentalists and device designers. This argument which holds for bulk III–V–N compounds is reinforced for quantum wells based on them. These drawbacks inspired us for proposing a different, heuristic approach. This approach is based on well-known symmetry arguments: nitrogen which substitutes the group V atom gives an a_1 impurity level which couples with the a_1 zone center folded states that are fully symmetric linear combinations of the contributions of the X or L conduction band extrema. The study of quantum wells is restricted to the fundamental conduction band potential line-up for which we make the approximation that the Bloch wavefunctions do not change from one layer to the other. Interactions with upper confined states are restricted to their influences on effective masses.

2. Coupling of the Electron States in the Context of the Effective Mass Approximation The conduction states of GaAsN alloys are obtained by using the following 4×4

matrix description:

$ N\rangle$	$ a_1^\Gamma\rangle$	$ a_1^L\rangle$	$ a_1^X\rangle$
E_N	$V_{N\Gamma}$	V_{NL}	V_{NX}
$V_{N\Gamma}$	Ea_1^Γ	0	0
V_{NL}	0	Ea_1^L	0
V_{NX}	0	0	Ea_1^X

where $|N\rangle$ is a Wannier state, the energy of which is the limit value at the asymptotic nitrogen doping conditions. The matrix above describes the zone center states; but the dispersion relations can be obtained very easily if we suppose that the Bloch theorem still holds in the low nitrogen concentration range. We restrict ourselves to the [001] direction and write:

$$Ea_1^\Gamma(k_z) = Ea_1^\Gamma(0) + \frac{\hbar^2 k_z^2}{2m_\Gamma^*}, \quad Ea_1^X(k_z) = Ea_1^X(0) + \frac{\hbar^2 k_z^2}{6} \left(\frac{1}{m_l^{*X}} + \frac{2}{m_t^{*X}} \right),$$

$$Ea_1^L(k_z) = Ea_1^L(0) + \frac{\hbar^2 k_z^2}{6} \left(\frac{1}{m_l^{*L}} + \frac{2}{m_t^{*L}} \right)$$

with: $E_N(0)$ (meV) = 1675–2520 x , $Ea_1^\Gamma(0)$ (meV) = 1430–1550 x , $Ea_1^L(0)$ (meV) = 1745, $Ea_1^X(0)$ (meV) = 1870, $V_{N\Gamma}$ (meV) = –2400 \sqrt{x} , V_{NL} (meV) = –400 \sqrt{x} , V_{NX} (meV) = –200 \sqrt{x} . We used the effective mass values $m_\Gamma^* = 0.067$, $m_l^{*X} = 1.3$, $m_t^{*X} = 0.23$, $m_l^{*L} = 1.8$, $m_t^{*L} = 0.26$.

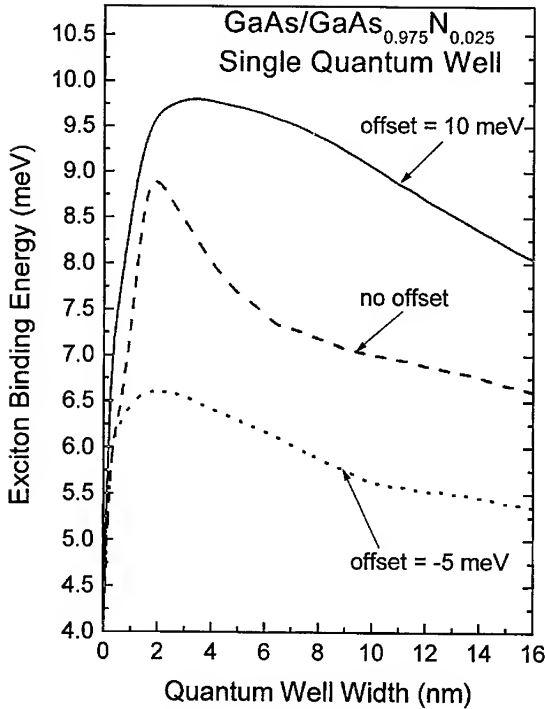


Fig. 1. Exciton binding energy for the fundamental transition in a single GaAsN–GaAs quantum well as a function of the well width for different values of the valence band offset

3. Excitonic Parameters When embedding a slice of GaAsN between two semi-infinite layers of GaAs, we constitute a quantum system. We have considered that the valence band potential profile is marginal: the valence band offset is either zero, slightly type I (10 meV) or type II (–5 meV). Due to lack of information, we took the same valence band effective masses for each layer, the ones of the heavy hole in GaAs. Concerning the lowest conduction band, for a nitrogen content $x = 2.5\%$ we have an effective well whose depth is equal to 326 meV, the energy difference between the fundamental Γ bands of the binary and the ternary layers. In the ternary layer, we took the electron effective mass computed at the zone center. This one is larger than in GaAs due to the couplings with the other conduction bands. To determine the exciton parameters for this marginal potential profile, we compute self-consistently the exciton binding energy and the quantized hole state in a valence potential profile modified by the presence of the exciton [2].

In Fig. 1 are displayed the exciton binding energies (E_b) obtained as a function of the well width (L_w) for different values and signs, of the offset. Starting from the bulk

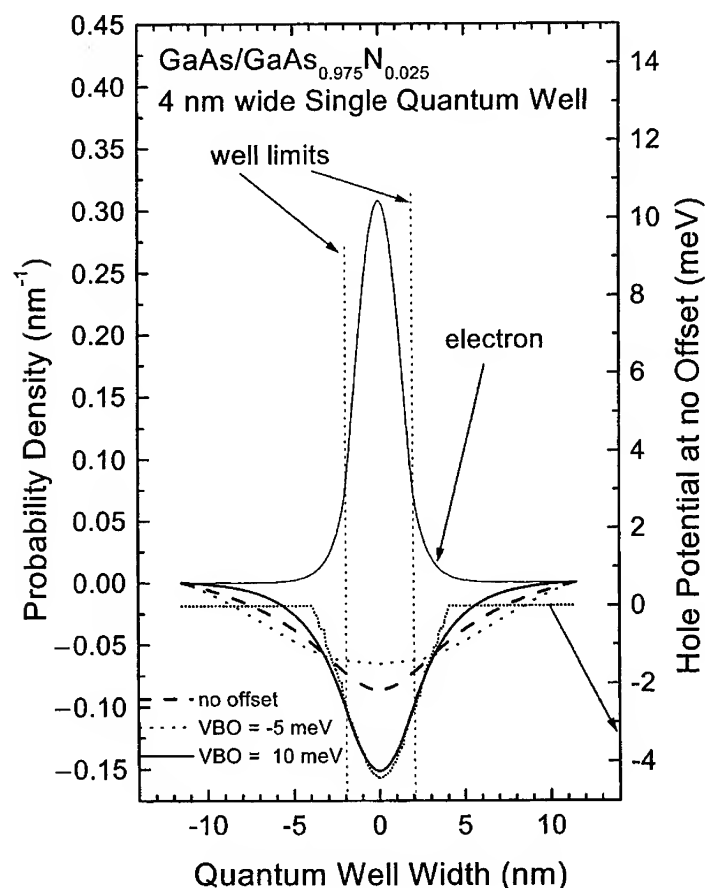


Fig. 2. Self-consistent densities of probability for the electron and hole states in a GaAsN–GaAs, 4 nm wide single quantum well for different values of the valence band offset and confining potential for the hole

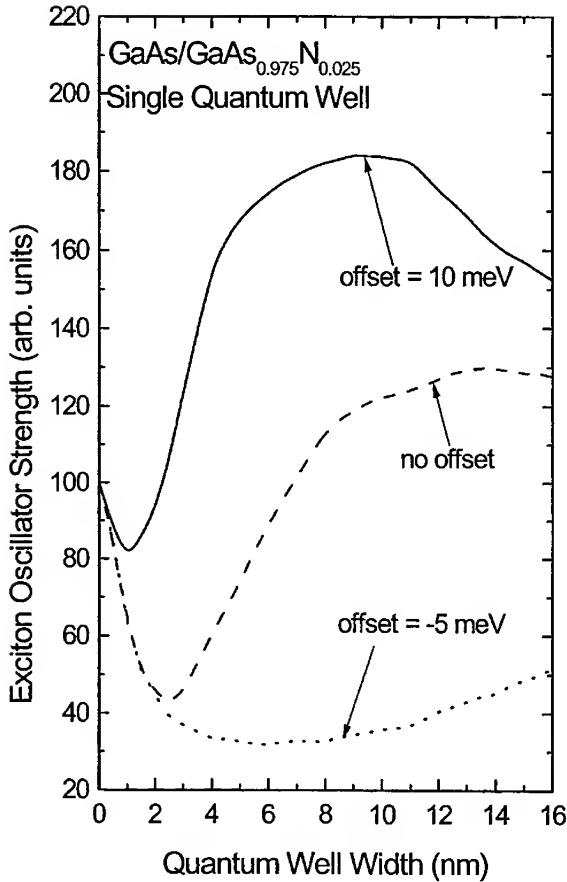


Fig. 3. Excitonic oscillator strength of the fundamental transition in a GaAsN–GaAs single quantum well as a function of the well width for different values of the valence band offset

value of 4 meV, we find the usual trend of a large increase for thin wells, then a decrease to reach again the bulk value for very large wells. A maximum of E_b is observed that corresponds to the best confinement of the electron–hole pair. In Fig. 2 are shown some typical electron and hole densities of probability.

Figure 3 shows the evolution of the excitonic oscillator strength (OS) versus the well width (L_w) for different values of the offset. The initial decrease of OS versus the well width is due to the faster confinement of electron states compared to heavy hole states: the mass parameters are comparable but the well potential remains marginal for the hole, the square overlap of eigenfunctions is small and the exciton Bohr radius is large as shown in Fig. 4. At large values of L_w , we recover the bulk value of 100%. Here again, the oscillator strength depends strongly on the valence band offset for a fixed value of well width. The larger the offset, the more efficient is the radiative recombination process between electrons and holes.

We now discuss the information that this model furnishes. We believe that the strong modification of the GaAs conduction band by nitrogen alloying leads to a type I configuration for GaAsN–GaAs quantum wells. An evidence for this configuration are the strong absorption features that were observed in GaAsN–GaAs quantum wells [3]. It could be argued that strain fields were not included in the alloy layer. The GaN lattice

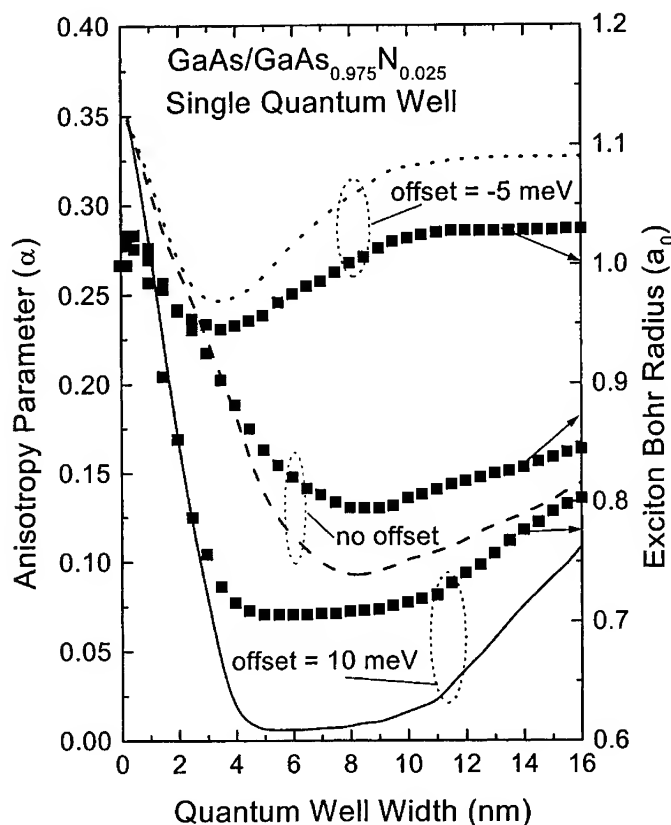


Fig. 4. Exciton parameters (anisotropy and Bohr radius) for the fundamental transition in a single GaAsN–GaAs quantum well as a function of the well width for different values of the valence band offset

parameter is smaller than the GaAs one. Coherent growth of GaAsN onto GaAs would produce a biaxial tension in the GaAsN layer. The topmost of the valence band would be a light-hole instead of a heavy-hole one, with a slightly enhanced type I configuration. Then the question which is raised concerns the nature of the excitonic transition in terms of heavy or light holes. But in all cases the predictions of our calculation still holds since on-axis and in-plane hole masses are used in the calculation. What is important besides the exciton binding energy is the oscillator strength, which is in straightforward relation with the wavefunctions of the confined carriers. Comparison with [3] indicates a type I configuration. In quaternary GaInAsN alloys lattice-matched to GaAs, strain effect considerations are not required; due to the incorporation of indium, the configuration is definitively type I for such quantum wells.

In conclusion, we have performed self-consistent calculations of the excitonic binding energies and oscillator strengths in GaAsN–GaAs quantum wells. Our results indicate that the band lineups are in a type I configuration.

Acknowledgement This work is supported in part by the E.C. contract HPRN-CT-1999600132 'CLERMONT'.

References

- [1] B. GIL, Solid State Commun. **114**, 623 (2000), and references cited therein.
- [2] P. BIGENWALD and B. GIL, Solid State Commun. **91**, 33 (1994).
- [3] B. Q. SUN, D. S. JIANG, X. D. LUO, Z. Y. XU, Z. PAN, L. H. LI, and R. H. WU, Appl. Phys. Lett. **76**, 2862 (2000).

phys. stat. sol. (a) **183**, 117 (2001)

Subject classification: 78.55.Cr; S714

A Mystery Wrapped in an Enigma: Optical Properties of InGaN Alloys

K. P. O'DONNELL¹⁾

Semiconductor Spectroscopy and Devices Group, Department of Physics and Applied Physics, University of Strathclyde, Glasgow G4 0NG, Scotland, UK

(Received October 8, 2000)

The high efficiency of luminescence from InGaN has underpinned widespread recent developments in blue-green optoelectronics. A loose consensus on the nature of the luminescence has emerged in the last three years. Localisation of excitation, whether by composition fluctuations or self-formed quantum dots, appears to tilt the balance in favour of radiative recombination, despite the presence of huge densities of extended defects found in 'device-grade' material by electron microscopy. The luminescence is lowered in energy with respect to the excitation by internal electric fields. What is not clear at present is the relationship between the composition and the structure: what exactly is responsible for optical effects in this material? We have argued previously that, contrary to accepted wisdom, current theoretical treatments fail to give a satisfactory account of the dependence of the optical energies on the composition of InGaN. We now advance a strong form of this argument: present theoretical treatments of light-matter coupling may be inadequate to take account of the complexities of structure inherent in this, or any other, luminescent material.

1. Introduction The fundamental problem of spectroscopy is to identify the physical origin of a given optical spectrum. For example, the atomic spectral line that we call H_{α} , seen in absorption or emission at 656.3 nm, originates in an electronic transition of the hydrogen atom. A single hydrogen atom, appropriately excited, can emit a photon of this characteristic wavelength. When we come to consider optical effects in solids, the situation is more complicated. As Garbuny [1] wrote: (Solid state spectra) hide rather than reveal complexities of structure and energy states far larger than those existing in free atoms and molecules. Following Garbuny, we can classify spectra of solids into several categories, as shown in Table 1. Let us focus on light emission or fluorescence. The origin of fluorescence from ruby is not in doubt: isolated chromium ions emit distinct luminescence lines that combine into a narrow band, called the R-line. Special spectral techniques, hole-burning for example, can reveal the narrow, homogeneously broadened components of the inhomogeneously broadened R-line. We can imagine that a near-field microscope could accomplish the same end in a sufficiently dilute sample. The Cr^{3+} ion in ruby is a good example of a localised optical centre, which we call a lumophore.

In semiconductors, various mechanisms give rise to light emission and absorption. Some of these involve localised states, while some involve band states of the crystal potential. Band states are delocalised, at least to the extent of the crystal dimensions, in real space, but are made up of a small range of k -states (ideally one) in phase space. Transitions involving extended states involve the whole sample as a lumophore. In what

¹⁾ Tel.: +44-141-548-3365; Fax: +44-141-552-2891; e-mail: k.p.odonnell@strath.ac.uk

Table 1
Classification of optical spectra in solids (after Garbuny [1])

physical process	example spectrum or system
plasma oscillations	phonon reststrahlen band free carrier absorption
localised states/defects	inner-shell transitions of rare-earth and transition-metal impurities electronic spectra of dye molecules in solid hosts exciton emission donor-acceptor pair emission
extended states	band-to-band absorption exciton absorption
mixed	carrier capture luminescence low-dimensional semiconductors

follows, I will review work aimed at discovering the origin of the luminescence in InGaN alloys in terms of the distinction between localised and delocalised states.

2. Experimental Details Much work has been done on InGaN via spatially resolved measurements (mapping) of a small number of macroscopically inhomogeneous epilayers. Sample growth and primary characterisation are detailed in [2]. Photoluminescence (PL), optical absorption and excitation spectra were carried out conventionally on samples mounted in closed-cycle helium cryorefrigerators. The composition of samples was measured using energy dispersive X-ray analysis at De Montfort University [3], Rutherford backscattering spectrometry, at the University of Leuven [4], electron probe microanalysis, at the University of Montpellier [5] and extended X-ray absorption fine structure in collaboration with CLRC Daresbury Laboratories [6].

3. Experimental Results The PL spectrum of a typical InGaN epilayer features a single broad band. The band is asymmetric in profile with exponential tails [7]. The composition dependence of the spectral peak energy is shown in Fig. 1.

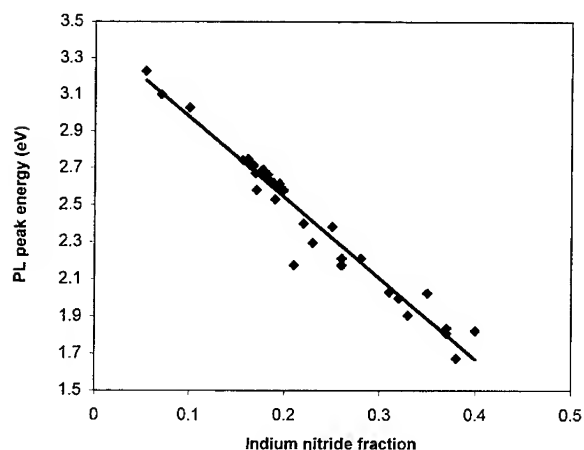


Fig. 1. Relation of PL peak energy to composition for InGaN epilayers

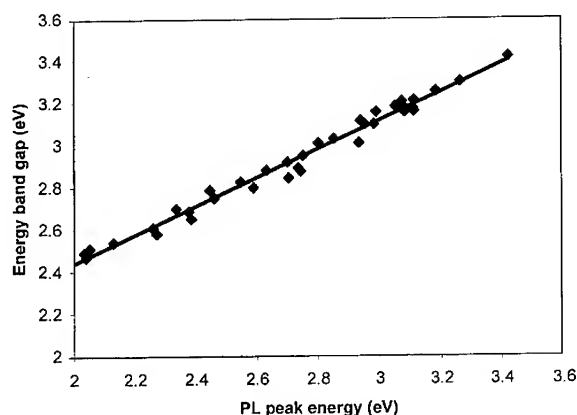


Fig. 2. Relation of band gap to PL peak energy for InGaN epilayers, quantum wells and quantum dot samples

The trendline is a linear fit to the data,

$$E_p = 3.41(03) - 4.36(16) x, \quad (1)$$

where E_p is the peak energy in eV and x is the indium nitride fraction. No luminescent InGaN sample with an indium fraction greater than 0.4 has been grown, to my knowledge.

The absorption spectrum of InGaN epilayer has a sigmoidal profile (while the PL spectrum is approximately the derivative of a sigmoid). Let us define the midpoint of the sigmoid as the band gap of the alloy [8]. The band gap and peak PL energy are related as shown in Fig. 2.

The trendline is

$$E_g = 0.677(12) E_p + 1.088(33). \quad (2)$$

Combining equations (1) and (2) shows that the band gap depends linearly on the indium nitride fraction. There is no statistical evidence of a bowing parameter in the composition dependence of the band gap from these data [9].

EXAFS shows further that the nearest neighbour (In–N) separation varies only from 2.09–2.11 Å and the next nearest neighbour (In–M) separation between 3.26–3.30 Å in samples with In content in the range from 5% to 40% [10]. The variations are much less than might be expected from a naive application of Vegard's law.

4. Discussion We want to answer the question: what is responsible for the optical properties of InGaN? The scalability of the optical spectra, their dependence on the (mean) indium nitride content and their relative indifference to sample macrostructure, encourages us to imagine that a common lumophore is responsible, but what clues do we have about the physical structure of this entity?

1. The light-emitting object is very small. A spectrum inhomogeneously broadened by site-to-site energy disorder is expected to 'break up' as the number of excited lumophores is reduced. Cathodoluminescence imaging of quantum wells, only a few nanometre thick, reveals a granular structure with a length scale of about 300 nm. If quantum discs of about this size were *responsible* for the luminescence from epilayers, one would expect to see statistical fine structure in microspectroscopy of epilayers. This has not been reported, as far as I am aware. Using a confocal microscope to restrict the excitation volume to about $500 \times 500 \times 250 \text{ nm}^3$ (the film thickness) does not materially alter the spectrum of an InGaN epilayer, compared to that observed using large-area excitation [11].

2. The light-emitting object is certainly bigger than a single atom. A conventional model of light emission from alloys pictures a Wannier exciton of a certain radius $R > a$, the lattice constant. The exciton samples a local region of the crystal, as it decays with an energy that depends upon the distribution of alloy components within its orbit. It is difficult to estimate the radius of the Wannier exciton in InGaN. The bandstructure of InN is uncertain. In addition, there is a tendency, first mentioned by Stokes [12], towards lowering of energy in the emission process. Regions with high ratios of InN, assuming for the moment a random distribution of components, will attract the exciton to regions where the recombination energy is lowered. This situation is complicated if there is non-random segregation and/or internal electric fields. In extreme circumstances, one can imagine strong local trapping of holes on In atoms or clusters leading to the collapse of Wannier excitons into Frenkel excitons, extending over a short percolation path, an object that may be called a "quantum what".

3. Composition fluctuations on a scale size of several nanometres have been identified by electron microscopy [13].

4. While light emission seems to be localised in InGaN, light absorption, which leads to the excitation of the lumophores, may not be local. For quantum well spectra, it is clear that delocalised excitation, followed by relaxation into classically localised states, leads to Stokes' shift in 2D [14].

5. Conclusion Despite a lot of work, we are still confronted by a mystery when considering the origin of luminescence from InGaN. More work is required on the influence of the organisation of the material (into quantum wells or dots) on the spectral and temporal characteristics of the emission. A fundamental question is whether the composition fluctuations revealed by microscopy are in fact responsible for the emission process? At the present time this conjecture remains unproved. In consequence the description of light-matter coupling in InGaN alloys must remain enigmatic.

References

- [1] M. GARBUNY, *Optical Physics*, Academic Press, New York 1965.
- [2] W. VAN DER STRICHT, Ph.D. Thesis, University of Ghent, 1999, unpublished.
- [3] K.P. O'DONNELL, P.G. MIDDLETON, C. TRAGER-COWAN, C. YOUNG, S.C. BAYLISS, I. FLETCHER, W. VAN DER STRICHT, I. MOERMAN, and P. DEMEESTER, *Appl. Phys. Lett.* **73**, 3273 (1998).
- [4] K.P. O'DONNELL, M.E. WHITE, S. PEREIRA, M.F. WU, A. VANTOMME, W. VAN DER STRICHT, and K. JACOBS, *phys. stat. sol. (b)* **216**, 171 (1999).
- [5] K.P. O'DONNELL, M.E. WHITE, C. MERLET, B. GIL, and W. VAN DER STRICHT, *Proc. E-MRS (Strasbourg)* (2000), in press.
- [6] K.P. O'DONNELL, R.W. MARTIN, M.E. WHITE, J.F.W. MOSSELMANS, and QIXIN GUO, *phys. stat. sol. (b)* **216**, 151 (1999).
- [7] K.P. O'DONNELL, T. BREITKOPF, H. KALT, W. VAN DER STRICHT, I. MOERMAN, P. DEMEESTER, and P.G. MIDDLETON, *Appl. Phys. Lett.* **70**, 1843 (1997).
- [8] R.W. MARTIN, K.P. O'DONNELL, P.G. MIDDLETON, I. MOERMAN, P. DEMEESTER, and W. VAN DER STRICHT, *Appl. Phys. Lett.* **74**, 263 (1999).
- [9] K.P. O'DONNELL, R.W. MARTIN, M.E. WHITE, K. JACOBS, W. VAN DER STRICHT, P. DEMEESTER, A. VANTOMME, M.F. WU, and J.F.W. MOSSELMANS, *Mater. Res. Soc. Symp. Proc.* **595**, W11.26 (2000).
- [10] J.F.W. MOSSELMANS, personal communication (2000).
- [11] K.P. O'DONNELL and M.J. TOBIN, unpublished work.
- [12] G.G. STOKES, *On Light*, Routledge & Sons, London 1897.
- [13] H. KALT, personal communication (2000).
- [14] F. YANG, M. WILKINSON, E.J. AUSTIN, and K.P. O'DONNELL, *Phys. Rev. Lett.* **71**, 1287 (1993).

phys. stat. sol. (a) **183**, 121 (2001)

Subject classification: 71.15.-m; 78.67.De; S7.14

Optical and Electronic Properties of GaN Based Heterostructures: A Self-Consistent Time-Dependent Approach

A. REALE (a), A. DI CARLO (a), P. LUGLI (a), and A. KAVOKIN (b)

(a) *INFM and Department of Electrical Engineering, University of Rome "Tor Vergata", via di Tor Vergata 100, I-00133 Roma, Italy*

(b) *Physics Department, University "Blaise Pascal", Clermont-Ferrand, France*

(Received October 8, 2000)

We present a study of optical properties in GaN based structures and devices. Our approach is based on a rate equation model, where the role of carrier screening on recombination rates is self-consistently included. We demonstrate that Time-Resolved Photoluminescence (TR-PL) in gallium-nitride quantum wells is influenced by two main effects: (i) the charge accumulation in the well, caused by the separation of the wavefunctions and by the increase of the radiative recombination time induced by the built-in field, and (ii) the loss of carriers from the ground level induced by the non-radiative recombination processes.

1. Introduction The recent developments in the field of GaN-based blue-UV optoelectronic devices have stimulated several experimental and theoretical studies on GaN/AlGaN MQWs devoted to the complete clarification of the role of internal piezoelectric and spontaneous polarization fields. Many time-resolved photoluminescence (TR-PL) experiments [1–4] have been carried out in several experimental groups. These results require an accurate theoretical model able to account for the peculiar characteristics of gallium-nitride compounds. In this paper we will develop a time-dependent self-consistent approach to study TR-PL measurements in nitride structure where polarization fields and charge screening are important. We demonstrate that the fundamental transition energy is influenced by two main effects: (i) the charge accumulation in the well, caused both by the separation of the wavefunctions and by the increase of the radiative recombination time induced by the built-in field, and (ii) the loss of carriers from the ground level induced by the non-radiative recombination processes. The proper account of these phenomena provides a new insight on the coupling of GaN-based structures with light, which has both fundamental and applied relevance.

To this aim, the information that can be drawn from photoluminescence and time resolved photoluminescence are extremely valuable. Our approach allows the calculation of the both time integrated and time dependent intensity of light emitted after optical excitation. We are also able to calculate the spectral profile of these quantities, and we think this feature can greatly enhance the comprehension of gallium nitride based optical properties.

2. The Rate Equation Model The role of carrier screening is extremely important in GaN based heterostructures [5, 6]. Many time-resolved experiments suggest that the

magnitude of the screening changes dramatically with time [4]. For this reason, we developed a model based on rate equations which include the variations with time of the main recombination processes, namely the spontaneous recombination time, and the non-radiative time. While the first one has a key role in describing how charge rearrangement modifies the internal structure of the well and thereafter the oscillator strength of the optical transition, the latter has to be considered since it can strongly modify the recovery time after the photoexcitation.

In the following we consider a typical multi-quantum-well (MQW) structure. To model the time evolution of the charge density inside the well we solve the following rate equation:

$$\frac{dn}{dt} = G - R_{sp}(n) - R_{nr}(n), \quad (1)$$

where the terms on the right-hand side indicate the rate of generation of carriers due to optical excitation (G), the rate of spontaneous recombination (R_{sp}), and the rate of non-radiative recombination (R_{nr}), respectively. We consider the cumulative effect of all the non-radiative recombination channels such as defects assisted and surface recombination, and assume that it is proportional to the average density n in the QW, i.e. $R_{nr} = n/\tau_{nr}$, with τ_{nr} the non-radiative time. The physical meaning of this simplified model is related to the fact that we want to isolate the radiative recombination dynamic from the other processes which may involve non-radiative recombination. These latter processes are usually slower and of the order of a nanosecond, as suggested by some experimental investigation, where it has been also suggested that their role may be dominant even at very low temperatures, depending on the well width [4].

Equation (1) should be solved, at each time step, in a self-consistent manner. The importance of self-consistent approach to the rate-equation problem becomes immediately clear if we recall the expression for the spontaneous recombination rate in effective mass approximation:

$$R_{sp} = \int_{-\infty}^{+\infty} \frac{e^2 \mu E_p \omega n_r}{\hbar^2 c^3 \pi^3 \epsilon_0 m_0} f_c (1 - f_v) \sum_{i,f} I_{i,f}^2 \theta(\omega - \omega_{if}) d\omega, \quad (2)$$

where all the symbols have their usual meaning, θ is the Heavyside function, $I_{i,f}$ is the wavefunction overlap and ω_{if} is the energy transition from the initial level i in conduction band to the final level f in valence band. In Eq. (2) both quasi-Fermi levels, overlap matrix elements, and transition energy are all charge density dependent. Overlap and transition energy are related to the density through the coupling between the Poisson and Schrödinger equations. Equation (2) represents the bimolecular recombination term widely used in rate equation models describing carrier dynamics in QWs, rewritten in terms of physical contributions to the overall rate of radiative recombination.

We thus solve Eq. (1) as follows: at each time step t_i we calculate the right-hand side of Eq. (1) by solving self-consistently the Schrödinger and Poisson equation for a charge density $n(t_{i-1})$. This defines the new charge density $n(t_i)$ and the procedure is iterated up to a desired time.

It must be noted that the integration of Eq. (1) allows also for the calculation at any given time and spectral component of the number of photons re-emitted by radiative recombination. This permits the calculation of both time integrated PL and time-resolved PL.

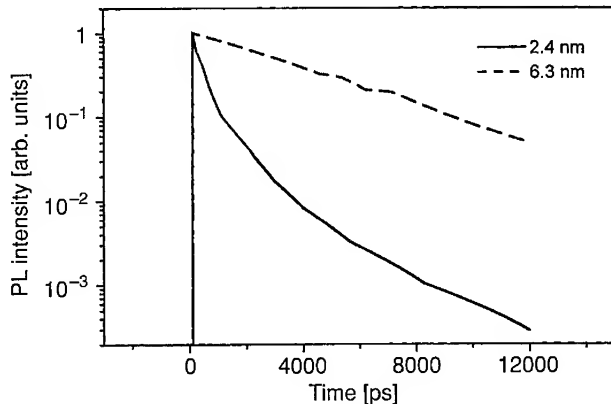


Fig. 1. Logarithmic plot of PL intensity as a function of time in 2.4 nm QW (upper trace) and 6.3 nm QW after excitation with an optical pulse of 5 ps with 10^{12} photons cm^{-2}

3. Time Resolved Photoluminescence We will consider $\text{Al}_{0.15}\text{Ga}_{0.85}\text{N}/\text{GaN}$ MQWs structures of two different well widths, the first one having well width of 2.4 nm and the second one of 6.3 nm. Barriers have a width of 7.5 nm. The structures are supposed to be grown on GaN substrate.

Figure 1 shows the time-resolved photoluminescence decay concentration for a 2.4 nm QW and for 6.3 nm QW after excitation with a gaussian optical pulse of 5 ps with 10^{12} photons cm^{-2} . We assumed for both the samples the same non-radiative recombination rate $\tau_{\text{nr}} = 5$ ns [4].

We notice that at longer times the photoluminescence in the two QW vary with a perfectly exponential decay with time constant equal to τ_{nr} , thus indicating that in both QWs non-radiative process dominates in Eq. (1). However, soon after the optical excitation, the 2.4 nm QW presents a much stronger decay rate than the other QW.

This decay rate is almost exponential, with a time constant of 0.5 ns. The fact that such behaviour is not observed in the wider QW is a clear indication that a much stronger oscillator strength builds up in the 2.4 nm QW, allowing the spontaneous recombination rate to overcome non-radiative dynamics.

4. Conclusion We presented a powerful method to determine optical properties of gallium nitride based heterostructures. Within our approach time-dependent behaviour of optical spectra can be predicted and discussed. We clarify the importance of self-consistency in the determination of spontaneous recombination rate and suggest also that the role of non-radiative recombination processes shall be considered for the recovery process after optical excitation. Self-consistency is also very important for the determination of the role of excitons in GaN QWs, and future analysis will be devoted to study also the relative importance of excitonic transitions in the time-dependent behaviour of optical spectra.

Acknowledgement Work supported in part by MURST and CLERMONT UE Network (Contract No. HPRN-CT-1999-00132).

References

- [1] P. LEFEBVRE, J. ALLEGRE, B. GIL, H. MATHIEU, N. GRANDJEAN, M. LEROUX, J. MASSIES, and P. BIGENWALD, *Phys. Rev. B* **59**, 15363 (1999).
- [2] J. SEO IM, H. KOLLMER, J. OFF, A. SOHMER, F. SCHOLZ, and A. HANGLEITER, *Phys. Rev. B* **57**, R9435 (1998).
- [3] J. DALFORS, J.P. BERGMAN, P.O. HOLZ, B.E. SERNELIUS, B. MONEMAR, H. AMANO, and I. AKASAKI, *Appl. Phys. Lett.* **74**, 3299 (1999).
- [4] J.C. HARRIS, T. SOMETA, K. HOSHINO, S. KAKO, and Y. ARAKAWA, *phys. stat. sol. (a)* **180**, 339 (2000).
- [5] F. DELLA SALA, A. DI CARLO, P. LUGLI, F. BERNARDINI, V. FIORENTINI, R. SCHOLTZ, and J.M. JANCU, *Appl. Phys. Lett.* **74**, 2002 (1999).
- [6] A. DI CARLO, F. DELLA SALA, P. LUGLI, V. FIORENTINI, and F. BERNARDINI, *Appl. Phys. Lett.* **76**, 3950 (2000).

phys. stat. sol. (a) **183**, 125 (2001)

Subject classification: 73.21.Fg; 78.20.Bh; S7.14

Temperature Induced Enhancement of the Exciton Binding Energy in Nitride Quantum Structures

P. BIGENWALD (a), B. GIL (b), A. KAVOKIN (c), and P. CHRISTOL (a)

(a) *Département de Physique, UFR Sciences, Université d'Avignon et des Pays de Vaucluse, 33 rue Louis Pasteur, F-84000 Avignon, France*

(b) *CNRS-GES, Université de Montpellier II, Place Eugene Bataillon CC 074, F-34095 Montpellier Cedex 5, France*

(c) *LASMEA, Université Blaise Pascal Clermont II-CNRS, 24 avenue des Landais, F-63177 Aubiere Cedex, France*

(Received October 8, 2000)

We theoretically study the evolution of exciton binding energies in GaN/AlGaIn quantum structures that are photo-pumped. The exciton binding energies are obtained by a variational approach. Dealing with strong intensities of injected carriers in the wells, we solve self-consistently Schrödinger and Poisson equations. Quantum exclusion principle due to the filling of the reciprocal space is included in the model via the proper choice of the exciton trial wavefunction. The excitation intensity leading to the bleaching of the electron-hole interaction is shown to depend strongly on the well width and on the lattice temperature.

1. Introduction We present in this communication a theoretical treatment for the problem of excitons in AlGaIn/GaN quantum structures, under high photo-injection conditions. We apply a variational approach to describe the electron-hole in-plane binding, while normal-to-the plane single-particle wavefunctions are found by a self-consistent numerical solving of Schrödinger and Poisson equations. We particularly analyze the photo-injection effect on the exciton state. The electron-hole plasma screens the piezoelectric fields that stabilizes the exciton. On the other hand, it screens the exciton itself, and finally, at high pumping intensities, suppresses the exciton. To describe correctly this latter effect, care has to be taken in the choice of the trial function [1]. In the present study, we account for the filling of the reciprocal space and for the quantum exclusion effects at large injection densities [2] by introducing limitations on the class of trial functions used in the excitonic calculation. The exciton cohesion is found to be dependent on the injection density σ : the larger σ , the greater the kinetic energy and the smaller the binding energy E_b . We have previously studied a series of quantum wells with varying widths and have demonstrated that a small increase of the exciton energy is expected up to a critical value of the injection density, this critical value decreases with the well width [3]. The bleaching of the exciton actually begins beyond this critical value of σ . The Fermi Dirac distribution of the carriers varies with the temperature. This has significant implication at the scale of the exciton binding energy. We show that the excitonic character of the fundamental transition in nitride quantum structures persists at larger carrier injection intensities when the temperature increases.

2. Formalism We extend the technique developed in Ref. [4] for the exciton state calculation in a $\text{Al}_{0.11}\text{Ga}_{0.89}\text{N}/\text{GaN}$ single QW sample to account for the free electron-hole plasma effect on excitons. Due to spontaneous and piezoelectric components, the electric field in the well is very strong (about 1 MV/cm). The self-consistent resolution of Poisson and Schrödinger equations required to obtain the correct electron and hole eigenfunctions $\chi_e(z)$ and $\chi_h(z)$ is described in Ref. [5]. Due to heavy carrier masses, we only consider fundamental states for $\sigma \leq 2 \times 10^{12} \text{ cm}^{-2}$.

In our model, a single free exciton state interacts with a non-correlated electron-hole plasma in the QW. This model is relevant to describe the optical reflection experiments under continuous band-to-band pumping. The plasma being characterized by its Fermi wavevector $k_F = \sqrt{2\pi\sigma}$, the quantum exclusion effect implies that we have to account for the filling of the reciprocal space: only exciton states whose wavefunction is constructed using the electron and hole harmonics with $k > k_F$ are allowed at $T = 0$ K. In reciprocal space, the kinetic and potential terms of exciton Hamiltonian write

$$H_{\text{ex}} = U + T = \frac{\hbar^2 k^2}{2\mu} - e\varphi_{\text{eh}}(k, z_e - z_h), \quad (1)$$

μ being the reduced mass of the exciton relative motion, k its in-plane wave vector. Averkiev et al. [6] and Pikus [7] have proposed a smart approach to this problem: their trial wavefunction writes

$$\varphi(q) = A e^{-\alpha q} \cos(\Omega(T) k_F q). \quad (2)$$

q is the in-plane coordinate of the electron-hole relative motion, A is the normalization constant and $\Omega(T) = \exp(-\beta \varepsilon_F)$. ε_F is the Fermi energy of the plasma and β the inverse of the thermal energy. The specific reasons that justify the choice of this trial function can be found in Ref. [3]. In the context of the Thomas-Fermi approximation [6], the potential energy of the exciton writes

$$e\varphi_{\text{eh}}(q, z_e - z_h) = \frac{e^2}{4\pi\epsilon_0\epsilon_r q} \left\{ e^{-q|z_e - z_h|} - \frac{\left[\int_{-\infty}^{\infty} f(u) e^{-q|u - z_e + z_h|} du \right]^2}{\frac{q}{q_s} + \int_{-\infty}^{\infty} f(u) du \int_{-\infty}^{\infty} f(u') e^{-q|u - u'|} du'} \right\}, \quad (3)$$

in which q_s is the reciprocal screening radius of the 2D electron gas, $f(z) = \chi_e^2(z) - \chi_h^2(z)$ the exciton wavefunction along z -axis and ϵ_r is the static dielectric constant.

3. Theoretical Results In Fig. 1 the evolutions of the two components – kinetic and potential – of the exciton binding energy versus σ are represented for $T = 0, 10$ and 100 K. Neglecting the very low injection conditions, we first see different tendencies for the two sets of curves. The square overlap of electron and hole eigenfunctions increases linearly with the injection density of carriers from 0.71% up to 2.67% when σ scales up to $2 \times 10^{12} \text{ cm}^{-2}$ resulting in smaller fields in the well layer. Logically, the potential energy increases simultaneously whereas not linearly. This energy reaches a maximum at a critical value of injection that depends on the temperature and then decreases: the higher the temperature, the higher the critical value. The saturation can be attributed to the screening of the dielectric constant for flatter and densely populated wells.

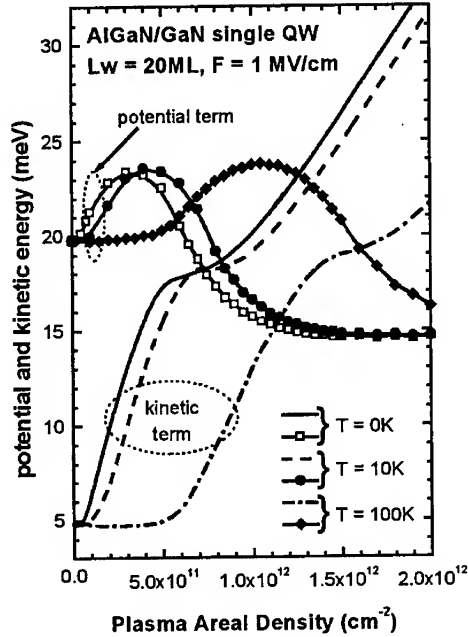


Fig. 1. The two components in the exciton binding energy for the fundamental transition in a 5.2 nm wide AlGaIn/GaN polarized single quantum well as a function of the density of injected carriers for different temperatures

Concerning the kinetic energy, we have a plateau as long as the Fermi energy is negligible compared to the kinetic energy at $\sigma = 0$ then we switch to quasi-linear regimes. A first linear regime is found simultaneously with the increase of the potential energy. The in-plane exciton radius diminishes. Then a second plateau regime is found: the higher the temperature, the more stable the exciton with σ in this regime. Finally, the in-plane radius increases and the kinetic energy increases linearly with σ , the bleaching of the exciton occurs when the kinetic energy exceeds the potential one. We note

that the Fermi-Dirac distribution allows the states with $k < k_F$ to be populated at $T > 0$. This contributes to the reduction of the exciton kinetic energy.

In Fig. 2, we display the evolution of the exciton binding energy as a function of the temperature for three values of the injection intensity. At 0 K, these values of σ are in the saturation regime since an increase of σ leads to a decrease of E_b . We note that,

when increasing the temperature, we increase the exciton binding energy and these curves tend to focus at high temperatures. This convergence comes from the fact that, at high temperature, the exciton trial function $\psi(\rho)$ is no longer influenced by k_F and does not oscillate: the only difference comes from the flatter well profile.

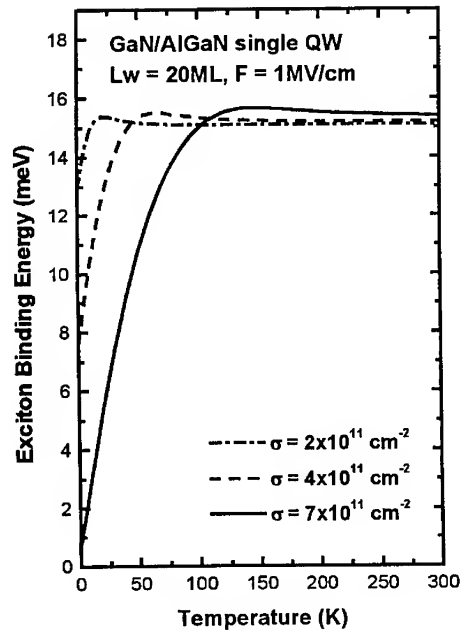


Fig. 2. Exciton binding energy of the fundamental transition in a 5.2 nm wide AlGaIn/GaN polarized single quantum well as a function of the temperature for different densities of injected carriers

In conclusion, we have investigated exciton physics in AlGaN/GaN single quantum wells under strong photo-injection conditions, by a variational approach, including the quantum exclusion effect. We show that, in these structures, the bleaching of the exciton by large carrier injection intensities may be reduced when the temperature is increased.

References

- [1] N.S. AVERKIEV, G.E. PIKUS, and M.L. SHMATOV, Soviet Phys. — Solid State **30**, 1884 (1989).
- [2] F.G. PIKUS, Soviet Phys. — Semicond. **26**, 26 (1992).
- [3] P. BIGENWALD, A. KAVOKIN, P. CHRISTOL, B. GIL, and P. LEFEBVRE, phys. stat. sol. (b) **216**, 481 (1999).
- [4] P. BIGENWALD, P. LEFEBVRE, T. BRETAGNON, and B. GIL, phys. stat. sol. (b) **216**, 371 (1999).
- [5] PH. BORING, B. GIL, and K.J. MOORE, Phys. Rev. Lett. **71**, 1875 (1993).
- [6] N.S. AVERKIEV, G.E. PIKUS, and M.L. SHMATOV, Soviet Phys. — Solid State **30**, 1884 (1989).
- [7] F.G. PIKUS, Soviet Phys. — Semicond. **26**, 26 (1992).

phys. stat. sol. (a) **183**, 129 (2001)

Subject classification: 78.47.+p; 78.66.Fd; 78.67.De; S7.14

Phonon Replica Dynamics in High Quality GaN Epilayers and AlGaIn/GaN Quantum Wells

D. ALDERIGHI (a, b), A. VINATTIERI (a, b), F. BOGANI (a, c), M. COLOCCI (a, b), S. GOTTARDO (b), N. GRANDJEAN (d), and J. MASSIES (d)

(a) *Istituto Nazionale Fisica della Materia INFM, Unità di Firenze, Largo E. Fermi 2, I-50125 Firenze, Italy*

(b) *Dipartimento di Fisica and LENS, Largo E. Fermi 2, I-50125 Firenze, Italy*

(c) *Dipartimento di Energetica, via S. Marta 3, I-50139 Firenze, Italy*

(d) *Centre de Recherche sur l'Hétéro-Epitaxie et ses Applications, CNRS, rue B. Grégory, Sophia Antipolis, F-06560 Valbonne, France*

(Received October 8, 2000)

We present an experimental study of the exciton and phonon replica dynamics in high quality GaN epilayers and AlGaIn/GaN quantum wells (QW) by means of picosecond time-resolved photoluminescence (PL) measurements. A non-exponential decay is observed both at the zero phonon line (ZPL) and at the $n = 1$ LO replica. Time-resolved spectra unambiguously assign the replica to the free exciton A recombination. Optical migration effects are detected both in the epilayer and the QWs samples and disappear as the temperature increases up to 60–90 K. Even though the sample quality is comparable to state-of-the-art samples, localization effects dominate the exciton dynamics at low temperature in the studied GaN based structures.

1. Introduction Strong phonon-replica-emission (PRE) of the free and bound exciton zero phonon lines (ZPL) are commonly observed in GaN based structures up to room temperature. In fact several lines are observed as replica of the main emission with a characteristic energy separation of ≈ 91 meV equal to the LO phonon energy. In the framework of a configuration-coordinate model (CC) developed by Huang and Rhys [1] the interaction between excitons and LO phonons is characterized by a coupling constant S which determines the intensity ratio among the ZPL and the different replica ($n = 1, n = 2$, etc.). While results have been reported on the spectral shape of the ZPL and PRE in GaN epilayers [2] and values of the S parameter have been deduced from the intensity ratio of the main PL and the phonon sidebands in GaN based quantum wells [3], to our knowledge, very scarce information is available on the temporal behavior of the replica emission compared with the ZPL time evolution. In fact, if we consider a free exciton recombination, both shape and temporal profile have to be described in the framework of an exciton-polariton model. As a consequence, in the case of radiative recombination for bulk crystals, the exciton has to conserve the photon momentum K to recombine; therefore only $K \approx 0$ excitons radiate. In the case of QWs only the component of K in the well plane has to be conserved with the known consequences on the value of the radiative rate, see e.g. [4]. If LO phonons participate in the recombination process, excitons with different K values can recombine transferring the momentum to the lattice before reaching a thermalized distribution. As re-

ported in [2, 5] the flatness of the LO phonon band for low momentum values should allow to extract the kinetic energy distribution of the excitons from the lineshape of the PRE and the evolution of the exciton temperature from the time-resolved spectra of the PRE. In this paper we show that even in state-of-the-art samples (epilayers and QWs) the fundamental hypothesis underlying the forementioned interpretation is lacking; in particular efficient non-radiative recombination channels are present even at low T and recombination from localized states dominates the emission. In particular we will show that for QW samples recombination from long-living states provides a significant contribution to the PRE. Finally, optical migration effects are observed both in epilayer and QW samples.

2. Results We investigated high quality 2 μm thick GaN epilayers grown by MBE technique on a c -plane sapphire substrate and $\text{Al}_x\text{Ga}_{1-x}/\text{GaN}$ single and multiple quantum wells with x ranging between 0.09 and 0.2. The barrier width was 50 \AA and the well width was 20 or 42 \AA , depending on the sample. Since the experimental findings

are similar in the epilayers and QW samples, we will present results on one epilayer and on a 42 \AA single QW. A 4 ps frequency-doubled mode-locked synchronously pumped dye laser and a 2 ps frequency-doubled mode-locked Ti:sapphire laser were used as excitation sources. Time-resolved spectra were acquired by means of a time-correlated single photon counting apparatus using as detector a multichannel plate (experimental time resolution 50 ps) or by means of a synchroscan streak-camera allowing for a time resolution of 2 ps. The samples were kept in a closed-cycle cryostat and the temperature was varied between 10 and 300 K. The excitation density was varied between 5×10^{-2} and 50 W cm^{-2} .

In Fig. 1a the time-integrated PL spectrum of the epilayer is shown at 10 K. A clear emission from the free exciton A and a shoulder at the free

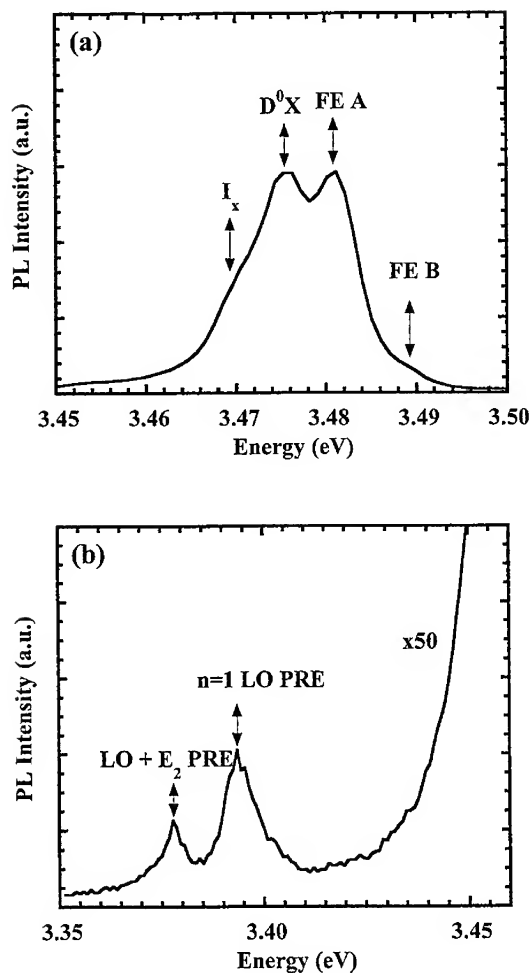


Fig. 1. a) PL time-integrated spectrum of the GaN epilayer at 10 K; b) time-integrated spectrum of the PRE for the same sample. Assignments are discussed in the text

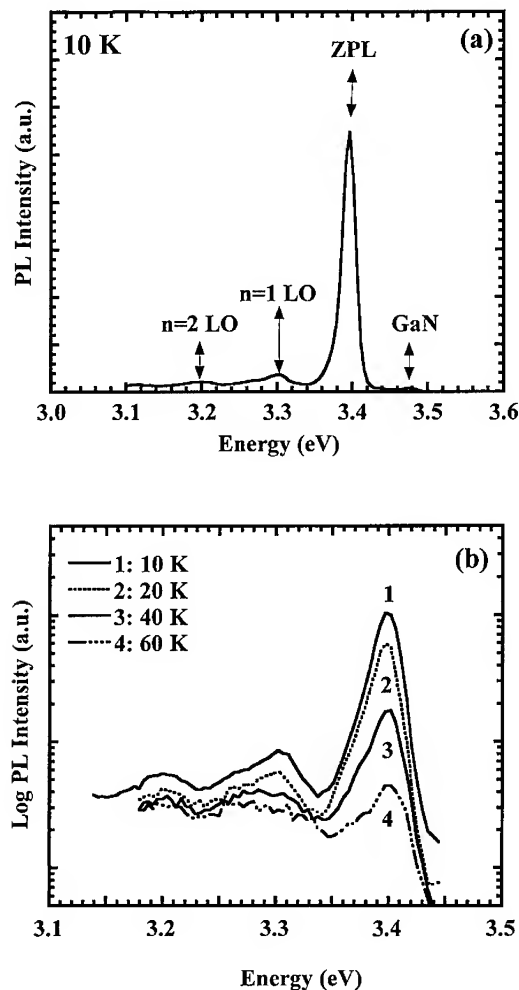


Fig. 2. a) PL time-integrated spectrum of the 42 Å AlGaIn/GaN QW; b) PL spectra at different temperatures for the same sample

exciton B are observed besides two features arising from bound exciton recombination [6]. In Fig. 1b the phonon replica spectrum is reported. From the energy separation we attribute the main replica to a LO phonon assisted emission of the FE A exciton, while the other peak corresponds to a LO + E_2 phonon assisted emission. Increasing the temperature, the emission from the bound excitons decreases while the FE A recombination becomes dominant. Correspondingly the intensity of the replica increases indicating again a dynamics correlated with FE A. A thermal quenching of the overall free exciton emission occurs with an activation energy of the order of 26 meV comparable with the exciton binding energy. Strong PRE are also observed in the QW sample (Fig. 2a); the well PL is red-shifted by the internal piezoelectric field with respect to the GaN emission. In Fig. 2b the PL temperature dependence is reported: apparently the main PL emission quenches more rapidly than the phonon replica

as a consequence of a long tail in the low energy side of the spectrum which persists as the temperature increases. Concerning the dependence on the excitation density a linear dependence is observed in the investigated range for both samples.

In Fig. 3 time-resolved spectra of the epilayer are shown at a lattice temperature of 10 K. In Fig. 3a the spectra are normalized at the peak intensity to make clear the change in the shape and the dominant contribution of the bound states at longer delays. In Fig. 3b the PRE is shown for the same time delays with no arbitrary normalization; it turns out that the replica dynamics follows the time evolution of the FE A exciton. In Fig. 4a the time decay of PRE (equal to that of FE A) and FE B excitonic recombination are compared for quasi-resonant excitation ($E_{\text{exc}} = 3.518$ eV). The rise-time of PRE is definitely slower (≈ 4 ps) than the FE B signal. The fast rise of the luminescence has to be noted even if no LO phonon can be emitted during the relaxation path, being the excitation excess energy smaller than 91 meV. Moreover, the fast decay of the exciton emission (≈ 15 ps) suggests a rapid capture in shallow states as

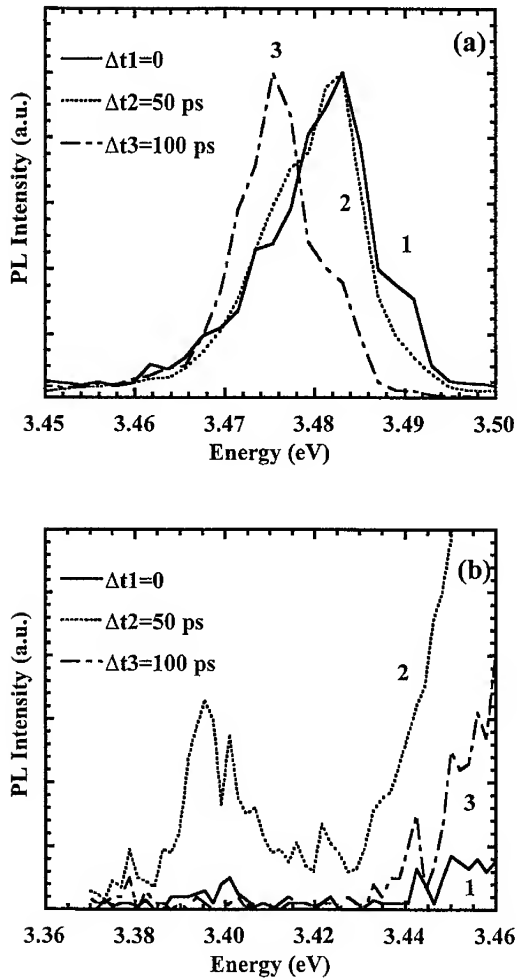


Fig. 3. Time-resolved spectra of the PL from the epilayer at 10 K for different delay times: a) normalized spectra, b) non-normalized spectra of the PRE

also shown by the time-resolved spectra. Also the decay of PRE is slower in agreement with the time-resolved spectra. Such differences disappear as the temperature increases up to 90 K when the two time evolutions become identical. In Fig. 4b time decays at low T are shown for different emission energies, corresponding to the four states labeled in Fig. 1a; the decays are not exponential and as the detection energy decreases the decay rate become slower. As T increases, such effect disappears. Summarizing the experimental findings on the epilayer samples we conclude that at low T the time-resolved spectra indicate a lack of thermalization suggesting a quite complex dynamics between excitons (bound and free) and carriers [7]. When the temperature increases, thermalization occurs, but the decrease of the quantum efficiency, measured from the time integrated spectra, comes from the opening of efficient non-radiative channels. Therefore, we observe that,

despite the fact that our samples show an overall high quality, the possibility is still questionable of extracting radiative rates and making comparison with a polariton model for the exciton dynamics in GaN based structures in the light of our and others experimental findings [7]. Such a conclusion is even more true (unfortunately) if we consider AlGaIn/GaN quantum well samples. In fact, as shown in Fig. 2b, the intensity strongly decreases both at the ZPL and PRE as the lattice temperature increases due to efficient non-radiative centers. It is worth noting that a broad emission at low energy still persists up to 80 K when the main PL band has already disappeared. In Fig. 5a time-resolved spectra at different time delays are shown for the same sample. A clear red shift of the emission is observed at longer delays and it is accompanied by a modification of the lineshape. Two consequences come from such results: firstly again a lack of thermalization in the band as observed in the epilayer, secondly the shift cannot be attributed to a reduced screening of the internal piezoelectric field from the photoexcited carriers. In fact this effect is not expected to significantly modify the spectral

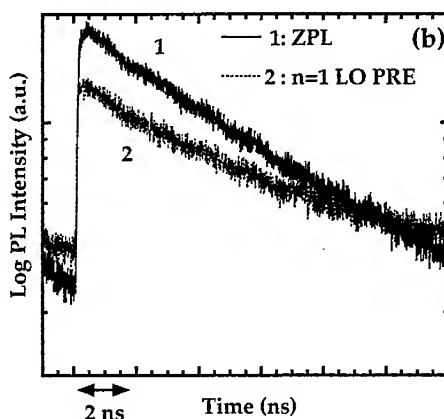
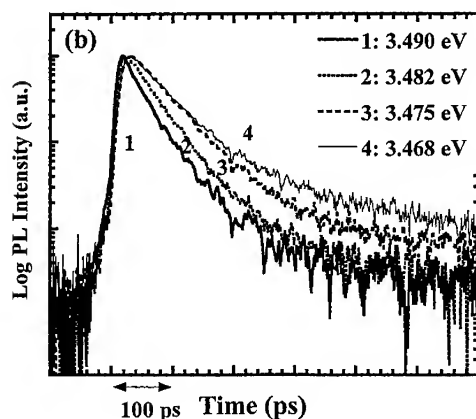
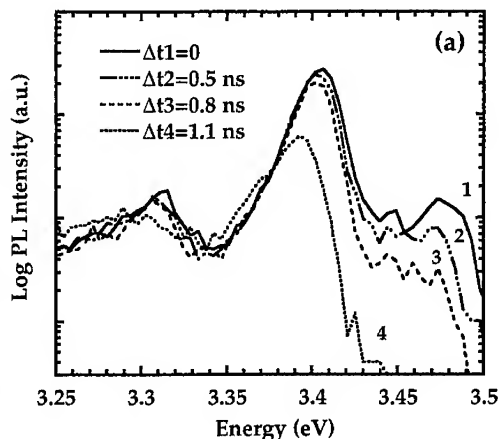
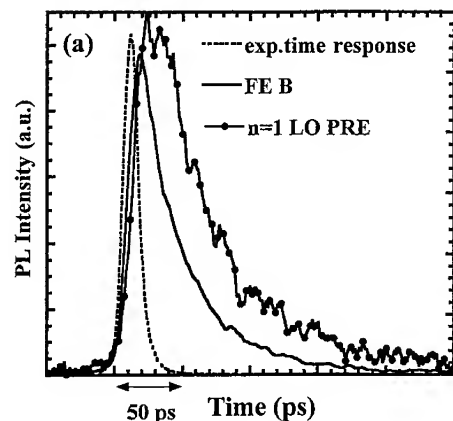


Fig. 4

Fig. 5

Fig. 4. PL time decays of the epilayer for different detection energies: a) dashed line: experimental time response, solid line FE B emission, solid line with points LO PRE. b) PL time decays detected at the emission energies labeled in Fig. 1a

Fig. 5. a) Time-resolved spectra of the QW PL for different delay times; b) PL time decay detected at the ZPL and at the PRE

shape of the PL spectrum. Moreover no dependence of the PL time decay has been observed in the investigated excitation density range. It has to be noted that the change in the lineshape is also present in the PRE. In Fig. 5b the time evolutions of the ZPL and $n = 1$ PRE are reported. Non-exponential decays are observed with a long decay tail (of the order of several ns) more important in the PRE. From the temperature dependence we attribute the long-living component of the PRE to the low energy states observed in the PL spectra (Fig. 2b). Therefore, in the comparison of the ZPL and PRE dynamics, an important contribution is given by deeply localized states. We observe that in ref. [5] a change in the PRE lineshape is reported for a GaN epilayer and it is explained in terms of a cooling of the exciton distribution. We exclude this explanation in our sample because the comparison of the time-resolved measurements

with the time-integrated data indicate an interplay between bound and free excitons dominant at low T , making unlikely the dominance of free exciton recombination in the measured signal.

3. Conclusions We have presented an experimental study of exciton and phonon replica dynamics with a ps time resolution on GaN based structures. The comparison of time-integrated and time-resolved measurements as a function of the lattice temperature show that the ZPL dynamics is determined by an interplay between free and bound excitons and non-radiative channels become significant at rather low temperature denoting an overall sample quality definitely poorer with respect to other III-V compounds even in state-of-the-art samples. In particular quite clear is the optical migration effect observed both in the epilayer and in the QW sample. At low temperature a fast capture (≈ 15 ps) into bound states is measured for the free exciton of the epilayer in agreement with fs pump-probe measurements [7]. The temperature dependence of decay rates and quantum yield suggest a dominant contribution from extrinsic effects to the exciton dynamics.

Acknowledgement This work has been partially supported by the EC-RTN contract HPRN-CT-1999-00132 Clermont.

References

- [1] B.K. RIDLEY, *Quantum Processes in Semiconductors*, Oxford Science Publications, Oxford 1988.
- [2] D. KOVALEV, B. AVERBOUKH, D. VOLM, B.K. MEYER, H. AMANO, and I. AKASAKI, *Phys. Rev. B* **54**, 2518 (1996).
- [3] M. SMITH, J.Y. LIN, H.X. JIANG, A. KHAN, Q. CHEN, A. SALVADOR, A. BOTCHKAREV, W. KIM, and H. MORKOC, *Appl. Phys. Lett.* **70**, 2882 (1997).
- [4] J. SHAH, *Ultrafast Spectroscopy of Semiconductors and Semiconductors Nanostructures*, Springer Series in Solid State Science, Ed. M. CARDONA, Vol. 115, Springer-Verlag, Berlin/Heidelberg/New York 1996.
- [5] D. HAGELE, R. ZIMMERMANN, M. OESTREICH, M.R. HOFMAN, W.W. RÜHLE, B.K. MEYER, H. AMANO, and I. AKASAKI, *Phys. Rev. B* **59**, R7797 (1999).
- [6] D.G. CHTCHEKINE, G.D. GILLILAND, Z.C. FENG, S.J. CHUA, D.J. WOLFORD, S.E. RALPH, M.J. SCHURMAN, and I. FERGUSON, *MRS J. Nitride Semicond. Res.* **4S1**, G6.47 (1999).
- [7] S. HESS, F. WALRAET, R.A. TAYLOR, J.F. RYAN, B. BEAUMONT, and P. GIBART, *Phys. Rev. B* **58**, R15973 (1998).

phys. stat. sol. (a) **183**, 135 (2001)

Subject classification: 78.20.Bh; S7.14

First Observations of 2D Photonic Crystal Band Structure in GaN–Sapphire Epitaxial Material

D. COQUILLAT¹) (a), A. RIBAYROL (b), R.M. DE LA RUE (b),
M. LE VASSOR D'YERVILLE (a), D. CASSAGNE (a), and C. JOUANIN (a)

(a) *Groupe d'Etude des Semiconducteurs, UMR 5650, CNRS, Université Montpellier 2, Place Eugène Bataillon, F-34095 Montpellier cedex 05, France*

(b) *Department of Electronics and Electrical Engineering, University of Glasgow, Rankine Building, Glasgow G12 8LT, Scotland, UK*

(Received October 8, 2000)

We report on the first characterisation of the band structure of two-dimensional triangular photonic crystals of air holes in an epitaxial group III nitride film. The structures were fabricated by electron beam lithography and reactive ion-etching.

1. Introduction The group III nitrides are now widely recognised as vital for efficient generation of blue light by current injection in LEDs and lasers. We report on the first characterisation, to our knowledge, of the band-structure properties of photonic crystals realised as two-dimensional triangular lattices of holes in an epitaxial III nitride film. Mapping the band structure of photonic crystals is important because of phenomena such as superprism effects [1, 2] and reduced group-velocity [3–5], as well as the modification of emission via bandgap effects.

The two-dimensional photonic crystals were fabricated by electron beam lithography and reactive ion-etching in a simple GaN/sapphire heterostructure [6], with strong vertical confinement resulting from the large film–substrate refractive index difference (contrast $\sim 2.35:1.7$). The position of resonance dips has been measured in transmission as a function of the angle of incidence and the dispersion relations have been experimentally constructed.

2. Experimental We have developed a process in order to transfer patterns from PMMA into GaN using an intermediate mask which consisted of a 300 nm thick SiN_x layer and a 50 nm thick Ti layer evaporated on top of SiN_x . The 50 nm Ti layer was etched in a SiCl_4 plasma using a 200 nm thick PMMA layer. The Ti layer was subsequently used as a mask in a CHF_3 plasma to etch the 300 nm thick SiN_x layer, which in turn was used to transfer the patterns into GaN epilayers [6]. In a CH_4/H_2 plasma vertical etching was achieved with sidewall angles up to 81° . The scanning electron micrograph of Fig. 1a shows a typical local region of the etched photonic crystal in a $1.6\ \mu\text{m}$ thick GaN epilayer grown on (0001) sapphire. The sample consisted of a number of triangular lattices of holes and pillars with different lattice constant a and with different air-filling factor f [6]. We have focused our study on three lattices of holes with the

¹) Corresponding author; Fax: +33 (0)4 67 14 37 60; e-mail: coquillat@ges.univ-montp2.fr

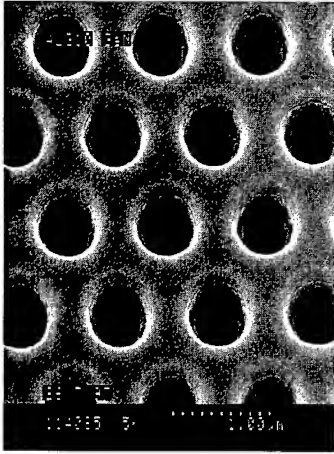
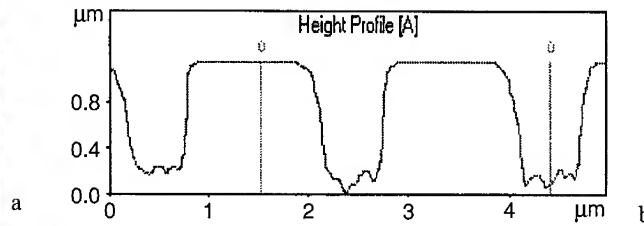


Fig. 1. a) Electronic microscopy image of a photonic crystal with a triangular arrangement of air holes etched in GaN/sapphire. The holes are 490 nm in diameter and the spacing is 1.0 μm so that $f = 0.22$ b) AFM profile of an air hole lattice. The holes are etched 1.1 μm deep into GaN



periodicity $a = 1 \mu\text{m}$ and with various hole diameters so that $f = 0.19, 0.21$ and 0.22 . The sidewall verticality of the holes is quite good as shown in the height profile obtained by atomic microscopy measurements in resonant mode (Fig. 1b). The hole penetration-depth into the epilayer was 1.1 μm .

Our general approach for measurement has followed that of Astratov et al. [3], which is based on the reflection spectra for collimated white light incident on the surface of the 2D photonic crystal over a range of angles with respect to the surface normal. The sharp resonances observed in the reflection spectra of Refs. [3] and [4] are due to the Bloch modes allowed to propagate through the photonic crystal when both energy and in-plane wavevector match those of the photonic structure. We used white light transmission measurements to determine the position of different resonances by scanning the angle of incidence θ from 0° to 28° with an accuracy of $\pm 1^\circ$. Transmission spectra were taken using a Fourier transform infrared spectrometer. The white light from a tungsten lamp is focused on a pinhole used as a point light source. The light is collimated within a 1° solid angle formed by a diaphragm in such a way that the diameter of the spot illuminating the sample was approximately 150 μm . The transmitted image of the lattice is magnified and projected on a second collimating diaphragm placed before the detector, which permits the collection of light transmitted only through the 100 μm large square area of the lattice. The sample is defined to lie in the (x,y) plane. Rotating the sample around the y axis by 2° up to 28° allows the study of the dispersion relation in the k_x direction. The transmission spectra were measured from 4000 to 12000 cm^{-1} for both E and H polarised light and the Γ -M orientation was chosen for k_x .

3. Results and Discussion We first measured the transmission at normal incidence ($\theta = 0^\circ$) from an unetched area on the sample very near to the lattice with $f = 0.22$. The Fig. 2a shows long-period oscillations arising from interferences of the beam multiply reflected by the interfaces and additional features due to the nearby photonic crystal. The transmission from the three photonic crystal lattices is markedly different than from the unetched area (Fig. 2a). The periods of the oscillations become larger, indicative of the decrease of average refractive index value n_{av} of the lattice and sharp reso-

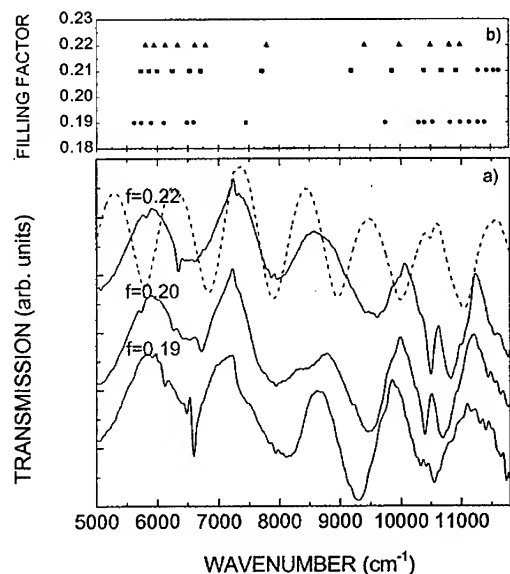


Fig. 2. a) Transmission spectra at normal incidence $\theta = 0^\circ$ from an unetched area (dashed line) and from the photonic crystals (solid line) with filling factor of 0.19, 0.21, 0.22. b) Spectral positions of the resonance dips at $\theta = 0^\circ$ for $f = 0.19$ (circle), 0.21 (square), and 0.22 (up triangle)

nance dips appear. With increasing filling factor, the resonance dips shift to higher energy as shown in Fig. 2b. Some of the energy of the incident light within a solid angle of $\sim 1^\circ$ couples into several propagating modes and these propagating modes appear on the spectra as resonance dips.

Typical results for E and H polarised incident light (E when the electric field of the light is parallel to the hole axis)

are shown in Fig. 3 for the lattice with $f = 0.19$. When θ increases from zero up to 28° , a remarkable difference between E and H appears. The sharp resonances were found to shift with of the angle of incidence θ and to be dependent on the polarisation of the incident beam.

The experimental results in Fig. 4 represent the spectral position of the dips plotted as $\omega a/2\pi c$ versus the in-plane wavevector $k_x = \omega/c \sin \theta$ for E and H polarisation. Such complex and varied dispersive behaviour is attributable to photonic crystal band-structure effects. This interpretation receives support by comparing these experimental results with a theoretical 2D simulation using the plane wave expansion method with a basis of 1024 plane waves for a refractive index of 2.0. Although the experimental and numerical values are not too close, the theoretical simulation provides good guidance for understanding the spectral behaviour.

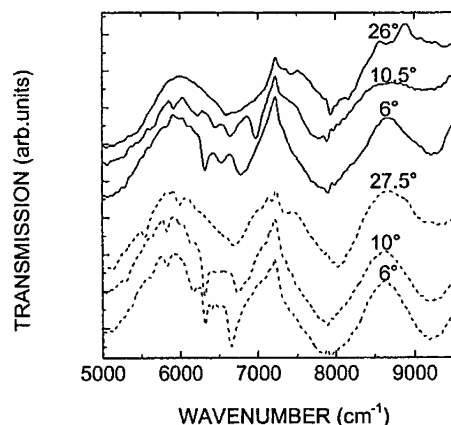


Fig. 3. Transmission spectra for three different angles of incidence θ , for E (solid line) and H (dashed line) polarisation from the lattice with $f = 0.19$. Light was incident along the Γ -M direction

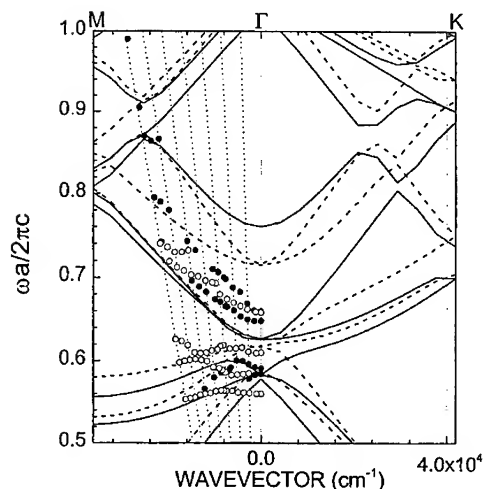


Fig. 4. The full (open) circles are the measured data for E (H) polarisation from the $1\text{ }\mu\text{m}$ period photonic crystal with an air-filling factor of 0.19. The photonic band structure is calculated for a refractive index of 2.0, for E (solid line) and H polarisation (dashed line). Oblique dotted lines correspond to light incident on the lattice at angles of incidence from 4° to 28° by 4° .

4. Conclusion The behaviour of the dips observed in the transmission spectra as a function of different parameters (lattice period, angle of incidence, polarisation) is clear evidence of photonic band-structure effects in our GaN photonic crystals. Moderately good agreement is obtained between experiment and strictly 2D computations of the photonic band structure based on an effective index approximation. The full impact of finite layer thickness on the relationship between experimental measurements and computation, including polarisation cross-coupling possibilities, requires a strictly three-dimensional and vectorial computation. These results highlight the excellent quality of the fabrication achieved and launch the field of photonic bandgap engineering in large electronic bandgap nitride semiconductors.

References

- [1] H. KOSAKA, T. KAWASHIMA, A. TOMITA, M. NOTOMI, T. TAMAMURA, T. SATO, and S. KAWAKAMI, *J. Lightwave Technol.* **17**, 2033 (1999).
- [2] H. KOSAKA, T. KAWASHIMA, A. TOMITA, M. NOTOMI, T. TAMAMURA, T. SATO, and S. KAWAKAMI, *Appl. Phys. Lett.* **74**, 1212 (1999).
- [3] V. ASTRATOV, R. STEVENSON, M. SKOLNICK, D. WHITTAKER, S. BRAND, I. CULSHAW, T. KRAUSS, R. DE LA RUE, and O.Z. KARIMOV, *Inst. Elec. Engng. Proc. Optoelectron.* **145**, 398 (1998).
- [4] V. ASTRATOV, R. STEVENSON, S. CULSHAW, D. WHITTAKER, M. SKOLNICK, T. KRAUSS, and R. DE LA RUE, *Appl. Phys. Lett.* **77**, 178 (2000).
- [5] V. PACRADOUNI, W. MANDEVILLE, A. COWAN, P. PADDON, S. JOHNSON, and J. YOUNG, *Phys. Rev. B* **62**, 4204 (2000).
- [6] D. COQUILLAT, S. MURAD, A. RIBAYROL, C. SMITH, R. DE LA RUE, C. WILKINSON, O. BRIOT, and R.L. AULOMBARD, *ICSCIII-N'97, Stockholm, Mater. Sci. Forum* **264/268**, 1403 (1998).

phys. stat. sol. (a) **183**, 139 (2001)

Subject classification: 78.67.De; S7.14

Absorption and Emission of (In,Ga)N/GaN Quantum Wells Grown by Molecular Beam Epitaxy

L. SIOZADE¹) (a), P. DISSEIX (a), A. VASSON (a), J. LEYMARIE (a), B. DAMILANO (b),
N. GRANDJEAN (b), and J. MASSIES (b)

(a) LASMEA, UMR 6602, CNRS/UBP, 24 Avenue des Landais, F-63177 Aubière, France

(b) CRHEA, CNRS, rue Bernard Grégory, Sophia Antipolis, F-06560 Valbonne, France

(Received October 8, 2000)

Thermally detected optical absorption (TDOA) and photoluminescence experiments are carried out on $\text{In}_{0.16}\text{Ga}_{0.84}\text{N}/\text{GaN}$ multi-quantum wells (MQWs) grown by molecular beam epitaxy on (0001) sapphire substrates. A model proposed to adjust the TDOA line shape, allows to deduce the band-edge energies, the absorption coefficients and the broadening parameters of the (In,Ga)N MQWs for different thicknesses. The Fabry-Pérot oscillations, which structure the TDOA spectra, are considered in this modelling to accurately account for the experimental data. The emission, which covers the whole visible spectrum at room temperature, is achieved by varying the thickness from 1.5 to 5 nm. A very large Stokes shift between the emission and absorption energies is deduced at low temperature, for the (In,Ga)N MQWs.

1. Introduction The (In,Ga)N alloy is very attracting because it offers interesting potentialities for the fabrication of light emitting devices operating in the red to ultraviolet energy region. The use of (In,Ga)N/GaN multiple quantum wells (MQWs) as the active material in commercialized blue and green light-emitting diodes has already been demonstrated [1]. However, the comprehension of radiative and non-radiative recombination mechanisms in relation to the absorption process is still a subject of active discussion. On one side, the influence of localized states induced by composition fluctuations of (In,Ga)N alloys is advanced [2]. On the other side, the effects of the built-in piezoelectric field in strained (In,Ga)N heterostructures determine the energy position and the oscillator strength of the optical transitions [3]. Spontaneous polarization effects have also been evidenced in such heterostructures [4]. In this paper, thermally detected optical absorption (TDOA) and photoluminescence (PL) experiments are used to deduce the absorption and emission energies of (In,Ga)N/GaN MQWs grown by molecular beam epitaxy (MBE), on sapphire substrates, as a function of the MQW thickness. The absorption energies, the absorption coefficients and the broadening parameters are deduced from a modelling of the TDOA line shape, by also taking the Fabry-Pérot interferences into account.

2. Growth and Experimental Details GaN and (In,Ga)N layers were grown by MBE on c-plane sapphire substrates. Before the growth of the (In,Ga)N/GaN MQWs, a few

¹) Corresponding author; phone: 0473405208; Fax: 0473407262;
e-mail: siozade@lasmea.univ-bpclermont.fr

micron thick GaN template was deposited at 800 °C [5]. The substrate temperature was then reduced to 550 °C to grow the (In,Ga)N layers. On top of each (In,Ga)N layer, the GaN barrier was deposited while the temperature was progressively increased up to 800 °C. The well thickness varies from 1.5 to 5 nm and the top GaN barrier is about 14 nm thick. An In composition of $(16 \pm 2)\%$ was measured by high-resolution X-ray diffraction experiments which also concluded that the whole structure is pseudomorphically strained onto the GaN template [6].

TDOA experiments were carried out at 0.35 K. This technique consists in the detection of the heating of the sample induced by the phonon emissions due to non-radiative de-excitations occurring after the optical absorption. Details about the experimental set-up can be found in Ref. [7]. PL experiments were carried out at 4 K using a 325 nm HeCd laser.

3. Adjustment of the TDOA Line Shape TDOA and PL spectra performed on four (In,Ga)N/GaN MQWs are shown, as solid lines, in Fig. 1. On the TDOA spectra, two absorption thresholds appear. One shifts from one sample to the other and is related to (In,Ga)N, the other is due to GaN. On each PL and TDOA spectrum, oscillations with different periods appear in the energy range lower than the GaN band-gap energy; they correspond to Fabry-Pérot (FP) interferences which are due to the flatness of the layers. Regarding the PL spectra, it clearly appears that the emission energy of (In,Ga)N MQW decreases when the well thickness increases. But, concerning the TDOA spectra, it is difficult to determine precisely the absorption edge energy of each

MQW without using a theoretical description. In order to accurately account for the experimental TDOA line shape, the FP oscillations are also adjusted by this model. It is based on the conservation of the total intensity if diffusion phenomena are neglected: $1 = A + R + T$, where A , R and T represent respectively the absorbed, reflected and transmitted light intensities. The TDOA signal is assumed to be proportional to A . The samples are described by a succession of multi-layers deposited on a substrate. To take the oscillations into account, each GaN and (In,Ga)N layer is described by a FP cavity, in which

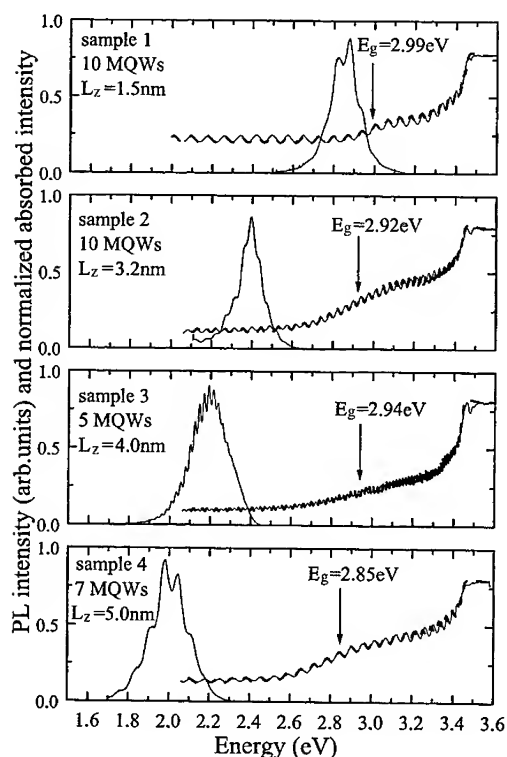


Fig. 1. TDOA (0.35 K) and PL (4 K) spectra of $\text{In}_{0.16}\text{Ga}_{0.84}\text{N}/\text{GaN}$ MQWs with various well thicknesses (L_z). The dashed lines represent the fit to the TDOA experimental line shape

the multiple reflections and transmissions are considered, by using a 2×2 matrix formulation. The propagation of the light in the sapphire substrate is considered to be incoherent due to its large thickness which is assumed to be greater than the coherent length of the light source. The reflectance and transmittance of the whole structure are then calculated. Each layer is described by a complex refractive index $(n - jK)$, where the extinction coefficient (K) allows to account for the absorption ($K = \alpha\lambda/4\pi$ where α is the absorption coefficient and λ the wavelength in vacuum). The FP oscillations appearing on the spectra are principally due to the GaN template layer whose thickness is much larger than the (In,Ga)N MQW and GaN barrier ones. Then, the variation of the oscillation period as a function of energy, is adjusted by using the evolution of the real part of the GaN refractive index. The latter has been previously deduced, at low temperature, from combined ellipsometry and reflectivity measurements, on a GaN sample elaborated in the same growth conditions [8]. The energy dependence of the corresponding extinction coefficient is also deduced from ellipsometry experiments at 300 K, and the values are obtained at low temperature by considering the shift of the gap energy. Concerning the (In,Ga)N MQWs, n is considered to be equal 2.5, because no reliable ellipsometry measurements have been performed at low temperature. The imaginary part of the refractive index is described by considering an absorption coefficient classically described by the following sigmoidal function:

$$\alpha(E) = \frac{\alpha_0}{1 + \exp\left(\frac{E_g - E}{\Delta E}\right)},$$

where ΔE is equivalent to the Urbach tailing energy [9] and E_g the band edge energy of the alloy. The normalisation of the TDOA spectra is carried out in the energy range higher than the GaN band gap energy, where the sample is not transparent ($T = 0$), the experimental signal being then proportional to the quantity $1 - R$ which is extracted from the model. The adjustment of the normalized TDOA spectra are shown in Fig. 1, as a dashed line. The parameters deduced from this fitting procedure are reported in Table 1, together with the PL emission energies.

The band gap and PL energies of the (In,Ga)N MQWs are plotted, in Fig. 2, as a function of the well width. Both energies decrease when the well width increase, but the slopes are different. A large shift appears between absorption and emission, and increases linearly with the increase of PL energy as it is shown in the inset of Fig. 2. This behaviour has already been observed in MOCVD grown (In,Ga)N/GaN QWs and explained by a localisation of carriers in indium rich regions acting as quantum dots

Table 1

Band-gap energy, α_0 and ΔE parameters related to $\text{In}_{0.16}\text{Ga}_{0.84}\text{N/GaN}$ MQWs deduced from the adjustment of the absorption line shape

parameters	sample 1	sample 2	sample 3	sample 4
E_g (eV)	2.99 ± 0.01	2.92 ± 0.01	2.93 ± 0.02	2.85 ± 0.01
α_0 (10^5 cm^{-1})	1.1 ± 0.1	2.0 ± 0.1	1.8 ± 0.1	1.9 ± 0.1
ΔE (eV)	0.05 ± 0.01	0.11 ± 0.01	0.15 ± 0.02	0.12 ± 0.01
E_{PL} (eV)	2.853 ± 0.005	2.391 ± 0.005	2.197 ± 0.005	2.003 ± 0.005

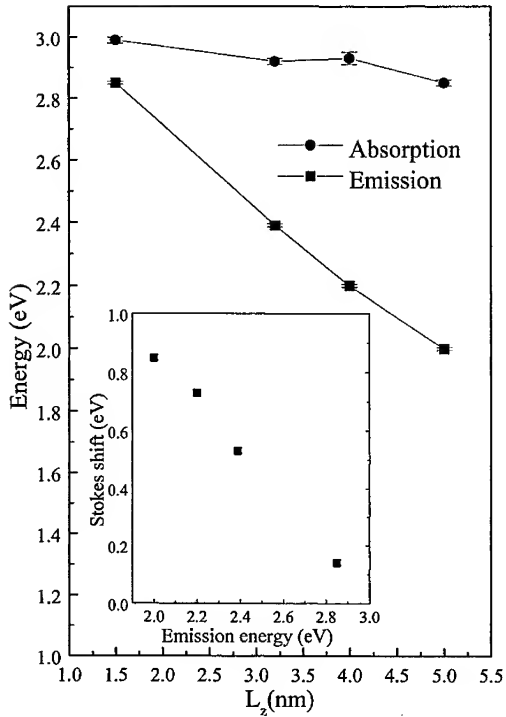


Fig. 2. Evolution of the absorption and emission energies of $\text{In}_{0.16}\text{Ga}_{0.84}\text{N}/\text{GaN}$ MQWs as a function of well thickness. The dependence of the large Stokes shift as a function of the emission energy is reported in the inset

(QDs) [10], the size and distribution of these QDs being responsible for the emission characteristics. However, the difference between the evolutions of the emission and absorption energies as a function of well thickness can be also explained by the presence of a piezoelectric field in these strained MQWs. Indeed, the quantum confined stark effect induces a red shift of the transition energies and this effect increases with the well thickness. Moreover, the built-in electric field which lowers the symmetry, induces a drastic reduction of the oscillator strength related to the fundamental transitions whereas that of

transitions involving excited states is increased. Forbidden transitions are also allowed under the large built-in field. Consequently, the emission signals could be attributed to the recombination of carriers from fundamental levels, whereas the absorption could rather involve transitions between excited states. By comparing these experimental behaviours with those reported by Berkowicz et al. [3] which have adjusted their results using an height band $\mathbf{k} \cdot \mathbf{p}$ model, our observations are in good agreement with the above interpretation.

Thus, two assumptions can be proposed to interpret the evolution of the large Stokes shift as a function of emission energy. The first considers the localisation of carriers in In-rich regions (QDs), the second explains this phenomenon in terms of built-in electric field. However, these two assumptions are not in contradiction. In fact, it is very difficult, at present time, to evaluate the part of the Stokes shift which is due to the localization process. A large electric field which would influence the recombination in the QDs has also to be considered.

4. Conclusion The modelling of the absorption line shape of $(\text{In,Ga})\text{N}/\text{GaN}$ MQWs grown by MBE on sapphire substrates enables the band-gap energy, the absorption coefficient and the broadening parameter to be determined. The large Stokes shift between absorption and emission increases with the increase of the well thickness. Two interpretations are suggested to explain this evolution: carrier localization process in In-rich region and/or built-in electric field effect.

References

- [1] S. NAKAMURA and G. FASOL, *The Blue Laser Diode*, Springer-Verlag, Berlin 1997.
- [2] H.P.D. SCHENK, M. LEROUX, and P. DE MIERRY, *J. Appl. Phys.* **88**, 1525 (2000), and references therein.
- [3] E. BERKOWICZ, D. GERSHONI, G. BAHIR, E. LAKIN, D. SHILO, E. ZOLOTYABKO, A.C. ABARE, S. P. DENBAARS, and L.A. Coldren, *Phys. Rev. B* **61**, 10994 (2000).
- [4] O. AMBACHER, R. DIMITROV, M. STUTZMANN, B.E. FOUTZ, M.J. MURPHY, J.A. SMART, J.R. SHEALY, N.G. WEIMANN, K. CHU, M. CHUMBES, B. GREEN, A.J. SIERAKOWSKI, W.J. SCHAFF, and L.F. EASTMAN, *phys. stat. sol. (b)* **216**, 381 (1999).
- [5] N. GRANDJEAN, J. MASSIES, P. VENNEGUES, M. LEROUX, F. DEMANGEOT, M. RENUCCI, and J. FRANDON, *J. Appl. Phys.* **72**, 350 (1998).
- [6] B. DAMILANO, N. GRANDJEAN, J. MASSIES, L. SIOZADE, and J. LEYMARIE, *Appl. Phys. Lett.* **77**, 1268 (2000).
- [7] A.M. VASSON, A. VASSON, J. LEYMARIE, P. DISSEIX, P. BORING, and B. GIL, *Semicond. Sci. Technol.* **8**, 303 (1993).
- [8] L. SIOZADE, S. COLLARD, M. MIHAIOVIC, J. LEYMARIE, A. VASSON, N. GRANDJEAN, M. LEROUX, and J. MASSIES, *Jpn. J. Appl. Phys.* **39**, 20 (2000).
- [9] F. URBACH, *Phys. Rev.* **92**, 1324 (1953).
- [10] K.P. O'DONNELL, R.W. MARTIN, and P.G. MIDDLETON, *Phys. Rev. Lett.* **82**, 237 (1999).

phys. stat. sol. (a) **183**, 145 (2001)

Subject classification: 68.37.Hk; 77.55.+f; 78.55.Cr; S7.14

Buried Dielectric Mirrors for the Lateral Overgrowth of GaN-Based Microcavities

R. W. MARTIN¹) (a), P. R. EDWARDS (a), R. PECHARROMAN-GALLEGO (a),
C. TRAGER-COWAN (a), T. KIM (b), H-S. KIM (b), K-S. KIM (b), I. M. WATSON (b),
M. D. DAWSON (b), T. F. KRAUSS (c), J. H. MARSH (c), and R. M. DE LA RUE (c)

(a) *Department of Physics, University of Strathclyde, Glasgow, G4 0NG, UK*

(b) *Institute of Photonics, University of Strathclyde, Glasgow G4 0NW, UK*

(c) *Department of Electronics and Electrical Engineering, University of Glasgow,
Glasgow G12 8LT, UK*

(Received October 8, 2000)

The use of lateral overgrowth techniques to develop III-nitride microcavities with both mirrors fabricated from very highly reflecting dielectric multilayers (e.g. SiO₂/ZrO₂) will be discussed. Multilayer mirror stacks with broad high reflectivity stop-bands and peak reflectivities in excess of 99% at wavelengths near the emission energies of typical InGaN/GaN quantum well structures, have been patterned in order to be compatible with subsequent lateral epitaxial overgrowth or pendeoepitaxy. Improvements in material quality resulting from lateral overgrowth above single layer masks are demonstrated using spatially resolved photoluminescence and cathodoluminescence imaging.

1. Introduction The impressive development of violet and blue edge-emitting laser diodes with InGaN/GaN active regions has been well documented [1] and promises great technological impact. Microcavity devices, such as resonant cavity LEDs and vertical cavity surface emitting lasers (VCSELs), constructed from III-nitride materials should possess a number of additional advantages over these edge-emitters, including lower thresholds, improved mode quality and possibilities for planar arrays of large numbers of devices. Recent reports of optically-pumped surface emitted lasing [2–4] have indicated good progress towards short wavelength GaN-based VCSELs. However, viable devices still require improvements in the quality of the active material and in the performance of the distributed Bragg reflectors (DBRs) forming the microcavity.

We have proposed the use of lateral overgrowth techniques, including lateral epitaxial overgrowth (LEO) [5] and pendeoepitaxy [6], to achieve concurrent improvements in both these areas [7]. High quality laser material is known to result from these overgrowth techniques, which conventionally employ single layer dielectric masks or etched seed structures. In this paper we will describe improvements in the quality of GaN grown at Strathclyde using conventional LEO. We will then discuss how both lateral growth techniques can be used to “bury” dielectric DBRs in order to form the lower

¹) Corresponding author; Tel.: +44-141-548-3466, Fax: +44-141-552-2891,
e-mail: r.w.martin@strath.ac.uk

reflector in a microcavity. Such DBRs have significant advantages, including higher peak reflectivities and wider reflectivity stop-bands, compared to conventional AlGaIn-based DBRs [8].

2. Dielectric Mirrors Fabricated from $\text{SiO}_2/\text{ZrO}_2$ The measured reflectivity of an electron-beam-deposited $10^{1/2}$ -period dielectric DBR, composed of $\text{SiO}_2/\text{ZrO}_2$ and centred near 420 nm, is shown in Fig. 1 and the high-reflectivity bandwidth is seen to be in excess of 80 nm. The lower part of the figure shows the effect of a similar DBR on the low temperature photoluminescence (PL) from an InGaIn/GaN single quantum well structure.²⁾ The high reflectivity of the upper mirror is indicated by the appearance of cavity modes in the luminescence following DBR deposition. The fringe spacing indicates that the lower reflector is formed by the weakly reflecting GaIn-sapphire interface region. The incorporation of a second highly reflecting dielectric DBR beneath the quantum well region will significantly enhance the finesse of the cavity. Methods to achieve this will now be considered.

3. Lateral Epitaxial Overgrowth Replacement of the single SiO_2 layers conventionally used as masks for LEO with SiO_2 -terminated, multilayer dielectric DBRs, of the type discussed above, makes it possible to "bury" these mirrors beneath laterally grown III-N material. As shown in Fig. 2 we have prepared arrays of striped dielectric mirror elements suitable for LEO over the surface of 2-inch GaIn-on-sapphire wafers using lift-off techniques [8]. The widths of the mirror stripes and "window" regions between stripes have been varied in the range 4–10 μm .

In advance of utilising these patterned mirror layers as masks for overgrowth we have investigated the properties of GaIn LEO above a single dielectric layer in the

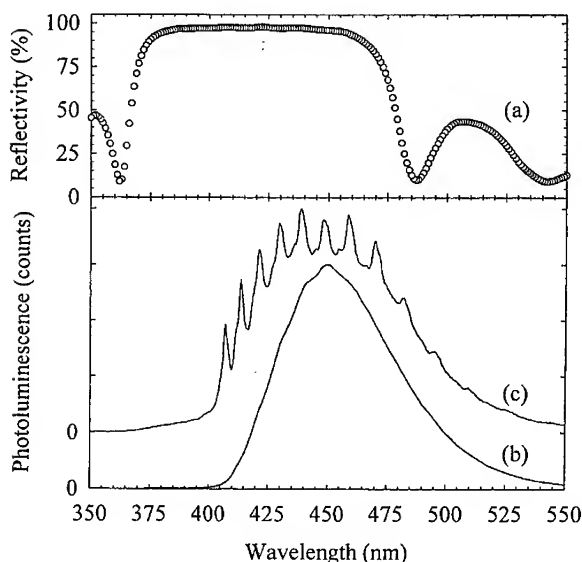


Fig. 1. Upper panel: Reflectance spectrum (a) measured from a $10^{1/2}$ -period $\text{SiO}_2/\text{ZrO}_2$ DBR on GaIn. Lower panel: PL data from an InGaIn/GaN single quantum well before (b) and after (c) deposition of such a DBR above the quantum well

²⁾ The authors are grateful to Dr. S. Nakamura for supply of this InGaIn/GaN material, which emits over an unusually large spectral range.

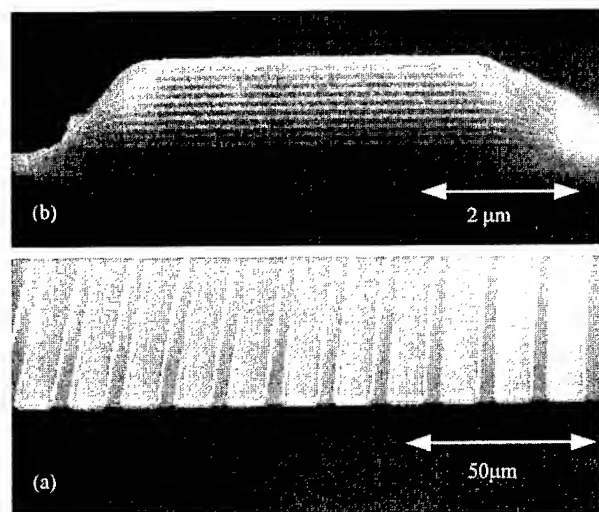


Fig. 2. a) Scanning electron micrograph of a $10^{1/2}$ -period $\text{SiO}_2/\text{ZrO}_2$ DBR on GaN patterned into $4\text{ }\mu\text{m}$ stripes using a single layer lift-off technique. b) Cross-sectional view of a $6\text{ }\mu\text{m}$ wide stripe

Aixtron MOCVD reactor at Strathclyde. Good coalescence is observed above 200 nm thick $[1\bar{1}00]$ -oriented SiO_2 stripes, with a range of widths and spacings. Room temperature cathodoluminescence (CL) imaging clearly shows the improved quality of the laterally grown material. The inset to Fig. 3 shows a CL image of the GaN band-edge luminescence ($365 \pm 10\text{ nm}$) from an LEO region with $9\text{ }\mu\text{m}$ wide stripes and $7\text{ }\mu\text{m}$ wide window regions. The bright bands correspond to the higher quality laterally grown GaN lying above the SiO_2 stripes. Photoluminescence is collected from regions containing

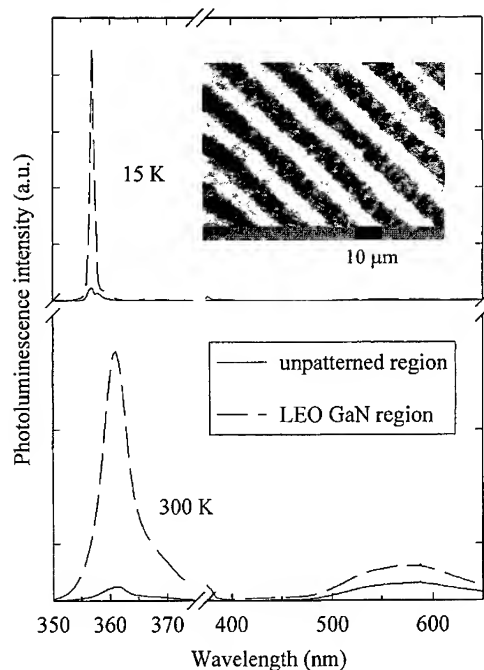


Fig. 3. PL data from LEO GaN at room temperature and low temperature, showing the improvement in moving from an unpatterned region to an area above silica stripes of width $4.1\text{ }\mu\text{m}$, with $4.5\text{ }\mu\text{m}$ wide windows. The inset shows a room temperature CL image at $(365 \pm 10)\text{ nm}$ from an LEO region, with $9\text{ }\mu\text{m}$ wide stripes and $7\text{ }\mu\text{m}$ wide window regions

Table 1

The ratio of the GaN band-edge PL peak intensities for striped and unpatterned regions of LEO wafers

stripe width (μm)	window width (μm)	ratio of PL peak intensities	
		$T = 300\text{ K}$	$T = 15\text{ K}$
4.1	4.5	15	18
4.1	6.8	17	
9.1	4.5	14	14
9.1	6.8	16	

several stripes and windows, using HeCd laser light focussed to a spot of approximately $20\text{ }\mu\text{m}$ diameter, and compared with PL data from unpatterned regions of the same wafer. As shown in Fig. 3 the striped regions show considerably better luminescence than the unpatterned regions. The ratio of the GaN band-edge PL peak intensities in the striped and unpatterned regions is approximately 15 for several stripe/window combinations and at both high and low temperature, as shown in Table 1.

4. Dielectric Mirrors for Pendeoepitaxial Overgrowth During pendeoepitaxy [6] lateral growth of III-N is seeded from ridge structures. If the dielectric mirrors are prepared in the regions between ridges this overgrowth technique may be used to bury them under a III-N active region. We have demonstrated [9] fast and controllable inductively coupled plasma etching of III-nitrides, using a STS multiplex system and $\text{Cl}_2/\text{BCl}_3/\text{Ar}$ gas chemistries, and have used this to produce ridges suitable for GaN pendeoepitaxy. Micrographs showing the results of an initial attempt to prepare $\text{SiO}_2/\text{ZrO}_2$ multilayer DBRs between the ridges are shown in Fig. 4. Some deposition of dielectric material is observed on the ridge side-walls and further work is in progress to produce clean GaN side-walls suitable for seeding lateral growth across the mirror surface.

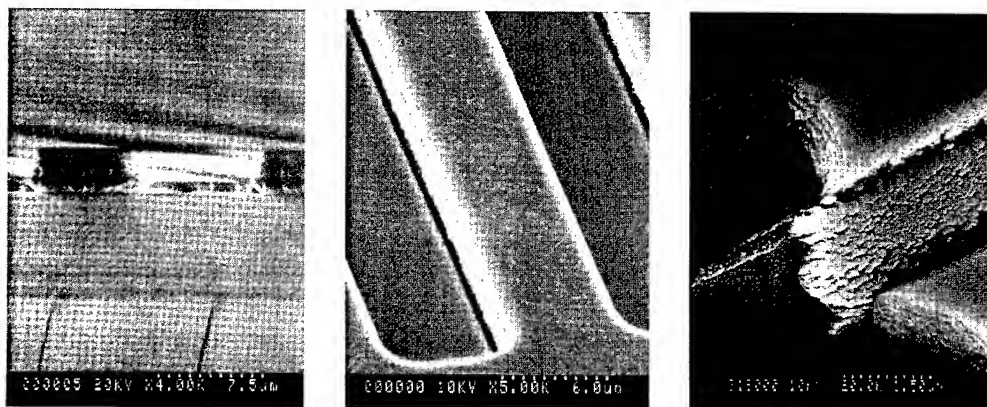


Fig. 4. Scanning electron micrographs showing a $\text{SiO}_2/\text{ZrO}_2$ dielectric DBR deposited above and between ICP etched ridges in GaN. The first and second images show cross-sectional and plan views of the ridges, whilst the third image illustrates the DBR structure along with the side-wall deposition discussed in the text

5. Conclusions The use of lateral overgrowth techniques for the production of high quality GaN-based microcavities has been discussed. These are predicted to enhance the performance of III–N microcavities, due to simultaneous improvement in the quality of the active material and in the performance of the reflector beneath the cavity. Improvements in GaN luminescence resulting from lateral overgrowth and progress towards the use of dielectric multilayers in overgrowth have been described.

Acknowledgement The authors are grateful for funding from the U.K. EPSRC and HSK is grateful for a research fellowship from the Korea Research Foundation.

References

- [1] S. NAKAMURA et al., Jpn. J. Appl. Phys. **37**, L309 (1998).
- [2] T. SOMEYA et al., Jpn. J. Appl. Phys. **37**, L1424 (1998).
- [3] I.L. KRESTINOV et al., Appl. Phys. Lett. **75** 1192 (1999).
- [4] Y.-K. SONG et al., Appl. Phys. Lett. **76** 1662 (2000).
- [5] T.S. ZHELEVA, O.H. NAM, M.D. BREMSER, and R.F. DAVIS, Appl. Phys. Lett. **71** (1997) 2472.
- [6] T.S. ZHELEVA et al., MRS Internet J. Nitride Semicond. Res. **4S1**, G3.38 (1999).
- [7] R.W. MARTIN et al., phys. stat. sol. (a) **176**, 67 (1999).
- [8] T. KIM et al., Presented at eMRS 2000 Spring Meeting, Mater. Sci. Eng. B (in press).
- [9] H-S. KIM et al., Presented at International Workshop on Nitride Semiconductors, Sept. 2000, Nagoya.

phys. stat. sol. (a) **183**, 151 (2001)

Subject classification: 71.35.Cc; 78.47.+p; 78.55.Cr; 78.66.Fd; S7.14

Time-Resolved Photoluminescence in Strained GaN Layers

G. POZINA¹) (a), N. V. EDWARDS (a), J. P. BERGMAN (a), B. MONEMAR (a),
M. D. BREMSER (b), and R. F. DAVIS (b)

(a) *Department of Physics and Measurement Technology, Linköping University,
S-581 83 Linköping, Sweden*

(b) *Department of Materials Science and Engineering, North Carolina State University,
Raleigh, North Carolina 27695, USA*

(Received October 8, 2000)

A set of GaN epilayers grown by metalorganic chemical vapor deposition on 6H-SiC substrates was studied by time-resolved photoluminescence (PL) spectroscopy. The PL spectra are dominated by the free A exciton (FE_A) and by the neutral-donor-bound exciton (D_0X) transitions. The position of FE_A indicates that the GaN layers are under tension. We observe that the recombination lifetime for the FE_A is about 40–50 ps in all the layers, whereas the recombination time for the D_0X varies for different samples. We found that the recombination lifetimes for D_0X have a clear dependence on the position of FE_A ; i.e. the recombination lifetime increases with decreasing strain in the layers. The results can be explained in terms of the character of the hole states involved in the donor-bound exciton recombination.

1. Introduction GaN and related alloys are presently the most attractive materials for fabrication of optoelectronic devices in the ultraviolet and blue energy region [1, 2]. For this purpose epitaxial growth on sapphire and 6H-SiC substrates is usually applied. Due to the large lattice and thermal mismatches between GaN and the substrate materials the strain relaxation as well as residual strain can create serious problems influencing the device quality. For instance, for device physics the carrier (or exciton) lifetime (τ) is a parameter of great importance; however it is still unclear how strain affects the carrier lifetime. In this work we report on results of time-resolved photoluminescence (PL) spectroscopy of strained wurtzite GaN epilayers of different thickness (and correspondingly different strain states) grown by metalorganic chemical vapor deposition (MOCVD) on 6H-SiC substrates. We have observed that the PL recombination time for the neutral donor-bound exciton (D_0X) varies depending on the samples and the value of the residual strain in the layers, whereas the recombination time for the free A exciton (FE_A) is practically the same in all studied samples.

2. Experimental A set of GaN layers of comparable quality were grown on 6H-SiC substrates by MOCVD with a 1000 Å thick AlN buffer layers at a temperature of 1000 °C. The layer thickness varies from 0.5 to 4 µm. All samples were undoped and grown with the same III–V flux ratio. Optical excitation was performed with a ps pulse frequency-tripled beam of an Al₂O₃:Ti mode-locked laser ($\lambda_{ex} = 266$ nm). Photolumines-

¹) Corresponding author; Tel.: +46 13 282629, Fax: +46 13 142337, e-mail: galia@ifm.liu.se

cence (PL) was detected by using a GaAs photo multiplier tube. The time-resolved measurements were performed using a syncroscan streak-camera system with a time resolution of about 20 ps.

3. Results and Discussion Figure 1a shows the low temperature PL spectra for the GaN epilayers of different thickness (the thickness is indicated for each GaN epilayer). All spectra are dominated by FE_A and by D_0X . This identification is done in accordance with previous studies [3, 4]. It is clear that the energy of FE_A and, consequently, the energy of D_0X vary with each sample. The energy positions for FE_A and D_0X are plotted vs the sample thickness in Fig. 1b. The data in Fig. 1b can be expressed in terms of in-plane stress (right axis). Here, we apply conventional elastic theory for the case of GaN layers after Edwards et al. [5]. The hydrostatic, and therefore the in-plane strain, can be obtained within an additive constant E_{A0} from the measured gap energy E_A and the deformation potential α according to the empirical expression $E_A = E_{A0} + \alpha \varepsilon_H$, where $\varepsilon_H = \Delta V/V = \varepsilon_{11} + \varepsilon_{22} + \varepsilon_{33}$, $E_{A0} = 3.4764$ eV is the energy of FE_A in unstrained GaN grown by MOCVD [6], and $\alpha \approx -10$ eV. We see from Fig. 1b that the investigated GaN layers grown on 6H-SiC are under tension with stress values varying from 1 kbar up to 3 kbar depending on the sample thickness.

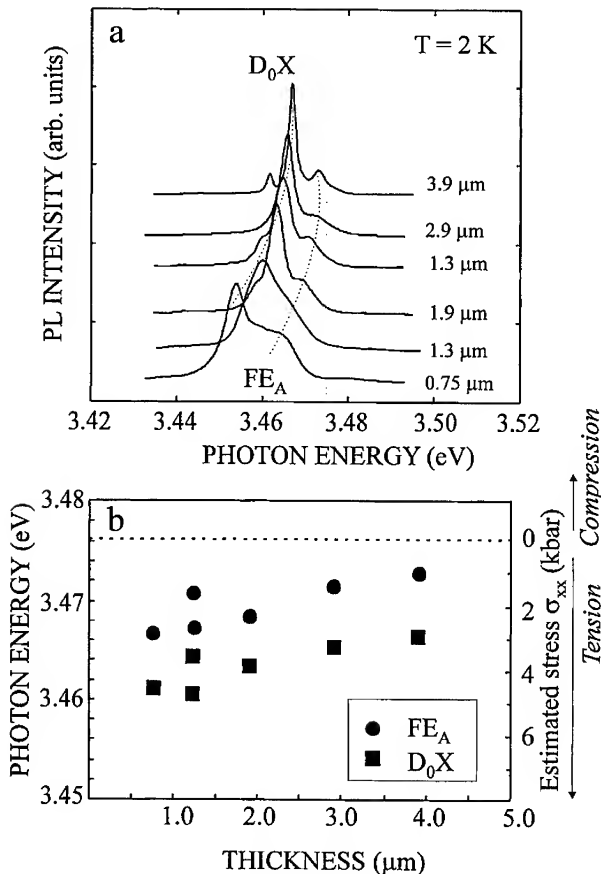


Fig. 1. a) PL spectra measured at temperature $T = 2$ K for GaN layers grown by MOCVD on 6H-SiC substrates. The layer thickness is indicated for each spectrum. b) The positions of the free A exciton (circles) and of the donor-bound exciton (squares) obtained from PL spectra plotted versus the sample thickness. The right axis shows estimated in-plane stresses

From time-resolved PL spectroscopy we have found that the PL decays for FE_A show similar behavior in all the layers, with near exponential kinetics and recombination times about $\tau = 40\text{--}50$ ps under the lower excitation density of 100 mW/cm^2 . Figure 2a and b presents several typical PL decay curves measured at the peak position of FE_A and D_0X , respectively. With increasing excitation density up to 2500 mW/cm^2 the recombination time of FE_A increases within 25%, which indicates a significant effect of nonradiative recombination channels. The PL decay curve measured at an excitation density of 2500 mW/cm^2 is shown in Fig. 2a by the dashed line. On the other hand, we have found that the D_0X recombination time varies for different layers and it is practically independent of the excitation conditions (the difference is about 5%). The excitation power influences mainly the tail part of the PL decay curves as shown in Fig. 2b by the solid and the dashed lines for the high and low excitation density, respectively.

The recombination lifetime τ includes both the radiative lifetime τ_r and the nonradiative lifetime τ_{nr} ($1/\tau = 1/\tau_r + 1/\tau_{nr}$). At low temperature, nonradiative processes usually limit τ for free excitons. However, for the donor-bound excitons we can estimate τ_r by extrapolation of τ to $T = 0$ assuming that τ_r is temperature independent and that the nonradiative recombination rate is thermally activated according to an exponential law [3]. Figure 3a illustrates the temperature dependence of the recombination lifetimes for D_0X . One can conclude that the recombination lifetimes τ for the D_0X measured at 2 K correspond rather well to the radiative lifetime τ_r .

We have found, that the PL decay times for D_0X increases with increasing FE_A energy (i.e. with decreasing strain) for the layers under tension. In Fig. 3b the recombination lifetimes for FE_A (squares) and for D_0X (circles) measured for the each GaN layer are plotted versus the in-plane stress σ_{xx} , while the upper axis shows the FE_A energies. From Fig. 3b it is clearly seen that the D_0X recombination times vary rather significantly from ≈ 60 ps in the most strained layer up to ≈ 110 ps in the less strained layer. On the other hand we have not observed any difference for the recombination lifetime of FE_A in these samples.

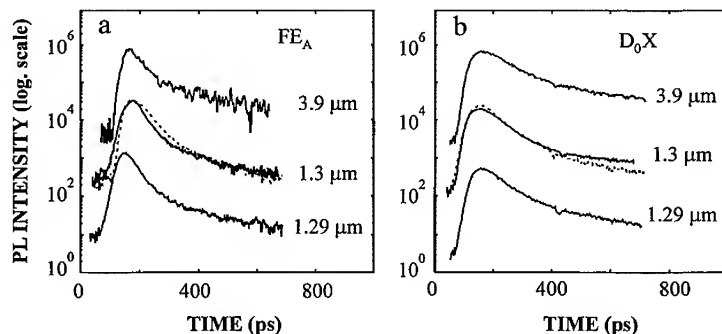


Fig. 2. a) PL decay curves measured at 2 K for FE_A . The solid lines correspond to the data taken at the low excitation density of 100 mW/cm^2 . The PL decay curve measured at the high excitation density of 2500 mW/cm^2 is shown by the dashed line. b) PL decay curves measured at 2 K for D_0X at the excitation density of 2500 mW/cm^2 (solid lines). The PL decay curve taken at 100 mW/cm^2 is shown by the dashed line. Curves are shifted in the vertical direction for clarity. The sample thickness is indicated for each plot

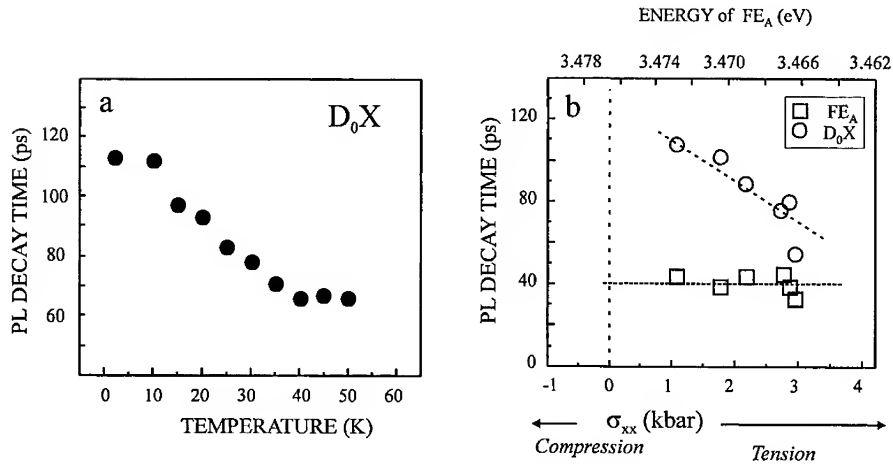


Fig. 3. a) Recombination lifetimes as a function of temperature for D_0X . b) The recombination lifetimes for FE_A (squares) and for D_0X (circles) plotted versus the in-plane stress. The upper axis is calibrated in terms of the FE_A energy. The dashed lines are a guide for eye

It is likely that D_0X has the same origin in all measured structures since all samples were grown under similar conditions. The quality of the selected structures is similar as determined by X-ray diffraction, scanning electron microscopy [7] and PL measurements and by the values of the recombination lifetime for FE_A . At $T = 2$ K the D_0X recombination lifetime is approximately equal to τ_r , which is correlated with overlapping of the wave functions of the electron and hole [8]. In fact, the neutral bound exciton wave function involves an interaction between an outer hole with a two-electron state. It is therefore directly related to the hole states involved (Γ_7 or Γ_9). Thus, since we know that the band structure in GaN changes significantly with strain (i.e., the energy splitting ΔE_{AB} between bands A and B changes), we may indirectly observe this change through the radiative lifetime for D_0X . We suggest the following explanation of our results. With increasing tensional strain the energy splitting between the valence bands A and B decreases for our stress values. Since the hole masses are different for the A and B subbands, the decrease of ΔE_{AB} naturally results in a more extensive contribution of the B-hole (or light hole) to the hole state involved in the bound exciton interaction, i.e. the hole mass will be more light and, consequently, the hole wavefunction will be more extended. It leads, in turn, to an increased electron-hole overlap matrix element (or oscillator strength) since the electron wave function is more extended. The increased electron-hole overlap in the D_0X state results in a reduction of the radiative lifetime [8], as observed in this work.

4. Conclusions We have studied a number of GaN film/AlN buffer/6H-SiC substrate heterostructures with different GaN thickness up to 4 μm . The structures were grown by MOCVD. From the energies of the free A exciton we have determined that the layers were under tension. We have found that the recombination lifetime for FE_A has value about 40–50 ps in all the layers, whereas the recombination time for D_0X varies for different samples from 60 ps up to 110 ps at $T = 2$ K. The variation of the D_0X radiative lifetime is consistent with the GaN band structure change due to strain.

References

- [1] S. NAKAMURA, M. SENOH, N. IWASA, and S. NAGAHAMA, *Jpn. J. Appl. Phys. 2, Lett.* **34**, L797 (1995).
- [2] S. NAKAMURA, M. SENOH, S. NAGAHAMA, N. IWASA, T. YAMADA, T. MATSUSHITA, Y. SUGIMOTO, and H. KIIYOKU, *Jpn. J. Appl. Phys. 2, Lett.* **36**, L1059 (1997).
- [3] G. POZINA, J. P. BERGMAN, T. PASKOVA, and B. MONEMAR, *Appl. Phys. Lett.* **75**, 4124 (1999).
- [4] K. P. KORONA, A. WYSMOLEK, J. M. BARANOWSKI, K. PAKULA, J. P. BERGMAN, B. MONEMAR, I. GRZEGORY, and S. POROWSKI, *Mater. Res. Soc. Symp. Proc.* **482**, 501 (1998).
- [5] N. V. EDWARDS, S. D. YOO, M. D. BREMSER, T. W. WEEKS, JR. O. H. NAM, R. F. DAVIS, H. LIU, R. A. STALL, M. N. HORTON, N. R. PERKINS, T. F. KUECH, and D. E. ASPNES, *Appl. Phys. Lett.* **70**, 2001 (1997).
- [6] K. PAKULA, A. WYSMOLEK, K. P. KORONA, J. M. BARANOVSKI, R. STEPNIOWSKI, I. GRZEGORY, M. BOCKOWSKI, J. JUN, S. KRUKOWSKI, M. WROBLEWSKI, and S. POROVSKI, *Solid State Commun.* **97**, 919 (1996).
- [7] N. V. EDWARDS, M. D. BREMSER, R. F. DAVIS, A. D. BATCHELOR, S. D. YOO, C. F. KARAN, and D. E. ASPNES, *Appl. Phys. Lett.* **73**, 2808 (1998).
- [8] G. D. SANDERS and Y-C. CHANG, *Phys. Rev. B* **28**, 5887 (1983).

phys. stat. sol. (a) **183**, 157 (2001)

Subject classification: 63.22.+m; 78.30.Fs; S7.14

Inelastic Light Scattering by Phonons in Hexagonal GaN–AlN Nanostructures

J. GLEIZE (a), F. DEMANGEOT (a), J. FRANDON (a), M.A. RENUCCI¹), M. KUBALL (b), B. DAUDIN (c), and N. GRANDJEAN (d)

(a) *Laboratoire de Physique des Solides de Toulouse, UMR 5477 CNRS, Université Paul Sabatier, F-31062 Toulouse Cedex 04, France*

(b) *H.H. Wills Physics Laboratory, University of Bristol, Bristol BS8 ITL, UK*

(c) *Département de la Recherche Fondamentale sur la Matière Condensée, CEA/Grenoble, SPMM, F-38054 Grenoble Cedex 09, France*

(d) *Centre de Recherche sur l'Hétéro-épitaxie et ses Applications, CNRS, F-05560 Valbonne, France*

(Received October 8, 2000)

Two selected examples have been chosen to illustrate the ability of non-resonant Raman scattering to probe phonons in hexagonal GaN–AlN artificial structures. The angular dispersion of polar phonons is investigated in a long period GaN–AlN superlattice and compared with the results of calculations based on a dielectric continuum model. On the other hand, the Raman signature of the self-assembled GaN quantum dots and of the AlN spacers of a multi-layered structure is used to determine the strain field in the structure. The dots are shown to be fully strained on the AlN lattice parameter while the spacers exhibit on the average a slight tensile strain.

1. Introduction We present selected studies on lattice dynamics of artificial structures based on group-III nitrides with wurzite structure, namely GaN/AlN superlattices (SLs) and multi-layered GaN quantum dots (QDs) in AlN. They refer to inelastic light scattering experiments performed at high spatial resolution with a confocal micro-Raman set-up, in off-resonant conditions, using various polarization configurations and geometries. The paper is organized into two parts, one devoted to the angular dispersion of polar phonons in a GaN–AlN superlattice, the other connected to the determination of the strain field in a structure made of periodic stackings of GaN QDs in an AlN matrix.

2. Angular Dispersion of Extraordinary Phonons in a GaN–AlN Superlattice A long period SL was studied in order to get rid of quantization effects on phonon frequencies. The sample is a GaN(6.3 nm)–AlN(5.1 nm) SL of 100 periods grown by plasma-assisted molecular beam epitaxy (MBE) on a (0001) sapphire substrate, after the deposition of a 1 μ m thick AlN buffer layer. The AlN buffer layer is totally relaxed and the SL layers are strained due to the lattice mismatch between AlN and GaN [1].

According to the dielectric continuum model developed by us previously for SLs with wurzite layers [2], extraordinary phonons (i.e. polar modes p-polarized with respect to

¹) Corresponding author; Phone: +33 (0)5 61 55 61 58, Fax : +33 (0)5 61 55 62 33;
e-mail: renucci@ramansco.ups-tlse.fr

the (\mathbf{c} , \mathbf{q}) plane defined by the \mathbf{c} -axis of the layers and the phonon wavevector \mathbf{q} can be classified into: (i) confined modes (C); (ii) quasi-confined modes (QC), confined in one type of layer and evanescent in the other; (iii) interface modes (IF), decaying exponentially from the interfaces in both layers.

The model predicts for QC and IF modes an angular dispersion $\omega(\theta)$, where θ is the angle between \mathbf{q} and \mathbf{c} . The dispersion reflects respectively the layer anisotropy for the former, and the anisotropy of the whole structure, induced by the modulation of the dielectric properties along the growth axis, for the latter. In our experiment performed in off-resonant conditions, the control of momentum transfer \mathbf{q} from the incident and scattered photons is ensured by the scattering geometry. Variation of θ is achieved in backscattering geometry by tilting the sample with respect to the laser beam by $\theta = 0^\circ$, $\theta = 45^\circ$ (on a bevel edge obtained by focused ion beam etching [3]), and $\theta = 90^\circ$. The large value of the mean refractive index of the SL (about 2.31) prohibits from scanning θ ranges larger than $\pm 25^\circ$.

Room temperature Raman spectra have been recorded for various wave-vector orientations. Figure 1 shows the spectra recorded at 2.54 eV on the sample surface for $\theta < 22^\circ$. The angular dispersion of extraordinary phonons is evidenced both in the AlN TO range and in the GaN LO range, as predicted for QC modes. The two frequencies evolve continuously, decreasing from the $E_1(\text{TO})$ frequency of strained AlN (635 cm^{-1}) on one hand, increasing from the $A_1(\text{LO})$ frequency of strained GaN (738 cm^{-1}) on the other hand. This behavior contrasts with that of the non-polar E_2 modes, confined in each type of layers.

We have calculated the angular dispersion of the SL extraordinary phonons within the dielectric continuum model, taking into account the strain state of the SL layers ($\epsilon_{xx} = -1.3\%$ and $+1.1\%$ for GaN and AlN, respectively [1]). The results of calculations are compared to the experimental phonon frequencies in Fig. 2. Calculated phonon dispersions of *bulk* GaN and AlN in the same strain state as in the SL layers are displayed on the figure for comparison.

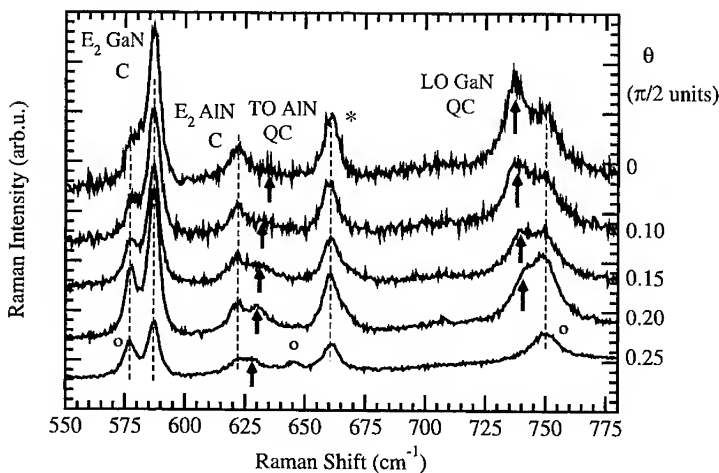


Fig. 1. Room temperature spectra recorded at 2.54 eV for $\theta < 0.25 \pi/2$. Dispersive extraordinary phonons from the SL are indicated by arrows. Contributions from the AlN buffer layer and from the sapphire substrate are marked with an asterisk and with open circles, respectively

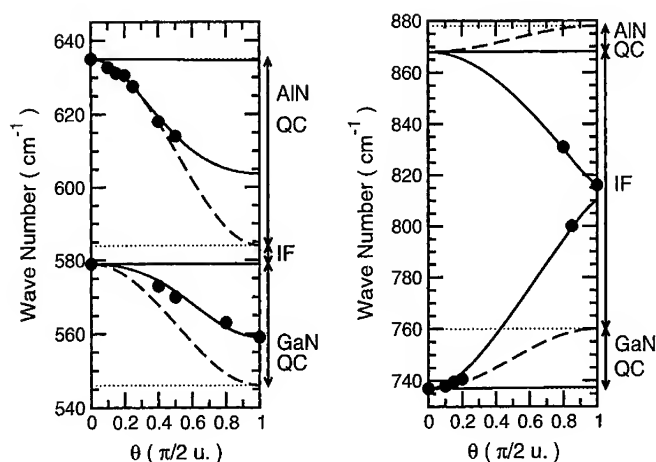


Fig. 2. Calculated angular dispersion of the quasi-confined (QC) and interface (IF) modes of the SL (full line) and experimental phonon frequencies (black circles). Dispersion calculated for polar phonons of bulk GaN and AlN in the same strain state as in the SL is shown for comparison (dashed lines)

The agreement between the experimental results and the calculations is rather good, in view of the simplicity of the model. The dielectric continuum model gives thus a realistic insight into the phonon picture in wurtzite SLs when quantization effects due to confinement can be neglected.

3. Raman Signatures of GaN QDs and AlN Matrix in Multilayered Structures Results presented in this work concern a stacking of self-assembled GaN QD layers embedded in an AlN matrix, grown by MBE on a Si(111) substrate after the deposition of both

AlN and GaN buffer layers, using NH_3 as a precursor [4]. The GaN dots are typically a few nm high and tens of nm wide. No evidence of vertical correlation was found in this sample.

Raman spectra excited with visible light in off-resonant conditions were recorded in back-scattering geometry, in various polarization configurations. We show in Fig. 3 micro-Ra-

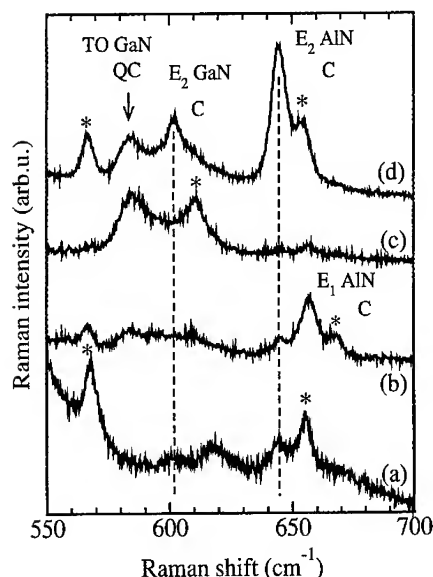


Fig. 3. Room temperature Raman spectra of the QD structure recorded at 1.92 eV in configurations $z(xy)\bar{z}$, $x(yz)\bar{x}$, $x(zz)\bar{x}$ and $x(yy)\bar{x}$ shown as (a) to (d), respectively. Asterisks mark phonons from the buffer layer. Features at about 618 cm^{-1} are related to the Si substrate

man spectra taken at 1.92 eV. Four phonons originating from the structure are identified by their selection rules: (i) two non-polar modes of symmetry E_2 at 603 cm^{-1} and 645 cm^{-1} , which are confined modes in GaN QDS and AlN spacers, respectively; (ii) one polar E_1 phonon at 657 cm^{-1} , an ordinary (s-polarized) TO mode confined in the spacers; (iii) one polar A_1 phonon at 580 cm^{-1} , an extraordinary (p-polarized) TO mode, quasi-confined in the dots.

However, the ability of Raman spectroscopy to probe separately QDs and spacers in off-resonant conditions may be questioned. As a check, a relaxed $\text{Al}_{0.77}\text{Ga}_{0.23}\text{N}$ layer with an Al content very close to that of the QD sample ($\langle x \rangle = 0.81$) has been investigated. As shown in Fig. 4, two E_2 modes assigned to the GaN-like and AlN-like phonons of the alloy show up approximately at the same location as those in the structure, at 606 cm^{-1} and 647 cm^{-1} , respectively. But the GaN-like feature is a broad band and does not follow definite selection rules, in contrast with its counterpart in the QD structure. Moreover, the well known “one-mode” behavior of the $A_1(\text{LO})$ phonon [5, 6] is clearly evidenced in the alloy by the emergence of a single peak at 863 cm^{-1} , while no Raman feature has been observed in this frequency range for the QD structure. Once the random alloy hypothesis has been ruled out, the strain state of the structure is deduced from the frequency shift of the $E_2(\text{C})$ modes compared to bulk materials, as quantization effects related to phonon confinement can be neglected due to typical QD dimensions. From the measured frequency shift of the $E_2(\text{C})$ mode of GaN, a -2.4% in-plane biaxial strain due to compressive stress is obtained from data on strain induced phonon shifts in GaN [7, 8], in agreement with previous studies by high resolution transmission electron microscopy on a similar QD structure [9]. Experimental data on strain induced phonon shifts in AlN are still lacking in the literature, so we made use of our unpublished results on AlN for an estimate of the tensile strain of the spacers. From the frequency shift $\Delta\nu = -3500\text{ cm}^{-1}$ per $+100\%$ biaxial strain for the E_2 mode of AlN, we obtain a mean in-plane strain of $+0.45\%$ for the spacers.

Probing of phonons confined respectively in the dots and in the spacers of a multi-layered GaN–AlN structure confirms that the GaN QDs are fully strained on the AlN lattice parameter, while it indicates on the average a slight tensile state of the AlN spacers.

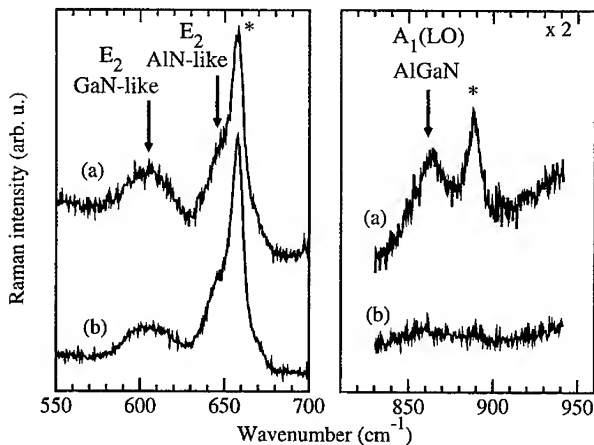


Fig. 4. Room temperature Raman spectra of a thick $\text{Al}_{0.77}\text{Ga}_{0.23}\text{N}$ layer recorded at 1.92 eV in configurations $z(\text{xx})\bar{z}$ (a) and $z(\text{xy})\bar{z}$ (b). Asterisks mark phonons from the buffer layer

References

- [1] J. GLEIZE, F. DEMANGEOT, J. FRANDON, M.A. RENUCCI, F. WIDMANN, and B. DAUDIN, *Appl. Phys. Lett.* **74**, 703 (1999).
- [2] J. GLEIZE, M.A. RENUCCI, J. FRANDON, and F. DEMANGEOT, *Phys. Rev. B* **60**, 15985 (1999).
- [3] M. KUBALL, F.H. MORISSEY, M. BENYOUCEF, I. HARRISON, D. KORAKAKIS, and C.T. FOXON, *phys. stat. sol. (a)* **176**, 355 (1999).
- [4] B. DAMILANO, N. GRANDJEAN, F. SEMOND, J. MASSIES, and M. LEROUX, *phys. stat. sol. (b)* **216**, 451 (1999).
- [5] A. CROS, H. ANGERER, R. HANDSCHUH, O. AMBACHER, and M. STUTZMANN, *Solid State Commun.* **104**, 35 (1997).
- [6] F. DEMANGEOT, J. GROENEN, J. FRANDON, M.A. RENUCCI, O. BRIOT, S. CLUR, and R.L. AULOMBARD, *Appl. Phys. Lett.* **72**, 2674 (1998).
- [7] F. DEMANGEOT, J. FRANDON, M.A. RENUCCI, O. BRIOT, B. GIL, and R.L. AULOMBARD, *Solid State Commun.* **100**, 207 (1996).
- [8] N. Y. DAVYDOV, N.S. AVERKIEV, I.N. GONCHARUK, D. K. NELSON, I.P. NIKITINA, A.S. POLOVNIKOV, A. N. SMIRNOV, and M.A. JACOBSON, *J. Appl. Phys.* **82**, 5097 (1997).
- [9] M. ARLERY, J. L. ROUVIERE, F. WIDMANN, G. FEUILLET, and H. MARIETTE, *Appl. Phys. Lett.* **74**, 3287 (1999).

phys. stat. sol. (a) **183**, 163 (2001)

Subject classification: 68.55.Ac; 78.55.Cr; 78.66.Fd; S7.14

Growth by Molecular Beam Epitaxy and Optical Properties of a Ten-Period AlGaN/AlN Distributed Bragg Reflector on (111)Si

F. SEMOND (a), N. ANTOINE-VINCENT (b), N. SCHNELL (a), G. MALPUECH (b),
M. LEROUX (a), J. MASSIES (a), P. DISSEIX (b), J. LEYMARIE (b), and A. VASSON (b)

(a) CRHEA-CNRS, Rue Bernard Grégory, Sophia Antipolis, F-06560 Valbonne, France

(b) LASMEA, Université Blaise Pascal-Clermont Ferrand II, F-63177 Aubière Cedex, France

(Received October 8, 2000)

This paper reports the growth of GaN, (Al,Ga)N and AlN layers on (111)Si substrates by molecular beam epitaxy using ammonia. Using proper conditions, GaN layers with threading dislocation densities as low as $5 \times 10^9 \text{ cm}^{-2}$ can be obtained on (111)Si. The structural and optical properties of GaN and (Al,Ga)N have been studied using electron microscopy, photoluminescence and reflectivity. In particular, the tensile strain has been assessed. Finally, a ten-period $\text{Al}_{0.2}\text{Ga}_{0.8}\text{N}/\text{AlN}$ Bragg mirror has been grown, with a UV (340 nm) centered bandwidth of 35 nm and peak reflectivity of 78%.

1. Introduction Since the advent of group-III nitrides in the field of semiconductor optoelectronics almost a decade ago [1], materials and device research aims at improving their performances. A promising way is the use of Bragg mirrors and optical cavities. This can increase light emitting diode external efficiencies [2], improve photodetector performances and is the basis of vertical cavity surface emitting lasers [3]. Moreover, this permits the study of novel fundamental phenomena arising from light-matter interactions in such structures [4]. High reflectivity ($R > 90\%$) GaN/AlN or GaN/(Al,Ga)N quarter wave mirrors on sapphire substrates have already been reported, grown by metalorganic vapor phase epitaxy [5] or plasma assisted molecular beam epitaxy (MBE) [6, 7]. The present work reports the growth by MBE of a UV centered (Al,Ga)N/AlN Bragg mirror on (111)Si substrates. Using (Al,Ga)N as the high index material instead of GaN will allow such mirrors to be resonant with the polaritons of bulk GaN or (Al,Ga)N/GaN quantum wells. The advantages of Si substrates are high crystalline perfection, large dimensions and low cost. Furthermore, they can be etched away in order to get free standing mirrors and/or cavities. However, major drawbacks are the large lattice parameter and thermal expansion coefficient mismatches with nitrides, resulting in large dislocation densities and biaxial tensile strains [8], that may lead to sample cracking for large thicknesses.

2. MBE Growth of GaN, AlN and (Al,Ga)N and Material Characterization Growths are performed by MBE using elemental Al and Ga sources and NH_3 as nitrogen precursors [9]. In order to prevent silicon nitridation and to rapidly obtain a layer by layer growth of the AlN buffer layer, the starting growth conditions are carefully adjusted [9, 10]. GaN is then grown on this buffer layer. Growth temperatures (T) are 800 °C and

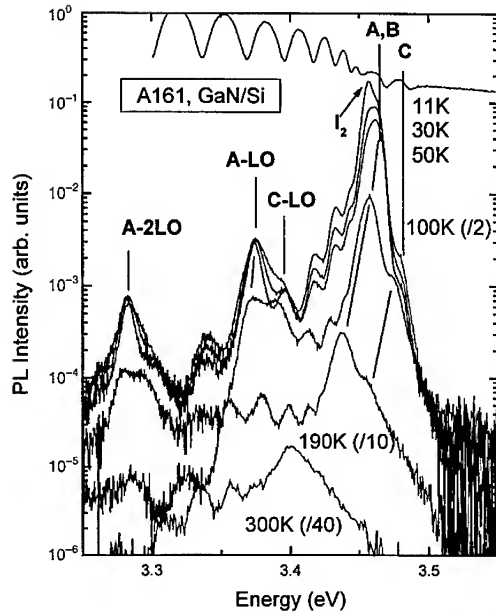


Fig. 1. Photoluminescence and reflectivity (11 K) spectra of GaN/Si. The energy of the A-excitonic gap obtained from reflectivity and luminescence indicates that the layer is under a tensile strain ϵ_{xx} of 1.4×10^{-3} .

900 °C for GaN and AlN, respectively. The resulting GaN crystals have a room temperature background free carrier concentration below 10^{16} cm^{-3} . Secondary ion mass spectroscopy indicates that the main dopant impurities are oxygen, carbon and silicon with concentrations of 5×10^{17} , 1×10^{17} and $1 \times 10^{17} \text{ cm}^{-3}$, respectively. The threading dislocation densities in such nitrides-on-Si structures, measured through atomic force microscopy and/or transmission electron microscopy, lie typically in the 5×10^9 to 10^{10} cm^{-2} range. Figure 1 shows the re-

fectivity and photoluminescence (PL) spectra of a 3 μm thick GaN sample grown on (111)Si. The low temperature PL spectrum is dominated by the recombinations of both donor-bound excitons (I_2 line) and free A excitons, as shown by the reflectivity spectrum. When comparing to typical PL spectra of GaN grown on sapphire [11], one notes for growth on Si a broadening of the transitions, and an overall lowering of the transition energies, related to the tensile strain induced by the nitride-on-silicon epitaxy. The A and C free exciton energies of the sample of Fig. 1 correspond to a biaxial deformation ϵ_{xx} of 1.4×10^{-3} [8]. For such strain values, the B exciton energy is very near the A one, and B-related structures cannot be resolved in the spectra of Fig. 1. This tension also increases the oscillator strength of C excitons in σ geometry, as emphasized also by the emergence of C optical phonon replica.

Turning to (Al,Ga)N, which is an ingredient of our Bragg mirrors, Fig. 2a displays the PL spectra of a 1.6 μm thick $\text{Al}_{0.18}\text{Ga}_{0.82}\text{N}$ sample. The Al composition, evaluated during the growth by using in situ reflectivity ($\lambda = 670 \text{ nm}$), has been cross-checked using energy dispersive X-ray analysis. At low temperature, the PL spectrum consists of a near edge emission band, 30 meV wide, followed by LO phonon replica. With the increase of temperature, the PL energy varies following a typical 'S-shape'. Figure 2b allows us to interpret such spectra. The upper solid lines show the temperature dependence of the A gap of GaN/(111)Si (slightly different from that of GaN on sapphire due to different thermo-elastic strains [8, 11]) and shifted to match the low temperature A-excitonic gap of the alloy ($3.875 \pm 0.005 \text{ eV}$, as measured from the reflectivity spectrum). This shows that for $T > 120 \text{ K}$, the PL is dominated by free exciton recombinations. This is nicely confirmed by the energy of the phonon replica: at low T , they are separated from the zero phonon line by exactly one or two times the LO phonon energy (93.5 meV in this sample). However, above 120 K, this separation decreases to the values expected for the one- and two-phonon replica of free excitons [11]. The localiza-

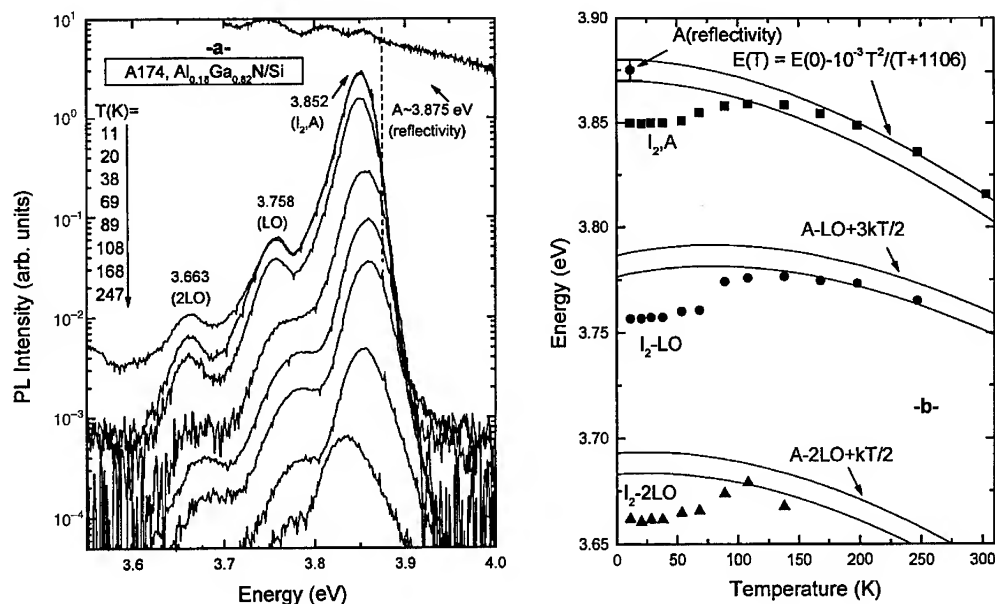


Fig. 2. a) Photoluminescence and reflectivity (11 K) spectra of $\text{Al}_{0.18}\text{Ga}_{0.82}\text{N}/\text{Si}$. b) Temperature dependence of luminescence energies in $\text{Al}_{0.18}\text{Ga}_{0.82}\text{N}/\text{Si}$. Two parallel solid lines separated by 10 meV correspond to the ± 5 meV uncertainty in the energy of the A-excitonic gap

tion energy of excitons is 25 meV at 11 K, which corresponds to both binding to residual donors and alloy disorder effects. The A energy is in agreement with the measured Al composition, using a band gap bowing parameter of 0.7 ± 0.1 eV.

3. MBE Growth and Optical Characterization of an (Al,Ga)N/AlN Bragg Reflector An (Al,Ga)N/AlN quarter-wave stack has been grown. The sample consists of ten periods of AlN (40 nm)/(Al,Ga)N (35.9 nm) alternances. The Al composition of the high-index layers is $23 \pm 2\%$, as estimated through low- T photoluminescence. The nominal thicknesses aim at centering the stop-band around 340 nm, using published values of the refractive index related to (Al,Ga)N and AlN [12, 13].

A scanning electron microscope (SEM) image of the mirror stack is shown in Fig. 3. The alternances are well defined and the respective thicknesses are in agreement with their values deduced from in situ reflectivity. The period was also checked by transmission electron microscopy. One notes in Fig. 3 the presence of a crack (small depression at the surface on the right part of the picture). From plan view SEM images we can see

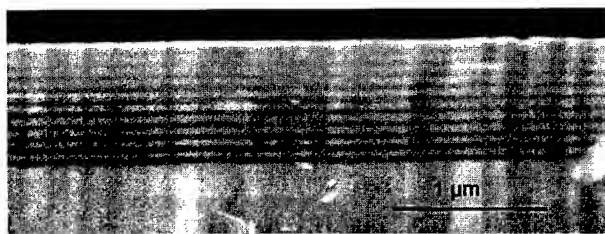


Fig. 3. SEM cross-section view of a ten-period $\text{Al}_{0.2}\text{Ga}_{0.8}\text{N}/\text{AlN}$ Bragg mirror on (111)Si

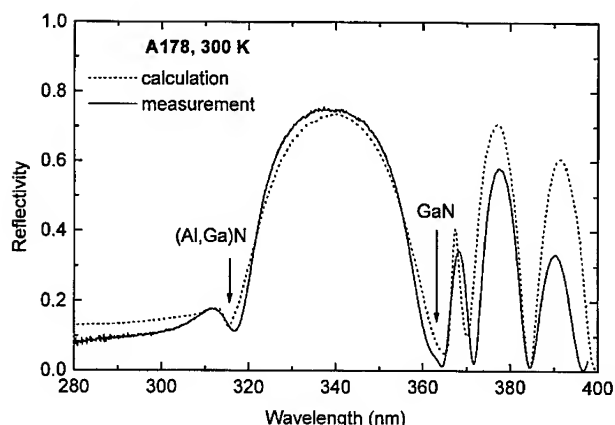


Fig. 4. Reflectivity spectrum of the mirror shown in Fig. 3. Solid line: experimental results, dotted line: calculated spectrum

that these cracks are separated by a few μm . Apparently, they are formed at the interface between the first AlN layer and the GaN-on-Si template. While crack-free GaN layers up to 3 μm thick can be grown with our procedure, this is not the case for thick heterostructures. Work is under progress in order to reduce the density of these cracks.

The normal incidence reflectivity spectrum of this sample is shown in Fig. 4. The stop band width at half maximum is 35 nm. Arrows point out the features related to the gaps of (Al,Ga)N and of underlying GaN. A calculated spectrum is shown as dotted line. The calculation is performed using the transfer matrix method [14] and takes into account the entire structure (mirror, buffer layer, Si). A real refractive index of 2.15 is used for AlN. The imaginary part of the (Al,Ga)N index is modeled using a band gap of 3.96 eV, in agreement with the low temperature PL determination. A constant real part of the index equal to 2.33 is used, which is consistent with published values (that anyhow show some scatter) [12, 13]. For the underlying GaN layer, the complex refractive index has been measured through ellipsometry experiments [15]. Note that in Fig. 4 the absolute reflectivity is calibrated with the help of the calculated spectrum in the absorption region of (Al,Ga)N, but the maximum value of $\approx 75\%$ is in rather good agreement with that measured using a calibrated mirror ($\approx 78\%$).

Reaching a peak reflectivity of 90% should require to increase the number of periods to 17. However, we mention that calculations on microcavities using known oscillator strengths of nitrides [4, 15] show that strong coupling effects can already exist for a reflectivity of 75%.

4. Conclusions GaN, AlN and (Al,Ga)N have been grown by molecular beam epitaxy on (111)Si substrates. A ten-period (Al,Ga)N/AlN mirror displays a stop band centered at 340 nm with peak reflectivities of $\approx 78\%$. These results, together with the flexibility in the structures allowed from the use of Si substrates, in particular the possibility of a chemical etching of the substrate, are promising for obtaining strong coupling phenomena in nitride based microcavities.

Acknowledgements The authors wish to thank H. Lahrèche, P. Vennéguès, M. Passerel, O. Tottereau (CRHEA, Valbonne) and C. Grattapain (Thomson CSF, Corbeville) for their assistance. This work is supported in part by E.C. contract HPRN-CT-1999600132 'CLERMONT'.

References

- [1] S. NAKAMURA and G. FASOL, *The Blue Laser Diode*, Springer-Verlag, Berlin 1997.
- [2] H. BENISTY, H. DE NEVE, and C. WEISBUCH, *IEEE J. Quantum Electron.* **34**, 1612 (1998); **34**, 1632 (1998).
- [3] T. SOMEYA, R. WERNER, A. FORCHEL, M. CATALANO, R. CINGOLANI, and Y. ARAKAWA, *Nature* **285**, 1905 (1999).
- [4] A. KAVOKIN and B. GIL, *Appl. Phys. Lett.* **72**, 2880 (1998).
- [5] T. SOMEYA and Y. ARAKAWA, *Appl. Phys. Lett.* **73**, 3653 (1998).
- [6] R. LANGER, A. BARSKI, J. SIMON, N.T. PELEKANOS, O. KONOVALOV, R. ANDRÉ, and D. LE SI DANG, *Appl. Phys. Lett.* **74**, 3610 (1999).
- [7] H.M. NG, T.D. MOUSTAKAS, and S.N.G. CHU, *Appl. Phys. Lett.* **76**, 2818 (2000).
- [8] M. LEROUX, H. LAHRÈCHE, F. SEMOND, M. LAÜGT, E. FELTIN, N. SCHNELL, B. BEAUMONT, P. GIBART, and J. MASSIES, *Proc. Europ. Conf. SiC and Related Materials, ESCRM 2000*, to be published.
- [9] F. SEMOND, B. DAMILANO, S. VÉZIAN, N. GRANDJEAN, M. LEROUX, and J. MASSIES, *phys. stat. sol. (b)* **216**, 101 (1999).
- [10] S.A. NIKISHIN, N.N. FALIEV, V.G. ANTIPOV, S. FRANCOEUR, L. GRAVE DE PERALTA, G.A. SERYOGIN, H. TEMKIN, T.I. PROKOFYEVA, M. HOLTZ, and S.N.G. CHU, *Appl. Phys. Lett.* **75**, 2073 (1999).
- [11] M. LEROUX, N. GRANDJEAN, B. BEAUMONT, G. NATAF, F. SEMOND, J. MASSIES, and P. GIBART, *J. Appl. Phys.* **86**, 3721 (1999) and references therein.
- [12] D. BRUNNER, H. ANGERER, E. BUSTARRET, F. FREUDENBERG, R. HÖPLER, R. DIMITROV, O. AMBACHER, and M. STUTZMANN, *J. Appl. Phys.* **82**, 5090 (1997).
- [13] M.J. BERGMANN, Ü. ÖZGÜR, H.C. CASEY JR., H.O. EVERITT, and J.F. MUTH, *Appl. Phys. Lett.* **75**, 67 (1999).
- [14] R.M.A. AZZAM and N.M. BASHARA, *Ellipsometry and Polarized Light*, North Holland Publ. Co., Amsterdam 1977.
- [15] L. SIOZADE, S. COLARD, M. MIHAILOVIC, J. LEYMARIE, A. VASSON, N. GRANDJEAN, M. LEROUX, and J. MASSIES, *Jpn. J. Appl. Phys.* **39**, 20 (2000).

phys. stat. sol. (a) **183**, 169 (2001)

Subject classification: 73.40.Cg; S1.2; S7.14

Investigation of Low-Resistance Metal Contacts on p-Type GaN Using the Linear and Circular Transmission Line Method

A. WEIMAR¹⁾, A. LELL, G. BRÜDERL, S. BADER, and V. HÄRLE

OSRAM Opto Semiconductors GmbH & Co OHG, D-93049 Regensburg, Germany

(Received October 8, 2000)

In this work we investigated the specific contact resistances of the different metallizations Pt, Pd, and Ni on p-type GaN. Those materials were deposited both by thermal and electron beam evaporation on LED wafer material grown on SiC by MOCVD after using a standard surface treatment. Realizing various annealing steps we were able to achieve results in the low $10^{-3} \Omega \text{ cm}^2$ range. To determine those values, TLM (transmission line method) patterns were made by photolithography technique. To proof the usability of the TLM measurements on LED wafer material a comparison of the results obtained by linear and circular test structures with different geometries is given. Furthermore, the Pt, Pd and Ni contacts were examined by temperature dependent TLM measurements to get information concerning the current transport mechanism at the p-GaN-metal interface. The experiments showed only a weak temperature dependence of the contact resistances which indicates that mainly the field emission determines the contact resistance.

1. Introduction Ga(In,Al)N is one of the most promising materials to realize short wavelength light emitting diodes (LEDs) and laser devices. At OSRAM Opto Semiconductors those structures are grown by metalorganic vapour phase epitaxy on SiC substrates as well as on sapphire. One of the most demanding challenges on the way to achieve cw operation for laser diodes is to ensure very low metal-p-GaN contact resistances to decrease the heat generation due to ohmic losses. In this work we report about a well known measurement technique for the determination of the contact resistance using LED wafer material, annealing experiments for different contact materials and temperature dependent TLM (transmission line method) measurements.

2. Theoretical Background Contacting a metal to the p-GaN layer results in a bending of valence and conduction band within the semiconductor and an energy barrier for carriers at the interface. The barrier height Φ_B is determined by the metal work function Φ_M , the bandgap E_G and the electron affinity χ of the p-GaN and can be expressed by

$$\Phi_B = (\chi + E_G) - \Phi_M. \quad (1)$$

This expression is valid for an ideal Schottky diode [1]. Another physical effect is the so called Fermi level pinning. Due to interface states within the bandgap the relative position of the Fermi level is pinned to a certain distance of the valence band and so

¹⁾ Corresponding author; Tel.: +49-941-2022594, Fax: +49-941-2027287;
e-mail: andreas.weimar@osram-os.com

the barrier height would be independent of the metal work function. Which of the two effects is dominating, depends on the semiconductor material and the interface condition [1].

There are no metals available with work functions above 6 eV [2] and the electron affinity of GaN is reported to be 4.1 eV [3] with a bandgap of 3.4 eV. This means for p-GaN, that in both cases – ideal Schottky diode and/or Fermi level pinning – there is a positive barrier for the majority carriers. Since the p-GaN–metal contact in LDs and LEDs under operation corresponds to a Schottky-contact in reverse direction, thermionic and field emission are the two main current transport mechanisms.

Murakami et al. [4] reported about an estimation for the contact resistance R_c for both thermionic and field emission. The corresponding formulas are

$$R_c = \frac{h^3}{q^2 4\pi m^* kT} \exp\left(\frac{q\Phi_B}{kT}\right) \quad (2)$$

for thermionic and

$$R_c = C \exp\left[\frac{4\pi \sqrt{\epsilon m^*}}{h} \left(\frac{\Phi_B}{\sqrt{N_A}}\right)\right] \quad (3)$$

for field emission, where q is the electronic charge, h is the Planck constant, m^* the effective mass of the tunneling hole, k the Boltzmann constant, T the absolute temperature, ϵ the dielectric constant of p-GaN, and N_A its net acceptor concentration. The pre-factor C has a weak temperature dependence [4].

To lower the contact resistance one should realize the lowest possible barrier height ϕ_B , increasing both thermionic and field emission, and the highest possible net acceptor concentration, increasing tunneling.

3. Measurement Technique The commonly used method to determine the contact resistance is the so called TLM measurement [5].

For that, either rectangular or circular test structures like those shown in Fig. 1 are needed. For determination of the contact resistance the voltage drop is measured by forcing a constant current through the neighboring pads of the rectangular geometry and between the inner circle and the adjacent field of the circular geometry. To avoid current flow at the contact edge in the rectangular contacts a mesa structure is fabricated which defines the semiconductor area for the rectangular TLM patterns. The total resistance values R_{pp} (obtained by U/I) can be expressed by

$$R_{pp} = R_s \frac{d + 2L_T}{Z} \quad (4)$$

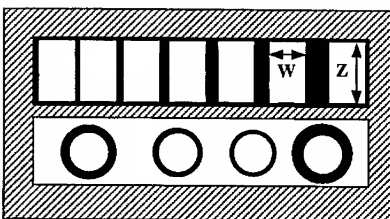


Fig. 1. Rectangular and circular test structures (white: semiconductor and metallization, black: semiconductor, hatched: substrate)

for rectangular geometry and

$$R_{pp} = \frac{R_s}{2\pi} \left[\ln \left(\frac{r_o}{r_i} \right) + L_T \left(\frac{1}{r_o} + \frac{1}{r_i} \right) \right] \quad (5)$$

for circular geometry. R_s is the sheet resistance of the semiconductor layer, d the spacings and Z the length of the rectangular pads; r_i and r_o are the inner and the outer radii of the circular patterns. The transfer length L_T is the averaged portion of the contact width W which is really flown through by current. It depends on the ratio of the contact resistance R_c in $\Omega \text{ cm}^2$ and the sheet resistance R_s in Ω under the contact and can be expressed by $L_T = \sqrt{R_c/R_s}$. Fitting the R_{pp} values of different spacings to the appropriate formulas (4) or (5) yields the free parameters R_s and L_T and so R_c can be calculated. The accuracy of this method depends mainly on the error $\Delta L_T/L_T$. The principal share of ΔL_T is due to the error in defining the exact spacings. For example a R_c of $1 \times 10^{-3} \Omega \text{ cm}^2$ and a sheet resistance of $50 \text{ k}\Omega/\text{square}$ leads to a L_T of about $1.4 \mu\text{m}$. An error Δd of $0.2 \mu\text{m}$ would lead to a $\Delta L_T/L_T$ of about 7%. In general the accuracy increases with decreasing sheet resistance and increasing contact resistance, which both lead to a higher value of L_T . More details about the TLM theory can be found elsewhere [5].

The validity of this method depends on some general conditions like $L_T \gg W$, d much larger than thickness of the conducting p-GaN layer, and a neglectable metal sheet resistance.

For contact resistance experiments using Ga(In,Al)N LED wafer material there are two additional aspects of interest. The obtained sheet resistance is averaged since the conducting semiconductor layer is a multilayer containing a p-GaN and p-AlGaIn layer.

This multilayer is limited by the pn-junction as long as the applied voltage is low enough to prevent an unwanted parallel current path through the n-side of the device. This can be ensured by applying an additional reverse voltage between n-side and p-side of the wafers.

3.1 p-GaN/Pd contact resistance measurements In the following section a comparison of results obtained by linear and circular TLM structures with different geometries is given. The investigated wafers are Ga(In,Al)N LED samples grown on SiC substrates by MOCVD. After a standard multiple-step cleaning process including the removal of organic and metallic contaminations as well as the native oxide, a 100 nm thick Pd layer was vacuum evaporated. The TLM patterns were realized by photolithography and wet etching of the contact material. Finally the mesa-structures were defined by reactive ion etching (RIE) using a second photolithographic step. Following dimensions were chosen for the TLM patterns: $W = 150 \mu\text{m}$, $L = 150, 300$ and $600 \mu\text{m}$ for the linear and $r_i = 50$ and $100 \mu\text{m}$ for the circular structures. The spacings are $2, 4, 8, 16, 32$ and $64 \mu\text{m}$. Before analysing the data, the exact spacings were verified with an optical microscope (error $\pm 0.2 \mu\text{m}$).

The current-voltage characteristics for evaluating the R_{pp} values showed non-linear behaviour. One possible reason is that the contact resistance obtained by this method is averaged for a Schottky diode in forward and in reverse direction as long as no ohmic behaviour is achieved for the p-GaN-metal interface.

A second possible reason is due to the LED wafer material: different applied voltages could lead to a voltage dependent current path due to the multiple layer structure and the pn-junction.

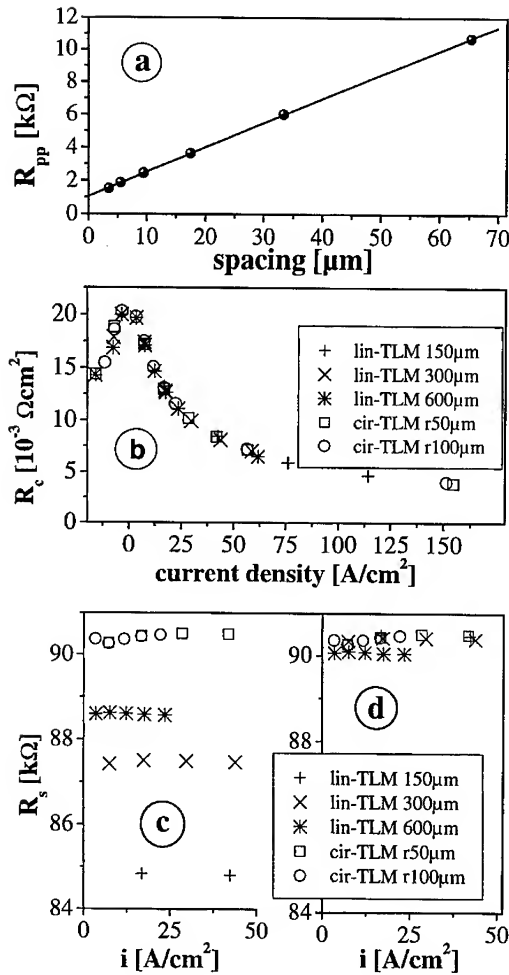


Fig. 2. TLM measurement results of Pd contacts by linear and circular test structures

Figure 2a shows the R_{pp} values versus the spacings of the linear TLM pattern with a contact length of 600 μm and a measurement current of 0.5 mA. The observed linear behaviour indicates that the current path is independent of the applied voltage. In Fig. 2b the contact resistances R_c are plotted versus the current density $I/(L_T Z)$. The values obtained by the different geometries show an excellent agreement and a decrease of contact resistance with increasing current density. The corresponding R_s values are plotted in Fig. 2c up to 50 A/cm². The independence of R_s from current density is another indicator for constant current paths. The difference in the absolute values between the linear and the circular TLM results is due to geometrical effects, because the width of the mesa structures is 10 μm greater than the pad lengths which leads to an underestimation of R_s . The corrected R_s values for the linear TLM patterns

are plotted in Fig. 2d and equal to the results from circular TLM measurements.

Concluding this section, the results show that the TLM measurement technique can be applied to diode wafer material consisting of a multiple p-layer and a pn-junction without remarkable errors due to varying current paths. Paying attention to the current density dependence of the contact resistance and the exact geometry of the mesa structure the determination of R_c and R_s by linear and circular TLM patterns with different geometries leads to comparable results.

3.2 Annealing experiments for Pd, Pt and Ni contacts For the different metallizations Pd, Pt and Ni we measured the contact resistances and their behaviour with various annealing treatments. Those metals were chosen because of their high work function (5.12 eV for Pd, 5.15 eV for Ni and 5.65 eV for Pt [2]). Again we used LED wafers for this experiment. The results were obtained by circular TLM measurements with spacings of 5, 10, 15 and 25 μm and an inner radius of 50 μm. The thicknesses of the metallizations were 100 nm for Pd and Pt and 200 nm for Ni. While the TLM patterns

for Pd and Ni were defined by wet etching, the removal of Pt was done by back sputtering. For correct comparison of the different metal-p-GaN contacts the R_c values were determined for various measurement currents allowing to interpolate R_c for a current density of 100 A/cm². Figure 3 shows the results obtained from nine samples (three for each metallization), which were all measured at room temperature before and after a 3 min annealing at 400 °C. In a second annealing step always one of the three samples was heated up to 500, 600 or 700 °C for another 3 min.

For the Pt samples the contact deteriorates with increasing annealing temperature. The lowest R_c value of $2.8 \times 10^{-3} \Omega \text{ cm}^2$ was measured at an unannealed sample. Two of the Ni samples showed a decrease of contact resistance after a 400 °C heat treatment whereas another sample needed a further annealing up to 500 °C to show a comparable improvement. The best value for Ni contacts was measured to be $5.9 \times 10^{-3} \Omega \text{ cm}^2$ (annealed at 400 °C). Temperatures of 600 °C and more, strongly deteriorate the contact. The results of the Pd samples show a continuous improvement of the contact resistance with increasing annealing temperature up to 600 °C with a best value of $2.4 \times 10^{-3} \Omega \text{ cm}^2$. At higher temperature this contact also gets unstable.

The annealing experiment showed comparable contact resistances for untreated Pt contacts and Pd contacts annealed up to 600 °C. The Ni contacts were worse and showed conflicting behaviour for annealing at 400 °C.

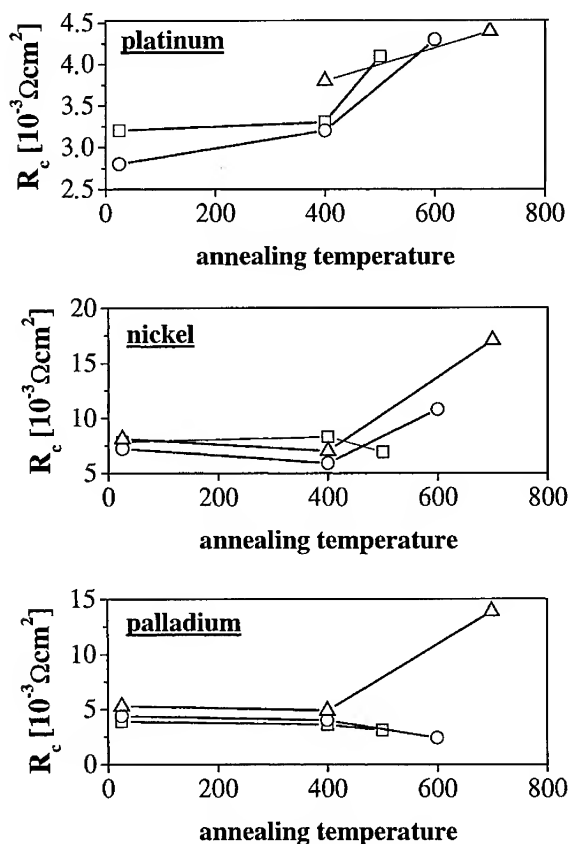


Fig. 3. Contact resistances of Pt, Ni and Pd metallizations for different annealing treatments

3.3 Temperature dependent TLM measurements In this experiment, the temperature dependence of the contact resistance was investigated for Pd, Pt and Ni to p-GaN contacts. The same TLM test-structures as in the experiment reported above were realized. To measure the current-voltage characteristics for the TLM analysis we used a measurement equipment for temperature dependent conductivity measurements at the crystal growth laboratory of the Erlangen University.

The samples were measured in a small vacuum chamber at temperatures ranging from 270 up to 470 K in steps of 20 K. In Fig. 4 the R_s and R_c results are shown for the different metallizations. The R_{pp} values were determined at a measurement current of 0.5 mA.

In Fig. 4a the $1/R_s$ values are shown in an Arrhenius plot and have the typical decrease of semiconductor resistance with increasing temperature. Neglecting the temperature dependence of the hole mobility the slope of the curves yields the activation energy for the Mg acceptors. The dashed lines show the expected slope for acceptor levels of 180 and 200 meV over the conduction band edge, which represents the published range for Mg acceptor levels in GaN and Ga(Al)N with Al contents up to 10% [6]. The deviation of the results from the linear behaviour at lower temperatures could be explained by an additional hopping conduction taking place for highly doped GaN [6]. Anyway, the temperature dependence of the R_s values are in a reasonable range and therefore corroborates the validity of this measurement technique.

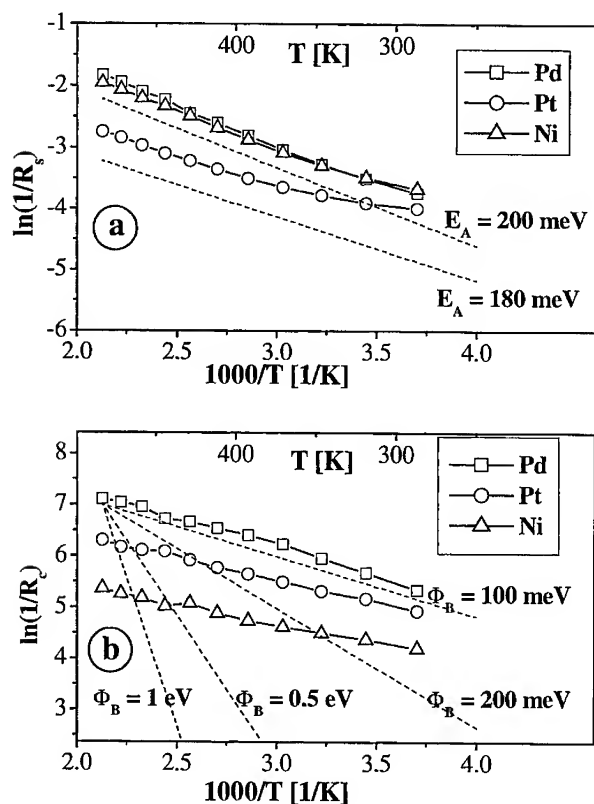


Fig. 4. Arrhenius plots of $1/R_s$ and $1/R_c$ for Pt, Pd and Ni contacts obtained by temperature dependent TLM measurements

According to formula (2) the temperature dependence of the contact resistance in case of pure thermionic emission is mainly exponential. The slopes of the $1/R_c$ curves in the Arrhenius plot of Fig. 4b would enable the determination of the barrier heights at the metal–semiconductor interface. The dashed lines show the expected slopes in case of pure thermionic emission. The R_c results would lead to a barrier height of about 0.1 eV independent of the contact material. We do not believe in those values because, according to formula (2), the calculated R_c values for thermionic emission over a 100 meV barrier would lead to a contact resistance in the range of 10^{-6} to $10^{-8} \Omega \text{ cm}^2$. From another point of view a R_c of $10^{-3} \Omega \text{ cm}^2$, which is a realistic value for the investigated samples, would lead to a barrier height of about 0.3 eV at room temperature.

The change in contact resistance up to 470 K should then be about three orders of magnitude which again is not comparable to our experimental results. In our eyes, these results indicate that the tunneling of electrons from the p-GaN to the metal is the main current transport mechanism, since the experiment showed only weak T -dependence expected for field emission according to formula (3).

To optimize the p-contact resistance, it is therefore essential to increase the net-acceptor concentration near the interface as well as to avoid any interfacial layers like a residual native oxide. Interfacial reactions of the metallization and the p-GaN forming intermetallic phases could further lower the barrier height and would increase both field and thermionic emission.

4. Conclusions From the p-GaN–Pd contact resistance measurements by linear and circular TLM patterns with different geometries we showed the suitability of this technique for LED wafer material containing a multiple p-layer and a pn-junction.

The annealing experiments for the different metallizations Pt, Pd and Ni resulted in a best value of $2.4 \times 10^{-3} \Omega \text{ cm}^2$ for a Pd-contact annealed three minutes at 400 °C and 600 °C, respectively.

For all three metallizations we believe that field emission is the dominating current transport mechanism at the p-GaN–metal interface since we observed only a weak temperature dependence of the contact resistances obtained by temperature dependent TLM measurements in the range of 270 K up to 470 K.

Acknowledgements A.W. thanks Prof. Dr. G. Mueller of the crystal growth laboratory at the Erlangen University in Germany for advising his PhD education and for placing the measurement equipment to the author's disposal. A.W. also thanks Dr. M. Fehrer (OSRAM-OS) for a critical reading of the manuscript. This work (part of the laser research program) was supported by the German government (BMBF).

References

- [1] S. M. SZE, *Physics of Semiconductor Devices*, John Wiley & Sons, New York 1989 (pp. 245–311).
- [2] H. B. MICHAELSON, *J. Appl. Phys.* **48**, 4729 (1977).
- [3] J. T. TREXLER, S. J. PEARTON, P. H. HOLLOWAY, M. G. MIER, K. R. EVANS, and R. F. KARLICEK, *Mater. Res. Soc. Symp. Proc.* **449**, 1091 (1997).
- [4] M. MURAKAMI and Y. KOIDE, *Crit. Rev. Solid State Mater. Sci.* **23**, 1–60 (1998).
- [5] G. S. MARLOW and M. B. DAS, *Solid State Electron.* **25**, 91 (1982).
- [6] W. GÖTZ and N. M. JOHNSON, *Semicond. Semimet.* **57**, 185 (1999).

phys. stat. sol. (a) **183**, 177 (2001)

Subject classification: 78.67.De; S7.14

Photon Recycling White Light Emitting Diode Based on InGaN Multiple Quantum Well Heterostructure

V. V. NIKOLAEV (a), M. E. PORTNOI (a), and I. ELIASHEVICH (b)

(a) *School of Physics, University of Exeter, Stocker Road, Exeter EX4 4QL, UK*

(b) *GELcore LLC, 394 Elisabeth Ave., Somerset, NJ 08873, USA*

(Received October 8, 2000)

A numerical method based on the transfer matrix technique is developed to calculate the luminescence spectra of complex layered structures with photon recycling. Using this method we show a strong dependence of the emission spectra on the optical eigenmode structure of the device. The enhancement of the photon recycling and the LED external efficiency can be achieved by placing the active regions inside single or coupled microcavities.

1. Introduction Recently, great interest has been shown in the use of light emitting diodes (LEDs) as a light source for illumination [1]. LEDs offer many potential advantages compared to conventional light sources due to their relatively low energy consumption, long lifetime and high shock resistance.

Currently white-light LEDs use photo-excitation of phosphors to convert the blue light from an InGaN/GaN LED into white light. However, phosphor has a broad emission spectrum, thus, white LEDs based on this principle do not have the maximum possible luminous efficacy.

The aim of this work is to investigate the feasibility and limitations of creating a white LED by integration within the same structure of several semiconductor layers emitting three basic colours. The recent progress in the growth of InGaN-based double heterostructures and quantum wells makes this alloy an ideal material for the LED active regions, due to the wide variety of the energy gaps in the InGaN system, covering frequencies from red to ultraviolet. The working regime of such a device can be achieved by electrical pumping of active layers with the widest bandgap (blue regions), and by making use of re-emission of the light, absorbed by all the active regions (so called photon recycling).

2. Modelling of Photon Recycling We start by writing an expression for the intensity of spontaneous emission from a quantum well (QW) into a bulk dielectric material. The number of photons with energy within the interval $[\hbar\omega, \hbar\omega + d(\hbar\omega)]$, which are emitted from the surface dS into the solid angle $d\Omega_0$ during the time interval dt is given by

$$dN = W_0 dt d(\hbar\omega) dS d\Omega_0$$

$$= \frac{\varepsilon\omega^3 \hbar e^2 p_{cv}^2 g_{2D}}{2\pi^2 c^3 m_0^2} \left[\int_0^{+\infty} \frac{f_{\text{hf}} \Gamma d\varepsilon}{(E^{2D} + \varepsilon)^2 ((E^{2D} + \varepsilon - \hbar\omega)^2 + \Gamma^2)} \right] dt d(\hbar\omega) dS d\Omega_0. \quad (1)$$

Here E^{2D} is the energy gap between the electron and hole quantized levels in the QW, g_{2D} is the reduced two-dimensional density of states, f_e and f_h are the electron and hole occupation probabilities, ε is the dielectric constant of the material containing the well, m_0 is the free electron mass, and Γ accounts for the interband relaxation and other broadening mechanisms. The squared momentum matrix element p_{cv}^2 is given in the effective mass approximation for deep QWs by [2]

$$p_{cv}^2 = \frac{p_0^2}{2} (1 + \gamma)$$

for TE modes, and by

$$p_{cv}^2 = \frac{p_0^2}{2} [(1 + \gamma) \cos \theta + (1 - \gamma) \sin \theta]$$

for TM modes. Here θ is the angle between the plane-wave propagation direction and Z-axis (normal to the QW plane), and $\gamma = (E_{2D} - E_g)/(\hbar\omega - E_g)$, where E_g is the bandgap energy of the QW material, and p_0 is the interband momentum matrix element.

We will use the transfer matrix technique in the plane waves basis [3] to analyse the optical properties of layered structures. The plain-wave mode interaction with the QW is described by a QW transfer matrix. If the quantum well width is much smaller than the light wavelength, the transfer matrix has the form

$$\hat{M} = \begin{pmatrix} 1 + Y & Y \\ -Y & 1 - Y \end{pmatrix}.$$

Here Y is defined by the two-dimensional QW optical susceptibility χ_{2D} :

$$Y = i \frac{2\pi k_0^2}{k_z} \chi_{2D}, \quad (2)$$

where \mathbf{k} is the wavevector of light, $k_0 = \omega/c$; and χ_{2D} for a single-subband QW is given by [4]

$$\chi_{2D} = \frac{\hbar^2 e^2 p_{cv}^2 g_{2D}}{m_0^2} \int_0^{+\infty} \frac{1 - f_h - f_e}{(E^{2D} + \varepsilon)^2 (E^{2D} + \varepsilon - \hbar\omega - i\Gamma)} d\varepsilon.$$

To calculate the rate of photon extraction from a complex structure we consider the interference of all possible processes resulting in light emission out of the structure. These calculations require a knowledge of the amplitude transmission and reflection coefficients t_l and r_l for the structure part on the left of the QW, and similar coefficients t_r and r_r for the structure part on the right of the QW. We also need to know the transmission and reflection coefficients t_{QW} and r_{QW} for the quantum well itself. Each of these coefficients can be obtained from the corresponding transfer matrix.

Let us derive, for example, the power emitted from the right side of the structure. A photon emitted inside the structure to the right can be transmitted directly to the outside medium, or it can be consecutively reflected from the right and left sides of the structure and finally will be transmitted outside and so on. The outgoing electric field, resulting from all these processes is given by the sum

$$E_{r \rightarrow r} = t_r + r_r r_l^* t_r + r_r r_l^* r_l^* t_r + \dots = \frac{t_r}{1 - r_l^* r_r},$$

where the star in r_1^* indicates, that this coefficient includes the reflection from the emitting QW.

Similarly, photons emitted inside the structure to the left can undergo multiple reflections and eventually escape from the structure to the right. These processes give a second part of the external field:

$$E_{l \rightarrow r} = \frac{\eta t_{\text{QW}} t_r}{(1 - r_1^* r_r)(1 - r_{\text{QW}} r_l)}.$$

Thus, we obtain the expression for the emission from the right side of the structure:

$$dN_{E_r} = W_0 \left| \frac{t_r}{1 - r_1^* r_r} \left[1 + \frac{\eta t_{\text{QW}}}{1 - r_{\text{QW}} r_l} \right] \right|^2 \frac{\sqrt{\epsilon_r} k_{zr}}{\sqrt{\epsilon_0} k_{z0}} dt d(\hbar\omega) dS d\Omega_e, \quad (3)$$

where the ratio $\sqrt{\epsilon_r} k_{zr} / \sqrt{\epsilon_0} k_{z0}$ accounts for the change in solid angle that is due to refraction for plane waves. The indices r and 0 are related to the outside medium and the layer containing the QW, respectively. To obtain the total density of the external light intensity we have to sum over all QWs and integrate Eq. (3) over the external solid angle Ω_e .

If we neglect the reflection from the QW by substituting $t_{\text{QW}} = 1$ and $r_{\text{QW}} = 0$ into Eq. (3), the formula for extraction becomes analogous to the one obtained using the source-term method [5].

For the quantitative description of the recycling process, we have to calculate the rate of absorption by the quantum well QW_a of the spontaneous emission from the other well, QW_e . Thus, we need to know the induced electric field at the position of QW_a . The power flux balance shows that the rate of absorption of emitted photons by the unit area of surface of QW_a is given by

$$W_a = -\frac{1}{2} \sqrt{\epsilon} k_z |E|^2 \text{Re}(Y_{\text{QW}_a}) W_{0\text{QW}_e}, \quad (4)$$

where E is the complex amplitude of the field at the QW_a location, Y_{QW_a} is defined by Eq. (2), and $W_{0\text{QW}_e}$ is defined by Eq. (1). The induced field can be calculated in a similar fashion as it was done for extraction:

$$E = \frac{t(1 + r_{al}^*)}{(1 - r^* r_{er}^*)(1 - r_{al}^* r_{ar})} \left(1 + \frac{t_{\text{QW}_e} r_{er}}{1 - r_{er} r_{\text{QW}_e}} \right),$$

where r_{al} (r_{ar}) is a reflection coefficient for the part of structure to the left (right) of the well QW_a , r_{er} is a reflection coefficient for all the layers to the right of the well QW_e , and the coefficients r and t correspond to the part of the structure between QW_e and QW_a . Here we assume that QW_a is on the left of QW_e . The formula for the opposite case is similar.

One of the channels for the photon to escape from the recycling process is to be absorbed in a metallic mirror. Placing such a mirror onto the left side of the structure, and denoting the reflection coefficient of the left part of the structure, excluding the mirror, as r_l , the reflection coefficient from the mirror as r_m , the reflection coefficient for the wave incident from the mirror as r_s , and the transmission coefficient from the

QW to the mirror as t , we obtain the following expression for the number of absorbed photons:

$$dN_m = W_0 (1 - |r_m|^2) \left| \frac{t}{(1 - r_l r_r^*)(1 - r_m r_s)} \left(1 + \frac{r_l t_{QW}}{1 - r_l r_{QW}} \right) \right|^2 dt d(\hbar\omega) dS d\Omega_0. \quad (5)$$

We restrict our consideration by relatively low pumping levels, which are typical for the diode operation regime. Thus, the expression for the electron density [4] in the one-subband QW can be simplified (temperature is measured in energy units):

$$n = \frac{m_c}{\hbar^2 \pi} T \ln [1 + \exp(\mu_e/T)] \approx \frac{m_c}{\hbar^2 \pi} T \exp(\mu_e/T),$$

and the occupation probabilities can be expressed as

$$f_e = \frac{1}{1 + \exp\left(\frac{\varepsilon_e - \mu_e}{T}\right)} \approx \exp\left(\frac{\mu_e - \varepsilon_e}{T}\right) \approx n \frac{\hbar^2 \pi}{m_c T} \exp(-\varepsilon_e/T),$$

$$f_h = \frac{1}{1 + \exp\left(\frac{\varepsilon_h - \mu_h}{T}\right)} \approx \exp\left(\frac{\mu_h - \varepsilon_h}{T}\right) \approx p \frac{\hbar^2 \pi}{m_{hh} T} \exp(-\varepsilon_h/T),$$

where m_e (m_{hh}) and μ_e (μ_h) are the electron (heavy hole) effective mass and quasi-Fermi-level, respectively. Under the low-pumping assumption we can rewrite W_0 in the form:

$$W_0 = \frac{\varepsilon \omega^3 \hbar e^2 p_{cv}^2 g_{2D}}{2\pi^2 c^3 m_0^2} \left[\int_0^{+\infty} \frac{\Gamma \exp(-\varepsilon/T) d\varepsilon}{(E^{2D} + \varepsilon)^2 ((E^{2D} + \varepsilon - \hbar\omega)^2 + \Gamma^2)} \right] np. \quad (6)$$

The total rate of light emission into the external medium can be obtained by substituting Eq. (6) in Eq. (1) and integrating Eq. (1) over the external solid angle and photon energies. As a result the rate of radiative recombination depends on the carrier densities as $R_{ext} = E np$.

Due to the large photon energy separation between different colours, the absorption rate for the short-wavelength light is independent of the carrier density in the narrow-gap QW. For the light emitted from QW_e the rate of absorption in QW_a is given by the expression $R_{abs} = A n_e p_e$, where A is calculated by integrating Eq. (4) over the total solid angle of emission and over the photon energies. Here we assume that all QWs are embedded in layers of dielectric material with the refractive index equal to the highest one in the real structure. This trick allows us to handle the interaction of active layer with the evanescent wave. However, introducing several sufficiently thin layers with high dielectric constant does not alter the optical properties of the structure.

A similar relation holds for the rate of absorption in a metallic mirror: $R_m = M np$. Coefficient M is obtained by substituting Eq. (6) in Eq. (5) and integrating the result over the solid angle and photon energies. Note, that due to charge-neutrality the electron and hole densities in each QW are equal to each other, $n = p$.

The steady-state carrier densities are given by the balance between generation of electron-hole pairs in the QWs and their recombination, both radiative and non-radiative. The generation processes include electric current pumping of the blue QWs and the re-absorption of emitted light throughout the structure. The recombination output

goes to external emission and internal losses, which we treat as absorption in the other QWs and non-radiative recombination in the given QW. In our approach this leads to the following equation for each QW:

$$R_i = E_i n_i^2 + A_i n_i^2 + M_i n_i^2 + n_i / \tau_i,$$

where R_i is the pumping rate and τ_i is the non-radiative recombination time. Assuming that τ_i does not depend on the carrier density, we get

$$n_i = \frac{\sqrt{(1/\tau_i)^2 + 4(A_i + E_i + M_i)R_i} - 1/\tau_i}{2(A_i + E_i + M_i)}. \quad (7)$$

Then the external efficiency for each QW can be obtained as

$$\eta_i = \frac{E_i n_i^2}{(A_i + E_i + M_i) n_i^2 + n_i / \tau_i}.$$

3. Results and Discussion We used the numerical method described above to investigate a number of different types of structures. It was revealed, that the emission spectra and external efficiencies depend drastically on the active layer positions and on the mode structure of the device. Figure 1 shows the calculated spontaneous emission for a structure, which represents a GaN microcavity containing three QWs and covered on one side by a metallic mirror. The width of the GaN layer and the energies of interband transitions in red, green and blue QWs are chosen in such a way that the structure can be regarded as the $5\lambda/2$ resonator for the normally propagating red-light waves, $6\lambda/2$ resonator for the green-light waves and $7\lambda/2$ resonator for the blue-light waves. We placed each QW in an antinode of a resonant mode, associated with the QW colour. Our calculations were performed for different times of non-radiative recombination ranging from 1 ns to 10 ns, and we assumed the carrier density in blue QW to remain constant. One can see, that if the internal losses are high, the recycling

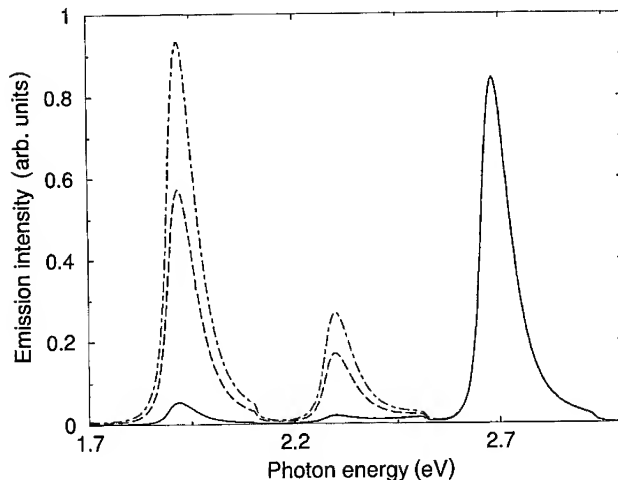


Fig. 1. Spontaneous emission spectra from a microcavity, containing three quantum wells. The non-radiative recombination times are 1 ns (solid line), 5 ns (dashed line) and 10 ns (dot-dashed line). The carrier density in the blue QW is the same for all three curves

efficiency is low and only blue light is emitted. When the internal efficiency increases, the emission from the optically pumped QWs becomes comparable with the blue-light intensity. The green-light intensity usually remains smaller than both blue and red because of the strong re-absorption in the red active region. However, this is beneficial for the white-light generation, because of the high sensitivity of the human eye in the green region of the spectrum. If high non-radiative losses are present, the recycling process can be enhanced by introducing more red and green QWs in the structure and by building a Bragg reflector for the blue wavelength. A possible way to enhance the external efficiencies of all three colours is to place the active regions into coupled microcavities.

References

- [1] S. NAKAMURA and G. FASOL, *The Blue Laser Diode*, Springer-Verlag, Berlin/Heidelberg/New York 1997.
- [2] M. ASADA, A. KAMEYAMA, and Y. SUEMATSU, *IEEE J. Quantum Electron.* **20**, 745 (1998).
- [3] M. BORN and E. WOLF, *Principles of Optics*, Pergamon Press, Oxford 1970.
- [4] H. HAUG and S.W. KOCH, *Quantum Theory of the Optical and Electronic Properties of Semiconductors*, World Scientific, Singapore 1990.
- [5] H. BENISTY, R. STANLEY, and M. MAYER, *J. Opt. Soc. Am. A* **15**, 1192 (1998).

phys. stat. sol. (a) **183**, 183 (2001)

Subject classification: 78.20.Bh

Optical Eigenmodes of a Spherical Microcavity

R. A. ABRAM (a), S. BRAND (a), M. A. KALITEEVSKI¹⁾ (a), and V. V. NIKOLAEV (b)

(a) Department of Physics, University of Durham, South Road, Durham DH1 3LE, UK

(b) School of Physics, University of Exeter, Stocker Road, Exeter EX4 4QL, UK

(Received October 8, 2000)

The optical mode structure of a spherical microcavity has been investigated using a transfer matrix approach. Exact algebraic equations from which the frequencies of the optical eigenmodes of the two polarizations can be obtained, as well as approximate explicit algebraic expressions for those frequencies have been derived. The distribution of the electric field in the eigenmode is analysed.

One of the major trends of modern semiconductor research is towards the achievement of electron and photon states of low dimensionality [1, 2]. Photons can be localized by periodic modulation of the refractive index of the medium in different types of microcavities, with a feature size of the order of a micrometer or below, and comparable with the wavelength of light.

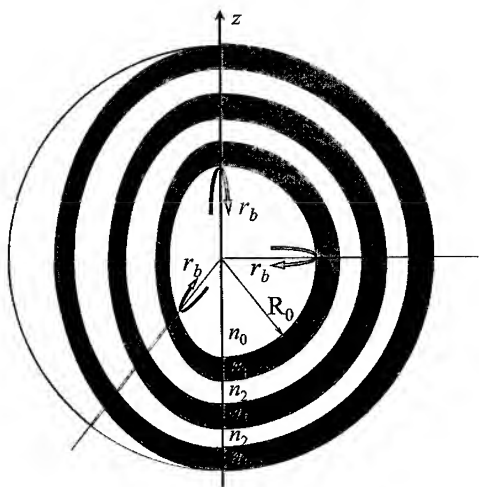
Two-dimensional localization by cylindrical multilayered structures has been demonstrated experimentally [3] and an interaction of excitons and photons in a cylindrical [4] and pillar [5] microcavities has been studied. Full three-dimensional localization of light can be achieved by introducing a defect into a three-dimensional photonic crystal [6].

The aim of this work is to investigate theoretically the optical eigenmode structure of a multilayered microcavity possessing spherical symmetry, as shown in Fig. 1. An advantage of such a structure is the possibility

to investigate the properties of zero-dimensional photonic states analytically.

A spherical electromagnetic wave can be represented as a superposition of two waves with independent polarization [7]: a TE wave with components $(H_r, E_\theta, E_\varphi, H_\theta, H_\varphi)$, and a TM wave with components $(E_r, E_\theta, E_\varphi, H_\theta, H_\varphi)$.

The spatial dependence of the electric and magnetic field in a spherical wave can



be expressed through the use of spherical harmonics characterized by orbital momentum l and its projection m , which can be any integer in the interval from $-l$ to l . An orbital momentum $l = 0$ corresponds to a fully spherically symmetric electromagnetic wave, which does not exist [7]. In the case of the TE wave field, a spherical wave with frequency ω in the media with refractive index n can be represented by

$$\mathbf{E} = -\mu k_0 \left(\frac{m}{\sin \theta} P_l^{|m|}(\cos \theta) \mathbf{e}_\theta + i \frac{\partial}{\partial \theta} P_l^{|m|}(\cos \theta) \mathbf{e}_\varphi \right) V(r) \exp(im\varphi), \quad (1a)$$

$$\begin{aligned} \mathbf{H} = & \left\{ \frac{l(l+1)}{r} V(r) P_l^{|m|}(\cos \theta) \mathbf{e}_r \right. \\ & \left. + \left(\frac{\partial}{\partial \theta} P_l^{|m|}(\cos \theta) \mathbf{e}_\theta + \frac{im}{\sin \theta} P_l^{|m|}(\cos \theta) \mathbf{e}_\varphi \right) \frac{1}{r} \frac{\partial}{\partial r} (rV(r)) \right\} \exp(im\varphi), \end{aligned} \quad (1b)$$

where A and B are constants, $V(r) = Ah_l^{(1)}(kr) + Bh_l^{(2)}(kr)$, the spherical functions $h_l^{(1)}(x)$ and $h_l^{(2)}(x)$ are coupled to the Hankel functions via $h_l^{(1,2)}(x) = \sqrt{\pi/2x} H_{l+1/2}^{(1,2)}(x)$. $P_l^{|m|}(\cos \theta)$ is the Legendre function and $k = n\omega/c$.

In spherical layered structures, the spatial dependence of the electromagnetic field, as well as the reflection and transmission coefficients, can be obtained by the transfer matrix technique [8], which also allows the investigation of the localization of light in spherical microcavities.

An electromagnetic field in the central core of the microcavity can be represented as the sum of incoming and outgoing waves. The field at the center of the microcavity should be finite, and this requires that the incoming and outgoing waves have equal amplitude in the central core. Also, the radial dependence of the field is described by the spherical Bessel function $j_l^{(1)}(x) = (h_l^{(1)}(x) + h_l^{(2)}(x))/2$. On the other hand, at the interface of the core and the adjacent layer the amplitude of the incoming wave should be equal to the amplitude of the outgoing wave multiplied by the amplitude reflection coefficient r_b of the spherical wave from the interface and the multilayered spherical structure beyond. Hence, the dispersion equation for the optical eigenmode of a spherical microcavity can be represented in the form

$$r_b h_l^{(1)}(kR_0) = h_l^{(2)}(kR_0). \quad (2)$$

This equation gives the eigen frequency of both TE and TM eigenmodes, but one should note that in the case of the TE mode the reflection coefficient represents the ratio of the tangential component of the electric fields in the incoming and outgoing waves, while for the TM wave r_b is the ratio of the tangential components of the magnetic field. If the reflection coefficient r_b is close to unity and absorption in the cavity is small the Q-factor of the cavity is large and equation (2) can be rewritten in the form

$$\arg(r_b) + \arg(h_l^{(1)}(kR_0)) - \arg(h_l^{(2)}(kR_0)) = 2\pi N, \quad (3)$$

where N is an integer.

When the radius of the central core R_0 becomes as large as the wavelength of the light the spherical functions $h_l^{(1)}(x)$ and $h_l^{(2)}(x)$ can be replaced by their asymptotic forms. Also, in the frequency region close to the Bragg frequency ω_{BR} the phase of the reflection coefficient can be approximated [9] by $\arg(r_b) = b(\omega - \omega_{BR})/\omega_{BR}$ for the TE

wave and $\arg(r_b) = \pi + b(\omega - \omega_{\text{BR}})/\omega_{\text{BR}}$ for the TM wave, where $b = \pi n_1 n_2 / (n_0(n_2 - n_1))$. As a result, equation (3) for the TE modes can be rewritten in the form

$$\omega = \frac{b + \pi(2N + l + 1)}{b/\omega_{\text{BR}} + 2n_0 R_0/c}, \quad (4a)$$

and for the TM modes

$$\omega = \frac{b + \pi(2N + l)}{b/\omega_{\text{BR}} + 2n_0 R_0/c}. \quad (4b)$$

Figure 2 shows the dependences of the TE and TM optical eigenmode frequencies of the spherical microcavity formed by a central core of radius R_0 surrounded by a quarter-wavelength spherical Bragg reflector as a function of the central core radius R_0 in the range close to the reflector's stopband. When R_0 is large, the curves for the TE and TM modes are interleaved and correspond closely to the behaviour predicted by the simplified formula (4). When R_0 becomes smaller, the qualitative dependence of the frequency on cylinder radius remains unchanged but the difference between the curves for the simplified formula and corresponding TE and TM branches increases.

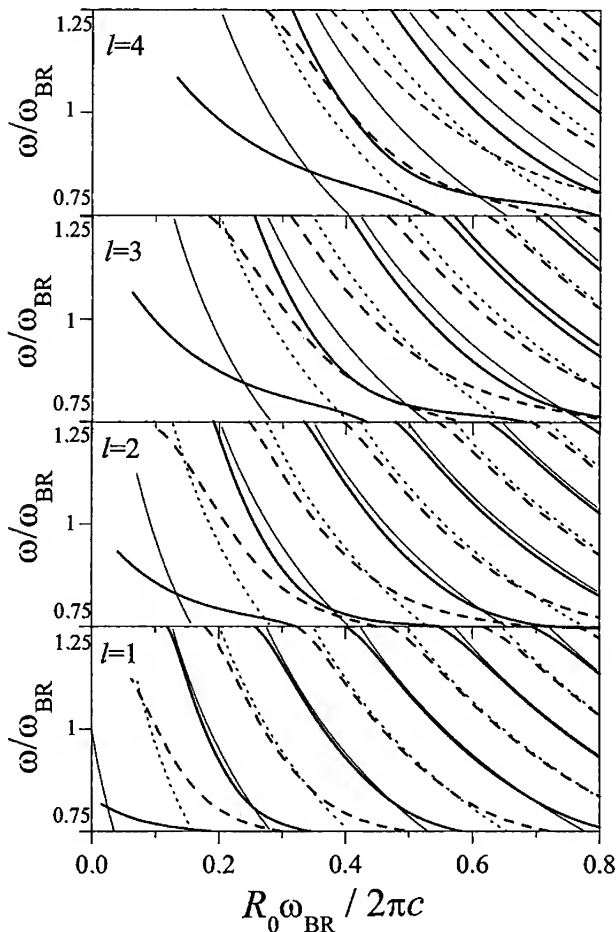


Fig. 2. The eigenmode photon energies for orbital momentum $l = 1, 2, 3, 4$ versus central core radius R_0 obtained using eqns. (3). The solid and dashed lines correspond to TE and TM modes, respectively. The faint and dotted lines correspond to the results obtained using the approximate formula (4) for TE and TM waves, respectively.

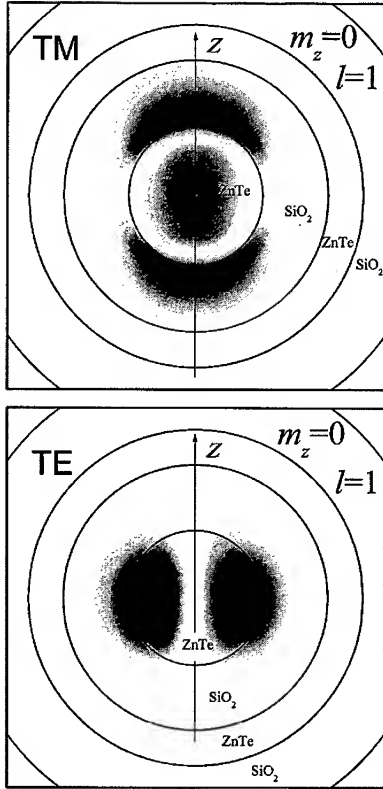


Fig. 3. Cross-section of the intensity of the electric field in the TE and TM eigenmodes of the spherical microcavity characterized by orbital momentum $l = 1$ and momentum projection $m_z = 0$

For TE optical eigenmodes the electric field in the centre of the microcavity is always equal to zero. The same result can be obtained for TM eigenmodes (recognizing that when $x \ll 1$, $j_l^{(1)}(x) \sim x^l$), if their orbital momentum $l \geq 2$. However, if we have $l = 1$ for the TM eigenmode the electric field in the centre of the cavity is not zero:

- the photonic state, characterized by $l = 1$ and $m_z = 0$ has an electric field oriented along the z -axis $\mathbf{E}(r = 0) = E_0 \mathbf{e}_z$;
- the photonic state, characterized by $l = 1$ and $m_z = \pm 1$, has an electric field rotating in the xy -plane $\mathbf{E}(r = 0) = E_0 (\mathbf{e}_x \pm i \mathbf{e}_y)$.

Figure 3 shows the distribution of the electric field in the optical eigenmode with $l = 1$ in the spherical microcavity. The central core of the microcavity has a refractive index of 2.7 and the radius R_0 obeying the relation $R_0 \omega_{BR} / 2\pi c = 0.15$, so the diameter of the cavity approximately corresponds to half the wavelength of light. The central

core is surrounded by a spherical quarter-wavelength Bragg reflector, formed by eight pairs of layers of refractive indices 1.45 and 2.7, whose widths $d_{1,2}$ obey the Bragg condition $d_i = \pi c / 2\omega_{BR} n_i$. The frequencies of TE and TM eigenmodes are $1.1195\omega_{BR}$ and $0.8785\omega_{BR}$. One can see that for the TE eigenmode, the field has toroidal structure and in the centre of the cavity the electric field is equal to zero. For the TM eigenmode the magnitude of an electric field in the centre of the cavity is non-zero and the maximum of the field is achieved in the polar areas in the low index layers, just outside the core. The high intensity contribution to this polar maximum of intensity is provided by a radial component of the electric field which has a discontinuity at the boundary of the two dielectrics.

For both polarizations the far field pattern of the cavity eigenmodes characterized by orbital momentum $l = 0$, $m_z = 0$ corresponds to the radiation of a dipole oscillating along the z -direction, while for the mode characterized by $l = 0$, $m_z = \pm 1$ the far field pattern corresponds to the radiation of an elementary rotator in xy -plane.

In summary, the transfer matrix method for spherical electromagnetic waves has been applied to the study of the properties of the Bragg spherical microcavity. A method of calculation of the optical eigenmodes of a spherical microcavity has been developed and the eigenmode structure of the cylindrical microcavity has been investigated. When the radius of the central core of the microcavity is large the spectral position of the optical eigenmodes can be described using a simple approximate formula. It is shown,

that for the TM eigenmode characterised by $l = 1$, an electric field in the centre of the microcavity is non-zero. For all other optical eigenmodes the electric field in the centre of microcavity vanishes.

Acknowledgements This work was partly funded by an EPSRC research grant and partly by INTAS and the RFBR .

References

- [1] E. BURNSTEIN and C. WEISBOUSH (Eds.), *Confined Exciton and Photons: New Physics and Devices*, Plenum Press, New York 1994.
- [2] C. WEISBOUSH and J. PARITY (Eds.), *Microcavities and Photonic Bandgaps: Physics and Applications*, Vol. 324 of NATO Advanced Study Institute, Kluwer Publ. Co., Dordrecht 1996.
- [3] D. OCHOA, R. HOUDRE, M. ILEGEMS, H. BENISTY, T. F. KRAUSS, and C. J. M. SMIRH, *Phys. Rev. B* **61**, 4806 (2000).
- [4] M. A. KALITEEVSKI, S. BRAND, R. A. ABRAM, V. V. NIKOLAEV, M. V. LEDENTSOV, C. M. SOTOMAYOR TORRES, and A. V. KAVOKIN, *Phys. Rev. B* **61**, 13791 (2000).
- [5] L. C. ANDREANI, G. PANZARINI, and J. M. GERARD, *Phys. Rev. B* **60**, 13276 (1999).
- [6] P. R. VILLENEUVE, SHANUI FAN, and J. D. JOANNOPOULOS, *Phys. Rev. B* **54**, 7837 (1996).
- [7] D. S. JONES, *The Theory of Electromagnetism*, Pergamon Press, London/Oxford 1964 (p. 483).
- [8] M. A. KALITEEVSKI, S. BRAND, R. A. ABRAM, and V. V. NIKOLAEV, *J. Mod. Opt.* (2000), submitted.
- [9] E. L. IVCHENKO, M. A. KALITEEVSKI, A. V. KAVOKIN, and A. I. NESVIZHSHII, 1996, *J. Opt. Soc. Amer. B* **13**, 1061 (1996).

phys. stat. sol. (a) **183**, 189 (2001)

Subject classification: 78.55.Cr; 78.67.De; S7.14

Study of MBE-Grown GaN/AlGa_N Quantum Well Structures by Two Wavelength Excited Photoluminescence

J. M. ZANARDI OCAMPO¹⁾ (a), H. KLAUSING (b), O. SEMCHINOVA (b), J. STEMMER (b), M. HIRASAWA (a), N. KAMATA (a) and K. YAMADA (a)

(a) *Department of Functional Materials Science, Saitama University, 255 Shimo-Ohkubo, Urawa, Saitama 338-8570, Japan*

(b) *Laboratorium für Informationstechnologie, Universität Hannover, Schneiderberg 32, D-30167, Hannover, Germany*

(Received October 8, 2000)

We report experimental results of two wavelength excited photoluminescence (TWEPL) applied to GaN/Al_{0.2}Ga_{0.8}N multiple quantum well structures grown by plasma assisted molecular beam epitaxy. An increase or a decrease in photoluminescence (PL) indicate the presence of trap centers with dissimilar characteristics for each case. In these samples, a spatial inhomogeneity of trap distribution originating from the growth process was detected due to different change in PL for distinct regions. Also a time-dependent phenomenon in PL was observed: after a continuous mid-term irradiation with UV light (4.12 eV), the amount of change in PL, which is characteristic of TWEPL, became nil. We argue this phenomenon is a complex issue that can be due to migration of native defects or a kind of saturation process involving trap centers.

1. Introduction Nitride-based semiconductor compounds for optoelectronic devices experienced a revolutionary breakthrough in the last decade [1]. Nevertheless, despite substantial improvement of their performance and reliability, there is still a considerable number of their physical properties that remain unclear to the scientific community. Among those materials, GaN/AlGa_N-based multiple quantum well (MQW) systems are important and attract much attention due to their variety of potential applications as in quarter-wave reflectors [2], active medium for inter sub-band transitions in cascade lasers, etc. In that sense, a thorough understanding of light-matter coupling processes in these compounds is of fundamental importance. Here we present experimental studies on non-radiative recombination (NRR) processes in GaN/AlGa_N MQWs, which have shown a change in the characteristics of their photoluminescence (PL) and NRR centers due to UV irradiation. We study the NRR processes by a completely optical method which is called Two Wavelength Excited Photoluminescence (TWEPL) [3].

2. Experimental Two samples, 1 and 2, were grown by plasma assisted molecular beam epitaxy (PAMBE) [4]. The active layer of the MQW structures under investigation consists of GaN wells (4 nm) sandwiched between Al_{0.2}Ga_{0.8}N barriers (40 nm). The number of barrier-well units is three or five for sample 1 and 2, respectively. The active layer is deposited on a 380 nm (350 nm for sample 2) thick Si doped GaN layer

¹⁾ Tel.: +81-48-858-3529; Fax: +81-48-858-9131; e-mail: jose@yamadalab.fms.saitama-u.ac.jp

with a silicon concentration of $5 \times 10^{17} \text{ cm}^{-3}$ for sample 1 and $2 \times 10^{18} \text{ cm}^{-3}$ in sample 2. The underlying AlN/GaN buffer layers grown on a sapphire substrate have a thickness of about 20 nm and 6 nm, respectively.

In TWEPL, by using two light sources, a below gap excitation (BGE, with energy $E_{\text{BGE}} < E_g$) is superposed on a conventional above gap excitation (AGE, $E_{\text{AGE}} > E_g$). The BGE, when matched to the energy of a trap center in the forbidden gap, unbalances the dynamical carrier equilibrium in the traps, producing a change on the intensity of the PL due to AGE. The value of the normalized intensity change $\Delta\text{PL} = I_{\text{AGE+BGE}}/I_{\text{AGE}}$ gives an observable measure of the NRR process selected by the BGE energy (here I_{AGE} is the PL intensity under only AGE irradiation and $I_{\text{AGE+BGE}}$ is that when both light sources are applied). Photoluminescence measurements were performed at 77 K. The optical excitations were provided by a filtered D₂ lamp (AGE) and the 1.064 μm line (1.164 eV) of a Nd:YAG laser (BGE). The sensitivity of the system is improved when working at low AGE and high BGE powers (P_{AGE} and P_{BGE}) [3], therefore a single-photon counting technique is used for detecting PL under an AGE density as low as possible.

Experimentally, two cases can arise due to addition of BGE: an *increase* or a *decrease* of PL, which are explained as follows.

2.1 PL increase A theoretical model to explain an increase in PL ($\Delta\text{PL} > 1$) is given in Fig. 1a; it includes one trap center (*one level model*) located at energy E_T inside the forbidden gap of the material [5]. When a suitable BGE energy is selected, either electrons from the valence band (V.B.) are excited into the trap center or electrons originally located at the trap are pumped into the conduction band (C.B.). As a result of this process, the number of holes in V.B. and/or electrons in C.B. increases ($+\Delta p$ and/or $+\Delta n$) finally giving an increase in PL. In case the cascade excitation of both processes

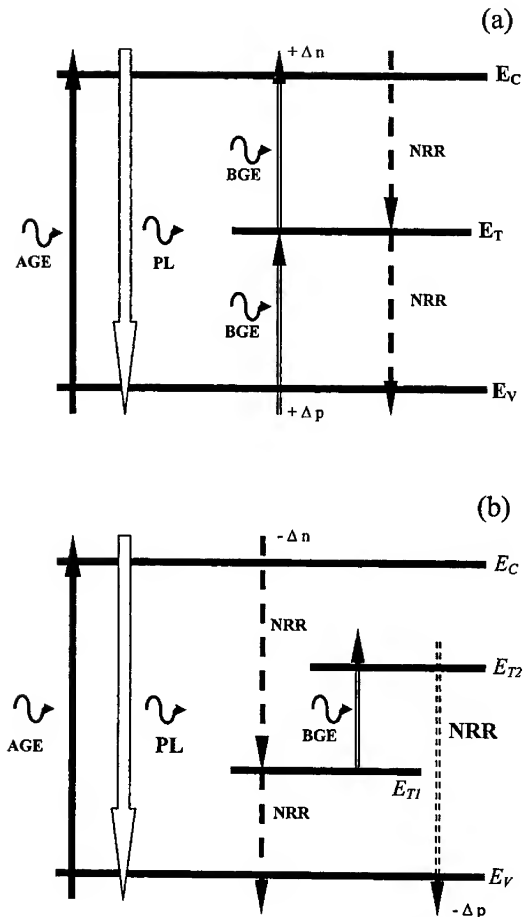


Fig. 1. Two theoretical models to explain TWEPL results: a) the *one level model* explains an increase in PL ($\Delta\text{PL} > 1$); b) the *two levels model* accounts for a decrease in PL ($\Delta\text{PL} < 1$)

occurs at the same time, band-to-band PL only by the BGE takes place. We have observed such up-conversion PL in an undoped GaAs/AlGaAs MQW [5].

2.2 PL decrease The model that accounts for a decrease in PL ($\Delta PL < 1$) is presented in Fig. 1b; it includes two traps (*two levels model*) referred as state 1 and state 2 at energies E_{T1} and E_{T2} , respectively [6]. In this case, BGE stirs electrons originally present in state 1 up to state 2 from which they recombine with holes in V.B. via a NRR process, reducing the hole concentration in the band ($-\Delta p$). In a parallel way, a NRR path can also be created by electrons from the C.B. onto state 1, which is now less populated (causing $-\Delta n$). This double decrease of free carriers in the bands produces a decrease in PL. By utilizing the saturation of PL intensity quenching with increasing BGE power, which is due to a trap-filling effect, we have succeeded in determining trap parameters self-consistently for the first time [7].

3. Results Preliminary conventional PL measurements proved that the samples present spatial non-uniformity, the PL intensity varying when rotating the sample on its holder. Due to that fact, for TWEPL we fixed the size of the excitation spot to 3 mm in diameter and selected two spatial regions at a separation of about 5 mm from the spot

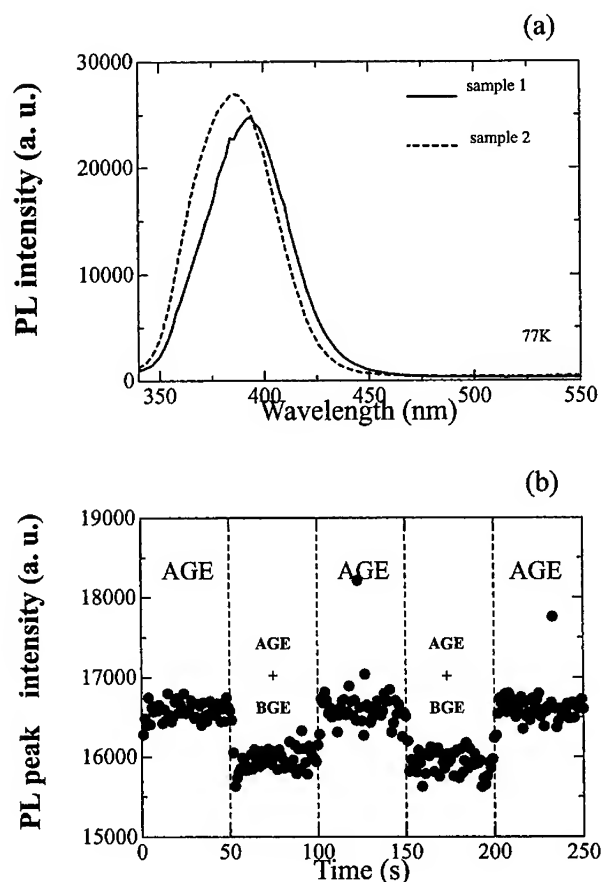


Fig. 2. a) PL spectra of samples 1 and 2 taken in *region A* ($E_{AGE} = 4.12$ eV, $P_{AGE} = 447$ nW/mm²); b) as-measured recorded data of TWEPL: a statistical time averaging is calculated for each of the segments of the abscissa and from there the ratio leading to ΔPL is calculated ($P_{AGE} = 447$ nW/mm², $P_{BGE} = 4.49$ mW/mm²)

center; they were designated as *region A* and *region B*. By setting the AGE energy to $E_{\text{AGE}} = 4.12$ eV, optical excitation was provided only to the GaN wells; BGE energy was set to $E_{\text{BGE}} = 1.16$ eV.

Photoluminescence spectra of both samples measured for *region A* under only AGE ($P_{\text{AGE}} = 447$ nW/mm²) can be observed in Fig. 2a. From these data we determine the spectral position of the PL intensity peak and proceed to fix the detection wavelength for TWEPL at that point.

Depicted in Fig. 2b is a typical recorded result of TWEPL: PL intensity (vertical axis) is plotted against time in the horizontal axis, which is divided in five segments of 50 s each. In this particular case it is clearly seen how PL intensity decreases ($\Delta\text{PL} < 1$) in the second and fourth segment, i.e., when BGE is added. A statistical time average of these results allows us to calculate the value of ΔPL , introduced as experimental points in Figs. 3 to 5.

3.1 Spatial inhomogeneity Figure 3 shows results of TWEPL performed on sample 1, for both spatial *regions A* and *B*, as the amount of change in PL (ordinate) versus AGE power density, P_{AGE} (abscissa). The power density of BGE was fixed at $P_{\text{BGE}} = 4.49$ mW/mm². In Fig. 3a, for *region A* a decrease in PL of roughly 4% is observed through the whole P_{AGE} range, which is explained by the *two levels model*. On the other hand, when measured on *region B* an increase in PL of about 2% was obtained, which fits our *one level model* (Fig. 3b). These distinct results indicate that the charac-

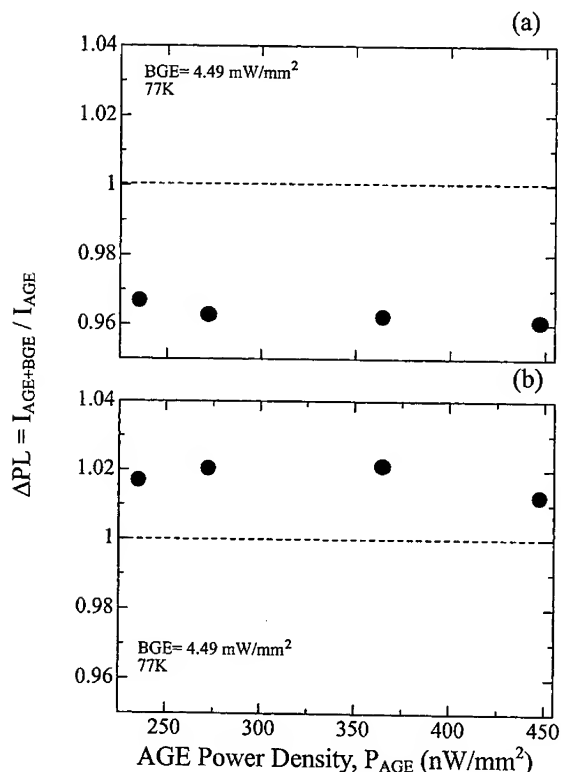


Fig. 3. Distinct change in PL intensity for different regions in sample 1: a) measurements in *region A* show a decrease in PL (*two levels model*), b) in *region B* an increase in PL was detected (*one level model*)

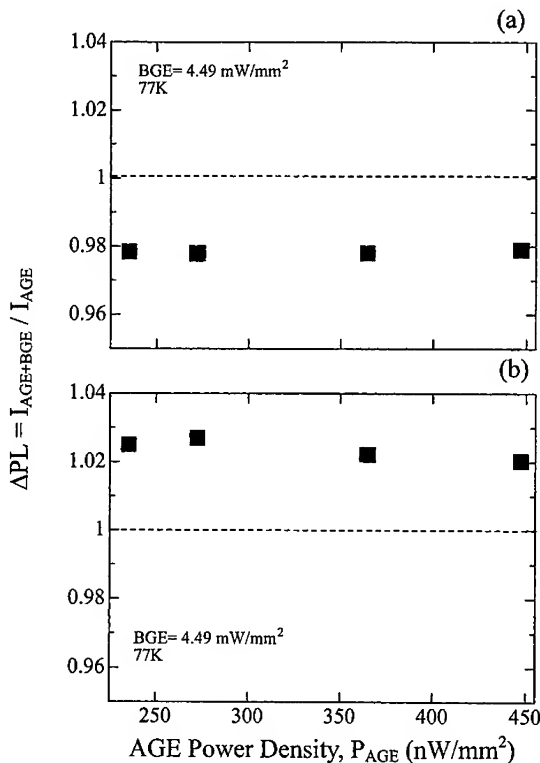


Fig. 4. Distinct change in PL intensity for different regions in sample 2: a) measurements in *region A* show a decrease in PL (*two levels model*), b) in *region B* an increase in PL was detected (*one level model*)

teristics of the trap centers detected in each region are basically different, each one explained by a different model.

In sample 2, for localized measurements we observed again a different behavior of ΔPL (see Fig. 4). A 2% reduction in PL for *region A*, contrary to a 2% increment in *region B* tells about the inhomogeneity of the sample through the presence of NRR centers of dissimilar characteristics.

3.2 Instability after mid-term UV irradiation

The amount of change in PL showed also a temporal dependence. After the experiments shown in Fig. 3a were concluded and without interrupting the AGE (UV) radiation, we fixed P_{AGE} at 447 nW/mm^2 and proceeded to sweep the BGE power density in the range $0.90 < P_{BGE} < 4.49 \text{ mW/mm}^2$ so as to further investigate the dynamics of the trap centers. The experimental results thus obtained are shown in Fig. 5, where each one of the subfigures has correspondence to an experimental point in Fig. 3a. In that way, concentrating on Fig. 5a, the rightmost point was taken under the same experimental settings as the rightmost point of Fig. 3a (notice the concordance of 4% decrease in PL intensity) and from there to the left a sweeping of P_{BGE} was done. As expected, the less the P_{BGE} the less the change in PL intensity, as it comes from our model [3].

The next step was to fix P_{AGE} to the three other values and perform in each case the same P_{BGE} sweeping. The sequence of subfigures in Fig. 5 follows the experimental chronology; the time ciphers denote the elapsed time of continuous AGE irradiation when each of the P_{BGE} sweepings started. From Fig. 5a through c it can be seen that no abnormal results were measured but, as depicted in Fig. 5d, after a critical time of 160 min of UV irradiation ($E_{AGE} = 4.12 \text{ eV}$) the change in PL intensity surprisingly faded out, that is $\Delta PL = 1$. This is an evidence of sudden change in the balance of the radiative and non-radiative processes involved. After that, even by performing measurements at the previous P_{AGE} values, ΔPL remained at unity. After interrupting AGE irradiation, the time it took to obtain again an appreciable change in PL was in the range of several hours, usually after one or two days, while in the

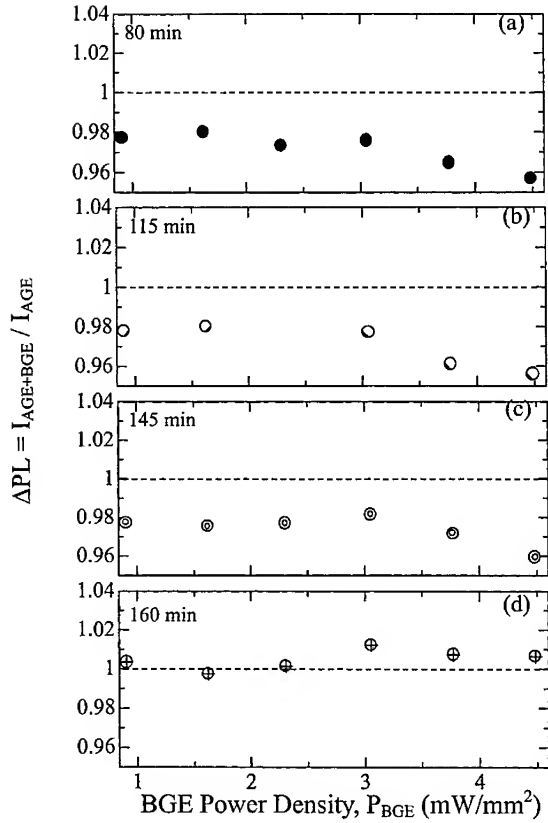


Fig. 5. The effect of BGE disappears after mid-term UV irradiation (AGE): up to 145 min (parts a to c), expected values of ΔPL were obtained; when 160 min of continuous AGE irradiation was reached, ΔPL became unity (part d)

meantime the sample was returned to room temperature.

The same temporal phenomenon in ΔPL was observed in *region B* of sample 1 and both *regions A* and *B* of sample 2, although the critical time was 90, 75 and 70 min, respectively.

4. Conclusions TWEPL was applied to study NRR recombination processes in MBE-grown GaN/Al-GaN MQWs. An inhomogeneity of the samples was detected, denoted by an increase or a decrease of the PL intensity change for different spatial regions, apparently due to non-uniformity of the growth process. In TWEPL, theo-

retical models that characterize NRR centers are different for the case of increase or decrease of PL, therefore we can argue that the trap centers detected in each region were unlike.

Concerning the amount of change in PL, given by ΔPL , an unconventional phenomenon occurred after continuously irradiating the sample with UV light for the AGE. After mid-term irradiation ranging from 70 to 160 min (depending on the sample and spatial region), ΔPL shifted to unity indicating that the effect of adding a BGE had disappeared. No previous values of ΔPL could be obtained again unless the AGE was interrupted for several hours (sample was also returned to room temperature). The reason for this anomalous behavior is certainly a complex issue that can be assigned to different processes involving either the carrier dynamics in the trap centers or light-matter coupling, as it has been reported [8, 9]. Though more systematic and thorough studies are to be done, in our case we reason that a migration of native defects (possibly surface states) can be promoted by the UV irradiation, thus changing the configuration of NRR systems. Also some kind of saturation process involving the trap centers could be taking effect after prolonged AGE excitation, in such a way that the effect of adding BGE is annulled.

References

- [1] S. C. JAIN, M. WILLANDER, J. NARAYAN, and R. VAN OVERSTRAETEN, *J. Appl. Phys.* **87**, 965 (2000).
- [2] T. SOMEYA and Y. ARAKAWA, *Appl. Phys. Lett.* **73**, 3653 (1998).
- [3] N. KAMATA, J. M. ZANARDI OCAMPO, K. HOSHINO, K. YAMADA, M. NISHIOKA, T. SOMEYA, and Y. ARAKAWA, *Recent Res. Developm. Quantum Electronics* **1**, 123 (1999).
- [4] M. A. L. JOHNSON, S. FUJITA, W. H. ROWLAND, JR., K. A. BOWERS, W. C. HUGHES, Y. W. HE, N. A. EL-MASRY, J. W. COOK, JR., J. F. SCHETZINA, J. REN, and J. A. EDMOND, *J. Vac. Sci. Technol. B* **14**, 2349 (1996).
- [5] N. KAMATA, K. HOSHINO, T. UCHIDA, K. YAMADA, M. NISHIOKA, and Y. ARAKAWA, *Superlattices and Microstructures* **22**, 521 (1997).
- [6] N. KAMATA, E. KANOH, K. HOSHINO, K. YAMADA, M. NISHIOKA, and Y. ARAKAWA, *Mater. Sci. Forum* **196/201**, 431 (1995).
- [7] N. KAMATA, E. KANOH, K. HOSHINO, K. YAMADA, M. NISHIOKA, and Y. ARAKAWA, *J. Lum.* **63**, 235 (1995).
- [8] B. KIM, I. KUSKOVSKY, I. P. HERMAN, D. LI, and G. F. NEUMARK, *J. Appl. Phys.* **86**, 2034 (1999).
- [9] M. A. RESHCHIKOV, P. VISCONTI, H. MORKOÇ, R. J. MOLNAR, and C. W. LITTON, *Proc. Internat. Workshop Nitride Semicond. 2000, Nagoya (Japan) 2000*.

phys. stat. sol. (a) **183**, 197 (2001)

Subject classification: 68.37.Ps; 78.55.-m; 78.60.Hk; S7.14

Defect Reduction in HVPE Growth of GaN and Related Optical Spectra

T. PASKOVA¹⁾, P. P. PASKOV, V. DARAKCHIEVA, S. TUNGASMITA, J. BIRCH,
and B. MONEMAR

*Department of Physics and Measurement Technology, Linköping University,
S-581 83 Linköping, Sweden*

(Received October 8, 2000)

GaN technology is still based on highly mismatched heteroepitaxial growth on foreign substrates, and therefore needs to overcome a high defect density and a high level of stress in the epitaxial layers. Various attempts have been made to reduce the defects and stress in thick GaN layers. We here report a reduction of the defect density in thick GaN layers grown by hydride vapour phase epitaxy, using regrowth on free-standing GaN films, as well as introducing an AlN buffer and AlN interlayer in the growth sequence. Special focus is put on the optical properties of the material.

1. Introduction Despite the outstanding recent achievements of GaN based optical and electrical devices, the technology still suffers from strongly mismatched heteroepitaxial growth. Although several groups have attempted to cope with heteroepitaxial growth, from the use of nucleation layers to the growth on free-standing crystals, the growth of GaN layers on sapphire is plagued by high densities of extended defects such as dislocations, domain boundaries and cracks. Some of the problems have been significantly reduced in thin metalorganic chemical vapour deposition (MOCVD) grown layers by using low temperature grown AlN or GaN buffer layers [1, 2]. A great promise for the combination of MOCVD grown GaN templates with subsequent homoepitaxially grown GaN by molecular beam epitaxy has been reported as well [3]. Another approach is to develop hydride vapour phase epitaxy (HVPE) grown thick layers and utilising the recently developed laser induced lift-off technique to obtain free-standing quasi-bulk material suitable for subsequent homoepitaxial growth [4]. Over the last years considerable progress has been made in the crystalline quality of thick GaN layers grown by HVPE [5, 6], although the defect density in thick films is still rather high. A defect density $< 10^6 \text{ cm}^{-2}$ is desirable for such free-standing GaN layers, and the recent work towards this goal has been focused on lateral epitaxial overgrowth techniques (LEOG [7] or PENDEO [8]).

In this work, we report on two alternative approaches aiming at reducing the dislocation density in thick GaN films, a HVPE overgrowth on free-standing GaN crystals, and introducing AlN interlayers deposited by high temperature reactive sputtering. Here we focus on the optical properties of such material, in relation to the defect density.

2. Experimental A first series of HVPE-GaN films was initially grown either directly on sapphire, or using a 2 μm thick undoped MOCVD-GaN template. The details of this

¹⁾ Corresponding author; Tel.: 46 13 288961; Fax: 46 13 142337; e-mail: tanya@ifm.liu.se

growth and the physical properties of such thick HVPE-GaN layers have been reported elsewhere [9, 10]. These crack-free GaN films with a thickness in the range of 30–50 μm were easily separated from the sapphire substrates by a laser lift-off process. The third harmonic of a Q-switched YAG:Nd laser has been utilised for delamination of free-standing GaN films. After chemical treatment, the free-standing films have been overgrown on the Ga-face. Quasi-bulk GaN substrates, having a current maximum thickness up to 250 μm , were obtained by HVPE overgrowth on free-standing HVPE-GaN films.

A second series of samples has been grown on sapphire using an AlN buffer layer with a thickness of 500 \AA which had been determined to be the optimum buffer thickness based on the crystalline and electrical quality of the main GaN film [11]. The AlN buffer and interlayer films were deposited on sapphire by low energy ion-assisted reactive dc magnetron sputtering from an elemental Al target in an ultra high vacuum system using pure N_2 as the working gas at $\sim 1000^\circ\text{C}$ substrate temperature. The AlN interlayer thickness was about 200 \AA .

Atomic force microscopy (AFM) measurements were performed with a Nanoscope IIIa instrument operated in tapping mode using Si tips. Photoluminescence (PL) measurements were performed under excitation with the fourth harmonic of a cw Nd:Vanadate laser ($\lambda_{\text{exc}} = 266 \text{ nm}$). The luminescence was detected with a 0.85 m double monochromator and a GaAs photomultiplier using a conventional lock-in technique or with a Czerny-Turner type monochromator and a cooled charge coupled detector (CCD).

3. Results and Discussion There is a clear improvement of the surface morphology in both series of samples, as revealed by AFM data imaging. Figure 1 shows two images of a 40 μm thick GaN layer as-grown on sapphire and of an overgrown layer with a thickness of about 150 μm on the same free-standing layer separated from the sapphire. The surface of the as-grown layer on sapphire is quite smooth consisting of an array of terraces with a width of about 120 nm separated by 5–6 \AA steps. One can also see that some of the steps are terminated tangentially at the edges of large surface depressions due to dislocations of mixed type [3]. The overgrown film on the free-standing GaN film has a lower surface roughness compared to that of the as-grown layer. No terrace depressions were observed and the density of pits affecting the surface smoothness is about a factor two smaller, indicating a decrease of threading dislocations and a change in the dominant growth mechanism. A typical dislocation density in the range of $2 \times 10^9 \text{ cm}^{-2}$ for a 40 μm thick GaN film grown directly on sapphire and of about $5 \times 10^8 \text{ cm}^{-2}$ for the overgrown film has been determined. Two images of a GaN layer grown with an AlN buffer and of another GaN layer grown on the same buffer and including a 200 \AA thick AlN interlayer as well are shown in Figs. 2a and b, respectively. A decrease of dislocation density with a factor of 3 can be estimated from the images with respective values of 1.5×10^9 and $4 \times 10^8 \text{ cm}^{-2}$. A reduction of threading dislocations was always observed with an introduction of interlayers in the MOCVD growth [12]. We observed a similar dislocation filtering effect of the interlayer in the HVPE growth. Moreover, the effect is slightly stronger because the reduction of three times was obtained by using a single interlayer, while the reduction per interlayer in the MOCVD growth is about a factor 2 as reported by introducing several interlayers [12]. Cathodoluminescence (CL) spectra taken from the same layers without and with an AlN interlayer are shown in Fig. 3a. The strongest DBE peak in the spectrum of the

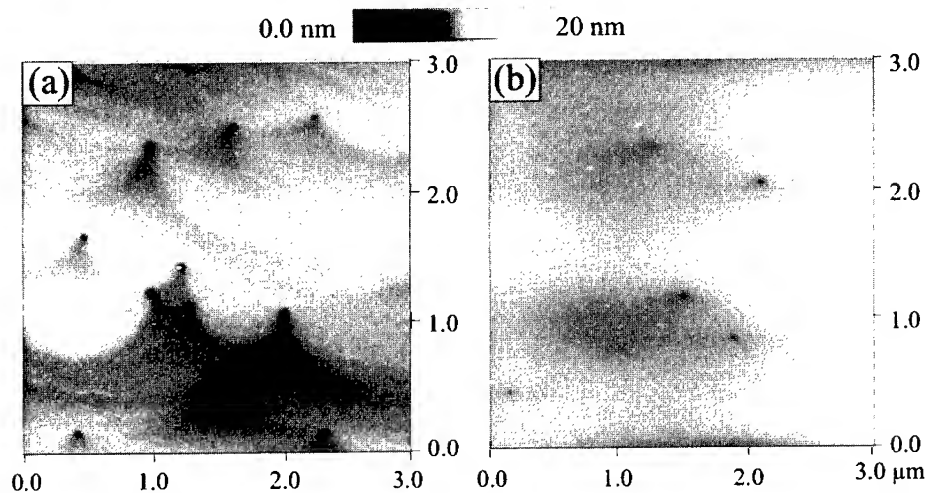


Fig. 1. AFM images of the top surface of GaN layers a) grown directly on sapphire and b) grown on free-standing GaN

film with the interlayer is shifted to lower energies by 7 meV, indicating a significant decrease of the strain due to the AlN interlayer. At the same time there is no significant decrease of the linewidths of the excitonic peaks in the PL spectra.

A precise investigation of the strain in such films was performed by photoluminescence for the first series of samples. A PL spectrum of an as-grown 40 μm thick GaN layer on sapphire together with a spectrum of the same film after separation, and two spectra of the overgrown free-standing GaN films (up to thicknesses of 100 and 200 μm) are shown in Fig. 3b. As can be seen, the narrow (≈ 2 meV) exciton peaks in the spectrum of the as-grown film are fully reproduced in the overgrown films indicat-

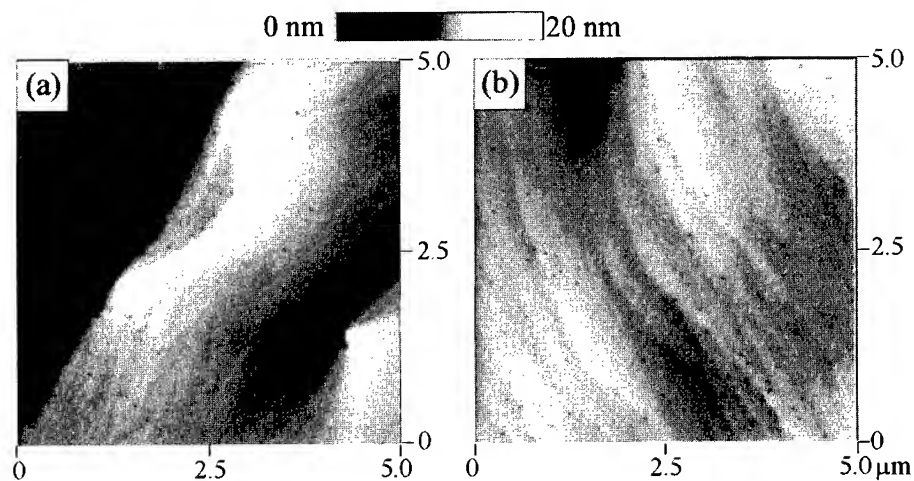


Fig. 2. AFM images of the top surface of the GaN layers grown on sapphire with a) an AlN buffer and with b) additionally introducing an AlN interlayer

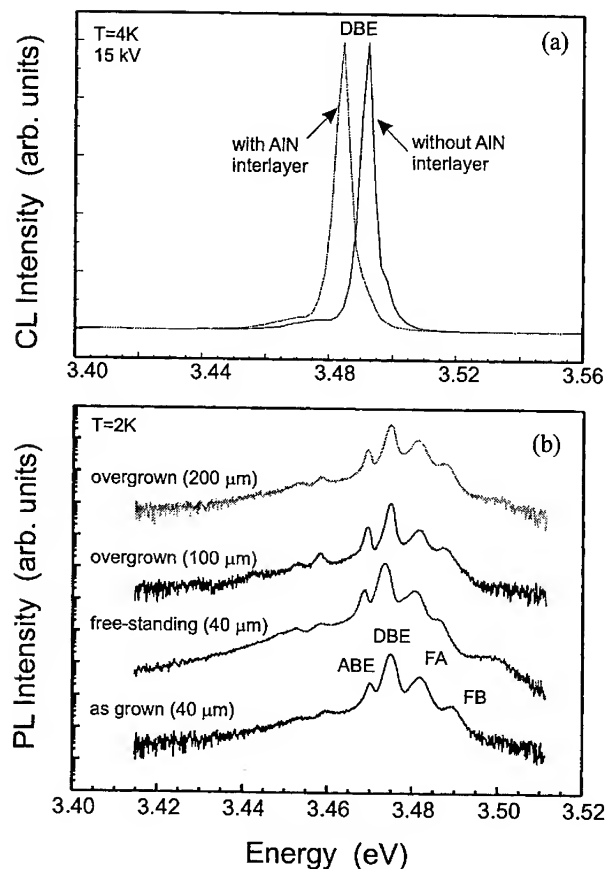


Fig. 3. a) Cathodoluminescence spectra of GaN films without and with an AlN interlayer. b) Photoluminescence spectra of as-grown, free-standing and overgrown GaN films

ing their good crystalline quality. There is a small shift of the DBE position of the as-grown film compared to those of the separated and the overgrown films. Such a shift is expected due to the substrate-induced compressive strain and its small magnitude may be explained by a relaxation present in the thick film even before the lift-off. However, there is a shift of about 3 meV in all free-standing samples thicker than 40 μm with respect to the reported energy position of the DBE (3.471 eV [13]) in the MOCVD-grown homoepitaxial strain-free material. We performed a systematic study of the PL peak positions of thick HVPE layers with different thicknesses before and after the separation process, and the results are shown in Fig. 4a. It can be seen that the shift of the PL peaks is more pronounced for relatively thin films with a thickness of about 15 μm while the shift is rather small ≈ 1 meV in thicker films and remains almost constant independent of increasing thickness. Similar behaviour of PL shifting (Fig. 4b) and the tendency of stress decrease with increasing thickness has been obtained in a series of separated and overgrown samples when the initial film was grown on sapphire using MOCVD templates, which exhibit one order of magnitude lower defect density. In such films, the DBE peak position is very close to the reported value for a homoepitaxial MOCVD layer on bulk crystals [13]. These rather small variations in the PL peak positions correspond to a small variation in the bandgap and the corresponding lattice param-

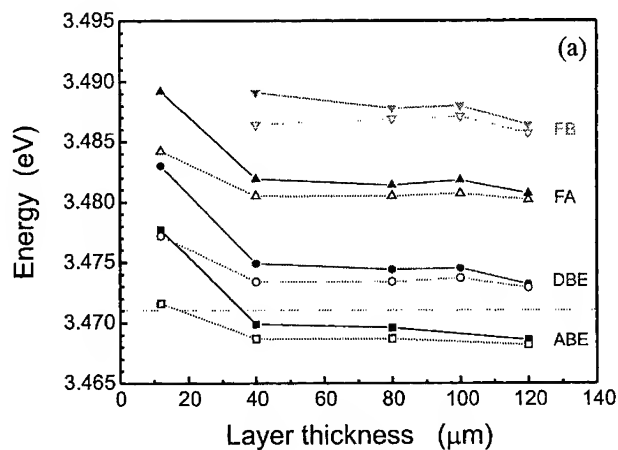
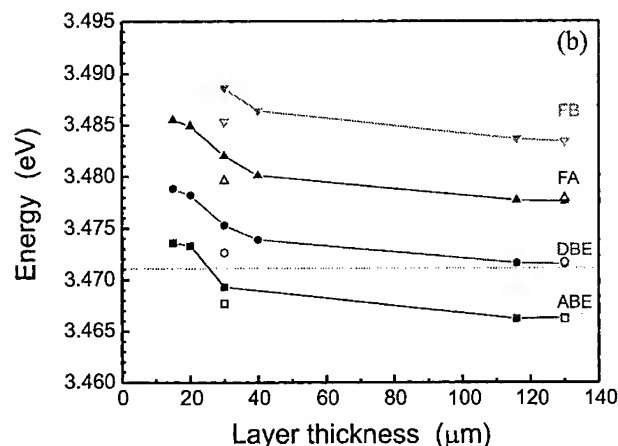


Fig. 4. Photoluminescence peak positions of thick HVPE-GaN films, before and after separation, with different thicknesses

a) grown directly on sapphire and b) grown on sapphire with MOCVD template. The solid lines connect the points of as-grown layers, the dotted lines connect the points of the same samples after separation. The horizontal line indicates the position of the DBE in homoepitaxial strain-free films



eters in the films, and reflect the defect distribution in the material (both dislocations and point defects).

It should be noted that the linewidth of the DBE is about 2 meV in all spectra of the layers without cracks and with a dislocation density in the range of 10^8 – 10^{10} cm $^{-2}$. The linewidths narrow down to 1 meV in layers thicker than 80 μ m with dislocation density expected to be down to 10^6 – 10^7 cm $^{-2}$. In these samples crack formation is observed, believed to be connected with the lower dislocation density. In the same free-standing samples where the strain is reduced to a certain extent, even narrower DBE lines are observed (Fig. 5a).

We also present preliminary results of the polarization dependent PL measurements of the same as-grown sample (Fig. 5b). The laser beam was focused to a spot of ≈ 2 μ m diameter by a reflective objective. The spectra are taken from the cleaved edge facet of the sample about 10 μ m below the top surface. Due to the well resolved free-exciton peaks the spectra clearly reveal the selection rules for the optical transitions in wurtzite GaN. For the σ -polarization ($\mathbf{E} \perp \mathbf{c}$, $\mathbf{k} \perp \mathbf{c}$) the emission from the optically active excitons with Γ_5 symmetry is seen. In the case of π -polarization ($\mathbf{E} \parallel \mathbf{c}$, $\mathbf{k} \perp \mathbf{c}$), only the B

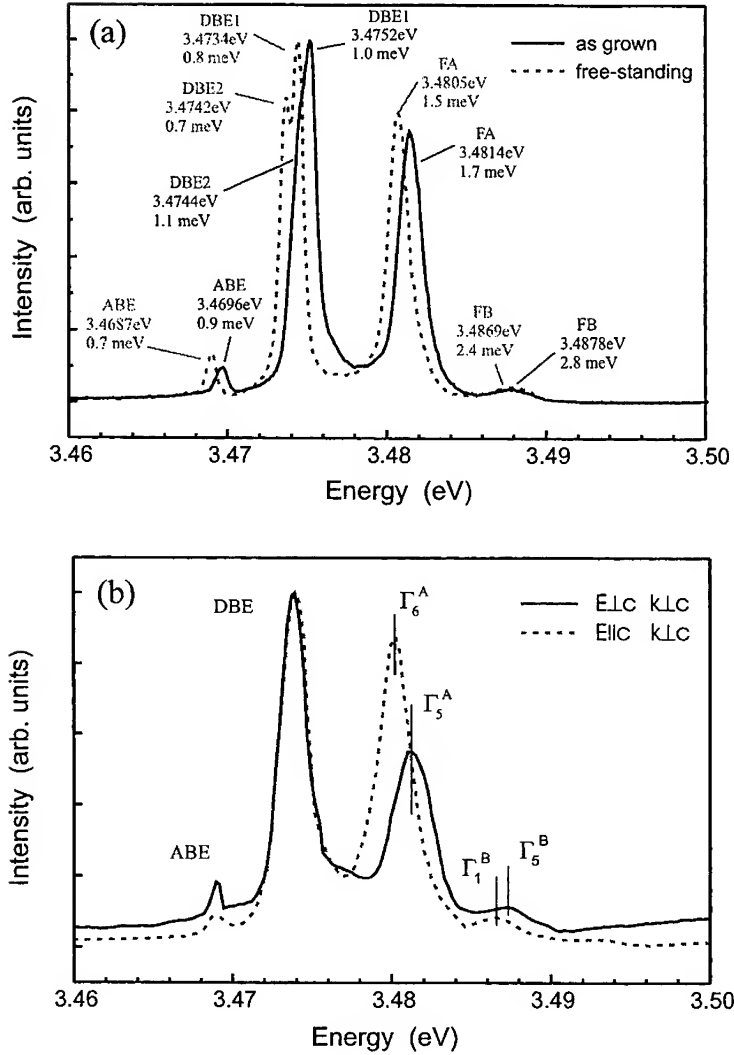


Fig. 5. a) Unpolarized PL spectra of as-grown and free-standing GaN films with a thickness of 80 μm . b) PL spectra taken from the cleaved edge facet of the as-grown sample for σ -polarization ($\mathbf{E} \perp \mathbf{c}, \mathbf{k} \perp \mathbf{c}$) and π -polarization ($\mathbf{E} \parallel \mathbf{c}, \mathbf{k} \perp \mathbf{c}$)

and C exciton states with Γ_1 symmetry are optically active. Nevertheless, an emission peak in the spectral region of the A exciton is observed. We identify this peak as the spin-triplet state (Γ_6 symmetry) of the A exciton. The Γ_6 state is optically forbidden in the wurtzite structure and its appearance in the spectra can be attributed to the mixing with the Γ_1 state of the B excitons. Such a mixing is expected for GaN due to the small energy splitting between the A and B excitons. The energy difference between the peaks assigned as Γ_5^A and Γ_6^A is a direct measure of the electron-hole exchange interaction. It is found to be (0.94 ± 0.03) meV for the A exciton. This value is more than three times larger than the one measured previously in a thicker HVPE sample [14],

but agrees with the value of (0.91 ± 0.05) meV derived from magnetorefectance data of an homoepitaxial MOCVD layer [15] and is close to the value of (0.6 ± 0.1) meV estimated by Julier et al. [16]. From the spectra in Fig. 5b we can also estimate the splitting between the two optically active B exciton states $[\Gamma_5^B \Gamma_1^B = (0.69 \pm 0.1) \text{ meV}]$. It is worth noting that the splitting between the exciton states with different symmetries strongly depends on the strain usually present in the GaN layers [17]. Therefore more precise determinations of the exchange interaction constant should be done on a strain-free sample or on a series of samples with different strain.

4. Summary Thick GaN films grown by HVPE using both overgrowth on free-standing GaN crystals and introducing an AlN interlayer have been demonstrated, with improved morphology and reduced defect density. The photoluminescence study shows the dependence of the linewidth of the excitonic peaks on the defect density, and the residual strain in the films via the spectral positions of the PL peaks. Preliminary data for the exchange splitting of the A and B excitons are reported from polarized PL measurements on a cleaved edge of a thick GaN layer.

References

- [1] I. AKASAKI, H. AMANO, Y. KOIDE, K. HIRAMATSU, and N. SAWAKI, *J. Cryst. Growth* **98**, 209 (1989).
- [2] S. NAKAMURA, *Jpn. J. Appl. Phys.* **30**, L1705 (1991).
- [3] E. J. TARSA, B. HEYING, X. H. WU, P. FINI, S. P. DENBAARS, and J. S. SPECK, *J. Appl. Phys.* **82**, 5472 (1997).
- [4] C. R. MISKYS, M. K. KELLY, O. AMBACHER, G. MARTINEZ-CRIADO, and M. STUTZMANN, *Appl. Phys. Lett.* **77**, 1858 (2000).
- [5] R. J. MOLNAR, W. GÖTZ, L. T. ROMANO, and N. M. JOHNSON, *J. Cryst. Growth* **178**, 147 (1997).
- [6] YU. MELNIK, A. NIKOLAEV, I. NIKITINA, K. VASSILEVSKI, and V. DMITRIEV, *Mater. Res. Soc. Symp. Proc.* **482**, 269 (1998).
- [7] A. USUI, H. SUNAKAWA, A. SAKAI, and A. A. YAMAGUCHI, *Jpn. J. Appl. Phys.* **36**, L899 (1997).
- [8] TS. S. ZHELEVA, S. A. SMITH, D. B. THOMSON, T. GEHRKE, K. J. LINTHICUM, P. RAJAGOPAL, W. M. ASHMAWI, and R. F. DAVIS, *Mater. Res. Soc. Symp. Proc.* **537**, G3.38 (1999).
- [9] T. PASKOVA, E. M. GOLDS, and B. MONEMAR, *J. Cryst. Growth* **203**, 1 (1999).
- [10] T. PASKOVA, S. TUNGASMITA, E. VALCHEVA, E. B. SVEDBERG, B. ARNAUDOV, S. EVTIMOVA, P. O. Å. PERSSON, A. HENRY, R. BECCARD, M. HEUKEN, and B. MONEMAR, *Mater. Res. Soc. Symp. Proc.* **595**, W3.14 (2000).
- [11] T. PASKOVA, E. VALCHEVA, J. BIRCH, S. TUNGASMITA, P. O. Å. PERSSON, P. P. PASKOV, S. EVTIMOVA, M. ABRASHEV, and B. MONEMAR, *J. Cryst. Growth* (in press).
- [12] H. AMANO, M. IWAYA, T. KASHIMA, M. KATSURAGAWA, I. AKASAKI, J. HAN, S. HEARNE, J. A. FLORO, E. CHASON, and J. FIGIEL, *Jpn. J. Appl. Phys.* **37**, L1540 (1998).
- [13] K. KORNITZER, T. EBNER, K. THONKE, R. SAUER, C. KIRCHNER, V. SCHWEGLER, M. KAMP, M. LESZCZYNSKI, I. GRZEGORY, and S. POROWSKI, *Phys. Rev. B* **60**, 1471 (1999).
- [14] A. HOFFMANN and L. ECKEY, *Mater. Sci. Forum* **264/269**, 1259 (1998).
- [15] R. STEPNIIEWSKI, M. POTEMSKI, A. WYSMOLEK, K. PAKULA, J. M. BARANOWSKI, J. LUSAKOWSKI, I. GRZEGORY, S. POROWSKI, G. MARTINEZ, and P. WYDER, *Phys. Rev. B* **60**, 4438 (1999).
- [16] M. JULIER, J. CAMPO, B. GIL, and J. P. LASCARAY, *Phys. Rev. B* **57**, R6791 (1998).
- [17] B. GIL, A. HOFFMANN, S. CLUR, L. ECKEY, O. BRIOT, and R. L. AULOMBARD, *J. Cryst. Growth* **189/190**, 639 (1998).

Author Index

P. ABOUGHÉ NZÉ	67	G.H. GAINER	105
R.A. ABRAM	183	I. GALBRAITH	87
I. AKASAKI	51	M. GALLART	61
D. ALDERIGHI	129	J.-M. GÉRARD	11
A. ALEXANDROU	29	B. GIL	61, 111, 125
J. ALLÈGRE	61	G. GLASTRE	35
H. AMANO	51	J. GLEIZE	157
R. ANDRÉ	29	S. GOTTARDO	129
L.C. ANDREANI	11	N. GRANDJEAN	35, 61, 129, 139, 157
N. ANTOINE-VINCENT	163		
E. AUJOL	5	V. HÄRLE	169
		M. HIRASAWA	189
S. BADER	169	A. HOFFMANN	99
J.P. BERGMAN	151	D. HULIN	29
S. BIDNYK	105	S.J. HWANG	105
P. BIGENWALD	111, 125		
J. BIRCH	197	K. INOUE	41
F. BŒUF	29	T. IZUMI	41
F. BOGANI	129		
S. BRAND	183	C. JOUANIN	17, 135
O. BRANDT	91		
M.D. BREMSER	151	M.A. KALITEEVSKI	183
G. BRÜDERL	169	N. KAMATA	189
C. BRU-CHEVALLIER	67	A. KANETA	41
G.E. BULMAN	105	M. KASUMI	51
		A.V. KAVOKIN	23, 75, 121, 125
R. CADORET	5	Y. KAWAKAMI	41
A. DI CARLO	81, 121	H.-S. KIM	145
D. CASSAGNE	17, 135	K.-S. KIM	145
S.F. CHICHIBU	91	T. KIM	145
P. CHRISTOL	125	H. KLAUSING	189
M. COLOCCI	129	H.S. KONG	105
D. COQUILLAT	135	J. KRASINSKI	105
		T.F. KRAUSS	145
B. DAMILANO	61, 139	I.L. KRESTNIKOV	99
LE SI DANG	29	M. KUBALL	157
V. DARAKCHIEVA	197	Y.H. KWON	105
B. DAUDIN	67, 157		
R.F. DAVIS	151	J.B. LAM	105
M.D. DAWSON	145	J.F. LAMPIN	29
F. DEMANGEOT	157	N.N. LEDENTSOV	99
S.P. DENBAARS	91	P. LEFEBVRE	61
P. DISSEIX	139, 163	P. LEGAGNEUX	35
K.P. O'DONNELL	117	A. LELL	169
L. DUA	35	M. LEROUX	163
C. DUBOIS	67	J. LEYMARIE	139, 163
J.-Y. DUBOZ	35	B.D. LITTLE	105
		P. LUGLI	121
N.V. EDWARDS	151		
P.R. EDWARDS	145	G. MALPUECH	23, 75, 163
I. ELIASHEVICH	177	J.H. MARSH	145
		R.W. MARTIN	145
S. FANGET	67	E. MARTINEZ-GUERRERO	67
J. FRANDON	157	J. MASSIES	35, 61, 129, 139, 163
Sg. FUJITA	41	H. MATHIEU	61

- | | | | |
|----------------------------------|----------|-----------------------------------|----------|
| B. MONEMAR | 151, 197 | O. SEMCHINOVA | 189 |
| Y. MONTEIL | 67 | F. SEMOND | 35, 163 |
| A. MOREL | 61 | B. SERMAGE | 23 |
| T. MUKAI | 41 | S.K. SHEE | 105 |
| S. NAKAMURA | 91 | L. SIOZADE | 139 |
| Y. NARUKAWA | 41 | J.J. SONG | 105 |
| V.V. NIKOLAEV | 177, 183 | T. SOTA | 91 |
| K. OKAMOTO | 41 | J. STEMMER | 189 |
| K. OMAE | 41 | M. STRASSBURG | 99 |
| G. PANZARINI | 11 | T. SUGAHARA | 105 |
| G.H. PARK | 105 | T. TALIERCIO | 61 |
| P.P. PASKOV | 197 | V. THIERRY-MIEG | 23 |
| T. PASKOVA | 197 | C. TRAGER-COWAN | 145 |
| R. PECHARROMAN-GALLEG0 | 145 | A. TRASSOUDAINÉ | 5 |
| E. PÉRONNE | 29 | S. TUNGASMITA | 197 |
| A. PHILIPPE | 67 | A. VASSON | 139, 163 |
| K.H. PLOOG | 91 | M. LE VASSOR D'YERVILLE | 17, 135 |
| M.E. PORTNOI | 87, 177 | A. VINATTIERI | 129 |
| G. POZINA | 151 | K. WADA | 91 |
| A. REALE | 121 | I.M. WATSON | 145 |
| M.A. RENUCCI | 157 | A. WEIMAR | 169 |
| A. RIBAYROL | 135 | C. WETZEL | 51 |
| R. ROMESTAIN | 29 | K. YAMADA | 189 |
| R.M. DE LA RUE | 135, 145 | J.M. ZANARDI OCAMPO | 189 |
| S. SAUJOU | 41 | | |
| N. SCHNELL | 163 | | |

The aim of "physica status solidi (b)" and "physica status solidi (a)" is the rapid publication of important and new results in the field of solid state physics, both in fundamental and applied research. Issues of "physica status solidi (b)" and "physica status solidi (a)" are published each in 15 issues which appear on the 1st (8th) and 16th (23rd) day of the month, respectively.

Papers in each issue are grouped into the following categories:

- **Review Articles:** Mainly by invitation of the Editors.
- **Original Papers:** Manuscripts containing original and previously unpublished work of general interest. Time for publication after review and acceptance is typical two months. Authors will receive page proofs for review articles and original papers prior to publication.
- **Rapid Research Notes:** A forum for fast publication of new and interesting results. These notes are limited to three printed pages. They will be available in electronic form on the Internet within typical two weeks and will also be published in printed form in the next issue.

All manuscripts will be thoroughly refereed before acceptance.

Reprints free of charge will be provided for Review Articles and Original Papers. Additional reprints can be purchased.

Instructions for Authors

Manuscripts may be submitted either by conventional mail to physica status solidi, WILEY-VCH Verlag Berlin GmbH, Böhrlingstr. 10, D-13086 Berlin, or by electronic mail to pss@wiley-vch-berlin.de or to one of the Regional Editors (see list on inside front cover).

Manuscripts submitted by conventional mail should be printed (or typed) double-spaced on one side of paper only and sent in triplicate. Authors who prepare their papers in LATEX (TEX), WORD, or WORD PERFECT are encouraged to submit a floppy disk together with their manuscript. (Please ensure that the text is identical in the hard copy and in the soft copy.)

Classification of the manuscripts (PACS numbers and substance classification), the author's name, institution, address, Fax/telephone number and electronic-mail address should be given. The classification scheme is available on our homepage <http://www.physica-status-solidi.com>.

An abstract of about ten lines in English is required for original papers. A second abstract in German, French, or Russian can be added at the author's request.

Equations should be typewritten and numbered sequentially. Separate lines for equations should be used. Special care should be taken to distinguish subscripts, superscripts, and certain symbols. SI-units should be used throughout.

References should be numbered [in square brackets] and listed in the order of appearance on a separate sheet, in the format used in physica status solidi.

Carefully prepared, photoreproducible figures are required. They should be enclosed on separate sheets of paper. The lettering and symbols should be large and clear enough for reduction. Avoid small open symbols, small dots and small decimal points. Photographs should be submitted on white paper; color prints are possible at additional cost. Duplicates for all figures are desirable. Figure captions should be printed on a separate sheet of paper (with special instructions concerning the size of illustrations, if applicable).

Badly arranged or illegible manuscripts or figures are returned.

Electronic submissions should be made to pss@wiley-vch-berlin.de. The Editorial Office can process files formatted in LATEX (TEX). All textual material of the paper (including tables, captions, etc.) should be in a single file. Original figures for production should be submitted by regular mail, review-quality copies of the figures can be sent by Fax. Also electronic-mail transmission of Postscript-formatted figures is possible.

Electronically submitted manuscripts should **not** be sent again by normal mail.

Bimberg, D. / Grundmann, M. /
Ledentsov, N. N.

Quantum Dot Heterostructures

1998. 338 pages. Hardcover.
Approx. DM 278.-/£90.00
ISBN 0-471-97388-2

Quantum dots and pyramids are nanometre-sized semiconductor structures and represent one of the key goals of semiconductor research. This publication presents a comprehensive overview of the most recent advances in the field, including the way such structures are grown, how experiments on the structures have clarified long-standing theoretical predictions, how the structures are characterised and the performance of devices developed from the structures.

Lorenz, W. J. / Plieth, W. (eds.)

Electrochemical Nanotechnology

**In Situ Local Probe Techniques
at Electrochemical Interfaces**

1998. XIV, 332 pages, 141 figs,
5 tabs. Hardcover. DM 228.-/£80.00
ISBN 3-527-29520-8

The in-situ application of local probe methods in different systems belongs to modern nanotechnology and has two aspects: an analytical aspect and a preparative aspect. This IUPAC monograph is a comprehensive treatment of both aspects and presents the current state of knowledge. It is written for scientists active in this area.

Ekardt, W. (ed.)

Metal Clusters

1999. Approx. 300 pages. Hardcover.
Approx. DM 248.-/Approx. £80.00
ISBN 0-471-98783-2

The study of metal clusters and aggregates is a mature discipline. This book sets out the current state of knowledge in the subject, including both the fundamental principles and the most recent results. Linking theory with experiments, this book is certain to become a standard reference in the field.

Evans, D. F. / Wenneström, H.

The Colloidal Domain

**Where Physics, Chemistry and Biology
Meet**
Second Edition

1999. Approx. 672 pages. Hardcover.
Approx. DM 178.-/£58.50
ISBN 0-471-24247-0

Providing authoritative coverage of theory, methods and applications of colloid science, this thoroughly updated edition of a popular book presents an authoritative description of the critical developments in colloid science over the past several decades. It contains new worked examples, short biographies of famous scientists, a new data table appendix and also a new final chapter on the historical development of key concepts and ideas in the field.

From Reviews:

"... very well written and brings a focus and a perspective that are not currently available in one convenient volume... I strongly recommend it to anyone interested in colloid science and especially those interested in surfactant systems."

*Journal of Colloid and Interface
Science*

"... extremely valuable for explaining the intricate and rather complex phenomenon that occurs in self-assembling systems"

Chemistry and Industry

Fendler, J. H. (ed.)

Nanoparticles and Nanostructured Films

**Preparation, Characterization and
Applications**

1998. XX, 468 pages, 275 figs,
36 tabs. Hardcover. DM 298.-/£105.00
ISBN 3-527-29443-0

In this concise handbook leading experts of the field give a broad overview of the latest developments in the emerging and fascinating field of nano-sized materials.

Synthesis, characterization, properties, and future applications are discussed in detail. This wealth of information makes it invaluable for graduate students entering this new field of research as well as to materials scientists, chemists and physicists looking for comprehensive treatment of the topic.



Nanotechnology

Please send for your
comprehensive
Microsystems- and
Nanotechnology Brochure
today!

WILEY-VCH
P.O. Box 10 11 61
69451 Weinheim, Germany
Fax: +49 (0) 62 01-60 61 84
e-mail: sales-books@wiley-vch.de
<http://www.wiley-vch.de/>

John Wiley & Sons, Ltd.
Baffins Lane
Chichester, West Sussex,
PO19 1UD, UK
Tel: +44 (0) 1243-843294
Fax: +44 (0) 1243-843296
e-mail: cs-books@wiley.co.uk

Prices are subject to change.

 **WILEY**

 **WILEY-VCH**